Study on the Top Quark Pair Production Mechanism in 1.96TeV Proton-Antiproton Collisions

1.96TeV 陽子・反陽子衝突実験における トップクォーク対生成機構の研究

March 2008

Junji Naganoma

Study on the Top Quark Pair Production Mechanism in 1.96TeV Proton-Antiproton Collisions

1.96TeV 陽子・反陽子衝突実験における トップクォーク対生成機構の研究

2008年3月

早稲田大学大学院 理工学研究科
物理学及応用物理学専攻 理論核物理学研究

永野間 淳二

Abstract

The study of the top quark pair production mechanism in proton-antiproton collisions at a center-of-mass energy of 1.96 TeV is described. The main subjects are the measurements of the top quark pair production cross section, the top quark mass and a search for a new particle decaying to the top quark pair. The analyses are based on 1.9 fb^{-1} of data collected by the Collider Detector at Fermilab (CDF) Run II experiment between March 2002 and May 2007, using the lepton+jets events. The measured top quark pair production cross section is 8.2 ± 0.5 (stat.) $\pm$ 0.8 (syst.) $\pm$ 0.5 (lum.) pb, which is slightly higher than the standard model prediction at the top mass of 175 GeV/c^2. The top quark mass is an important parameter in the standard model, and also in the experimental studies. The measured top quark mass is 171.6 ± 2.0 (stat.) $\pm$ 1.3 (syst.) GeV/c^2. Finally, we report on a search for a new gauge boson decaying to $t\bar{t}$, which interferes with the standard model gluon in the $q\bar{q} \to t\bar{t}$ production process. We call such a hypothetical particle a "Massive Gluon". The observed $t\bar{t}$ invariant mass distribution is consistent with the standard model expectations, and also the measured massive gluon coupling strength with quarks is consistent within a statistical fluctuation of the standard model expectation in the wide range of the massive gluon masses and widths. We set the upper and lower limits on the coupling strength of the massive gluon.

Acknowledgments

This dissertation could not have been finished without the dedication and support of many people. First of all, I would like to thank my supervisor, Prof. Kunitaka Kondo for giving me the opportunity to work on the interesting topics during my years at CDF, sharing his great insight into physics, and being a patient adviser. I would like to thank Prof. Masatoshi Takano for accepting me to his laboratory to perform the thesis work at Waseda University after Prof. Kondo retired from Waseda. I would also like to thank Prof. Shinhong Kim for giving me the opportunity to work at Fermilab, and providing me with the place to continue the CDF work at Tsukuba University when I was back to Japan.

I thank members of the CDF Collaboration and the technical staff of Fermilab for providing world-class research facilities with their endless hard work, days and nights. I thank Dr. Kaori Maeshima for providing me with the opportunity to work on the CDF online monitoring system which make me familiar with the CDF data acquisition system.

I thank Dr. Anton Anastassov, Dr. Kenichi Hatakeyama, and Dr. Steve Kuhlmann for giving me the opportunity to work on the jet energy resolution improvements at my early days at CDF. They are the real experts on the jet and the calorimetry system. I could become familiar with the real CDF work, and they taught me the importance of the careful and vigilant analysis.

I want to thank the experts of Lepton+Jets analysis, especially Dr. Kevin Lannon, Prof. Jason Nielsen, Prof. Anyes Taffard, and Prof. Weiming Yao. Their expertise was essential to my analysis.

I thank Prof. Florencia Canelli, Prof. Robin Erbacher, Prof. Takasumi Maruyama, Dr. Nick Van Remortel, Prof. Evelyn Thomson, Prof. Kirsten Tollefson, Dr. George Velev, Prof. Daniel Whiteson, and all the members of CDF TopMass and Top groups for encouraging me to pursue the analysis.

I would like to express the special thanks to all the members of CDF Japan group, especially Dr. Yoshiaki Kusakabe, for sharing a lot of great times with me at Fermilab.

This work was supported by the U.S. Department of Energy and National Science Foundation; the Ministry of Education, Culture, Sports, Science and Technology of Japan; the Italian Istituto Nazionale di Fisica Nucleare; the Natural Sciences and Engineering Research Council of Canada; the National Science Council of the Re-

public of China; the Swiss National Science Foundation; the A.P. Sloan Foundation; the Bundesministerium fuer Bildung und Forschung, Germany; the Korean Science and Engineering Foundation and the Korean Research Foundation; the Particle Physics and Astronomy Research Council and the Royal Society, UK; the Russian Foundation for Basic Research; the Comision Interministerial de Ciencia y Tecnologia, Spain; and in part by the European Community's Human Potential Programme under contract HPRN-CT-20002, Probe for New Physics.

I want to express the best of my thanks to my parents.

Contents

1 Introduction **1**
1.1 The Standard Model . . . 1
1.2 The Top Quark . . . 2
1.3 Top Quark Production . . . 3
1.4 Top Quark Decay . . . 4
1.5 Top Quark Mass . . . 5
1.6 Massive Gluon . . . 6

2 Experimental Apparatus **10**
2.1 The Fermilab's Accelerator Chain . . . 10
2.1.1 The Pre-accelerator . . . 10
2.1.2 The Linac . . . 12
2.1.3 The Booster . . . 12
2.1.4 The Main Injector . . . 13
2.1.5 The Antiproton Source . . . 13
2.1.6 The Recycler . . . 14
2.1.7 The Tevatron . . . 14
2.2 The CDF Detector . . . 15
2.2.1 Tracking System . . . 17
2.2.2 Calorimeters . . . 19
2.2.3 Muon Detectors . . . 20
2.2.4 Trigger System . . . 21

3 Dataset and Event Selection **23**
3.1 Electron . . . 23
3.1.1 Electron Trigger . . . 23
3.1.2 Electron Clustering . . . 23
3.1.3 Electron Corrections . . . 24
3.1.4 Electron Geometric and Kinematic Cuts . . . 24
3.1.5 Electron Identification Cuts . . . 25
3.2 Muon . . . 27
3.2.1 Muon Triggers . . . 27
3.2.2 Muon Geometric and Kinematic Cuts . . . 27

3.2.3 Muon Identification Cuts . . . 28
3.3 Jet . . . 29
3.3.1 Jet Clustering Algorithm, *JetClu* . . . 29
3.3.2 Variables in *JetClu* . . . 30
3.3.3 Jet Energy Corrections . . . 31
3.3.4 Jet Energy Scale Uncertainties . . . 33
3.4 Bottom Quark Tagging . . . 34
3.5 Missing Transverse Energy . . . 34
3.6 Primary Vertex . . . 35
3.7 Luminosity Measurement . . . 36
3.8 The Lepton+Jets Event Selection . . . 37

4 Top Pair Production Cross Section Measurements 39
4.1 *SecVtx* Tagging Algorithm . . . 39
4.1.1 Background Estimation . . . 41
4.1.2 Electroweak and Single Top (MC Based Background) . . . 42
4.1.3 QCD Fake Events (Non-W) . . . 43
4.1.4 W + Heavy Flavor . . . 44
4.1.5 Mistags . . . 44
4.1.6 Top Pair Production Cross Section with *SecVtx* Tag . . . 45
4.2 *JetProb* Tagging Algorithm . . . 46
4.2.1 Top Pair Production Cross Section with *JetProb* Tag . . . 48

5 Top Mass Measurements 49
5.1 Top Mass Measurement by DLM . . . 49
5.1.1 Likelihood Definition . . . 49
5.1.2 Mapping Function . . . 51
5.1.3 Result . . . 52
5.2 Tevatron Top Mass Combination at 1 fb^{-1} . . . 53

6 Top Pair Invariant Mass Reconstruction by DLM 55
6.1 Dynamical Likelihood Method (DLM) . . . 55
6.2 Transfer Function . . . 55
6.2.1 Matching between Quarks and Jets . . . 56
6.2.2 Responses of Each Observable . . . 56
6.2.3 Transfer Function of Jet Energy . . . 58
6.2.4 η and E_T Dependences of Jet Energy TF . . . 58
6.2.5 Parameterization of Light Quark Energy TF . . . 61
6.2.6 Parameterization of Bottom Quark Energy TF . . . 64
6.2.7 Transfer Function of Missing E_T and Its ϕ . . . 67
6.3 Top Pair Invariant Mass Reconstruction . . . 69
6.3.1 Path Calculations . . . 69
6.3.2 $\sqrt{s_{t\bar{t}}}$ Reconstruction with SM $t\bar{t}$ Correct Combination . . . 71

6.3.3 Combination Selection 73

7 Extraction of Coupling Strength **75**
7.1 Signal Reconstructed $\sqrt{s_{t\bar{t}}}$ P.D.F 75
7.1.1 Reconstructed $\sqrt{s_{t\bar{t}}}$ P.D.F with SM Process 81
7.1.2 Check of Resolution Function with Z' Sample 81
7.1.3 Reconstructed $\sqrt{s_{t\bar{t}}}$ P.D.F for Massive Gluon 84
7.2 Background Reconstructed $\sqrt{s_{t\bar{t}}}$ P.D.F 85
7.3 Likelihood Fit of Coupling Strength 87
7.4 Linearity Tests of Coupling Strength 87
7.4.1 Consistency with SM Expectations 90

8 Systematic Uncertainties **94**
8.1 Nominal Response of Coupling Strength 95
8.2 Top Quark Mass and Jet Energy Scale (JES) 96
8.3 Parton Distribution Function (PDF) 98
8.4 Initial and Final State Gluon Radiation 102
8.5 Generator 102
8.6 NLO 102
8.7 W+Jets Q^2 Scale 102
8.8 Background Fraction 102
8.9 B-tagging Efficiency 103
8.10 Multiple Interaction 103
8.11 Lepton P_T 103
8.12 Total Systematic Uncertainties 104
8.13 Incorporation of Systematic Uncertainties 105

9 Results and Conclusion **106**
9.1 Results 106
9.1.1 Top Pair Invariant Mass Distribution 106
9.1.2 Consistencies with the Standard Model Expectations 107
9.1.3 Limits on Coupling Strength 109
9.1.4 Cross Checks 112
9.2 Conclusion 114

A Massive Gluon Probability Density Functions **115**

B Monte Carlo Re-weighting **122**

C All Systematic Uncertainties **124**

D Comparison between Data and Simulations **131**

E Publication List **141**

List of Figures

1.1 Top: Leading-order production diagram for $q\bar{q} \to t\bar{t}$. Bottom: Leading-order production diagrams for $gg \to t\bar{t}$. 3
1.2 NLO calculations of $\sigma_{t\bar{t}}$ [13] for $p\bar{p}$ collisions at $\sqrt{s}$=1.96 TeV as a function of top quark mass. Also shown are the experimental measurements of $\sigma_{t\bar{t}}$ made at CDF using RunII data [14]. 4
1.3 Electroweak constraints on the Higgs boson mass using the current best measurements of W boson and top quark mass (left). Global fit of Higgs boson mass to several electroweak parameters (right). 6
1.4 Feynman diagram: Left diagram is SM $q\bar{q} \to g \to t\bar{t}$. Right diagram is the massive gluon process. These processes interfere. 7
1.5 Left and right plots show the $\lambda = -1$ and $+1$ cases respectively with $\Gamma/M = 0.20$, $M_t = 160$ GeV/c^2, and $\sqrt{s} = 1.8$ TeV. 8
1.6 Total cross section as a function of λ for the various masses and decay widths. 9

2.1 Overview of Fermilab accelerator complex. 11
2.2 Ion source and the electrostatic accelerating column. 12
2.3 A schematic view of the Fermilab Booster injection area. 13
2.4 A simple view of the target station. 14
2.5 Bunch spacing in the Tevatron. 15
2.6 A cross-sectional view of the CDF detector [35]. 16
2.7 A schematic overview of the CDF tracking system. The region of the detector with $|\eta| < 1.0$ is referred to as the central region. 18
2.8 Coverage of the CDF muon systems. 21
2.9 The CDF Trigger and Data Acquistion System. 22

3.1 The total uncertainties of JES as a function of corrected jet p_T in the central calorimeter ($0.2 < |\eta| < 0.6$). 33

4.1 The image of *SecVtx* tagging algorithm. Information of L_{xy} significance is used to be considered "displaced". 40
4.2 The b-tagging efficiency plots as a function of jet E_T (left) and η (right) for the two (tight and loose) operating points. 41

4.3 The plots show the false positive tag rate (including asymmetry corrections) as a function of jet E_T (left) and η (right). These have been measured from inclusive jet data. 41
4.4 The expected and observed number of events sorted by jet multiplicity. The $t\bar{t}$ contribution is normalized to the measured value of 8.2 pb. 45
4.5 The sign of the impact parameter of a track. The impact parameter is positive (negative) if the angle ϕ between the jet axis and the line connecting the primary vertex and the track's point of closest approach to the primary vertex is smaller (bigger) than $\pi/2$. 46
4.6 The *JetProb* b-tagging efficiency plots as a function of jet E_T (left) and η (right). 48
4.7 The expected and observed number of events sorted by jet multiplicity, the jet probability with 1%(left) and 5%(right). The $t\bar{t}$ contribution is normalized to the measured values. 48

5.1 The mapping function for measured ΔJES as a function of input M_{top} and input ΔJES. 52
5.2 The joint likelihood as a function of M_{top} and ΔJES. The cross mark in the center of figure is the maximum point of the likelihood and the blue curve is one σ curve. 52
5.3 2 dimensional fit of JES and top quark mass [55]. 53
5.4 A summary of the top quark mass measurements and the world average top quark mass, using the dataset up to ~ 1 fb^{-1} 54

6.1 The responses of each observable. The first to fourth lines are the lepton, neutrino, light quark, and bottom quark responses, respectively. The first, second, and third columns are the energy (or $\not\!\!E_T$), η, and ϕ responses, respectively. The response variables are shown in the tops of each plot. Numbers in bracket are mean and RMS values. 57
6.2 The physics η (left) and detector η (right) dependences of the jet energy transfer functions for W-daughter and bottom quarks. The vertical axes are the mean values of ξ. The lengths of bar represent the values of RMS in each bin. 59
6.3 The jet energy TF's separated by physics η and detector η regions for W-daughter and bottom quarks. 59
6.4 The jet E_T dependences of jet energy transfer functions for W-daughter (left) and bottom quarks (right). The vertical axes are the mean of ξ. The lengths of bar represent the values of RMS in each bin. 60
6.5 ξ distributions separated by the jet E_T ranges for W-daughter (left) and bottom quarks (right). 60

6.6 The light quark energy TF's for the different jet E_T ranges fitted by T-distributions: The top left 9 plots are ξ distributions in $|\eta(\text{det.})| < 0.07$, the top right 9 plots are those in $0.07 \leq |\eta(\text{det.})| < 1.5$, and the bottom left 9 plots are those in $1.5 \leq |\eta(\text{det.})|$. The bottom right plots in each 9-plot show the χ^2/ndf as a function of jet E_T. The bottom right 9 plots show the fitting results of p_0, p_1, and p_2 (The horizontal axes are the jet E_T). 62

6.7 The jet energy TF's of light quark: The left 3 plots show the parameterized TF's normalized at a given jet E_T. The right 3 9-plot's show the checks of parameterized TF's with the different jet E_T ranges from the ranges to make the parameterized TF's. 63

6.8 The bottom quark energy TF's for the different jet E_T ranges fitted by the modified form of Gaussian: The top left 9 plots are ξ distributions in $|\eta(\text{det.})| < 0.07$, the top right 9 plots are those in $0.07 \leq |\eta(\text{det.})| < 1.5$, and the bottom left 9 plots are those in $1.5 \leq |\eta(\text{det.})|$. The bottom right plots in each 9-plot show the χ^2/ndf as a function of jet E_T. The bottom right 9 plots show the fitting results of p_0, p_1, p_2, and p_3 (The horizontal axes are jet E_T). 65

6.9 The jet energy TF's of bottom quark: The left 3 plots show the parameterized TF's, normalized at given jet E_T. The right 3 9-plot's show the checks of parameterized TF with the different jet E_T ranges from ranges to make the parameterized TF's. 66

6.10 The missing E_T TF: The left 6 plots show the $\xi_{\not{E}_T}$ distributions with the different $\not{E}_T$ ranges. The right 6 plots show the $\not{E}_T$ dependences of fitting parameters. 67

6.11 The ϕ of missing E_T TF: The left 6 plots show the $\xi_{\phi(\not{E}_T)}$ distributions with the different $\not{E}_T$ ranges. The right 3 plots show the $\not{E}_T$ dependences of fitting parameters. 68

6.12 The parameterized $\not{E}_T$ and $\phi(\not{E}_T)$ TF's: The left plot shows the parameterized $\not{E}_T$ TF, and the right plot shows the parameterized $\phi(\not{E}_T)$. These are normalized at a given $\not{E}_T$. 68

6.13 The images of the reconstruction procedures in W boson hadronic decay (left) and W boson leptonic decay (right). Numbers in the bracket are the orders of reconstruction. 70

6.14 The example with $2p_T(l)p_T(\nu)\,[1 - \cos\Delta\phi(l,\nu)] = 90^2\ \text{GeV}^2/c^2$ case. Only ~3% of Lorentzian have the $p_z(\nu)$ solution in this case. 71

6.15 The examples of event likelihood using the SM $t\bar{t}$ MC with the correct combination. The red lines are the true values from generator information. 72

6.16 The left plot shows the $t\bar{t}$ invariant mass distributions of the generator level (histogram) and the reconstruction (dots). The right plot shows the difference between the true values and the reconstructed values of the $t\bar{t}$ invariant mass. 72
6.17 The logarithmic ratios of the correct combination likelihood to the others, $\log(L_{\text{comb.}}/L_{\text{correct}})$, (left: arbitrary scale), and the largest likelihood combination (right) for 1, 3 b-tagging and 2 b-tagging events. . 74
6.18 The comparison of the reconstructed $\sqrt{s_{t\bar{t}}}$ resolutions, using the all (red), the best (blue), and the best and second (green) combinations. 74

7.1 The SM parton level $q\bar{q} \to t\bar{t}$ $\sqrt{s_{t\bar{t}}}$ distribution after the event selection. 76
7.2 The event selection efficiencies as a function of $\sqrt{s_{t\bar{t}_p}}$ for the various massive gluon parameters. 77
7.3 The left plots show the parton level $q\bar{q} \to t\bar{t}$ $\sqrt{s_{t\bar{t}}}$ distributions. The right plots are the ratios of MG/SM histograms with the ratio function times $\sigma_{\text{total}}(\text{SM})/\sigma_{\text{total}}(\text{MG})$ (red line). 77
7.4 The resolution function fitted by Johnson SU function + Gaussian: The horizontal axis is $\sqrt{s_{t\bar{t}_r}} - \sqrt{s_{t\bar{t}_p}}$, and the vertical axis is probability. 79
7.5 The final iteration of the fitting of the parameters $p_i(\sqrt{s_{t\bar{t}_p}})$. 80
7.6 The parameterized resolution function, normalized at each $\sqrt{s_{t\bar{t}_p}}$ point. 80
7.7 The SM $q\bar{q} \to t\bar{t}$ reconstructed $\sqrt{s_{t\bar{t}}}$ distribution (light-blue histogram) and the convoluted signal $\sqrt{s_{t\bar{t}}}$ p.d.f at $\lambda = 0$ (red line). . . . 81
7.8 The example of Z' process: The parton level $\sqrt{s_{t\bar{t}}}$ distribution (left) and the difference between reconstructed and parton level $\sqrt{s_{t\bar{t}}}$ (right) with M(Z')=700 GeV/c^2. 82
7.9 The differences between reconstructed and parton level $\sqrt{s_{t\bar{t}}}$, and the resolution functions (red lines) for the various $M(Z')$, each top right plot is the parton level $\sqrt{s_{t\bar{t}}}$ distribution. 83
7.10 The reconstructed $\sqrt{s_{t\bar{t}}}$ distributions (light-blue histogram) and the convoluted signal $\sqrt{s_{t\bar{t}}}$ p.d.f's (red lines) for the various mass and λ points at $\Gamma/M = 0.2$. 84
7.11 The reconstructed "background $\sqrt{s_{t\bar{t}}}$" distributions. 86
7.12 The total "background $\sqrt{s_{t\bar{t}}}$" p.d.f, fitted by Johnson SU + 2 Gaussian's. 86
7.13 An example of pseudo experiment: The pseudo data distribution and the signal+background best fit functions (left), and $-2\log[L(\lambda)/L_{\max}]$ (right). 88
7.14 The best fit λ distributions from the 10 thousand PEs at $|\lambda| = 0.05$, 0.1, 0.2, $M = 500$ GeV/c^2 and $\Gamma/M = 0.2$. 89
7.15 The mean values of the fitted λ distributions as a function of the true λ from 10k PEs. The lengths of the bar represent the RMS. 89

7.16 The left figure shows the usual confidence interval of $1-\gamma$ confidence level, Φ^{-1} is the quantile, imitating Ref. [57]. The right plot shows the example of the actual pseudo experiments assuming $\Gamma/M = 0.2$ and $M = 500$ GeV/c^2. 90

7.17 The expected fitted λ fluctuations assuming each mass and width (statistical fluctuation only). The vertical axes represent the fitted λ fluctuations and the horizontal axes are the assumed masses, with the fixed widths. 91

7.18 One pseudo experiment example: The 96% C.L. lower and upper limits (left), the lower and upper limits distributions from the 10 thousand psueudo experiments (right), assuming $\Gamma/M = 0.2$ and $M = 700$ GeV/c^2 (statistical fluctuation only). 92

7.19 The expected 95%C.L. lower and upper limits assuming each Γ/M and mass point (statistical fluctuation only). 93

8.1 The likelihood fit results using the nominal distributions. 97

8.2 The example of systematic uncertainty due to the top quark mass and JES uncertainties: The left plots show the changes of shape by shifting top mass by ± 2 GeV/c^2 and JES by $\pm 1\sigma$. The right plot shows the best fitted λ by shifting top mass by ± 2 GeV/c^2 and JES by $\pm 1\sigma$ assuming the massive gluon $M = 400$ GeV/c^2 and $\Gamma/M = 0.05$. 98

8.3 $\Delta\lambda$ as a function of true λ from the top mass and JES uncertainties at the various massive gluon masses and widths. 99

8.4 The top 3 plots show the relative weights of the different PDF sets to CTEQ5L, and the bottom 20 plots show the relative weights of 20 eigen vectors to CTEQ6M central value, as a function of generator level $\sqrt{s_{t\bar{t}}}$. 100

8.5 The reconstructed SM $\sqrt{s_{t\bar{t}}}$ distributions in $q\bar{q} \to t\bar{t}$ (tops) and $gg \to t\bar{t}$ (bottoms) processes. In $q\bar{q} \to t\bar{t}$ process, the effects from the eigen vector uncertainties are small (Top right plots show the 20 eigen vector $\pm 1\sigma$ variations, which are almost identical). In $gg \to t\bar{t}$ process, the difference between MRST72 and MRST75 and the uncertainty of 15th eigen vector gives the visible shape change. 101

8.6 An example of the best fitted λs for the different PDFs at Γ/M=0.2, M=500GeV/c^2, and $\lambda = 0.2$. 101

8.7 The data-MC ratio of tagging efficiency as a function of jet E_T. The blue lines show the uncertainties. 103

8.8 The total Systematic uncertainties as a function of true λ at the massive gluon mass is 450 GeV/c^2 and $\Gamma/M = 0.1$. 104

8.9 Example of the lower/upper limit shifts by the systematic uncertainties at $\Gamma/M = 0.20$, $M = 700$ GeV, $\lambda = 0$ (left) and $\Gamma/M = 0.20$, $M = 600$ GeV and $\lambda = 0$ (right). The histograms are the likelihood functions without the systematic effects, and the smooth lines are the likelihood functions with the systematic effects. 105

9.1 $t\bar{t}$ invariant mass distribution (black points) with SM predicted distribution (histogram). The pink hatch is the background normalization uncertainty. 106
9.2 An example of the likelihood fit (left) and the consistency with the standard model from the statistical fluctuations (right). 107
9.3 The best fitted λs of data (red) as a function of massive gluon mass for the 6 width points, $0.05 \leq \Gamma/M \leq 0.5$. The blue, light blue, yellow, green regions are the central value, 1, 2, and 3 σs from SM expectations. 108
9.4 The left plot shows an example of the likelihood distribution to obtain the 95% C.L. limits at $\Gamma/M = 0.1$ and $M = 800$ GeV/c. The right plot shows the obtained limits (arrows) with the expected limits obtained by the standard model MC (histograms). 109
9.5 Limits on λ as a function of the massive gluon mass at each width including the systematic uncertainty effects. The yellow regions are excluded, and only the white regions are allowed in 95% confidence level. 110
9.6 The top quark p_T distributions of data (black points) and the SM predictions (histograms) in the hadronic (left) and leptonic (right) decays. 112
9.7 The data (black points) and the standard model MC (histograms) most probable response variables of E_T of b-quark (left), light-quark (middle), and the p_T of neutrino (right). 113
9.8 The likelihood distributions of data (black points) and the standard model MC (histogram). 113

A.1 The SM+MG reconstructed $\sqrt{s_{t\bar{t}}}$ p.d.fs with $\Gamma/M = 0.05$. 116
A.2 The SM+MG reconstructed $\sqrt{s_{t\bar{t}}}$ p.d.fs with $\Gamma/M = 0.10$. 117
A.3 The SM+MG reconstructed $\sqrt{s_{t\bar{t}}}$ p.d.fs with $\Gamma/M = 0.20$. 118
A.4 The SM+MG reconstructed $\sqrt{s_{t\bar{t}}}$ p.d.fs with $\Gamma/M = 0.30$. 119
A.5 The SM+MG reconstructed $\sqrt{s_{t\bar{t}}}$ p.d.fs with $\Gamma/M = 0.40$. 120
A.6 The SM+MG reconstructed $\sqrt{s_{t\bar{t}}}$ p.d.fs with $\Gamma/M = 0.50$. 121

B.1 The standard model (green), generated (red) and re-weighted (blue) reconstructed $\sqrt{s_{t\bar{t}}}$ distributions with $\lambda = \pm 0.2$, $M = 500, 700$ GeV/c^2, and $\Gamma/M = 0.2$. Each bottom plot shows the (re-weighted)/(generated) ratio. 122

B.2 The standard model (green), generated (red) and re-weighted (blue) observed level p_T distributions with $\lambda = \pm 0.2$, $M = 500, 700$ GeV/c^2, and $\Gamma/M = 0.2$. Each bottom plot shows the (re-weighted)/(generated) ratio. 123

C.1 Total systematic uncertainties as a function of true λ at $\Gamma/M = 0.05$. 125
C.2 Total systematic uncertainties as a function of true λ at $\Gamma/M = 0.10$. 126
C.3 Total systematic uncertainties as a function of true λ at $\Gamma/M = 0.20$. 127
C.4 Total systematic uncertainties as a function of true λ at $\Gamma/M = 0.30$. 128
C.5 Total systematic uncertainties as a function of true λ at $\Gamma/M = 0.40$. 129
C.6 Total systematic uncertainties as a function of true λ at $\Gamma/M = 0.50$. 130

D.1 Kinematic distributions of tight jets. 132
D.2 $SecVtx$ b-tagged jet distributions. 133
D.3 $SecVtx$ b-tagging related distributions. 133
D.4 Kinematic distributions of leptons. 133
D.5 The missing E_T, phi of $\not\!\!E_T$, W transverse mass, and H_T distributions. 134
D.6 Vertex related distributions. 134
D.7 ΔR distributions. 134
D.8 $\Delta\phi$ distributions. 135

List of Tables

2.1 Properties of the CDF II calorimeter systems. The energy resolutions for the electromagnetic calorimeters are for electrons and photons; the resolutions for the hadronic calorimeters are for isolated pions. 19

3.1 Systematic uncertainties in the luminosity calculation using the CLC and the CDF measurement of the inelastic cross section. 36
3.2 Summary of identification and kinematic cuts of electron, muon, and jet. 38

4.1 Cross sections used to estimate backgrounds. 43
4.2 Expected contribution from non-W backgrounds. The $t\bar{t}$ contribution is removed from the missing E_T distribution. Statistics are merged for all events with three or more jet multiplicity bins in the fit, and errors include the systematics. 43
4.3 The heavy flavor fractions for W+Heavy Flavor background. These are the fractions of generic W+jets (in %) containing heavy flavor jets. 44
4.4 Tagging efficiency for the various classes of heavy-flavor event in W+jets. 44
4.5 Selection criteria for tracks used by the jet probability algorithm. . . 47
4.6 The measured $t\bar{t}$ cross sections (pb) using the *JetProb*, the first errors are the statistical uncertainties and the seconds are the systematic uncertainties. 48

6.1 The regions to fit transfer functions at $3\eta \times (5+3)E_T$ ranges. 61
6.2 The $3\eta \times (5+3)E_T$ regions to fit the bottom quark transfer function. 64
6.3 The combination selection efficiencies by selecting largest likelihood combination. 73

7.1 The $\sqrt{s_{t\bar{t}_p}}$ step to fit the resolution function. 78
7.2 The background estimations in 1.9 fb^{-1}. 85
7.3 The parameter points to test the linearity of λ. 88
7.4 The massive gluon parameter points to test the fitted λ fluctuations with the standard model pseudo data. 90

8.1 The sources and the processes of systematic uncertainties. 95

8.2 The parameter points to study the systematic effects. 95
8.3 The slopes (top values in each block) and intercepts at $\lambda = 0$ (bottom value in each block) at the various mass and width points using nominal distributions. 96
8.4 Scale factors from the ratio of data/MC according to the number of vertices. 103

9.1 Observed 95% C.L. lower limits 111
9.2 Observed 95% C.L. upper limits 111

A.1 The parameter regions of the massive gluon p.d.fs in Figs. A.1-A.6. . 115

C.1 The meanings of the abbreviations in Figs. C.1-C.6. 124

Chapter 1

Introduction

This section provides a brief overview of the standard model of particle physics, of top quark phenomenology, and of the massive gluon.

1.1 The Standard Model

The standard model of particle physics describes all known fundamental particles (quarks and leptons) and their interactions in the strong, electromagnetic and weak nuclear forces. The model itself is a combination of the theory of quantum chromodynamics (QCD) [1, 2] and the Glashow-Salam-Weinberg (GSW) theory of electroweak interactions [3, 4, 5]. The former describes the strong nuclear force and is represented by the $SU(3)_C$ gauge group, while the latter describes weak and electromagnetic forces and is represented by the $SU(2)_L \times U(1)_Y$ gauge group. The standard model is locally invariant under transformations of the group,

$$G = SU(3)_C \times SU(2)_L \times U(1)_Y. \tag{1.1}$$

It is known that there exist three generations of fundamental fermions. Each generation consists of a pair of leptons, whose interactions are mediated by the electroweak forces,

$$\begin{pmatrix} e \\ \nu_e \end{pmatrix}, \begin{pmatrix} \mu \\ \nu_\mu \end{pmatrix}, \begin{pmatrix} \tau \\ \nu_\tau \end{pmatrix}, \tag{1.2}$$

and a pair of quarks, whose interactions are mediated by electroweak and strong (QCD) forces,

$$\begin{pmatrix} u \\ d \end{pmatrix}, \begin{pmatrix} c \\ s \end{pmatrix}, \begin{pmatrix} t \\ b \end{pmatrix}. \tag{1.3}$$

The existence of three generations of quarks and leptons gives a natural explanation of CP violation. However, any theory cannot succeed to give a natural explanation of the three generations. The vast majority of stable matter we observe is made up of particles entirely in the first generation. Bosons mediate each of the forces described by the standard model: the photon (γ) for the electromagnetic force, the $W^{\pm}$ and Z^0 bosons for the weak force, and the gluon (g) for the strong force.

The standard model has been successful at describing interactions of the particles described above, all of which have been discovered experimentally. In addition, many of the predicted properties of these particles have been confirmed, some to a high degree of precision. However, in order for the symmetry described in Eq.(1.1) to be exact, the fermions and the W and Z bosons would have to be massless. In order for the standard model to be compatible with the large masses of the W and Z bosons and thus the large division between weak coupling constant (Fermi coupling constant) and electromagnetic coupling constant (fine structure constant), spontaneous symmetry breaking must occur. This symmetry breaking would additionally be responsible for the mass hierarchy observed in the fermions. This Electroweak Symmetry Breaking (EWSB) is accomplished by the introduction of a scalar field known as the Higgs Field [6]. The existence of a massive boson, the Higgs boson, would be associated with the Higgs field.

The existence of the Higgs boson has yet to be confirmed experimentally, and remains one of the most important tasks for the field of high energy physics. Direct searches for the standard model Higgs boson at the CERN Large Electron Positron (LEP) collider have set a lower bound on its mass of $M_H > 114.4$ GeV/c^2 at the 95% confidence level [7]. In addition, indirect bounds on the mass of the Higgs boson can be set from precision measurements of the top quark and W boson masses, as these quantities are sensitive to $\ln M_H$ through radiative corrections. Using measurements of the top quark mass and the precision electroweak measuments made at LEP [8], the constraints on the standard model Higgs bosons are

$$M_H = 76^{+33}_{-24} \text{ GeV}/c^2, \tag{1.4}$$

$$M_H < 144 \text{ GeV}/c^2 \text{ at 95\% C.L..} \tag{1.5}$$

1.2 The Top Quark

Following the discovery of the bottom (b) quark in 1977, the existence of its doublet partner, the top (t) quark, could be inferred for several reasons. For one, the renormalizability of the standard model requires that the sum of electric charges of all left-handed fermions must equal zero. This condition is only satisfied with the existence of a sixth quark with an electric charge of $+2/3$. In addition, the precise measurements involving the isospin of the b-quark can be made at e^+e^- colliders which can be used to exclude the possibility of the b-quark being a member of a singlet [9]. The discovery of the top quark was accomplished in 1995 at the CDF

and DØ experiments [10, 11]. By the end of the 1992-1996 collider run (Run I), combined measurements from both experiments datasets of ~ 100 pb^{-1} provided a measurement of the top quark mass of $M_t = 178.0 \pm 4.3$ GeV/c^2 [12].

1.3 Top Quark Production

In $p\bar{p}$ collisions, top quarks are predominantly produced in pair form via the strong force, while single top quark production via the electroweak force is predicted in the standard model. At the current Tevatron center-of-mass energy of $\sqrt{s} = 1.96$ TeV, top-antitop pair ($t\bar{t}$) production occurs via the channel $q\bar{q} \rightarrow t\bar{t}$ approximately 85% of the time while occurring via the channel $gg \rightarrow t\bar{t}$ the remaining 15% of the time [13]. The leading order diagrams for these production channels are shown in Fig. 1.1.

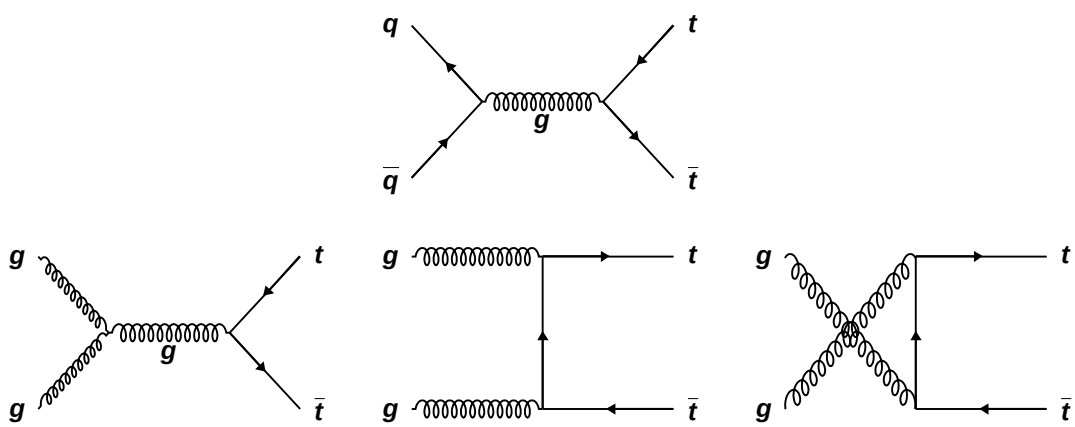

Figure 1.1: Top: Leading-order production diagram for $q\bar{q} \rightarrow t\bar{t}$. Bottom: Leading-order production diagrams for $gg \rightarrow t\bar{t}$.

The theoretical prediction of the $t\bar{t}$ production cross-section at Next-to-Leading Order (NLO) is $\sigma_{t\bar{t}}^{NLO} = 6.7^{+0.7}_{-0.9}$ pb at $M_t = 175$ GeV/c^2 [13]. Figure 1.2 shows the NLO calculation of $\sigma_{t\bar{t}}$ for $p\bar{p}$ collisions at $\sqrt{s} = 1.96$ TeV as a function of top quark mass. A combination of current measurements of $\sigma_{t\bar{t}}$ made at CDF during the current collider run, Run II ($\sqrt{s}$ =1.96 TeV) is also shown, and is in good agreement with the predicted value.

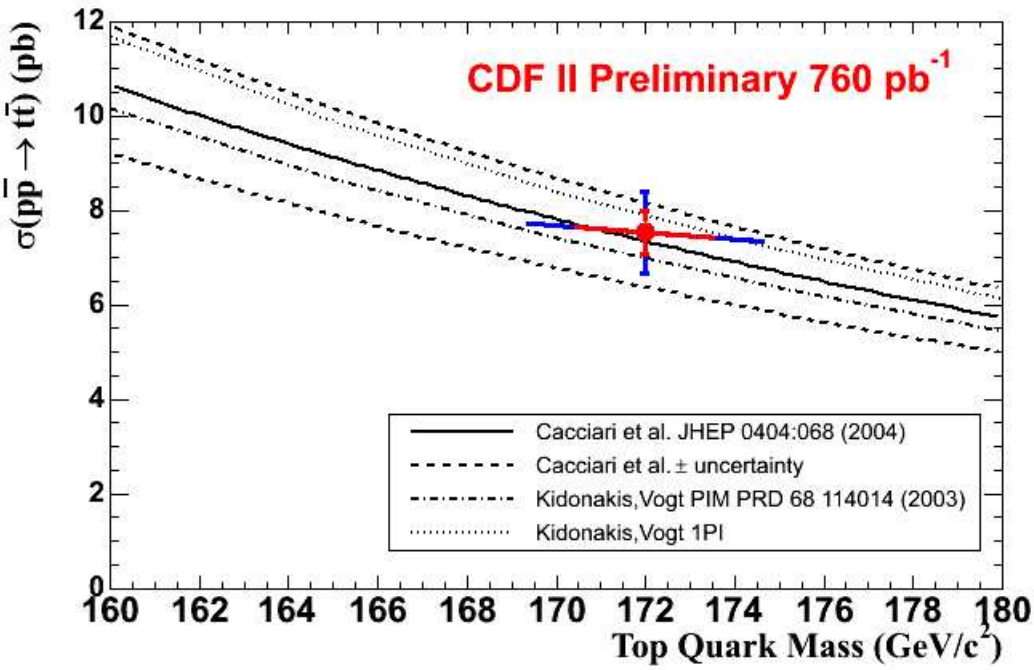

Figure 1.2: NLO calculations of $\sigma_{t\bar{t}}$ [13] for $p\bar{p}$ collisions at $\sqrt{s}$=1.96 TeV as a function of top quark mass. Also shown are the experimental measurements of $\sigma_{t\bar{t}}$ made at CDF using RunII data [14].

1.4 Top Quark Decay

Nearly 100% of top quarks are expected to decay via the channel $t \to Wb$. Other decay channels are permitted in the standard model, but are heavily suppressed by factors of $|V_{ts}|^2/|V_{tb}|^2 \approx 10^{-3}$ and $|V_{td}|^2/|V_{tb}|^2 \approx 5 \times 10^{-4}$, where V_{ij} is the Cabibbo-Kobayashi-Maskawa (CKM) weak-mixing matrix [15]. The large mass of the top quark results in a very rapid decay with a mean lifetime of $\tau_t \sim 10^{-24}$ s. As this is shorter than the timescale required for quarks to form bound states (or "hadronize"), the top quark essentially decays as a "free" quark. The b-quark resulting from the decay will then proceed to hadronize and manifest itself in the detector as a jet, or a collimated stream of hadrons. The W boson will decay rapidly into either a pair of quarks or a charged lepton and a neutrino. Thus, for the case of a $t\bar{t}$ pair decay, there are six particles in the final state: two b-quarks and two decay products from each of the W bosons. It is the decay mode of the W bosons that defines the decay channels of the $t\bar{t}$ system used in its experimental study. These decay channels are classified as:

The all-hadronic channel, where both W bosons decay to quarks, resulting in a final state having an experimental signature of six jets. This decay mode carries the largest branching ratio, of 46%, but suffers from the largest amount of irreducible QCD background.

The lepton+jets channel, where one W decays to a lepton and the other to quarks, resulting in an experimental signature of a high momentum lepton, four jets, and missing transverse energy associated with the neutrino. Due to the difficulty of identifying τ leptons at a hadron collider, only leptonic states with an electron or muon in the final state are considered. This channel carries a branching ratio of 30%. The analyses described in the dissertation are performed in the lepton+jets channel.

The dilepton channel, where both W bosons decay to leptons, resulting in an experimental signature of two high momentum leptons, two jets, and large missing transverse energy associated with two neutrinos. As with the lepton+jets channel, only leptonic states with an electron or muon on the final state are considered. The remaining 20% of $t\bar{t}$ decays involve the production of a lepton that does not decay to an e or μ. While measurements in this so-called "$\tau + X$" channel are possible, they do not afford nearly the same precision that any of the other three channels do.

1.5 Top Quark Mass

The top quark mass is a fundamental parameter in the standard model. Due to its relatively large value, it has a more critical influence on the standard model calculations than the other quarks. It influences higher order (radiative) calculations to electroweak processes. It also helps to constrain the mass of Higgs boson via the radiative correction to the mass of the W boson. Figure 1.3 shows two differing views of the constraint on the Higgs boson mass using the precise electroweak measurements, such as the W boson mass from LEP, and of the top quark mass from the Tevatron. As indicated in Fig. 1.3, the most likely value of the Higgs boson mass is ruled out by the direct observation at LEP. Failure of the standard model to properly describe these results may indicate new physics yet to be discovered.

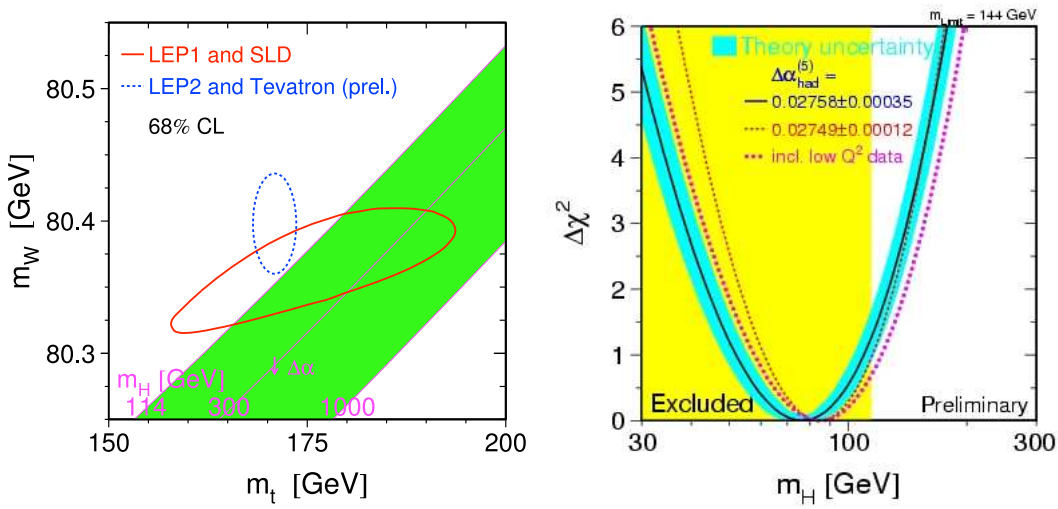

Figure 1.3: Electroweak constraints on the Higgs boson mass using the current best measurements of W boson and top quark mass (left). Global fit of Higgs boson mass to several electroweak parameters (right).

1.6 Massive Gluon

The mass of the top quark is the largest among all fermions and provides a sensitive probe of new physics. The heaviness of the top quark may reflect the presence of new physics at the electroweak scale. An attractive approach to understand electroweak symmetry breaking and the origin of fermion masses is that of new strong dynamics. The popular models of new strong dynamics are those of technicolor, topcolor, and their variants. In topcolor models, a spin-one Coloron (top-gluon), produced by quark-antiquark annihilations, would decay into $t\bar{t}$ and $b\bar{b}$ with roughly equal probability, and would be appear as a broad resonance [16]. In technicolor models, a spin-zero color-octet resonance, the techni-eta, is produced in gluon-gluon fusion and decay into $t\bar{t}$ [17]. The process, $q\bar{q} \to Z' \to t\bar{t}$ has been searched for at the Tevatron by both CDF and DØ [18, 19, 20]. We search for the process which interferes with the standard model $q\bar{q} \to g \to t\bar{t}$ process, assuming the existence of a gluon like particle with non-zero mass, which we call Massive Gluon (G) in the dissertation.

From an experimental point of view, it is preferable to perform the search with the generic case. Figure 1.4 shows the Feynman diagram of the massive gluon process.

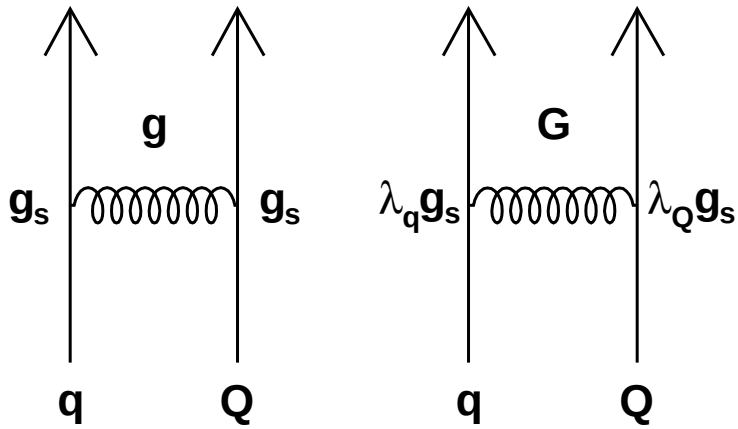

Figure 1.4: Feynman diagram: Left diagram is SM $q\bar{q} \to g \to t\bar{t}$. Right diagram is the massive gluon process. These processes interfere.

By assuming that the massive particle interferes with the gluon, the production matrix including parity violation is written by the following way:

$$
\begin{aligned}
|\mathcal{M}_{\rm prod}|^2 &= g_s^4 \Pi_g \hat{s}^2 (2 - \beta^2 + \beta^2 \cos^2\theta) \\
&+ \frac{g_s^4}{4} \lambda^2 \Pi_G \hat{s}^2 \left[(r^2 + l^2)(r + l)^2 - 2rl(r^2 + l^2)\beta^2 + 2(r^2 - l^2)^2 \beta \cos\theta + (r^2 + l^2)^2 \beta^2 \cos^2\theta \right] \\
&+ \frac{g_s^4}{4} \lambda \Pi_{\rm int.} \hat{s}^2 \left[(r^2 + l^2)(1 + \beta\cos\theta)^2 + 2rl(1 - \beta\cos\theta)^2 + (r + l)^2 (1 - \beta^2) \right] . \qquad (1.6)
\end{aligned}
$$

The first, second, and third terms correspond to the standard model $q\bar{q} \to t\bar{t}$ production, the massive gluon production, and the interference term, respectively. The color factor 2/9 is not written in Eq.(1.6).

- β and θ are the velocity (v/c) of top quark and the scattering angle of the top quark with respect to the initial quark direction in the $t\bar{t}$ rest frame.
- λ is the product of the massive gluon coupling to the light quark, λ_q, and to the heavy quark, λ_Q, relative to the strong coupling, g_s.
- The current: $j^\mu = \bar{v}(rR + lL)\gamma^\mu u$
- $R = (1 + \gamma_5)/2$, $L = (1 - \gamma_5)/2$
- $r^2 + l^2 = 2$

In Eq.(1.6), the gluon, massive gluon, and interference propagator factors are

$$\Pi_g = \frac{1}{\hat{s}^2}, \tag{1.7}$$

$$\Pi_G = \frac{1}{(\hat{s}-M_G^2)^2+M_G^2\Gamma_G^2}, \tag{1.8}$$

$$\Pi_{\text{int.}} = \frac{2}{\hat{s}}\frac{\hat{s}-M_G^2}{(\hat{s}-M_G^2)^2+M_G^2\Gamma_G^2}. \tag{1.9}$$

The helicity of heavy quark is

$$h|\mathcal{M}|^2 = -\bar{h}|\mathcal{M}|^2 = \frac{g_s^4}{4}\hat{s}^2 C\frac{P_Q}{E_Q}\left[(\lambda_q^2\lambda_Q^2)(r^2+l^2)\Pi_G + \lambda_q\lambda_Q\Pi_{\text{int.}}\right](r^2-l^2)(1+\beta\cos\theta)^2. \tag{1.10}$$

With the assumption of no parity violation ($r = l = 1$), the production matrix is simply written by

$$|\mathcal{M}_{\text{prod}}|^2 = \frac{2}{9}g_s^4\hat{s}^2(2-\beta^2+\beta^2\cos^2\theta)(\Pi_g+\lambda\Pi_{\text{int.}}+\lambda^2\Pi_G). \tag{1.11}$$

With the massless light quarks approximation, the decay width is written by

$$\Gamma_G = \frac{g_s^2 M_G}{24\pi}(n_f\lambda_q^2+\lambda_Q^2). \tag{1.12}$$

There are 3 independent parameters, λ, M_G, and Γ_G/M_G. λ can be both negative and positive, which distorts the $t\bar{t}$ invariant mass spectrum. Γ_G/M_G is typically large ($\Gamma_G/M_G \gtrsim 0.2$), but smaller widths are also explored.

Because there is no Monte Carlo generator for gluon and massive gluon interference, we put the massive gluon effect in PYTHIA [21]. Figure 1.5 shows the example of $t\bar{t}$ invariant mass distribution from the modified PYTHIA using GRV 94L PDF set with the various masses assuming $\Gamma/M = 0.20$, $\lambda = \pm 1$, $M_t = 160$ GeV/c^2, and $\sqrt{s} = 1.8$ TeV to compare with Ref. [16].

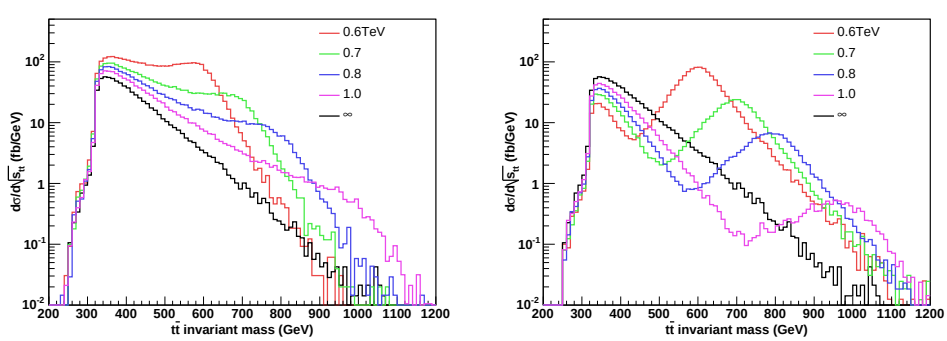

Figure 1.5: Left and right plots show the $\lambda = -1$ and $+1$ cases respectively with $\Gamma/M = 0.20$, $M_t = 160$ GeV/c^2, and $\sqrt{s} = 1.8$ TeV.

Leading order total cross sections (output of PYTHIA) are well fitted by the quadratic functions of λ, as shown in Fig. 1.6. Total cross section can be both higher and lower than the standard model due to the interference effect. The total cross section information is not used in the search, because the $t\bar{t}$ production cross section at the Tevatron can not be explained in the leading order and NLO cross sections with the massive gluon are not known.

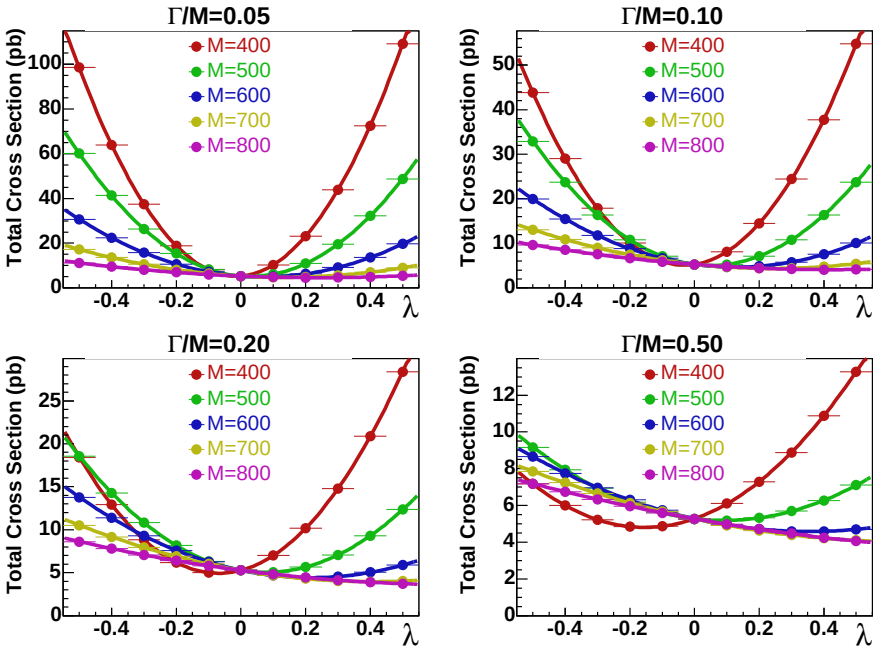

Figure 1.6: Total cross section as a function of λ for the various masses and decay widths.

Chapter 2

Experimental Apparatus

The experimental apparatus consists of the accelerators, the CDF detector, and the data acquisition systems. These have been continuously upgraded since the first Tevatron collision in October 1985.

2.1 The Fermilab's Accelerator Chain

(All the accelerator figures and contents are courtesy of Fermilab Accelerator Division)

The accelerator complex is described in detail in Ref. [22] and briefly summarized here. It consists of the pre-accelerator, the linear accelerators (linac) [23], the booster [27], the main injector [29], the antiproton source [30], the Recycler [32], and the Tevatron [34]. An overview of the accelerator complex is shown in Fig. 2.1.

2.1.1 The Pre-accelerator

The pre-accelerator produces the beam of 750 keV H^- ions, which consists of a negative hydrogen ion source [24], a Cockcroft-Walton generator [25], an electrostatic accelerating column, and a transport line. Hydrogen gas is passed through a magnetron to produce H^- ions at the dome with a potential of -750kV. The potential is created by the 5-stage diode voltage multiplier, which converts 75kV AC to the -750kV DC. The extracted H^- ions are accelerated to 750 keV by passing through the accelerating column. The amount of H^- beam allowed to pass from the source to the Linac is controlled by the chopper. The transport line includes the focusing magnets and a single gap RF cavity which bunches the beam at the RF frequency of the Linac. A schematic view of the pre-accelerator is shown in Fig. 2.2.

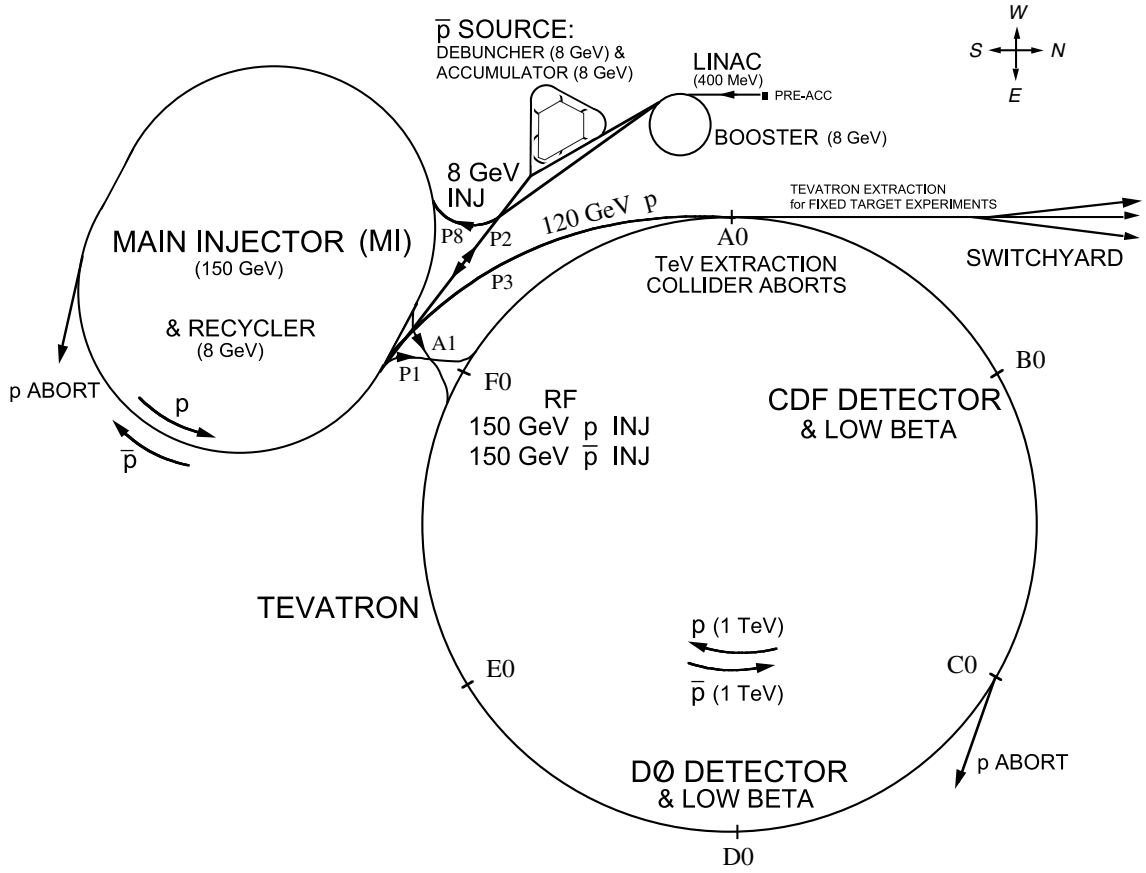

Figure 2.1: Overview of Fermilab accelerator complex.

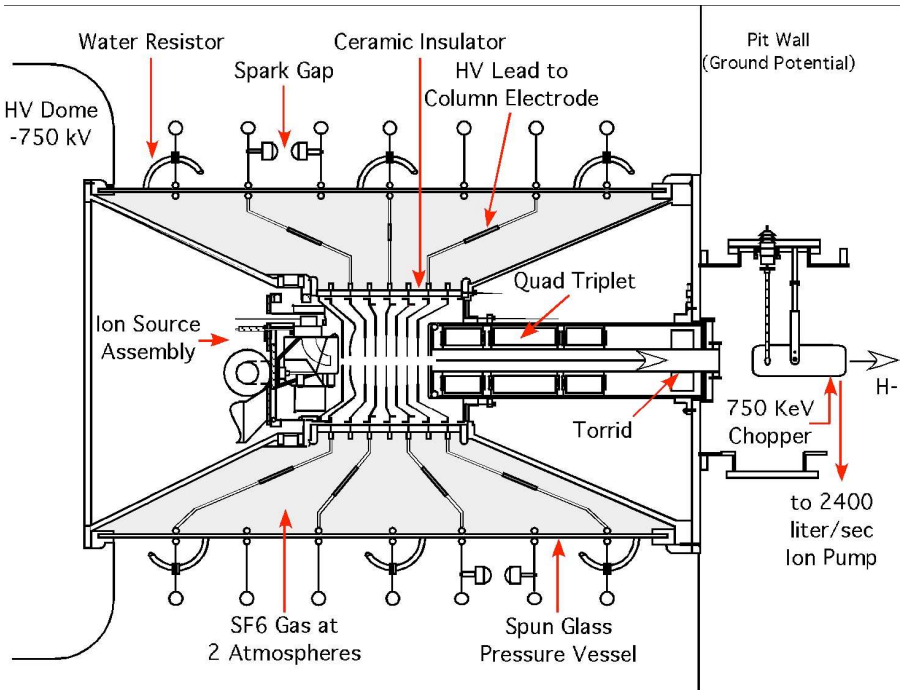

Figure 2.2: Ion source and the electrostatic accelerating column.

2.1.2 The Linac

The Linac is a two-stage linear accelerator that produces a pulsed beam of 400 MeV H^- ions for charge-exchange injection [28] into the Booster. The first stage is an Alvarez drift-tube accelerator [26], which accelerates the ions to 116 MeV. The second is a side-coupled linac, which accelerates the H^- beam to 400 MeV. The accelerating gradient for each side-couple cavity is about three times that of the drift-tube Linac. The H^- beam is focused by the quadrupole magnets at both Linacs.

2.1.3 The Booster

The booster [27] is an 8 GeV proton synchrotron as an injector for the Main Ring. It accelerates 400 MeV protons obtained from the Linac by stripping the electrons off the negative hydrogen ions. H^- ions are merged with protons circulating in the booster using dipole magnets, and the combined beam is passed through carbon foil to strip electrons, as shown in Fig. 2.3. The opposite charge of the injecting H^- and the circulating proton allows to merge the beam efficiently. The booster consists of a series of magnets arranged around a 75-meter radius with 18 RF cavities.

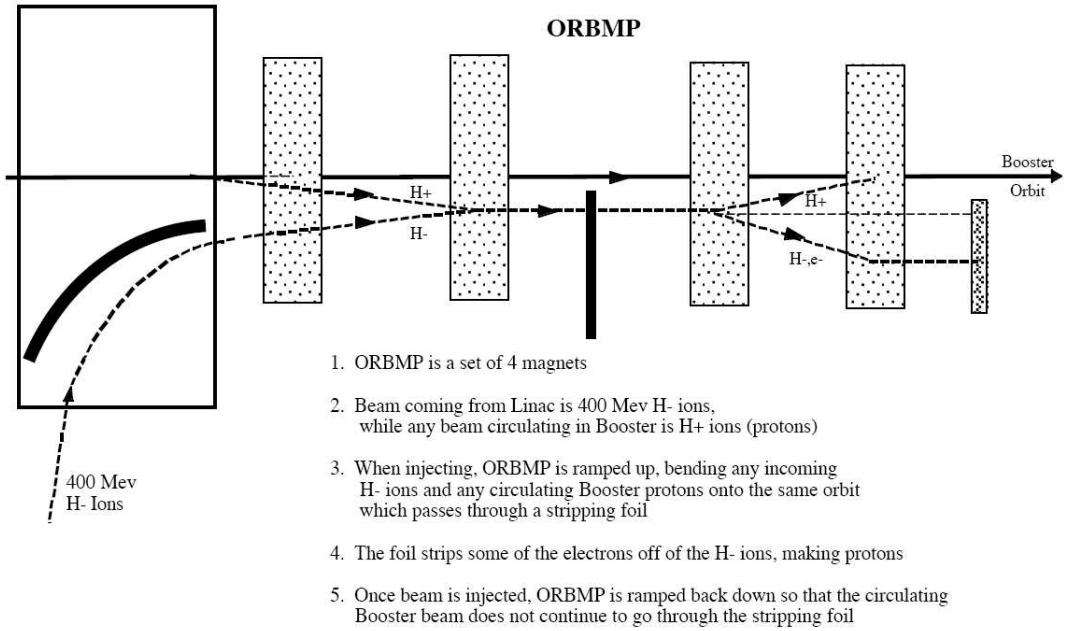

Figure 2.3: A schematic view of the Fermilab Booster injection area.

2.1.4 The Main Injector

The main injector is a synchrotron, which accelerates 8 GeV protons from the booster to either 120 GeV or 150 GeV. When used to produce the antiprotons, the final energy is 120 GeV. When used to inject into the Tevatron, the final beam energy is 150 GeV. The main injector can accept both protons from the booster and antiprotons from the antiproton source. The main injector contains 20 RF cavities for particle acceleration and a series of dipole/quadrupole magnets for beam focusing and steering.

2.1.5 The Antiproton Source

The antiproton source [30] consists of a target station, a Debuncher ring, and an Accumulator ring. The 120 GeV proton beam from the main injector is delivered to a nickel target, producing the antiprotons in a shower of secondary particles. Antiprotons of 8 GeV are most effectively produced by about 120 GeV proton beam. About one antiproton is produced for every 10^5 protons striking the target. The secondary particles are collected and focused by a cylindrical lithium lens, as shown in Fig. 2.4. Lithium is the least-dense solid conductor which reduces the antiproton absorption and multiple scattering. 8 GeV antiprotons are selected by a pulsed dipole magnet and delivered to the Debuncher.

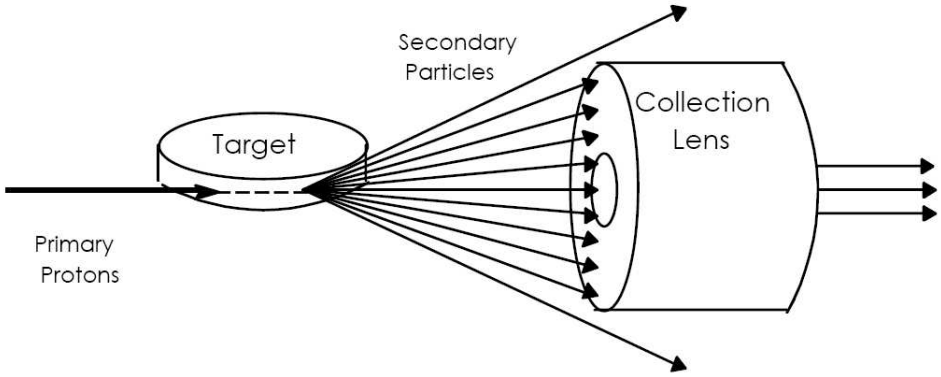

Figure 2.4: A simple view of the target station.

The Debuncher is a rounded triangular-shaped synchrotron with a mean radius of 90 meters. It reduces the high momentum spread of antiprotons from the target station to improve the Debuncher to Accumulator transfer through bunch rotation and adiabatic debunching. Both (transverse) stochastic cooling [31] and (longitudinal) momentum cooling are applied to reduce the beam size and momentum spread. The Debuncher keeps the antiproton energy at 8 GeV.

The Accumulator is also a triangular-shaped synchrotron of radius 75 meters and is in the same tunnel as the Debuncher. Its purpose is to accumulate antiprotons extracted from the Debuncher. All of the antiprotons made are stored here at 8 GeV and cooled through the several different cooling systems. After several hours, enough antiprotons have been accumulated, antiprotons are transfered to the Main Injector and the Tevatron for a store (or to the Recycler via the Main Injector).

2.1.6 The Recycler

The Recycler is an antiproton storage ring located along the ceiling of the Main Injector tunnel, which keeps the antiproton energy at 8 GeV. The proposed purpose of the Recycler was to recycle the antiprotons from a Tevatron store. The recycler now accepts the antiproton beam only from the antiproton source and cools further than the Accumulator is capable. The Recycler uses both a stochastic cooling and an electron cooling system [33]. The recycler uses the stochastic cooling until the intensity reaches 2×10^{12} particles per pulse. The electron cooling is used to cool the antiprotons further.

2.1.7 The Tevatron

The Tevatron is a 1 km radius synchrotron which accelerates proton and antiproton from 150 GeV to 980 GeV [34]. All dipoles, quadrapoles, and correction element

magnets are superconducting magnets, cooled to about 4.6 K with liquid Helium. Proton and antiproton collide at the positions of CDF and DØ detectors. The separators around the ring separate the proton bunches from the antiprotons except at the collision regions. There are 3 trains of 12 bunches and a abort gap between the trains in the Tevatron, as shown in Fig. 2.5.

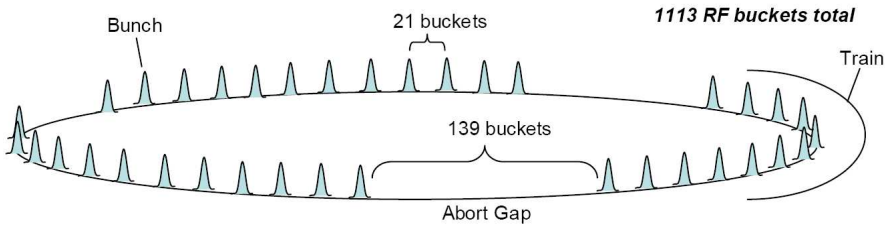

Figure 2.5: Bunch spacing in the Tevatron.

2.2 The CDF Detector

The CDF detector is an azimuthally and forward-backward symmetric detector designed to study $p\bar{p}$ collisions at the Tevatron. A schematic overview of the CDF detector is shown in Fig. 2.6.

The CDF coordinate system is right-handed, with the z-axis pointing along the proton direction. The remaining rectangular coordinates x and y are defined pointing outward and upward from the Tevatron ring respectively. Often, it is more convenient to work in polar coordinates (which are facilitated by the symmetry of the CDF detector in the xy-plane), where $r = \sqrt{x^2 + y^2 + z^2}$ and $\phi = \tan^{-1}(y/x)$. The canonical third variable in the polar coordinate system is $\theta \equiv \cos^{-1}(z/r)$. However, θ is not invariant under longitudinal boosts. Since the constituent particles of the proton and the antiproton will not have an initial energy of 980 GeV, the production of particles as a function of angle will depend on the initial velocities of the constituent particles. The rapidity, defined as:

$$\zeta \equiv \ln \frac{E + p_z}{E - p_z} \tag{2.1}$$

is invariant under boosts along the z-axis. For the massless case ($p \gg m$), the rapidity can be approximated as the pseudo-rapidity, defined as:

$$\eta \equiv \ln(\tan \frac{\theta}{2}). \tag{2.2}$$

This coordinate is invariant under Lorentz transformation and is used as the third coordinate in the CDF coordinate system. The basic structure of the CDF detector

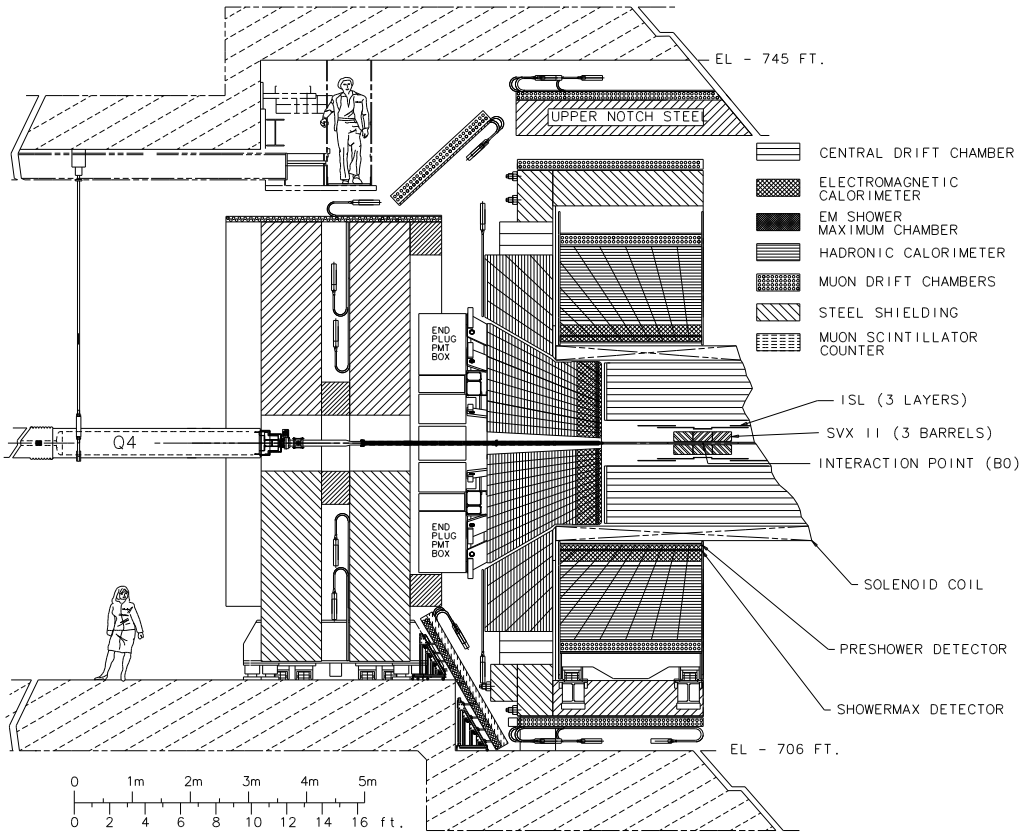

Figure 2.6: A cross-sectional view of the CDF detector [35].

can be subdivided from the inside (starting at the beam-pipe) out into: the tracking system (responsible for measuring momenta of charged particles), the calorimeters (responsible for measuring the energy of interacting particles), and the muon system (responsible for identifying muons).

2.2.1 Tracking System

The CDF tracking system consists of a silicon microstrip tracker and an open-cell drift chamber. The silicon tracker consists of three subdetectors, listed in order of distance from the beam-pipe: Layer 00 (L00), the Silicon Vertex detector (SVX), and the Intermediate Silicon Layers (ISL). The drift chamber, known as the Central Outer Tracker (COT), surrounds the silicon tracking system. The entire CDF tracking system is placed in a 1.4 T magnetic field that is generated by a superconducting solenoid magnet. The solenoid has a radius of 1.5 m, a length of 5 m, and a stored energy of 30 MJ when at full field strength. The magnetic field produced by the solenoid is uniform along the direction of the z-axis. Charged particles within the magnetic field follow the helical trajectories. The radius of curvature and the orientation of the helix can be used to determine the momentum and charge of a charged particle. A schematic overview of the CDF tracking system is shown in Fig. 2.7.

Silicon Detector

The silicon detector, which provides high-resolution position measurements of charged particles close to the interaction region, consists of three subdetectors. The main subdetector is the SVXII [36] detector, a five layer, double-sided silicon detector that covers the radial region between 2.5 cm and 10.6 cm. The SVXII detector is composed of three cylindrical barrels, each 16 cm long in the z-direction. Each barrel is divided into 12 azimuthal wedges of 30° each. Each of the five layers in a wedge is further divided into electrically independent modules called ladders. There are a total of 360 ladders in the SVXII detector. The double-sided silicon microstrips of the SVXII detector are arranged so that one side is aligned with the z-axis (known as "axial" strips) and the other side is either at an angle of 90° or 1.2° with respect to the axial layer. These arrangements make it possible to make three-dimensional position measurements by combining the r-ϕ and r-z measurements.

The innermost subdetector of the silicon detector, Layer 00 (L00) [37], is a single-sided layer of silicon wafers mounted directly on the beam-pipe at a radius of 1.6 cm and provides measurements closest to the interaction point. The outermost subdetector, the Intermediate Silicon Layers (ISL) [38], is comprised of one or two additional layers of double-sided silicon, depending on the polar angle, at radii from 20 cm to 28 cm. The ISL serves to extend silicon tracking coverage up to $|\eta| < 2$. The combined CDF silicon detector has a total of 722,432 channels.

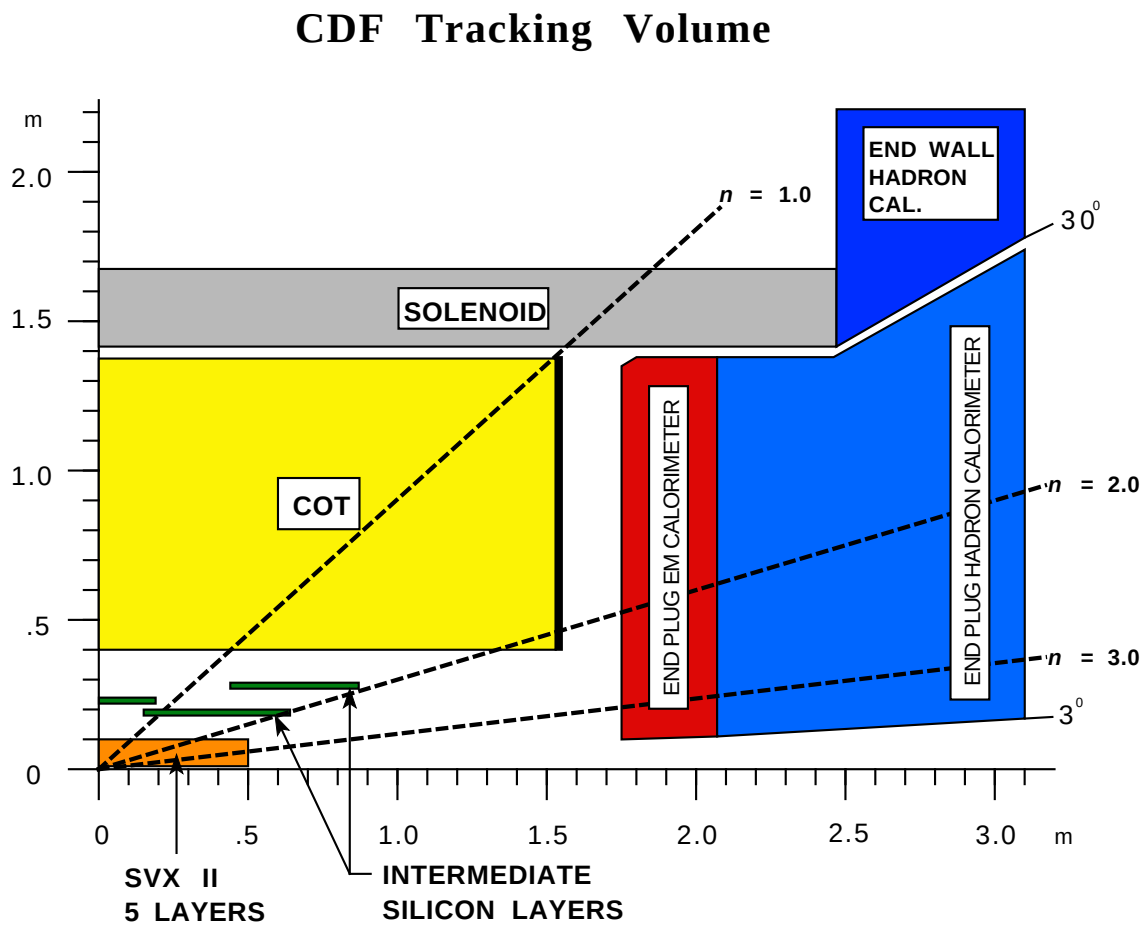

Figure 2.7: A schematic overview of the CDF tracking system. The region of the detector with $|\eta| < 1.0$ is referred to as the central region.

COT

The Central Outer Tracker (COT) [39], a large open-cell drift chamber, is positioned outside the silicon detector from radii of 0.43 m to 1.32 m. The COT contains 8 "super-layers" each containing 12 wire layers for a total of 96 layers. Four of the super-layers provide r-ϕ measurements (axial super-layers) while the other four have 2° inclined measurements (stereo super-layers). The drift chambers are filled with a 1:1 mixture of argon and ethane. This mixture provides for a maximum drift time of 177 ns with a drift velocity of 100 μm/ns, which prevents pileup of events in the drift chamber from previous events. The resulting transverse momentum resolution of the COT is $\sigma_{p_T}/p_T \approx 0.15\% \times p_T$. In combination the silicon and COT detectors provide the excellent tracking up to $|\eta| \leq 1.1$ with decreasing coverage to $|\eta| \leq 2.0$.

2.2.2 Calorimeters

The CDF calorimetry system sits outside the solenoid and is responsible for measuring particle energies. The calorimeters sample electromagnetic and hadronic showers produced as particles interacting with dense material. The system covers a full 2π in azimuth and is subdivided into a "central" region ($|\eta| < 1.1$) and a "plug" region ($1.1 < |\eta| < 3.6$). Each calorimeter is segmented into "towers", containing alternating layers of scintillator and inert material. Each calorimeter system described below consists of an electromagnetic component and a hadronic component. The electromagnetic component measures the energy of electrons and photons by sampling electromagnetic showers caused by bremsstrahlung of the electron or e^+e^- pair production of the photon. The hadronic component measures the energy of hadrons and jets by sampling electromagnetic showers due to neutral meson production and their subsequent electromagnetic decay and hadronic showers due to strong interactions of hadrons with heavy atomic nuclei. A summary of the CDF calorimeter systems is shown in Table 2.1.

System	Coverage in η	Thickness	Energy Resolution
CEM	$\|\eta\| < 1.1$	$18X_0, 1\lambda$	$13.5\% \ / \ \sqrt{E_T}$
PEM	$1.1 < \|\eta\| < 3.6$	$21X_0, 1\lambda$	$16\% \ / \ \sqrt{E_T}$
CHA	$\|\eta\| < 0.9$	4.5λ	$50\% \ / \ \sqrt{E_T}$
WHA	$0.7 < \|\eta\| < 1.2$	4.5λ	$75\% \ / \ \sqrt{E_T}$
PHA	$1.2 < \|\eta\| < 3.6$	7λ	$80\% \ / \ \sqrt{E_T}$

Table 2.1: Properties of the CDF II calorimeter systems. The energy resolutions for the electromagnetic calorimeters are for electrons and photons; the resolutions for the hadronic calorimeters are for isolated pions.

The Central Calorimeter

In the central region of $|\eta| < 1.1$, the calorimeter towers are 15° in ϕ and 0.1 in η. The central electromagnetic calorimeter (CEM) [40] constitutes the front of the wedges in the central region. The CEM consists of alternating layers of lead and scintillator, amounting to 18 radiation lengths of material. Embedded in the CEM is the central electromagnetic shower maximum detector (CES). The CES provides position measurements of the electromagnetic showers at a depth of 5 radiation lengths and is used in electron identification. Behind the CEM is the central hadronic calorimeter (CHA) [41], which provides energy measurements of hadronic jets. The CHA consists of 4.5 interaction lengths of alternating steel and scintillator. The CHA covers the region up to $|\eta| < 0.9$.

The End-Wall and Plug Calorimeter

Since the CHA covers only the region up to $|\eta| < 0.9$, the end-wall hadronic calorimeter (WHA) covers the region from $0.7 < |\eta| < 1.2$. Its construction is otherwise very similar to the CHA. The plug electromagnetic calorimeter (PEM) [42] consists of alternating lead absorber and scintillating tile readout with wavelength shifting fibers; the total thickness is 21 radiation lengths of material. A plug electromagnetic shower maximum detector (PES) [43] provides position measurement of electron and photon showers. The plug hadronic calorimeter (PHA) has alternating layers of iron and scintillating tile for a total of 7 interaction lengths.

2.2.3 Muon Detectors

As muons are 200 times more massive than electrons, they lose considerably less energy due to bremsstrahlung in the calorimeter and thus are not effectively detectable by the calorimeter. Thus, the muon detectors sit on the very outside of the CDF detector, and are separated from the calorimeter by a layer of steel shielding. This layer of shielding serves to absorb charged pions which can traverse the whole of the calorimeter and could incorrectly be interpreted as muons. Unlike the tracking and calorimetry systems, the muon system is incomplete in ϕ, due to space constraints. Its coverage is shown in Fig. 2.8.

The muon detection system consists of three sandwiched drift tube layers, each utilizing single wire drift cells 4 layers deep. Directly behind the central hadronic calorimeter and the layer of steel shielding is the central muon detector (CMU) [44] which can detect muons with $p_T > 1.4$ GeV/c in the region of $|\eta| < 0.6$. Additional muon coverage in this region is provided by the central muon upgrade (CMP) which is separated from the CMU by 60 cm of steel. The CMP detects muons with $p_T > 2.0$ GeV/c. The central muon extension (CMX) provides further coverage in the region of $0.6 < |\eta| < 1.0$.

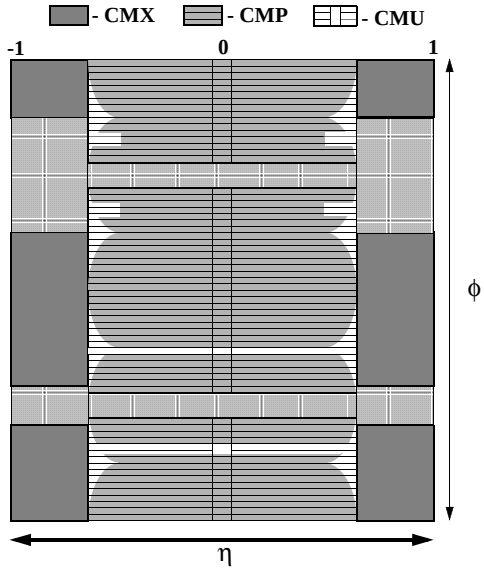

Figure 2.8: Coverage of the CDF muon systems.

2.2.4 Trigger System

Of the over 2 million $p\bar{p}$ collisions that occur every second during operation of the Tevatron collider, the vast majority are not interesting in the study of high energy physics. CDF employs a three-level trigger system to select events involving physically relevant phenomena and record them, while rejecting uninteresting events. Due to the physical limitations involved in physical storage and the rate at which data can be stored, the trigger system must reduce the data acquisition rate from the approximately 2 MHz collision rate to approximately 75 Hz. An overview of the CDF Trigger system is shown in Fig. 2.9.

Level 1 Trigger

The level 1 trigger utilizes the custom designed hardware to make decisions based on simple physics quantities within events. Raw information from the detector from every beam crossing is stored in a pipeline capable of buffering data from 42 beam crossings. Processing of this data takes place in one of three streams. One analyzes calorimeter information to identify objects that may further be reconstructed into electrons, photons, or jets. Another stream searches for track segments in the muon detector, or "stubs", which may be used in conjunction with tracks in the tracking system to reconstruct muons. The third stream utilizes tracking data to identify tracks that can be linked to objects in the calorimeter or muon detector. The level 1 trigger decision takes place 5.5 μs after a collision and reduces the event rate to approximately 50 kHz.

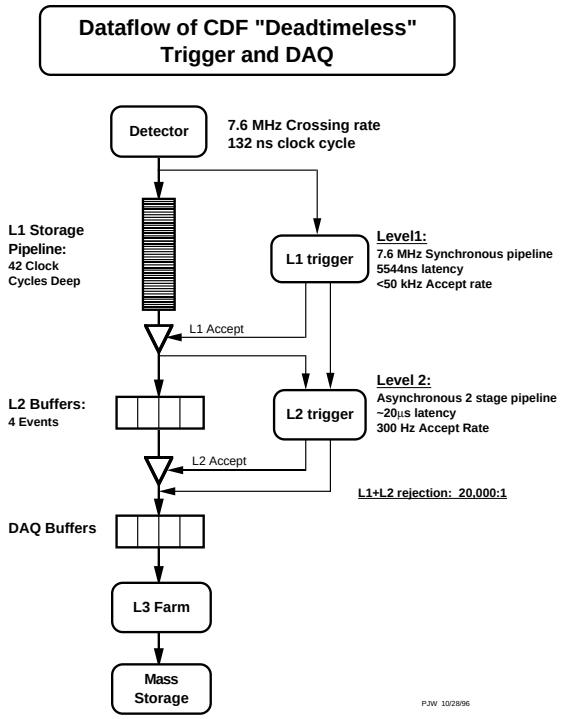

Figure 2.9: The CDF Trigger and Data Acquistion System.

Level 2 Trigger

The level 2 trigger utilizes the programmable processors to perform limited event reconstruction on events accepted by the level 1 trigger. These events are then stored in one of four asynchronous buffers and a decision is made as to whether the events pass one of the pre-defined level 2 trigger criteria. The decision time for the level 2 trigger is approximately 25 μs. The level 2 trigger further reduces the event rate to approximately 300 Hz.

Level 3 Trigger

The level 3 trigger consists of two components: an "event builder" that uses the custom hardware to assemble data from all subdetectors of CDF into a reconstructed event, and a large processing farm consisting of commodity computing hardware. Each processor in the processing farm can then make a decision as to whether an event reconstructed by the event builder satisfies pre-defined level 3 trigger criteria. The level 3 trigger then separates events into streams based on the physics objects that resulted in their trigger and commits them to permanent storage. The level 3 trigger reduces the event rate to approximately 75 Hz.

Chapter 3

Dataset and Event Selection

In this chapter, the dataset used in the analyses, the details of the particle identification, and the event selection criteria are described.

3.1 Electron

3.1.1 Electron Trigger

Using information from several detector subsystems, the trajectories of electron from $p\bar{p}$ collisions can be traced from the interaction region with high precision, through the tracking chambers, and into the electromagnetic calorimeters. The identification of electrons begins with the on-line trigger system. The data passed through that on-line system, which classifies the electron characteristics, are stored into the tape permanently. Then the offline reconstructions are performed for these events. All events are reprocessed with the re-calculated electron track parameters with the most up-to-date calibration constants. The best electron candidates are specified with several selection cuts. The results are a sample of tight central electron events that contain high-p_T events as a subset. The following descriptions are the principal requirements to identify a high-p_T electron event in the central region ($|\eta| < 1.1$). The ELECTRON_CENTRAL_18 trigger path is used in the analyses, which requires the electron objects with an energy in the central electromagnetic calorimeter and a track in the on-line track reconstruction.

3.1.2 Electron Clustering

A bunch of the electromagnetic calorimeter towers which satisfy the trigger selection criteria are formed as the electromagnetic (EM) clusters. The EM cluster is a collection of towers distributing around a seed tower with largest E_T (> 3 GeV), where the E_T of a calorimeter tower is defined by $E_T = E \sin\theta$ as the θ is the polar angle measured from the event vertex to the centroid of the tower. The neighbor towers around the seed tower are only two adjacent towers laid on the $|\eta|$ direction

(called "shoulder" tower), not on ϕ. The tower threshold in that cluster is $E_T > 100$ MeV. In addition, the ratio of the electromagnetic to hadronic energy associated with the cluster is required to be less than 0.125 in order to reject hadrons.

3.1.3 Electron Corrections

Various corrections are applied in data as well as the MC simulation after triggering the high p_T electron sample.

Vertex Correction : In the trigger level, the electron transverse energy is calculated assuming the interaction point is located at $z = 0.0$ cm. The z position of the interaction point is defined as the z_0 position of the electron track. Additionally, the angle of the electron track is used to calculate the E_T.

CEM Energy Corrections : Corrections of the CEM response as a function of the position in local coordinates are implemented. The CEM energies are also corrected for tower-to-tower gain variations. Additionally, the absolute energy is scaled in the data and in the simulation such that the $Z \to e^+e^-$ mass peak is around 91 GeV/c^2. This results in +1.2 % correction in the data and -0.6 % correction in the simulation. The energy in the simulation is also smeared by 2 % in order to match the resolution observed in the data. Energy dependent variables are re-calculated to reflect these corrections.

Beam Constrained Tracking : The tracks of the electron candidate are refitted by a beam constrained tracking algorithm only using COT information. The beam constrained track induces a bias in the track curvature since the track fitting is forced to the beam spot. The change of the track curvature has been studied by looking at the energy-momentum ratio E/p.

Leakage Correction : The electron cluster is basically formed only using one tower in CEM. Only one adjacent tower along the η direction is allowed to be merged into the electron cluster in CEM if that tower has an energy deposition larger than the seed tower E_T. If the electron hits near the edge of the tower in ϕ but not in η, the leakage energy thus increases significantly. The isolation requirement on the electron energy to discriminate between jets and electrons or photons will be disturbed by this energy leakage. The isolation energy is corrected using the parameterized formula.

3.1.4 Electron Geometric and Kinematic Cuts

Electrons from $W \to e\nu$ decays in the top quark pair process typically have the large transverse energy. The following geometric and kinematic cuts are applied to

identify electron from W.

Fiducial Requirements : The fiducial volume ensures the stable and good response from the electromagnetic calorimeter for the electron candidates. The boundary of the calorimeters in $|\eta_d| < 0.05$ and two chimney towers, which are located for the cryogenic penetration of the magnet, are excluded. In addition to the restriction due to the mechanical design, the fiducial requirements to eliminate regions of poor response are also imposed on the azimuthal boundaries in the local position coordinated of the electron at the calorimeter wedge, $|x_{\rm local}| \geq 21$ cm, and the 90° boundary of the CEM, $|z_{\rm local}| \leq 9$ cm and $|z_{\rm local}| \geq 230$ cm. The local positions on the electromagnetic cluster are extrapolated using the maximum p_T track to the plane of the CES in the wedge.

Kinematic Requirements ($E_T \geq 20$ GeV, $p_T \geq 10$ GeV/c, $|\eta_d| < 1.1$) : The electron candidates are required within the central region, $|\eta_d| < 1.1$, which is covered by CEM. That guarantees precise energy measurements and electron track quality. The transverse energy (E_T) of every electron candidate is required to be larger than 20 GeV within the central region. The track transverse momentum (p_T) have to be larger than 10 GeV/c. That distinguishes electrons from photons or neutral pions. The track transverse momentum is measured from the fully-reconstructed track curvature.

Interaction Vertex ($|Z_{\rm vtx}| \leq 60$ cm) : To keep the interaction within the fiducial volume of the detector, and to maintain the calorimeter projectile tower geometry, the interaction vertex is required to lie within 60 cm around the center of the detector in z. The interaction vertex is identified as the z_0 position of the electron track.

3.1.5 Electron Identification Cuts

Several electron identification variables are used to reject backgrounds and enhance the fraction of true electrons.

Energy-Momentum Ratio ($E/p \leq 2.0\ c$ or $E_T \geq 50$ GeV) : The electron passing through the COT material in the magnetic field makes bremsstrahlung. Due to the worse momentum resolution of the high-p_T track, the energy-momentum ratio is required to be in the range of $E/p \leq 2.0\ c$ if the electron transverse energy is less than 50 GeV.

Hadronic Energy Fraction (Had/EM $\leq 0.055 + 0.00045E$) : The electromagnetic showers are mostly contained within the EM calorimeter. To reject the contamination of hadronic jets that deposit a large fraction of energy in the hadronic

calorimeter, small amount of the fraction of hadronic energy is imposed. Since the leakage of electron energy into the hadronic calorimeter increases with energy, the sliding cut is applied to maintain a high efficiency for the electron. The hadronic-electromagnetic energy ratio (Had/EM) is required to be less than $0.055+0.00045E$, where E is the cluster energy in GeV.

Isolation (Iso(0.4) $\leq$ 0.1) : The isolation is defined as

$$\mathrm{Iso}(0.4) \equiv \frac{E_T^{0.4} - E_T}{E_T}, \tag{3.1}$$

where $E_T^{0.4}$ is the total transverse energy contained within a cone of radius $R = 0.4$ (in η-ϕ plane) with respect to the center of the electromagnetic cluster. This cut is also imposed to reject the contamination of hadronic jets. A small isolation cut leads to a well-separated cluster.

Lateral Shower Profile ($L_{\mathrm{shr}} \leq 0.2$) : The lateral sharing of energy between the calorimeter towers gives a criterion to identify electrons. The lateral shower profile, L_{shr}, is defined as

$$L_{\mathrm{shr}} = 0.14 \times \sum_i \frac{E_i^{\mathrm{adj}} - E_i^{\mathrm{exp}}}{\sqrt{(0.14)^2 E + (\Delta E_i^{\mathrm{exp}})^2}}, \tag{3.2}$$

where the summation is over the two towers adjacent to the seed tower in the same azimuthal wedge, E_i^{adj} is the measured energy in a tower adjacent to the seed tower, E_i^{exp} is the expected energy in that tower, $\Delta E_i^{\mathrm{exp}}$ is the uncertainty on E_i^{exp}, and $0.14\sqrt{E}$ is the uncertainty on the cluster energy. The expected energy, E_i^{exp}, is a function of the seed tower energy, impact point, event vertex, and a shower profile from the test-beam results. L_{shr} is required to be less than 0.2.

Strip Chamber Profile ($\chi^2_{\mathrm{str}} \leq 10$) : The pulse heights on the CES strips in the electromagnetic shower are compared with channel-by-channel between the observed shower and the expected shower profiles based on the test-beam results. The quantity from the fitted results, χ^2_{str} is required to be less than 10.

Track Matching (-3.0 cm $\leq Q\Delta x \leq$ 1.5 cm and $\Delta z \leq$ 3.0 cm) : A track matching is required that the extrapolated track of the electron candidate points out into the electromagnetic shower location measured by CES. The differences to each direction, Δx and Δz, denote the separation between electron track and electron cluster in CEM, where Q is a track charge.

Track Segment : The only well-reconstructed electron tracks are used. The stub of the electron track is required to have more than 3 axial super-layers and 2

stereo super-layers with at least 5 hits in COT.

Conversion Removal : When high energy photons convert to electron-positron pair, those signatures will be mimics of the high E_T electron signatures. Those fake signals are removed by the requirement of an electron track pair with opposite sign pointing the same origin. At the conversion point, both tracks are almost parallel and follow the direction of the parent photon. Thus $|\Delta xy| \leq 0.2$ cm and $|\Delta \cot\theta| \leq 0.04$ are required for an opposite-signed track, where $|\Delta xy|$ is the r-$\Delta\phi$ separation at the point of conversion. In order to avoid the over-filtering to the additional conversion of the photon radiated from the real electron, no existence of an additional conversion partner which is presumably coming from the real electron is required.

3.2 Muon

Muon candidates are expected to have a track in the COT which points to hits in the muon chambers. Muons are almost minimum ionizing particles, hence the energy deposited by muons in the calorimeter is expected to be only a few GeV, independent of its momentum.

3.2.1 Muon Triggers

There are three central muon detectors: CMU, CMP, and CMX. Muons in the dataset basically follow the MUON_CMUP18 or MUON_CMX18 trigger path. The trigger path for high-p_T muons observed in both the CMU and CMP detectors is MUON_CMUP18. Level-3 of this trigger requires a match between tracks in the COT and muon stubs in both the CMU and CMP detectors (r-$\Delta\phi$ less than 10 cm for CMU stubs and 20 cm for CMP stubs), and a COT track with $p_T \geq$ 18 GeV/c. The trigger path for high-p_T muons observed in the CMX detector is MUON_CMX18. Level-3 of this trigger requires a COT detector track matched to a CMX stub in a window of r-$\Delta\phi$ of less than 10 cm, and a COT track with $p_T \geq$ 18 GeV/c.

3.2.2 Muon Geometric and Kinematic Cuts

Position information from the COT and muon chambers can be used together to extrapolate the path of a muon through the CDF detector.

Kinematic Requirement ($p_T \geq$ 20 GeV/c): Muons from W decay in the top quark pair process are expected to have high-p_T.

CMU Track Matching ($|\Delta r|_{\mathrm{CMU}} < 7.0$ cm): This is a COT and the muon detector (CMU) matching requirement. The extrapolation of a COT track to the muon chambers must fall within $\Delta r < 7.0$ cm of the associated hits in the CMU detector.

CMP Track Matching ($|\Delta r|_{\mathrm{CMP}} < 5.0$ cm): This is a COT and the muon detector (CMP) matching requirement. The extrapolation of a COT track to the muon chambers must fall within $\Delta r < 5.0$ cm of the associated hits in the CMP detector.

CMX Track Matching ($|\Delta r|_{\mathrm{CMX}} < 6.0$ cm): This is a COT and the muon detector (CMX) matching requirement. The extrapolation of a COT track to the muon chambers must fall within $\Delta r < 6.0$ cm of the associated hits in the CMX detector.

COT exit radius (for CMX muons) > 140 cm: The exit radius requirement is imposed on CMX muon only to guarantee that muons passing through the COT detector have the opportunity to pass through a minimum number of COT layers.

Interaction Vertex ($|Z_{\mathrm{vtx}}| < 60$ cm): The same reason as electron.

3.2.3 Muon Identification Cuts

Several muon identification variables are used to reject backgrounds and enhance the fraction of true muon.

EM Energy ($E_{\mathrm{EM}} < \max(2.0, 2.0 + 0.0115 \times (p - 100.0))$ GeV): The energy deposited by a muon passing through a CEM tower must be less than 2.0 or $(2.0 + 0.0115 \times (p - 100.0))$ GeV, whichever is a maximum. This ensures that muon candidates are consistent with the expectations of minimum ionizing particles.

Hadronic Energy ($E_{\mathrm{HAD}} < \max(6.0, 6.0 + 0.0280 \times (p - 100.0))$ GeV): The energy deposited by a muon passing through a central hadronic calorimeter tower must be less than 6.0 or $(6.0 + 0.0280 \times (p - 100.0))$ GeV, whichever is a maximum. The threshold for the hadronic region of the calorimeter is higher than that for the electromagnetic region because the hadronic region contains more material for the muon to interact with.

Isolation (Iso(0.4) ≤ 0.1): Like electron candidates, muon candidates have a maximum value of isolation. For muons, isolation is calculated the same as for electrons, although the subtraction of the muon p_T is not necessary. To measure muon isolation the E_T in a cone of $\Delta R \leq 0.4$ around the track which has been

matched to hits in the muon detectors is use. The isolation is determined as:

$$\mathrm{Iso}(0.4) \equiv \frac{E_T^{0.4}}{p_T}, \tag{3.3}$$

where p_T is calculated by the muon track using the hit information from the COT and $E_T^{0.4}$ is the transverse energy within a cone of $\Delta R \leq 0.4$.

Impact Parameter ($d_0 < 0.2$ cm if no silicon hits, $d_0 < 0.02$ cm if silicon hits): The impact parameter, d_0, is used to help with the rejection of cosmic rays which pass through the CDF detector and might enter the dataset. d_0 is determined using the track which has been matched to the hits in the muon detector. The cut on impact parameter is looser for tracks which do not have silicon hits. The tighter cut is applied with the silicon hits due to the improvement of the tracking resolution.

Track Segment : The only well-reconstructed muon tracks are used. The stub of the muon track must have more than 3 axial super-layers and 2 stereo super-layers with at least 5 hits in the COT.

Cosmic Veto: The muons from cosmic rays are detected and reconstructed in the CDF detector although they do not originate from the interaction point. Most cosmic rays pass through the CDF detector leaving the two signatures in the muon detectors separated in ϕ by 180° and separated in time as the muon passes from one end of the detector to the other. The cosmic veto algorithm is capable of rejecting cosmic rays by cutting on the $\Delta\phi$ between a reconstructed muon and any other muon stub found in the detector while considering the timing information obtained for the calorimetry and the tracking detectors.

3.3 Jet

3.3.1 Jet Clustering Algorithm, *JetClu*

The partons produced by the hard interaction processes of the $p\bar{p}$ collisions experience the strong force of QCD, and then fragment to the bunch of hadrons. This parton fragmentation process with the subsequent deposition of single particle energies into the tower of the calorimeter creates the typical jet structures observed in collisions producing high transverse energy. Therefore the energy information on calorimeter towers is used to reconstruct a jet, but the assignment of towers to the jet is not unique.

The definition of a jet is obviously arbitrary and found by a suitable algorithm. If one tries to extrapolate a parton information using the suitable algorithm, one has to

pay attention to the parton configurations in the perturbative calculation. Higher-order QCD processes give more elaborate configurations of partons. For instance, the gluon radiation produced by the association with the hard-scattering partons may not be observed under the loose size of cone, while the dominant configurations are the presence of the high-p_T scattering from the outgoing hard-scattering partons. If the experimental definition of a jet is sufficiently loose, all configurations will fall into the single jet.

Various cone algorithms have been developed with many experiments, where a cone have a circular cross-section in the η-ϕ plane to account for the distortion expected to form the Lorentz transformation. A fixed cone algorithm, *JetClu*, is employed which is a widely used in many analysis at CDF. One merit of using the fixed cone algorithm is a definition of the tracks associated with the cone. This is supported by the algorithms of a heavy flavor tagging like a bottom quark.

The *JetClu* starts by making a list of all towers with an E_T greater than some threshold, called $E_T^{\rm seed}$. The second list containing candidates for clustering is made of all towers above the second threshold $E_T^{\rm cand}$. At the present the default values of $E_T^{\rm seed}$ and $E_T^{\rm cand}$ are 1 GeV and 0.1 GeV, respectively. In the plug and forward calorimeter regions, towers are grouped together in sets of three in ϕ, spanning 15° to correspond to the segmentation of the central calorimeter. Precluster is formed by combining all touching seed towers, which are required to have continuously decreasing tower E_T. The clustering is performed using the tower segmentation without gathering towers used in preclustering. A fixed cone in η-ϕ space of radius R is formed around the centroid determined from the E_T weighted centroid of their precluster. The candidate towers in this cone are merged into the cluster and the centroid is re-computed. Again, all candidates inside the cone around the new centroid are merged in. This process is iterated on until the tower list remains unchanged. The actual cone size used in the analyses is 0.4. The iterative cone algorithm also provides a scheme from treating overlapping clusters. If the towers of one cluster are completely contained within another, the smaller one (lesser E_T) is dropped. If the towers of different clusters partially overlap, an overlap fraction is computed as the sum of the E_T of the common towers divided by the E_T of the smaller cluster. If the fraction is above a cutoff (default is 0.75), then the two clusters are combined. If the fraction is less than the cut, the clusters remain separate, and each tower in the overlap region is assigned to the cluster with the nearest center in η-ϕ space. After the towers are uniquely assigned to clusters, the centroids are re-computed. This tower reshuffling process is iterative, and ends when the tower lists remain fixed.

3.3.2 Variables in *JetClu*

During the clustering process, the centroid associated with each cluster is calculated by assigning massless four-vectors to each of the electromagnetic and hadronic towers. The four-vectors have a magnitude equal to the energy deposited in the

tower, and a direction defined by a unit vector pointing from the event vertex to the center of the face of the calorimeter tower (calculated at the depth that corresponds to shower maximum). A cluster four-vector (p_x, p_y, p_z, E) is then defined by summing over the towers in the cluster:

$$p_x = \sum_i p_x^i,\ p_y = \sum_i p_y^i,\ p_z = \sum_i p_z^i,\ E = \sum_i E^i. \tag{3.4}$$

Given the cluster four-vector, several jet quantities are readily calculated:

$$E_T = E \sin\theta,\ \eta = -\ln\left\{\tan\left(\frac{\theta}{2}\right)\right\},\ \phi = \arctan\left(\frac{p_y}{p_x}\right), \tag{3.5}$$

where

$$\theta = \arcsin\left(\frac{\sqrt{p_x^2 + p_y^2}}{\sqrt{p_x^2 + p_y^2 + p_z^2}}\right). \tag{3.6}$$

Because the z vertex distribution is spread out along the beam line, forming a Gaussian with a σ of approximately 30 cm, it is necessary to correct the pseudorapidity of all jets from η_d to η. This shift implies a small energy correction to account for the incidence angle of the jets on the face of the calorimeter.

3.3.3 Jet Energy Corrections

The measured four-vector of jets generally differs from the energies of the initial partons. This is the result from both instrumental and physical effects such as low energy non-linearities, η crack energy losses, underlying events, and clustering. Some of the corrections are decided by the measurable quantities independent of the theory, while some of them rely on the theory prediction. Thus the row jet energies measured in the calorimeter must be corrected for detector effects at first before they can be compared to physics predictions/models. The correction strategy is the followings:

Relative Corrections : The first step in jet energy corrections is to correct the jets for any variation in the response with detector η. For this correction, dijet event samples are used. Since the transverse energy of the two jets in a $2 \to 2$ process should be equal, the energies of jets in the plug and forward calorimeters are scaled to give the energy of an equivalent jet in the central calorimeter. One well-measured central jet ($0.2 < |\eta| < 0.6$) is required and a scale factor is derived from the dijet balance to the second jet. The central calorimeters CEM/CHA are the best understood calorimeters in CDF and the selected region is far away from the cracks. The gain variation depending on the time (run range) in the plug calorimeters is also taken into account. The corrections for the Monte Carlo and data are determined

separately since some discrepancy between data and simulation can be seen due to a lack of the materials in the detector simulation.

Multiple Interaction Corrections : The multiple interaction affects the measured jet energy when the energy from these minimum bias events falls into the jet clustering cone. The transverse energy in a random cone is measured in minimum bias data and parameterized as a function of the number of vertices in the event. This transverse energy is subtracted from each jet to account for multiple interaction in the same bunch crossing as a function of the number of vertices in the event. This correction factor is a linear function of the number of reconstructed vertices in the event. Only vertices associated with at least 2 COT tracks in minimum bias events are used to decide this correction factor.

Absolute Corrections : The jet energy measured by the calorimeters must be corrected for any non-linearity and energy loss in the un-instrumented regions of each calorimeter. The absolute jet corrections account for the response to particle-level energy in the central calorimeter. This correction depends on the jet fragmentation properties. The calibration point is derived using a 50 GeV pion from test beam data. For the non-linearity response, the tuned Monte Carlo events are used for the charged and neutral particles. After fragmentation, the events are processed with a full CDF detector simulation. Each simulated event is compared to the total p_T of all generated particles lying in a cone centered about the measured jet axis. A quadratic spline fit is used to parameterize the mean jet response as a function of E_T for the each cone size.

Underlying Event Corrections : The underlying event contains all the soft interactions except the hard one. The underlying event energies must be subtracted from the measured jet energy when these particles fall into the clustering cone. The correction procedure is the same as the multiple interaction correction. Events with only one vertex are used to determine the underlying event correction.

Out-of-Cone Corrections : The jet clustering may not include all the energy from the initiating parton. Some of the partons generated during fragmentation may fall outside the cone chosen for clustering algorithm. Out-of-cone corrections are applied in order to correct the particle-level jet energy to the parton energy (as much as theoretically allowed). These corrections are completely independent of detector/calorimeter performance and depend on the parton fragmentation functions. The correction factor is parameterized as a function of jet p_T. Jet tends to become narrower at large energies, and the fractional energy deposited outside the cone decreases.

Thus, the jet energy is corrected by

$$p_T(R) = [p_T^{\rm raw}(R) \times f_{\rm rel} - {\rm UEM}(R)] \times f_{\rm abs}(R) - {\rm UE}(R) + {\rm OC}(R), \qquad (3.7)$$

where R denotes the clustering cone size, p_T and $p_T^{\rm raw}$ are the corrected and row transverse momenta of jet, $f_{\rm rel}$ is the relative jet energy correction, UEM(R) is the multiple interactions correction, $f_{\rm abs}(R)$ is the absolute jet energy correction, UE(R) is the underlying event correction, and OC(R) is the out-of-cone correction.

3.3.4 Jet Energy Scale Uncertainties

The differences between the data and CDF simulations of the jet responses are treated as the systematic uncertainties of the jet energy scale (JES) [58]. The uncertainties are estimated for each type of jet energy corrections. The uncertainties due to the absolute scale and the jet shape (out-of-cone) are dominant. The main systematic uncertainties on the absolute scale are obtained by propagating the uncertainties on the single particle response (E/p) and the fragmentation. Smaller contributions are from the calorimeter response close to tower boundaries in azimuth, and from the stability of the calorimeter calibration with time. The uncertainties from the jet shape are estimated by measuring the energy flow between cones of size 0.4 and 1.3 in both data and MC simulations. The total JES uncertainties in the central region are shown in Fig. 3.1.

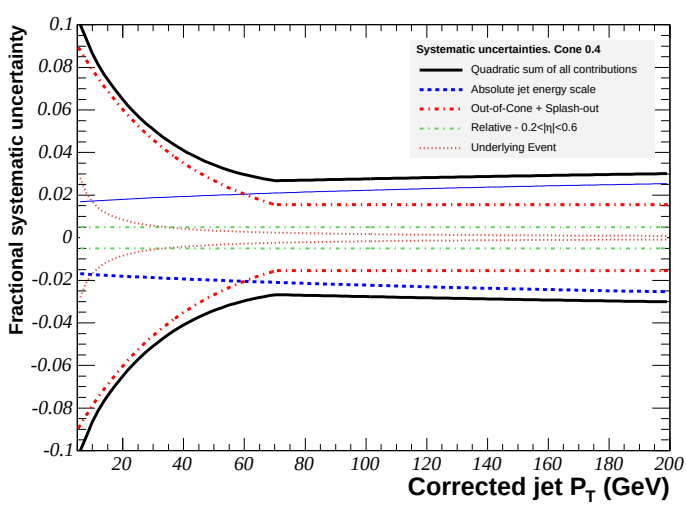

Figure 3.1: The total uncertainties of JES as a function of corrected jet p_T in the central calorimeter ($0.2 < |\eta| < 0.6$).

3.4 Bottom Quark Tagging

Most of the non-$t\bar{t}$ events which pass the lepton+jets event selection criteria are not processes which contain any heavy flavor b or c quarks in the final state. Thus the b-quark "tagging" technique is important for the top quark analysis. The bottom hadrons have the long life time ($c\tau \sim 460\mu$m), the large mass, and the semi-leptonic decay modes ($\sim$ 10%/lepton). The keys of b-quark tagging are the displaced secondary vertex, the large impact parameters of associated tracks, the soft lepton inside the jet, and the high invariant mass. The displaced secondary vertex tagging, *SecVtx* [45], and the large impact parameters of tracks inside the jet cone, *JetProb* [48], are commonly used in CDF. The details of these algorithms are described in Chapter 4.

3.5 Missing Transverse Energy

In proton-antiproton collisions at the Tevatron, the total transverse energy should sum into zero since the colliding protons and anti-protons are known to have zero momentum in the transverse $(x-y)$ plane. A vector sum of the transverse energy of all calorimeter towers and muons in the event is considered. The difference between zero and this vector sum is taken as the missing transverse energy, $\not\!\!E_T$. There are many sources of $\not\!\!E_T$: neutrinos in the event which escape the detector without having the energy measured directly, particles which escape the detector through cracks between calorimeter wedges, the small calorimeter energy deposition of muons, the beam slope which causes the non-central collisions, or the mis-measurement of the energy. In the lepton+jets dataset, the events with high missing transverse energy due to the neutrino from W decay are expected.

When tracks and vertex positions are reprocessed offline, a curvature correction has an impact on the muon p_T. Accordingly, the x and y components of the $\not\!\!E_T$ to account for this effect are corrected:

$$\not\!\!E_{x,\mathrm{corr}} = \not\!\!E_{x,\mathrm{uncor}} + (p_{T,\mathrm{uncor}} - p_{T,\mathrm{corr}})\cos(\phi_{\mathrm{uncor}}), \tag{3.8}$$

$$\not\!\!E_{y,\mathrm{corr}} = \not\!\!E_{y,\mathrm{uncor}} + (p_{T,\mathrm{uncor}} - p_{T,\mathrm{corr}})\sin(\phi_{\mathrm{uncor}}). \tag{3.9}$$

Up to this point, the $\not\!\!E_T$ has been calculated using the raw jet energies. Since the jet energies are corrected prior to the application of jet E_T cuts, the components of the $\not\!\!E_T$ now need to be adjusted for the difference between the raw and the corrected jet energies. This is done for all jets by replacing p_T of muon with E_T of jets in Eqs.(3.8) and (3.9). More than 20 GeV on the corrected $\not\!\!E_T$ is required.

3.6 Primary Vertex

Some of the lepton+jets selection criteria require the knowledge of the position of the interaction point, known as the primary vertex. The calculation of E_T as well as $\not\!\!E_T$ relies on the position in z where the collisions occur on an event-by-event basis. Initially, stand-alone tracking using information from only the silicon and COT detectors is used to determine the primary vertex z position. A set of minimal quality requirements are imposed on both silicon and COT tracks; tracks which pass these requirements are then used by the tracking algorithm to triangulate vertices in the r-z plane. Since there is a high fake rate for these vertices, the primary vertex finder imposes stronger criteria on the number of tracks and the minimum p_T. The primary vertex finder requires that vertices contain tracks with either silicon or COT hits associated with them.

A point of origin along the z-axis (z_0) is assigned for all tracks in the event. If a track happens to pass within 1 cm of a silicon stand-alone vertex, or within 5 cm of a COT stand-alone vertex, it is considered to belong to that vertex. To determine the position of the vertex, the z_0 of all tracks for a particular vertex are weighted by their errors,

$$z = \frac{\sum_i z_{0,i}/\delta_i^2}{\sum_i 1/\delta_i^2}, \tag{3.10}$$

where the sum is taken over all tracks associated with a particular vertex, $z_{0,i}$ and δ_i are the z_0 and the associated error of the i-th track, respectively.

The *PrimeVtx* algorithm is used to find the x and y coordinates of the primary vertex. This information is essential for the b-quark tagging algorithm. Starting from an input vertex with a given x_0, y_0 and z_0 position, the primary vertex is the beam-line position which has been measured during proton-antiproton collision. Some requirement on Δz and the impact parameter, d_0, are imposed on the tracks prior to being considered by the vertexing algorithm:

- $|z - z_{\text{vertex}}| < 1.0$ cm
- $|d_0| < 1.0$ cm (with respect to the beam-line)
- $|d_0|/\sigma < 3.0$ (with respect to the beam-line)

After passing these selection criteria, the tracks are ranked by decreasing p_T. Only the highest p_T tracks which pass the selection criteria are used in a fit to the primary vertex. The *PrimeVtx* algorithm removes the tracks with the worst fit, determined by requiring $\chi^2_{\text{fit}} < 10$. The algorithm continues this process of fitting and track rejection based on χ^2_{fit} iteratively, until these are no tracks in the fit which have a $\chi^2_{\text{fit}} > 10$. The precision obtained in the determination of the vertex x and y coordinates is $\sim 25 - 30$ μm, but strongly depends on the z position of the vertex.

3.7 Luminosity Measurement

The luminosity of hadron collider experiments can be determined from the counting measurement of inelastic $p\bar{p}$ interaction which has a large cross section measured with an uncertainty of approximately 3%. This process allows precisly to measure the total integrated luminosity. The luminosity monitor has been done at the Cerenkov Luminosity Counters (CLC) [49] by measuring the rate of the inelastic $p\bar{p}$ events. The Cerenkov Counters has a merit that the Cerenkov light is not insensitive to an accidental event such as the beam halo. The total integrated luminosity is expressed as

$$L = \frac{R_{p\bar{p}}}{\epsilon_{\mathrm{CLC}} \cdot \sigma_{in}}, \tag{3.11}$$

where $R_{p\bar{p}}$ is the rate of the inelastic $p\bar{p}$ events measured by CLC, ϵ_{CLC} is the CLC acceptance determined from data and simulation, and σ_{in} is the inelastic cross section. The inelastic cross section 61.7 mb is obtained by scaling the CDF measurement $\sigma_{in} = 60.4 \pm 2.3$ mb at $\sqrt{s} = 1.8$ TeV to 1.96 TeV. +1.9 % correction to the luminosity which comes from extrapolating the inelastic cross section from $\sqrt{s} = 1.8$ TeV to 1.96 TeV is also applied. Using these numbers and requiring the run to belong to the "Good Run List", which contains the run list of proper detector operation, the total luminosity is estimated to be

$$L = 1.9 \pm 0.1 \text{ fb}^{-1}. \tag{3.12}$$

The estimated uncertainty in the CLC measurement is 4.4% and is mostly due to the uncertainty in the absolute normalization of the CLC acceptance. By using the CDF measuerment of the inelastic cross section with the 2.5% uncertainty, the total systematic uncertainty of the integrated luminosity is about 6 %. The summary of the luminosity uncertainty is presented in Table 3.1.

Effect	Uncertainty Estimate
Inelastic cross section (CDF measurement)	2.5%
CLC acceptance	4.4%
Detector instability	< 2 %
Detector calibration	< 1.5 %
On-line to Offline transfer	< 1.0 %
Total Uncertainty	$\sim$5.7 %

Table 3.1: Systematic uncertainties in the luminosity calculation using the CLC and the CDF measurement of the inelastic cross section.

3.8 The Lepton+Jets Event Selection

Several additional cuts are applied to the candidate events to purify the lepton+jets sample. The selection criteria are listed in brief below:

- one tight high-p_T lepton
  A single tight electron or muon as described previously

- $\not\!\!E_T \geq 20$ GeV
  Missing transverse energy ≥ 20 GeV, also described previously

- multiple jets
  - Requirement of at least one b-tagged jet
  - More than three jets for the top quark pair production cross section measurements
  - Exact four jets for the top quark mass measurements and the resonance search

- Z boson veto
  The Z boson veto criteria removes events in which the invariant mass of the charged lepton and another object in the event falls within a specific range of the Z boson mass. It is the intention of this cut to eliminate events which come from the decays of Z bosons, but which managed to pass the more general lepton+jet selection criteria when one lepton from the decay of the Z is lost. Z bosons can mimic the signal of a W boson in the CDF detector when one of the leptons from the Z decay are mis-identified. For example, consider the decay $Z \rightarrow ee$ where one electron is included in the jet collection, or falls into a crack between calorimeter wedges. The veto rejects events where the tight lepton and any second object from an invariant mass between 76 and 106 GeV/c^2, which corresponds to a ± 15 GeV/c^2 window around the 91 GeV/c^2 Z boson mass.

- Dilepton veto
  This is done to ensure that no $t\bar{t}$ candidate events which belong in the dilepton sample make it into the lepton+jets event sample.

The identification and kinematic cuts of electrons, muons, and jets are summarized in Table 3.2.

Variable	Value
Global Event Quantities	
Z and Dilepton Veto	Applied
$\not\!\!E_T$	$\geq$ 20 GeV
number of tight leptons	1
Jets	
E_T	$\geq$ 15 GeV
$\lvert\eta\rvert$	$\leq$ 2.0
Tight Electrons	
Fiducial and CEM	True
E_T	$\geq$ 20 GeV
p_T	$\geq$ 10 GeV/c
$E_{\rm HAD}/E_{\rm EM}$	$\leq$ 0.055 + 0.00045 $\times$ E
E/p (if $E_T < 100$ GeV)	$\leq$ 2.0
p_T (if $E_T \geq 100$ GeV)	$\geq$ 50 GeV/c
$Q \times \Delta r$	$>$ 1.5 and $>$ 3.0 cm
$\lvert\Delta z\rvert$	$<$ 3.0 cm
$\lvert\chi^2_{\rm strip}\rvert$	$<$ 10
$L_{\rm shr}$	$<$ 0.2
Number of Axial Segments	$\geq$ 3
Number of Stereo Segments	$\geq$ 2
$\lvert z_{\rm vtx}\rvert$	$<$ 60 cm
Isolation	$<$ 0.1
Conversion	False
Tight Muons	
Cosmic Veto	Applied
CMUP or CMX	True
p_T	$\geq$ 20 GeV/c
$E_{\rm EM}$	$<$ max(2.0, 2.0 + 0.0115 $\times$(p-100.0)) GeV
$E_{\rm HAD}$	$<$ max(6.0, 6.0 + 0.0280 $\times$(p-100.0)) GeV
$\lvert\Delta x\rvert_{\rm CMU}$	$<$ 7.0 cm
$\lvert\Delta x\rvert_{\rm CMP}$	$<$ 5.0 cm
$\lvert\Delta x\rvert_{\rm CMX}$	$<$ 6.0 cm
$\lvert\Delta z_0\rvert$	$<$ 60 cm
$\lvert d_0\rvert$ if no silicon hits	$<$ 0.2 cm
$\lvert d_0\rvert$ if silicon hits	$<$ 0.02 cm
Number of axial hits	$\geq$ 3
Number of stereo hits	$\geq$ 2
Isolation	$<$ 0.1
COT exit radius (for CMX)	$>$ 140 cm

Table 3.2: Summary of identification and kinematic cuts of electron, muon, and jet.

Chapter 4

Top Pair Production Cross Section Measurements

In this chapter, the measurements of the top quark pair production cross section ($\sigma_{t\bar{t}}$) in the lepton+jets channel are described. The production cross section is calculated from the following formula:

$$\sigma_{t\bar{t}} = \frac{N_{\rm obs} - N_{\rm bkg}}{(F_{\rm scale}\epsilon_{\rm tag})(\epsilon_{\rm pretag}\int Ldt)}, \tag{4.1}$$

where $N_{\rm obs}$ is number of events in data passing event selection, $N_{\rm bkg}$ is number of non-$t\bar{t}$ events expected to pass event selection, $\epsilon_{\rm tag}$ is $t\bar{t}$ acceptance (geometric acceptance and event selection efficiency), $F_{\rm scale}$ is the ratio of event tagging efficiencies in data and Monte Carlo, and $\int Ldt$ is integrated luminosity.

The b-tagging algorithm is the most important part to measure the top quark pair production cross section. First we describe the $t\bar{t}$ production cross section using the *SecVtx*, and then using *JetProb*.

4.1 *SecVtx* Tagging Algorithm

The b-quarks are identified by vertexing the decay daughters of the b or c meson. The *SecVtx* tagging algorithm is described in detail in Ref. [45], and briefly summarized here. The *SecVtx* algorithm first obtains a primary interaction vertex on an event-by-event basis. This primary vertex has a resolution of order 10-20 μm. The algorithm considers each jet for tagging, and examines tracks within each jet, applying basic quality cut. The algorithm then attempts to find a secondary vertex that is displaced from the primary vertex by vertexing tracks with large impact parameter (d_0) significance with respect to the primary vertex, as shown in Fig. 4.1.

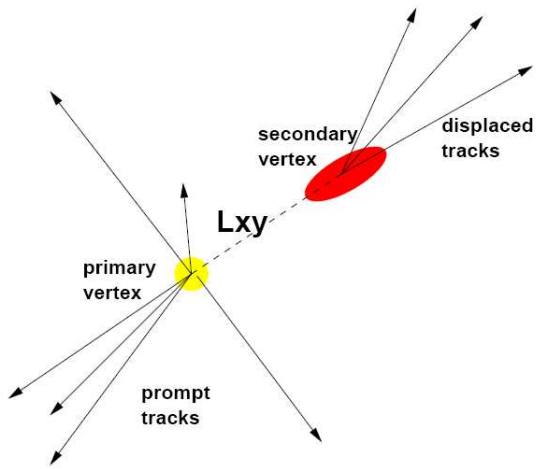

Figure 4.1: The image of *SecVtx* tagging algorithm. Information of L_{xy} significance is used to be considered "displaced".

Then a seed vertex is calculated from the two most displaced tracks, and the tracks are added to that seed vertex. The vertex under consideration has three tracks with impact parameter significance $|d_0|/\sigma_{d_0} > 2.0$ and transverse momentum $p_T > 0.5$ GeV/c, containing at least one track with $p_T > 1.0$ GeV/c. If no three-track vertex is found, the algorithm attempts to find a two-track vertex of tracks with higher quality cut, $|d_0|/\sigma_{d_0} > 3.5$, and $p_T > 1.0$ GeV/c, containing at least one track with $p_T > 1.5$ GeV/c. Once a secondary vertex is found, the distance between the primary and secondary vertices in the plane perpendicular to the beam-line is calculated. This vertex is then projected to the jet axis:

$$L_{2D} = (\vec{r_{SV}} - \vec{r_{PV}}) \cdot \hat{p_{jet}}, \tag{4.2}$$

where $\vec{r_{PV}}$ is the position of the primary vertex, $\vec{r_{SV}}$ is the position of the secondary vertex, $\hat{p_{jet}}$ is the jet direction, and L_{2D} is the two-dimensional decay length along the jet axis. $|L_{2D}|/\sigma_{L2D} > 7.5$ for the jet to be considered "displaced". If the sign of L_{2D} is positive (negative), this is considered as a positive (negative) tag.

Long-lived quarks (b's and c's) enhance the positive tag distribution, while the negative tags are primarily due to the resolution of the tracking. The negative tag distribution is taken as an estimate of the positive tags due to the resolution (*mistag*).

Both the positive and negative tag rates are parameterized in jet E_T, the number of tracks in the jet, jet η, jet ϕ, and the total scalar sum of the E_T of all the jets. These parameterizations are called *tag matrices*. The negative matrix (or *mistag matrix*) is used to determine the number of mistags.

The scale factor is calculated by taking the data-MC ratio of b-tagging efficiency,

$$F_{\text{scale}} = \frac{\epsilon_{\text{DATA}}}{\epsilon_{\text{MC}}} = 0.95 \pm 0.04. \tag{4.3}$$

Per jet tagging efficiencies for the top quark pair MC sample are shown in Fig. 4.2 and the *mistag* rates in Fig. 4.3.

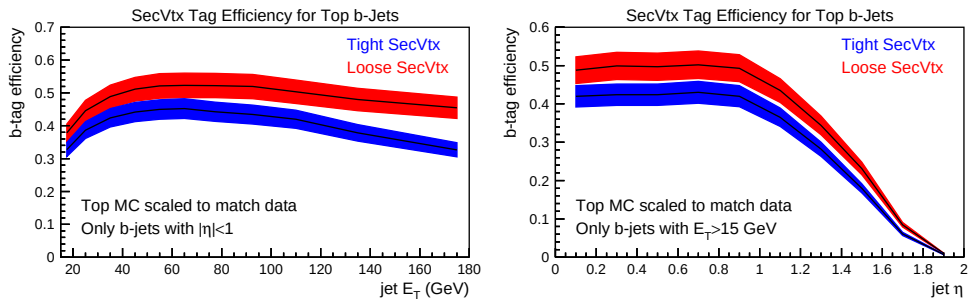

Figure 4.2: The b-tagging efficiency plots as a function of jet E_T (left) and η (right) for the two (tight and loose) operating points.

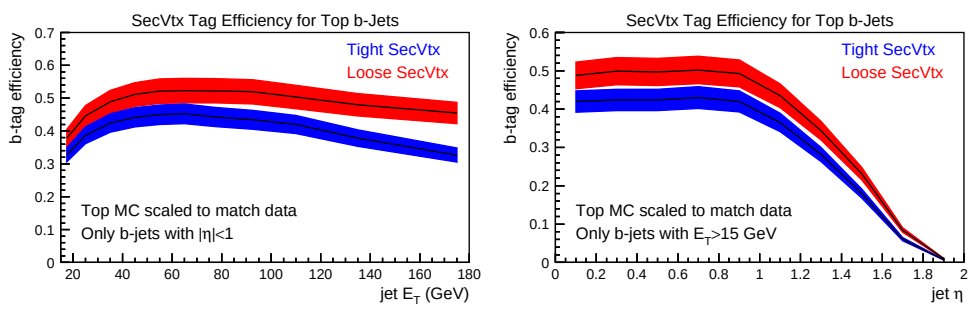

Figure 4.3: The plots show the false positive tag rate (including asymmetry corrections) as a function of jet E_T (left) and η (right). These have been measured from inclusive jet data.

4.1.1 Background Estimation

To estimate the background events in the lepton+jets sample, the data is used as much as possible to know the process normalizations. In particular, the W+jets contribution, which dominates the pretag (before the requirement of b-tagging) sample and the tagged 1 and 2 jet multiplicity bins, is not known due to the large corrections to the calculable cross section at higher order. Therefore the W+jets normalization

is estimated from the pretag data sample by subtracting the events with fake W's (non-W) and those with non-QCD jet production ($t\bar{t}$, diboson, single top). This normalization is done independently in each jet multiplicity bin.

In order to estimate the tag rate for such events, additionally the *heavy flavor fraction* in W+jets (the fraction containing real bottom and charm jets) must be evaluated. The fraction is assumed to be more stable at higher order than an absolute cross section. These fractions are measured at leading order in a Monte Carlo sample, which specifically takes into account $Wb\bar{b}$, $Wc\bar{c}$, and Wc processes, and the overall scale for $b\bar{b}$ and $c\bar{c}$ is calibrated in the generic jets. This scale is primarily intended to cover a mis-estimate of $g \to b\bar{b}$ and $g \to c\bar{c}$ processes which contribute largely to the heavy-flavor content of both W+jets and the generic QCD. For W+jets processes, the pretag and tag expectation numbers can be written as:

$$N^W_{\rm pre} = N^{\rm data}_{\rm pre}(1 - F_{{\rm non}-W}) - N^{t\bar{t}}_{\rm pre} - N^{\rm diboson}_{\rm pre} - N^{\rm single-top}_{\rm pre}, \tag{4.4}$$

$$N^W_{\rm tag} = N^W_{\rm pre}\left(\sum_i \epsilon^{hf}_i F^{hf}_i + \epsilon^{LF}(1 - \sum_i F^{hf}_i)\right), \tag{4.5}$$

where ϵ's are tagging efficiencies, F^{hf}'s are the heavy flavor fractions, and the sum is over different heavy flavor configurations ($1b$, $2b$, etc.). The quantity $F_{{\rm non}-W}$ is the fraction of the pretag sample not attributed to the process with a real W decay. It is clear from the above equations that the backgrounds, especially the W+jets normalization, depend on the assumed cross sections for other processes. Thus to measure the $t\bar{t}$ cross section this method is implemented iteratively. In the following explanations, this iteration is neglected to avoid the complications.

The four main categories of background are considered: diboson and single top production (MC based background), generic QCD with a faked W (non-W), W's produced in association with real heavy flavor (W + Heavy Flavor), and real W's with light flavor tags (*mistags*). These background estimations are described in the followings.

4.1.2 Electroweak and Single Top (MC Based Background)

Several distinct physics processes involving real W's can reproduce the signature of top pair production. The contributions from diboson production (WW, WZ, and ZZ), single top production, and $Z \to \tau^+\tau^-$ are considered. These processes have well-defined theoretical cross sections and a high probability of producing a tagged jet. WW and WZ events can result in a leptonic W and a heavy flavor decay of the other boson; single top yields at least one b-jet and a real W; ZZ requires one Z to decay leptonically with one missed (or misidentified) lepton, with the other decaying to $b\bar{b}$ or $c\bar{c}$; and $Z \to \tau\tau$ have one τ decay leptonically with a tag on the opposite-side three-prong hadronic decay. The recent theoretical cross section

results of these processes are assumed as in Table 4.1. The single top cross section is additionally scaled by 1/3 to account for the forced W decay to leptons.

Process	Cross Section (pb)
WW	12.4 ± 0.25
WZ	3.96 ± 0.06
ZZ	1.58 ± 0.06
single top (s-ch)	0.88 ± 0.05
single top (t-ch)	1.98 ± 0.08
$Z \to \tau\tau$	265 ± 30

Table 4.1: Cross sections used to estimate backgrounds.

4.1.3 QCD Fake Events (Non-W)

The requirements of an identified lepton and large missing energy enhance the W content of the pretag sample, but some events can pass these requirements without a real W. Fake leptons can come from conversions (electrons) or mis-identified pion's/kaons. Missing energy results from mis-measured jets, detector effects, and some energy at high η that misses the detector altogether.

Since non-W events will rarely have a high-p_T neutrino as the real cause of the missing energy, these events are separated from real W's by isolating excesses of events with low missing E_T. The missing energy distributions in the range 0 to 120 GeV are fitted separately in each jet bin and for the pretag and tagged sample. To conserve statistics in the higher jet multiplicity bins, three or more jets events are merged. The electron-like objects are used to model the non-W kinematics, which fail the two of electron ID cuts. A fraction of non-W, $F_{\text{non}-W}$ is measured. A summary of the results is shown in Table 4.2.

	1-jet	2-jet	$\geq$ 3-jet
$F^{\text{pre}}_{\text{non}-W}$ (%)	0.25 ± 6.4	16.0 ± 2.5	17.3 ± 2.8
$F^{\text{tag}}_{\text{non}-W}$ (%)	0.18 ± 0.16	0.76 ± 0.21	1.08 ± 0.29
$F^{\text{2tag}}_{\text{non}-W}$ (%)	-	0.03 ± 0.04	0.08 ± 0.11

Table 4.2: Expected contribution from non-W backgrounds. The $t\bar{t}$ contribution is removed from the missing E_T distribution. Statistics are merged for all events with three or more jet multiplicity bins in the fit, and errors include the systematics.

4.1.4 W + Heavy Flavor

After subtracting the non-W, electroweak, and $t\bar{t}$ contributions from the sample, the process of generic W+jets remains. Due to the poor knowledge of the higher order W+jets cross sections, the *heavy flavor fractions*, which determine how much of the remaining pretag sample contains b or c jets, is measured. Although the method is partially Monte Carlo driven, the final measurements are checked against generic jet data. The contributions from $Wb\bar{b}$, $Wc\bar{c}$, and Wc are considered. A summary of the heavy flavor fraction is shown in Table 4.3.

The tagging efficiency for each class of event is measured in Monte Carlo, then the scale factor is applied. A summary of the efficiencies is shown in Table 4.4. The efficiency times the heavy flavor fraction, summed over the four class of heavy flavor, yields the tag rate for W+Heavy Flavor. This total rate times the corrected pretag sample provides an estimate of the tagged background expectation.

	1-jet	2-jet	3-jet	$\geq$ 4-jet
Wbb, $1b$	0.7 ± 0.3	1.4 ± 0.6	2.4 ± 1.0	3.3 ± 1.4
$Wb\bar{b}$, $2b$	-	0.9 ± 0.4	1.8 ± 0.7	3.3 ± 1.3
$Wc\bar{c}$ or Wc, $1c$	5.5 ± 1.7	8.7 ± 3.2	11.7 ± 3.8	13.3 ± 4.9
$Wc\bar{c}$, $2c$	-	1.4 ± 0.6	3.3 ± 1.3	6.0 ± 2.4

Table 4.3: The heavy flavor fractions for W+Heavy Flavor background. These are the fractions of generic W+jets (in %) containing heavy flavor jets.

	1-jet	2-jet	3-jet	$\geq$ 4-jet
Single Tag Efficiency (%)				
$1b$	31 ± 2	34 ± 2	36 ± 2	37 ± 3
$2b$	-	55 ± 2	56 ± 2	57 ± 3
$1c$	7 ± 2	8 ± 2	9 ± 2	11 ± 2
$2c$	-	14 ± 2	15 ± 2	17 ± 3
Double Tag Efficiency (%)				
$1b$	-	0 ± 0	1 ± 0	2 ± 0
$2b$	-	12 ± 1	13 ± 1	13 ± 2
$1c$	-	0 ± 0	0 ± 0	0 ± 0
$2c$	-	1 ± 0	1 ± 1	1 ± 0

Table 4.4: Tagging efficiency for the various classes of heavy-flavor event in W+jets.

4.1.5 Mistags

After accounting for all non-W events, $t\bar{t}$, other electroweak processes, and heavy flavor tags in generic W+jets, the only remaining contribution is from tags in W

+ Light Flavor, or *mistags*. A leading order estimate is to run the *negative mistag matrix* on the pretag sample, then to scale down by the fraction of events which are not W+Light Flavor. The matrix is applied to jets in the pretag sample and determines a probability for each jet to be tagged. The sum of these probabilities is the expected number of mistagged jets. This estimate is corrected by the jet E_T dependent *mistag asymmetry* to account for the imbalance in positive and negative tags for light jets, as well as the effect of heavy-flavor tags in the sample where the matrix is created. Once each jet has been assigned a mistag probability, the probability for each event to have ≥ 1 or ≥ 2 mistagged jets can trivially constructed. To isolate the W+Light Flavor component, the total prediction is multiplied by the fraction of the pretag sample not yet attributed to $t\bar{t}$, dibosons, single top, non-W, and W+Heavy Flavor. In general, heavy flavor jets (especially from top) will have higher mistag probabilities than light jets, meaning that an average top event will contribute more to the total prediction than a typical W+4jets event.

4.1.6 Top Pair Production Cross Section with *SecVtx* Tag

The $t\bar{t}$ production cross section is calculated by Eq.(4.1). The $t\bar{t}$ acceptance and efficiency is calculated using a PYTHIA $t\bar{t}$ sample with a $M_t = 175$ GeV/c^2. Figure 4.4 shows the jet multiplicity after requiring at least one b-tag using the data of 1.12 fb^{-1}. The measured top quark pair production cross section is

$$\sigma_{t\bar{t}} = 8.2 \pm 0.5(\text{stat}) \pm 0.8(\text{syst}) \pm 0.5(\text{lum}) \text{ pb}. \tag{4.6}$$

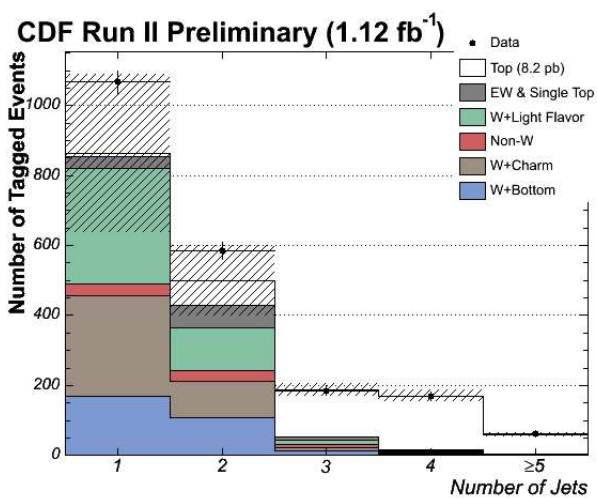

Figure 4.4: The expected and observed number of events sorted by jet multiplicity. The $t\bar{t}$ contribution is normalized to the measured value of 8.2 pb.

4.2 *JetProb* Tagging Algorithm

The jet probability tagging algorithm, *JetProb* [47], is also used to determine whether a jet has been produced from a light parton or a heavy parton. The latter results in long-lived hadrons whose decay gives rise to tracks displaced from the primary interaction vertex. This algorithm uses tracks associated with a jet to determine the probability for these to come from the primary vertex of the interaction. The calculation of the probability is based on the impact parameters (d_0) of the tracks in the jet and their uncertainties. The impact parameter is assigned a positive or negative sign depending on the position of the track's point of closest approach to the primary vertex with respect to the jet direction, as shown in Fig. 4.5. By construction, the probability for tracks originating from the primary vertex is uniformly distributed from zero to one. For a jet coming from heavy flavor hadronization, the distribution peaks at zero, due to tracks from long lived particles that have a large impact parameter with respect to the primary vertex.

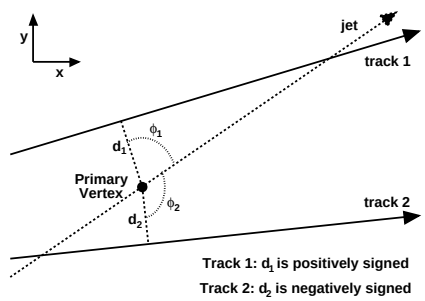

Figure 4.5: The sign of the impact parameter of a track. The impact parameter is positive (negative) if the angle ϕ between the jet axis and the line connecting the primary vertex and the track's point of closest approach to the primary vertex is smaller (bigger) than $\pi/2$.

The particles in a jet coming from a light parton originate at the primary vertex, but these tracks are reconstructed with a non-zero impact parameter due to the finite tracking resolution. They have an equal probability of being positively or negatively signed. Jets originated from a heavy parton contain long lived hadrons giving rise to tracks displaced in the jet direction, which preferentially populate the positive side of the signed impact parameter distribution.

The tracking resolution can be extracted from the data by fitting the negative side of the signed impact parameter distribution of tracks. Tracks are divided into different categories according to the number and quality of SVX hits, detector η, and p_T. To minimize the contribution from badly measured tracks with a large impact parameter significance, S_{d_0} (ratio of the impact parameter to its uncertainty), is parameterized for each track category. Tracks passing the quality cuts (Table 4.5) are called jet

probability tracks. The negative side of S_{d_0} is fitted with a function $R(S)$ called the resolution function, which is used to determine the probability, $P_{tr}(S_{d_0})$, that the impact parameter significance of a given track is due to the detector resolution, defined as:

$$P_{tr}(S_{d_0}) \equiv \frac{\int_{-\infty}^{-|S_{d_0}|} R(S)dS}{\int_{-\infty}^{0} R(S)dS}. \tag{4.7}$$

The S_{d_0} distribution peaks at zero and falls quickly with increasing value of $|S_{d_0}|$, but the tails are rather long.

The jet probability P_J that a jet is consistent with a zero lifetime hypothesis is defined as

$$P_J \equiv \prod \times \sum_{k=0}^{N_{trk}-1} \frac{(-\ln \prod)^k}{k!}, \tag{4.8}$$

where

$$\prod = \prod_{l=1}^{N_{trk}} P_{tr} \tag{4.9}$$

and N_{trk} is the number of jet probability tracks with positive impact parameter. Jets are required to have at least two jet probability tracks with positive impact parameter to be taggable. Tracks with negative impact parameter are used to define a negative P_J, which is used to estimate the mis-identification rate. The positive (negative) tagged jets are defined as those jets whose positive (negative) P_J is less than a cutoff of 1% or 5%. Positive tagged jets are expected to be enriched in heavy flavor.

Figure 4.6 shows the b-tagging efficiency using *JetProb* algorithm as a function of jet E_T and η in the top quark pair MC for the jet probability less than 5% and 1%.

Variable	Cut
p_T	> 0.5 GeV/c
$\|d_0\|$	< 0.1 cm
N_{SVX} axial	≥ 3 and ≤ 5
N_{COT} axial	≥ 20
N_{COT} stereo	≥ 17
$\|z_{trk} - z_{pv}\|$	< 5 cm

Table 4.5: Selection criteria for tracks used by the jet probability algorithm.

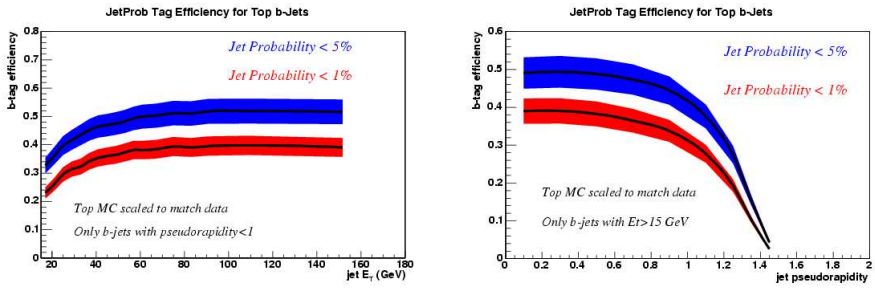

Figure 4.6: The *JetProb* b-tagging efficiency plots as a function of jet E_T (left) and η (right).

4.2.1 Top Pair Production Cross Section with *JetProb* Tag

The results of $t\bar{t}$ production cross section using *JetProb* [48] are summarized. The $t\bar{t}$ acceptance and efficiency is calculated using a PYTHIA $t\bar{t}$ sample with a $M_t = 178$ GeV/c^2. Figure 4.7 shows the jet multiplicity after requiring at least 1 *JetProb* tagging using 318 pb^{-1}. Table 4.6 is the summary of the measured cross sections using the jet probability less than 1% and 5%, requiring 1 or 2 b-tags.

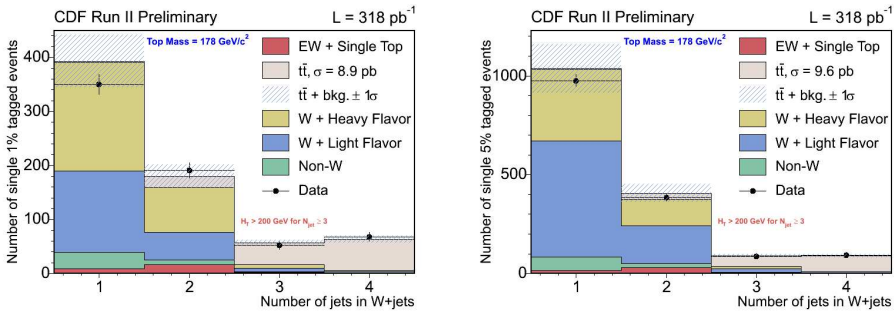

Figure 4.7: The expected and observed number of events sorted by jet multiplicity, the jet probability with 1%(left) and 5%(right). The $t\bar{t}$ contribution is normalized to the measured values.

	Single Tag	Double Tag
JP < 1%	$8.9^{+1.0}_{-1.0} \pm 1.1$	$11.1^{+2.3}_{-1.9} \pm 1.9$
JP < 5%	$9.6^{+1.0}_{-0.9} \pm 1.2$	$11.6^{+1.7}_{-1.5} \pm 1.9$

Table 4.6: The measured $t\bar{t}$ cross sections (pb) using the *JetProb*, the first errors are the statistical uncertainties and the seconds are the systematic uncertainties.

Chapter 5

Top Mass Measurements

The top quark mass is an important parameter of the standard model. The precise measurement of the top quark mass provides a constraint on the Higgs boson mass and other parameters in physics beyond the standard model.

5.1 Top Mass Measurement by DLM

The Dynamical Likelihood Method (DLM) [50, 51, 52, 53], is used to reconstruct the top quark mass. The basic idea of DLM is to use the necessary and sufficient information of physics process, which is defined by the products of the differential cross section ($d\sigma/d\Phi$) and Transfer Function (TF). The transfer function gives the probabilistic correspondence between the parton level variables and the observables. More information of DLM are described in Chapter 6. The top quark mass is determined by the maximum likelihood method. The most important improvement since the previous results from 318 pb^{-1} [54] is the improvement in the Jet Energy Scale (JES) uncertainty by including a variable of JES into the likelihood so that the likelihood is a function of $M_{\rm top}$ and ΔJES. With this improvement of likelihood, most of JES uncertainty is considered not as a systematic but as a statistical uncertainty.

5.1.1 Likelihood Definition

To reconstruct the top quark mass, the three types of likelihood, per path likelihood (Eq. 5.1), per event likelihood (Eq. 5.2) and the joint likelihood (Eq. 5.4) are defined. A process from the initial state of hard process to the observables is called a path.

$$L_{\rm path}(M_{\rm top}, JES, \mathbf{y}_j|\mathbf{x}_i) \equiv N\frac{d\sigma}{d\Phi^{(f)}}w(\mathbf{y}_j|\mathbf{x}_i; M_{\rm top}, JES) \tag{5.1}$$

$$L_{\rm ev}(M_{\rm top}, JES|\mathbf{y}_j) \equiv \frac{1}{N_{\rm path}} \sum_{i=1}^{N{\rm path}} \sum_{{\rm comb}=1}^{N{\rm comb}} \sum_{\nu_z{\rm sol}=1}^{N{\rm sol}} L_{\rm path}(\mathbf{y}_j, M_{\rm top}, JES|\mathbf{x}_i) \tag{5.2}$$

$$L(M_{\rm top}, JES) \equiv \prod_{j=1}^{N{\rm ev}} L_{\rm ev}(M_{\rm top}, JES|\mathbf{y}_j) \tag{5.3}$$

where i is path number, j is event number, $\mathbf{x}_i$ is parton level momenta of i-th path, $\mathbf{y}_j$ is observed quantities of j-th event and w is transfer function. In Eq. (5.1) we use the factorized formula of matrix element: production matrix element, t and $\bar{t}$ propagators ($Pr(t)$ and $Pr(\bar{t})$), and decay matrix element,

$$|\mathcal{M}|^2 \sim |\mathcal{M}_{\rm prod}|^2 Pr(t) Pr(\bar{t}) |\mathcal{M}_{{\rm decay}(t)}|^2 |\mathcal{M}_{{\rm decay}(\bar{t})}|^2. \tag{5.4}$$

The production matrix elements of $q\bar{q} \to t\bar{t}$ and $gg \to t\bar{t}$ processes are

$$\begin{aligned} |\mathcal{M}(q\bar{q} \to t\bar{t})|^2 &= \frac{4g_s^4}{9}\left(\tau_1^2 + \tau_2^2 + \frac{\rho}{2}\right) && (5.5)\\ &= \frac{2}{9} g_s^4 \left(2 - \beta^2 \sin^2\theta\right), && (5.6)\\ |\mathcal{M}(gg \to t\bar{t})|^2 &= g_s^4 \left(\frac{1}{6\tau_1\tau_2} - \frac{3}{8}\right)\left(\tau_1^2 + \tau_2^2 + \rho - \frac{\rho^2}{4\tau_1\tau_2}\right), && (5.7)\\ & && (5.8) \end{aligned}$$

where τ_1, τ_2, and ρ are

$$\tau_1 = \frac{2(p_1 \cdot p_2)}{\hat{s}},\ \tau_2 = \frac{2(p_2 \cdot p_3)}{\hat{s}},\ \rho = \frac{4M_t^2}{\hat{s}}. \tag{5.9}$$

The indices of p in Eq. (5.9) are $1 = q(g_1)$, $2 = \bar{q}(g_2)$, $3 = t(t)$ and $4 = \bar{t}(\bar{t})$ in $q\bar{q} \to t\bar{t}$ ($g_1 g_2 \to t\bar{t}$) process.

The decay matrix elements are

$$\begin{aligned} |\mathcal{M}_{{\rm decay}(t)}|^2 &= \frac{g_W^4}{4} \frac{(t \cdot \bar{f}')(b \cdot f)}{(s_{f\bar{f}'} - M_W^2)^2 + M_W^2 \Gamma_W^2}, && (5.10)\\ |\mathcal{M}_{{\rm decay}(\bar{t})}|^2 &= \frac{g_W^4}{4} \frac{(\bar{t} \cdot f)(b \cdot \bar{f}')}{(s_{f\bar{f}'} - M_W^2)^2 + M_W^2 \Gamma_W^2}, && (5.11) \end{aligned}$$

where f and $\bar{f}'$ are W daughters.

The normalized form of the propagators is used,

$$Pr(t) = \frac{1}{\pi} \frac{M_{\rm top}\Gamma_{\rm top}}{[s_t - M_{\rm top}^2]^2 + M_{\rm top}^2\Gamma_{\rm top}^2}. \tag{5.12}$$

CTEQ5L is used for parton distribution function. Other parameters are

$$\begin{aligned}
M_W &= 80.45 \text{ GeV}/c^2, && (5.13)\\
\Gamma_W &= 2.071 \text{ GeV}/c^2, && (5.14)\\
g_W^2 &= 8M_W^2 \frac{G_F}{\sqrt{2}}, && (5.15)\\
G_F &= \frac{\pi\alpha(M_W^2)}{\sqrt{2}x_W(M_W^2)M_W^2} \simeq 1.16637 \times 10^{-5}, && (5.16)\\
\alpha(M_W^2) &= \frac{1}{128}, \quad x_W(M_W^2) = 0.23, && (5.17)\\
\frac{g_s^2}{4\pi} &= \alpha_s(Q^2) = \frac{12\pi}{(33-2f)\ln(Q^2/\Lambda^2)}, \quad f = 5, \quad \Lambda = 0.192, && (5.18)\\
\Gamma_t &= G_F \frac{M_t^3}{8\pi\sqrt{2}}|V_{tb}|^2 \left(1 - \left(\frac{M_W}{M_t}\right)^2\right)^2 \left(1 + 2\left(\frac{M_W}{M_t}\right)^2\right) \text{GeV}/c^2, && (5.19)\\
|V_{tb}|^2 &= 1, && (5.20)\\
|A| &= |B| = 980 \text{ GeV}. && (5.21)
\end{aligned}$$

5.1.2 Mapping Function

Since the maximum point of the 2-dimensional likelihood, $L(M_{top}, \Delta JES)$ to determine M_{top} and ΔJES is affected by the wrong jet assignments and the background contamination, the offset from the true value needs to be corrected. To determine the offset from the true value, a large number of pseudo-experiments are done for the different top quark masses and different JES so that we make a 2-dimensional function $f(M_{top}, \Delta JES)$ called the mapping function. Figure 5.1 shows the mapping function for measured ΔJES as a function of input M_{top} and input ΔJES.

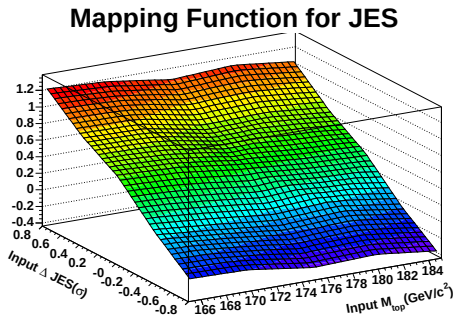

Figure 5.1: The mapping function for measured ΔJES as a function of input M_{top} and input ΔJES.

5.1.3 Result

The joint likelihood of 1.7 fb^{-1} data is fitted with a quadratic surface, shown in Fig. 5.2. The measured top mass using DLM at 1.7 fb^{-1} is

$$M_{\text{top}} = 171.6 \pm 2.0(\text{stat.}) \pm 1.3(\text{syst.})\ \text{GeV}/c^2. \tag{5.22}$$

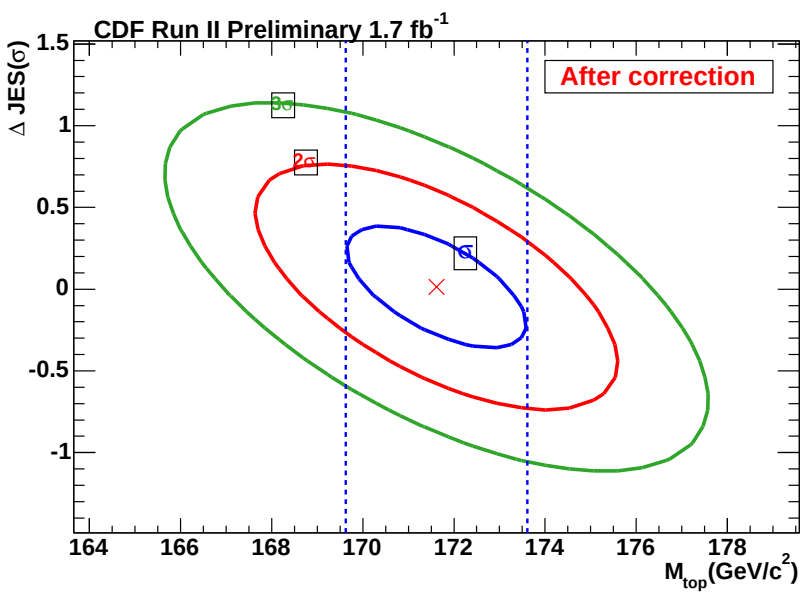

Figure 5.2: The joint likelihood as a function of M_{top} and ΔJES. The cross mark in the center of figure is the maximum point of the likelihood and the blue curve is one σ curve.

5.2 Tevatron Top Mass Combination at 1 fb^{-1}

At the CDF, the top quark mass have been measured using various techniques. Out of those technique, the use of the DLM and the similar technique using matrix element, and the in-situ jet energy scale (JES) calibration based on the invariant mass of $W \to qq'$ decays, improve the top mass measurement significantly [55]. By combining the Tevatron experiments, the top quark mass is now known with a relative precision of 1.1% limited by the systematic uncertainties, which are dominated by the jet energy scale uncertainty. This systematic uncertainty is expected to improve as larger data sets are collected since new analysis techniques contain the jet energy scale using in-situ $W \to qq'$ decays. It can be reasonably expected that with the full RunII data set the top quark mass will be known much better than 1%. Figure 5.3 shows the CDF best top quark mass measurement in the lepton+jets channel, using both matrix element and in-situ jet energy scale calibration with the integrated luminosity of 940 pb^{-1},

$$M_{\text{top}} = 170.9 \pm 2.2(\text{stat} + \text{JES}) \pm 1.4(\text{syst})\ \text{GeV}/c^2. \tag{5.23}$$

Figure 5.4 shows the summary of the top quark mass measurements and the their world average.

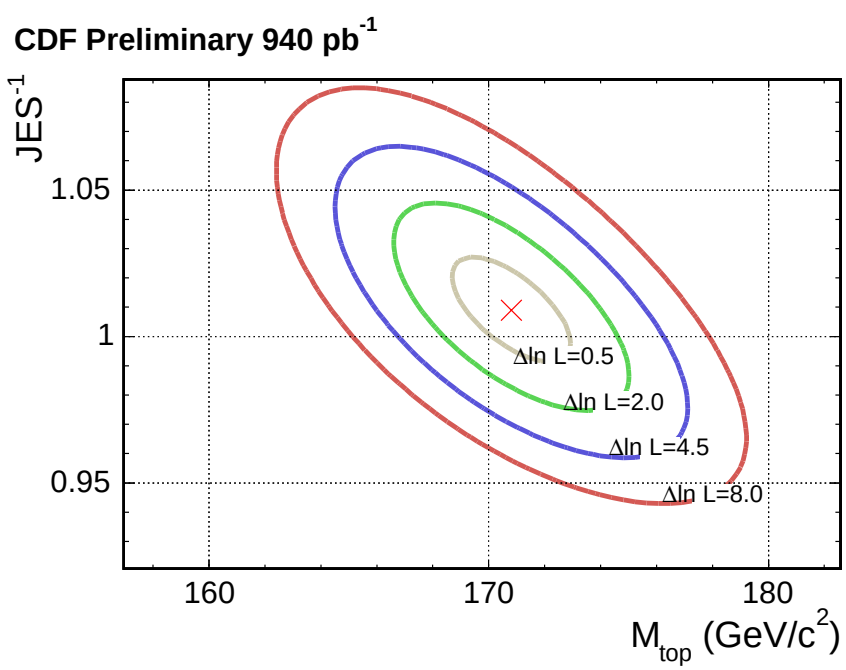

Figure 5.3: 2 dimensional fit of JES and top quark mass [55].

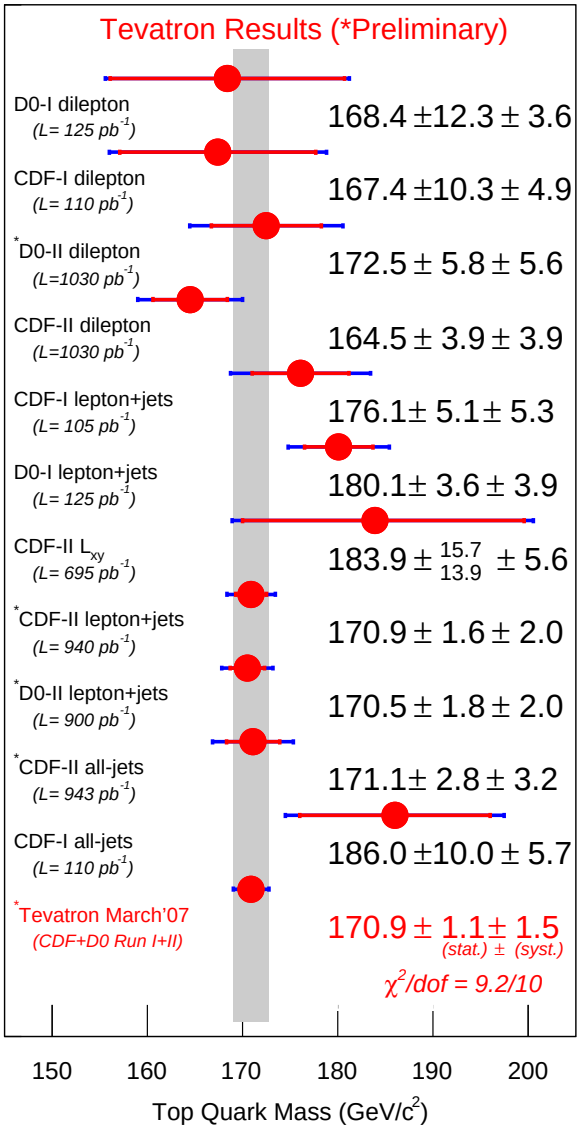

Figure 5.4: A summary of the top quark mass measurements and the world average top quark mass, using the dataset up to ~ 1 fb^{-1}

Chapter 6

Top Pair Invariant Mass Reconstruction by DLM

6.1 Dynamical Likelihood Method (DLM)

A process at the parton level is assumed to be described by

$$a/p + b/\bar{p} \to \cdots \to c_1 + \cdots + c_n (\equiv C), \tag{6.1}$$

where a and b are the initial partons in beam particles proton and anti-proton respectively, and $C(c_1, c_2, \cdots, c_n)$ are the final state partons.

$$\frac{d\sigma}{d\Phi^{(f)}} = I(a,b)|\mathcal{M}(a+b \to C; \boldsymbol{\alpha})|^2 \tag{6.2}$$

where

$$I(a,b) = \frac{(2\pi)^4}{4|\mathbf{A}||\mathbf{B}|\sqrt{(a\cdot b)^2 - m_a^2 m_b^2}} f_{a/p}(z_a, \boldsymbol{\alpha}) f_{b/\bar{p}}(z_b, \boldsymbol{\alpha}) f_T(p_T, \boldsymbol{\alpha}) \tag{6.3}$$

The symbol $\boldsymbol{\alpha}$ stands for a set of dynamical constants, e.g. masses, decay widths or coupling constants. Variables $z_a = a_z/|\mathbf{A}|$ and $z_b = b_z/|\mathbf{B}|$ are momentum fractions of a and b in proton and anti-proton, and p_T is the total momentum of initial/final system of process. $d\Phi^{(f)}$ is the phase space of the final state. $f_{a/p}(z_a)$ and $f_{b/\bar{p}}(z_b)$ are the parton distribution functions, CTEQ5L is used. $f_T(p_T)$ is the probability density function of the total-system transverse momentum. DLM is used to reconstruct the event-by-event top quark pair invariant mass in this chapter.

6.2 Transfer Function

The Transfer Function (TF) is the probability density function (p.d.f) which gives the relation between the parton state and the observed quantities. The transfer

function contains the effects of the gluon radiations in the parton evolution, the hadronizations, the detector responses and the object reconstructions. Ideally the transfer function in $t\bar{t}$ lepton+jets channel should be

$$w(\mathbf{y}|\mathbf{x}) = w\left(y(l), y(\nu), y(j_1), y(j_2), y(j_3), y(j_4)|x(l), x(\nu), x(q_1), x(q_2), x(q_3), x(q_4)\right), \quad (6.4)$$

where x/y represents the parton-level/observed quantity.

Equation (6.4) expresses the correspondence of the 18-dimension parton momentum space (3-momentum of 6 final partons) to 18-dimension observables, which requires the high statistics of Monte Carlo. The transfer function is assumed to be factorized as follows,

$$w(\mathbf{y}|\mathbf{x}) \equiv w(y(l)|x(l))w(y(\nu)|x(\nu))\prod_{i=1}^{4} w(y(j_i)|x(q_i)). \quad (6.5)$$

6.2.1 Matching between Quarks and Jets

In addition to the lepton+jets (exact 4 jets) selection, the 3 conditions of matching between the partons and the observables are required.
1) $t\bar{t}$ pair decays to lepton (electron or muon), neutrino, and 4 quarks from parton level information to remove the dilepton events passing the lepton+jets selection.
2) The events with top decay to $W + s$ or d quark are excluded. ($|V_{tb}|^2 = 1$ is assumed.)
3) One-to-one matching ($\Delta R < 0.4$) between quarks and jets is required.

6.2.2 Responses of Each Observable

If the particular observables are well measured, the transfer function for those variables is approximated by a delta-function. Figure 6.1 shows the responses of each observables from PYTHIA SM $t\bar{t}$ MC sample with $M_{\rm top} = 175$ GeV/c^2.

The observed lepton directions describe the generator level lepton directions well, because those directions are reconstructed in the good resolutions from the tracking information. The mean values of lepton energy responses, $[E(\text{obs}) - E(\text{gen})]/E(\text{gen})$, are well close to 0. The delta-functions are used in the responses of lepton momentum.

The peak positions of the missing E_T and it's ϕ response are well close to true ν, but the widths are relatively large. The response of missing E_T is not changed by the lepton detector types. The details of missing E_T and it's ϕ transfer functions are studied later.

The response of jet direction has a peak around 0, the jet direction transfer function is approximated to delta-function. The responses of jet energies are much wider compared to lepton energy and the response shapes are not Gaussian's, and these peaks are not around 0. The response of jet energy does not depend on lepton detector types. The details of jet energy response come later.

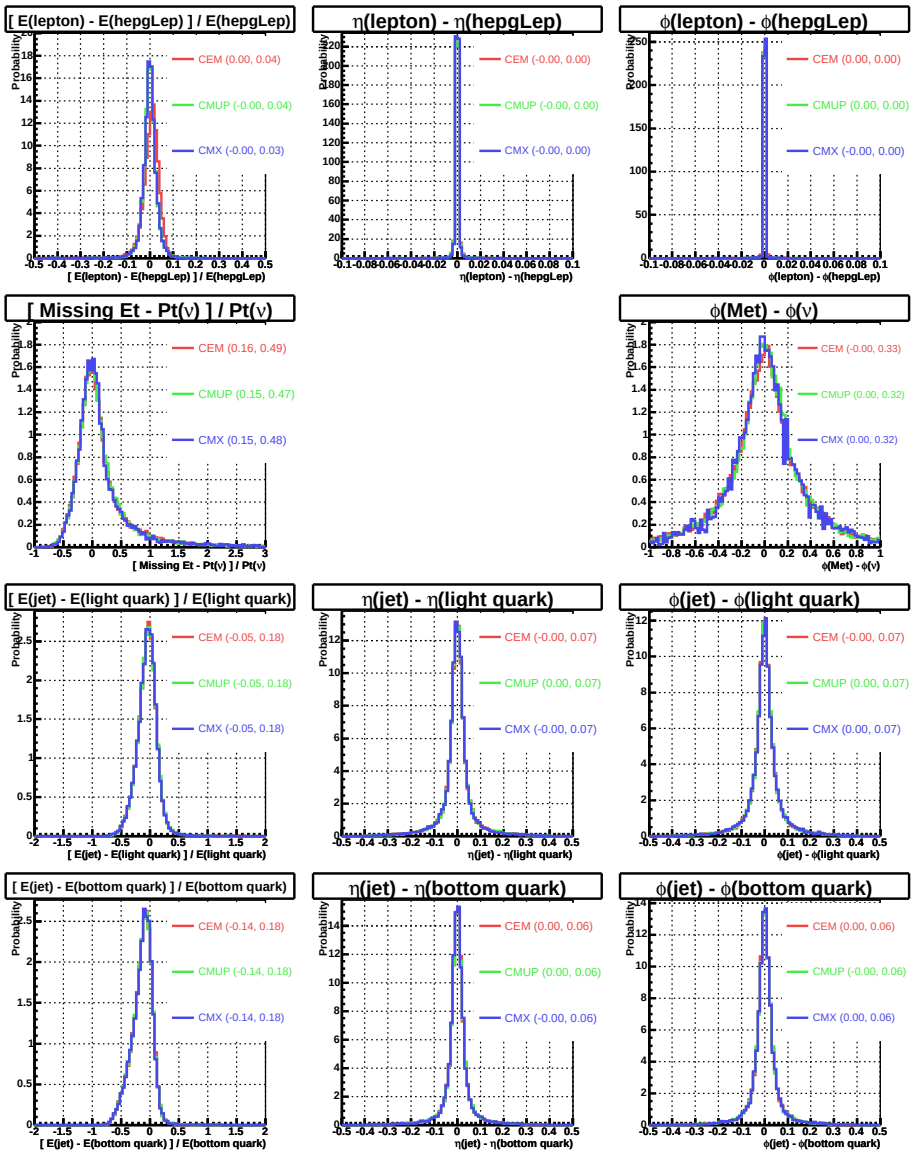

Figure 6.1: The responses of each observable. The first to fourth lines are the lepton, neutrino, light quark, and bottom quark responses, respectively. The first, second, and third columns are the energy (or $\not\!\!E_T$), η, and ϕ responses, respectively. The response variables are shown in the tops of each plot. Numbers in bracket are mean and RMS values.

6.2.3 Transfer Function of Jet Energy

The most important part of transfer function is in jet energy, because the uncertainties associated with the jet energy measurements are relatively large and there are 4 jets in the final state. The response variable, ξ, is defined as follows,

$$\xi = \frac{E(\text{parton}) - E(\text{jet})}{E(\text{jet})}. \tag{6.6}$$

The response variable, ξ, is expected to have less dependence on the jet energy than the variables like $[E(\text{parton}) - E(\text{jet})]$. The jet transfer functions of W-daughter quarks (u, d, c, s) and the bottom quarks from the top quark decay are studied separately due to the different jet evolutions.

6.2.4 η and E_T Dependences of Jet Energy TF

In the studies of jet energy transfer functions, the generic relative, multiple interaction, and absolute jet energy corrections described in Section 3.3.3 are applied. The underlying energy subtraction and the out-of-cone jet energy corrections are not applied because these depend on the physics processes. The observed jet E_T and η dependences remain in the response variable, ξ, which is particular in the $t\bar{t}$ lepton+jets channel. There is no ϕ dependence as expected. Figure 6.2 shows the η dependence of ξ. η dependences are largely reduced by the relative jet energy corrections, but there remains the η dependences. The response variable, ξ, is separated according to the red lines of Fig. 6.2. From Fig. 6.3, the dependences of physics and detector η are almost the identical, but the response at the central crack is clearer at the detector η. The transfer functions are separated by the detector η to 3 regions, $|\eta(\text{detector})| = \{(0-0.07), (0.07-1.5), (1.5-)\}$. The detector η regions from 0.07 to 1.5 are merged, because the responses in these regions are almost the same.

Figure 6.4 shows the E_T dependence of ξ. Because there are larger dependence at lower jet E_T, the response variable, ξ, should be separated finely at low jet E_T regions. The ξ is separated by the red lines of Fig. 6.4. Figure 6.5 shows the ξ distributions separated by jet E_T's, the clear E_T dependences can be seen.

Thus, the jet energy transfer functions are separated according to the detector η positions, because detector η dependence of ξ is not smooth. The jet energy transfer functions are parameterized as a function of jet E_T, because E_T dependence of ξ is smooth.

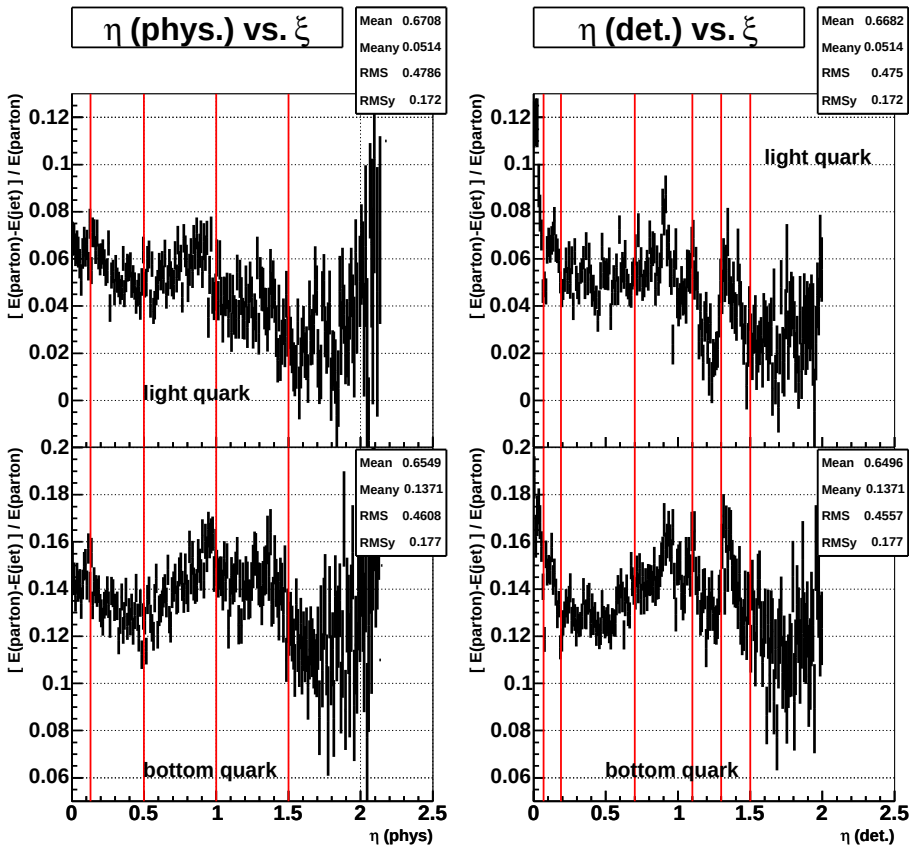

Figure 6.2: The physics η (left) and detector η (right) dependences of the jet energy transfer functions for W-daughter and bottom quarks. The vertical axes are the mean values of ξ. The lengths of bar represent the values of RMS in each bin.

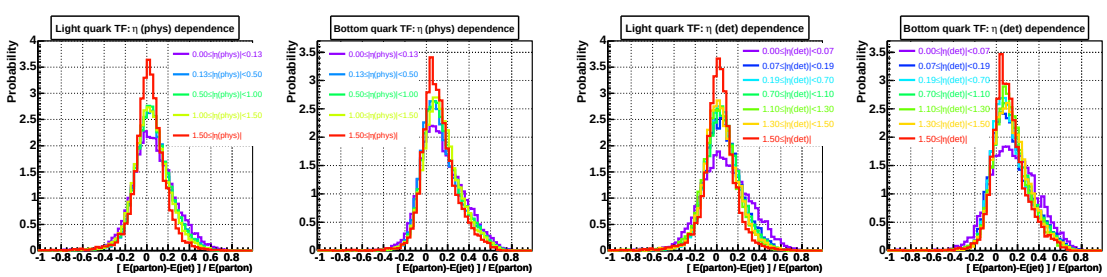

Figure 6.3: The jet energy TF's separated by physics η and detector η regions for W-daughter and bottom quarks.

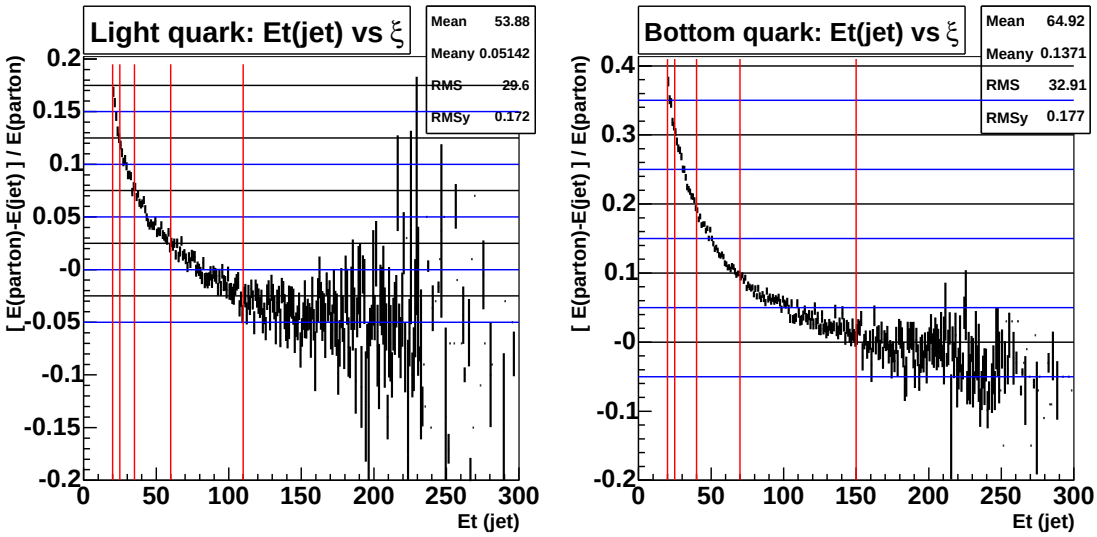

Figure 6.4: The jet E_T dependences of jet energy transfer functions for W-daughter (left) and bottom quarks (right). The vertical axes are the mean of ξ. The lengths of bar represent the values of RMS in each bin.

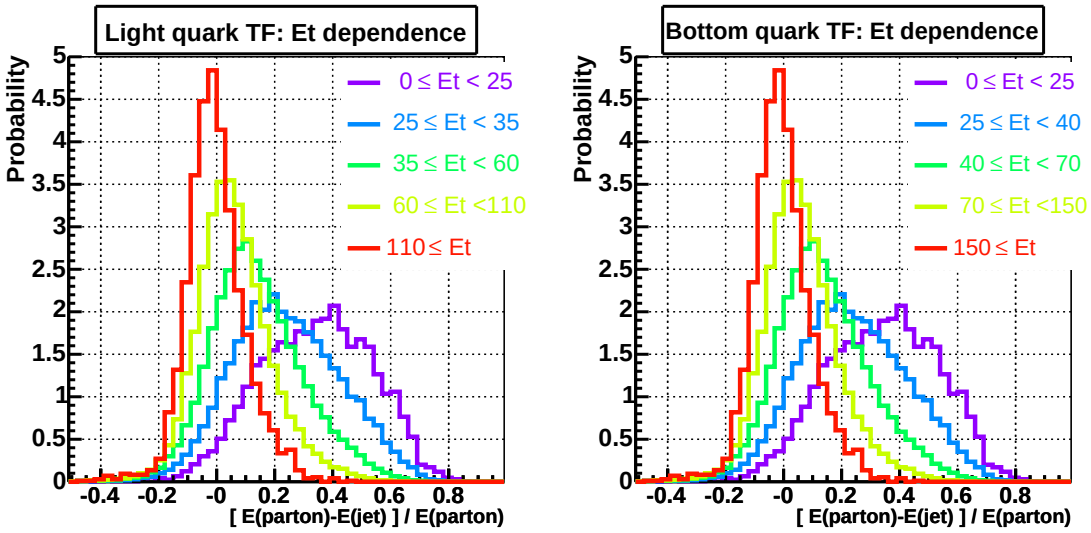

Figure 6.5: ξ distributions separated by the jet E_T ranges for W-daughter (left) and bottom quarks (right).

6.2.5 Parameterization of Light Quark Energy TF

The first step is to fit the transfer functions divided into 3 detector η positions, 5 jet E_T ranges and the additional 3 jet E_T ranges to increase the fitting points of jet E_T, as shown in Table 6.1.

detector $\|\eta\|$	0-0.07	0.07-1.5	1.5-		
	$\times$				
jet E_T (GeV) range	0-25	25-35	35-60	60-110	110-
additional jet E_T (GeV) range	22-29	29-45	45-81		

Table 6.1: The regions to fit transfer functions at $3\eta \times (5+3)E_T$ ranges.

The light quark ξ distributions are fitted by the several probability density functions (p.d.f's). Among these p.d.f's, T-distribution fits the ξ distribution well in the whole E_T range. Figure 6.6 shows the fitting results of the light quark ξ distributions by T-distribution,

$$p(\xi)d\xi = p_0 \frac{\Gamma(\frac{p_2+1}{2})}{\sqrt{\pi p_2}\Gamma(\frac{p_2}{2})}[1 + \frac{[p_0(\xi - p_1)]^2}{p_2}]^{-\frac{p_2+1}{2}} d\xi, \tag{6.7}$$

where p_0, p_1, and p_2 are the fitting parameters.

The next step is to fit the parameters, $p_i (i = 0, 1, 2)$, in Eq. (6.7). These parameters are fitted as a function of jet E_T, as shown in the bottom right 9-plot of Fig. 6.6. To perform the fitting of p_i, first p_1 related to the peak values is fitted and then all the ξ distributions are fitted keeping this $p_1(E_T)$. The same procedures for p_0 and p_2 are repeated. The bottom right 9-plot of Fig. 6.6 shows the final loop of p_i fittings. Thus the parameters of Eq. (6.7) are the functions of jet E_T, and T-distribution is written as,

$$p(\xi; E_T)d\xi = p_0(E_T) \frac{\Gamma(\frac{p_2(E_T)+1}{2})}{\sqrt{\pi p_2(E_T)}\Gamma(\frac{p_2(E_T)}{2})}[1 + \frac{[p_0(E_T)\{\xi - p_1(E_T)\}]^2}{p_2(E_T)}]^{-\frac{p_2(E_T)+1}{2}} d\xi. \tag{6.8}$$

The left 3 plots of Fig. 6.7 show the parameterized transfer functions, and right 3 9-plot's show the checks of the parameterized transfer functions with the different jet E_T ranges (10GeV interval) from Table 6.1.

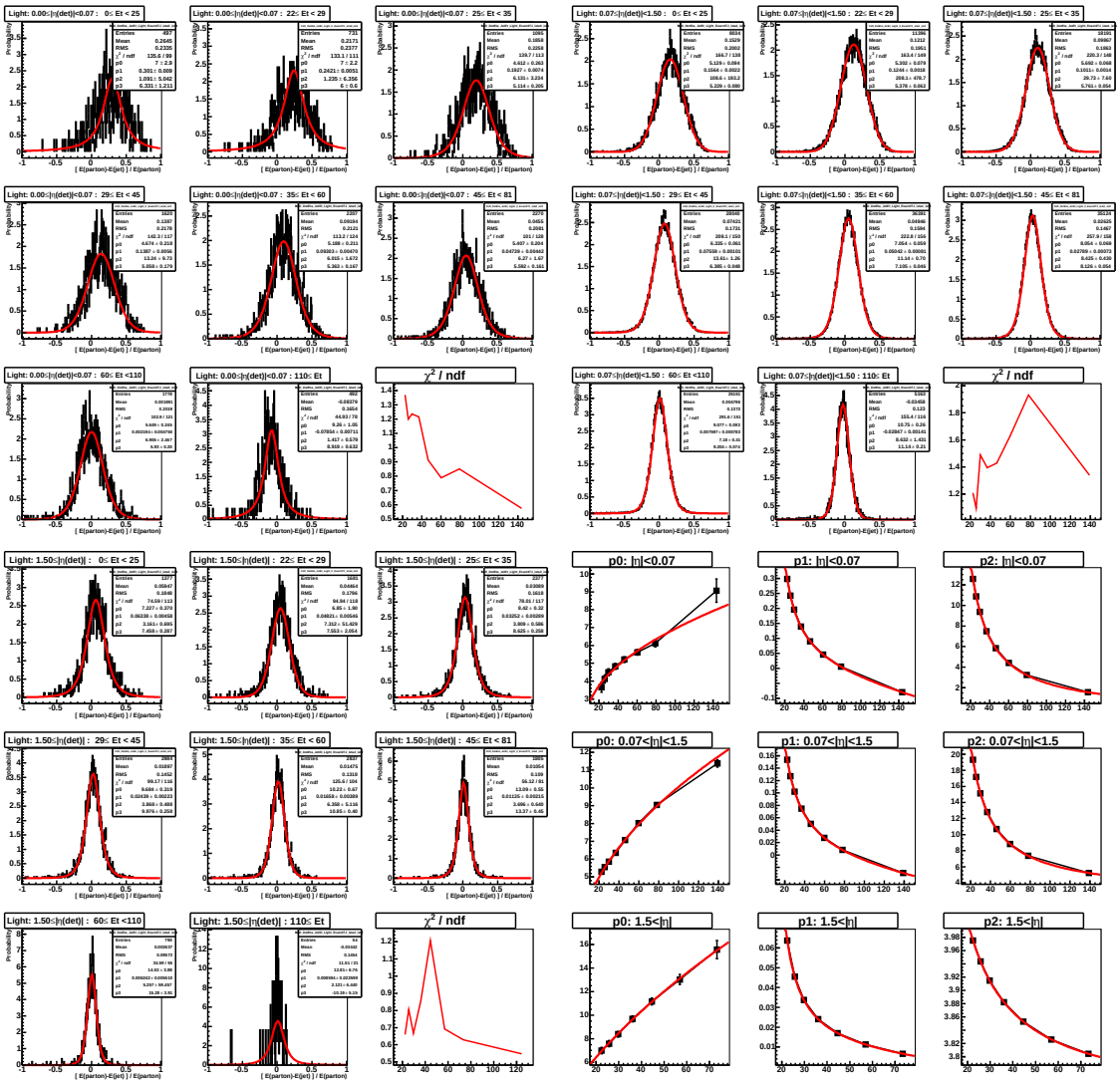

Figure 6.6: The light quark energy TF's for the different jet E_T ranges fitted by T-distributions: The top left 9 plots are ξ distributions in $|\eta(\text{det.})| < 0.07$, the top right 9 plots are those in $0.07 \leq |\eta(\text{det.})| < 1.5$, and the bottom left 9 plots are those in $1.5 \leq |\eta(\text{det.})|$. The bottom right plots in each 9-plot show the χ^2/ndf as a function of jet E_T. The bottom right 9 plots show the fitting results of p_0, p_1, and p_2 (The horizontal axes are the jet E_T).

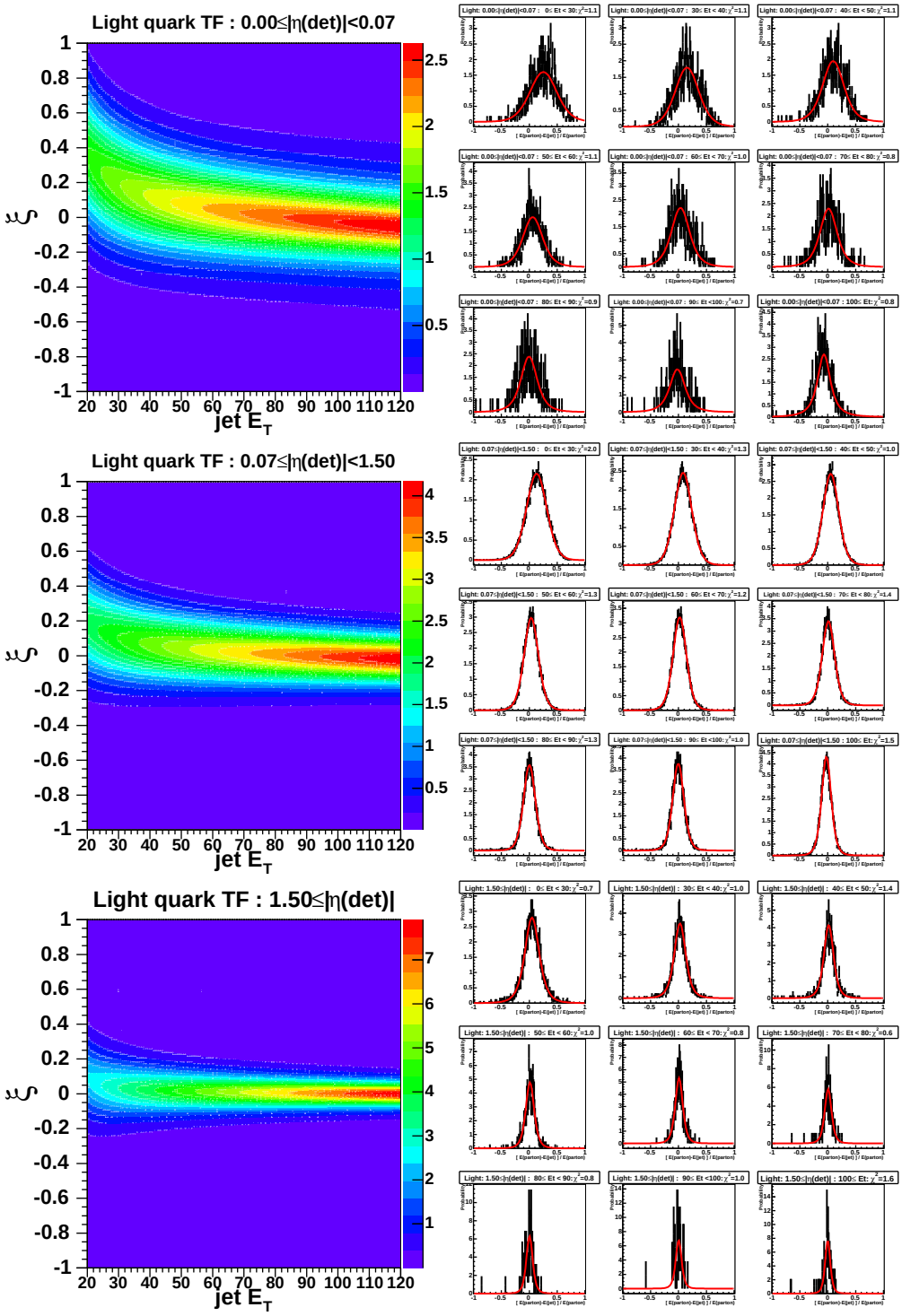

Figure 6.7: The jet energy TF's of light quark: The left 3 plots show the parameterized TF's normalized at a given jet E_T. The right 3 9-plot's show the checks of parameterized TF's with the different jet E_T ranges from the ranges to make the parameterized TF's.

6.2.6 Parameterization of Bottom Quark Energy TF

The bottom quark energy transfer functions are made by the same procedure as light quark. The modified form of Gaussian (Eq. 6.9) with the replacement of σ by the linear function of ξ is used to fit the bottom quark ξ distributions. The separated ranges to fit the ξ distributions are shown in Table 6.2. The η ranges are the same as light quark TF.

$$p(\xi; E_T)d\xi = p_0(E_T) \exp\left[-\frac{\{\xi - p_1(E_T)\}^2}{2\{p_2(E_T) + p_3(E_T)\xi\}^2}\right] d\xi \tag{6.9}$$

detector $\lvert\eta\rvert$	0-0.07	0.07-1.5	1.5-

$\times$

jet E_T (GeV) range	0-25	25-40	40-70	70-150	150-
additional jet E_T (GeV) range	22-32	32-50	50-100		

Table 6.2: The $3\eta \times (5+3)E_T$ regions to fit the bottom quark transfer function.

Because the integration of Eq. (6.9) becomes infinity, this function is not p.d.f. Thus the bottom quark TF's with $-1 < \xi < 1$ range are used, which covers most of possible ξ values from Monte Carlo simulations. Figure 6.8 shows the fitting results of the bottom quark ξ distributions. The bottom right 12-plot of Fig. 6.8 shows the final iteration of the p_i fittings.

The left 3 plots of Fig. 6.9 show the parameterized transfer functions, and the right 3 9-plot's show the checks of the parameterized transfer functions with the different jet E_T range (10GeV interval) from Table 6.2.

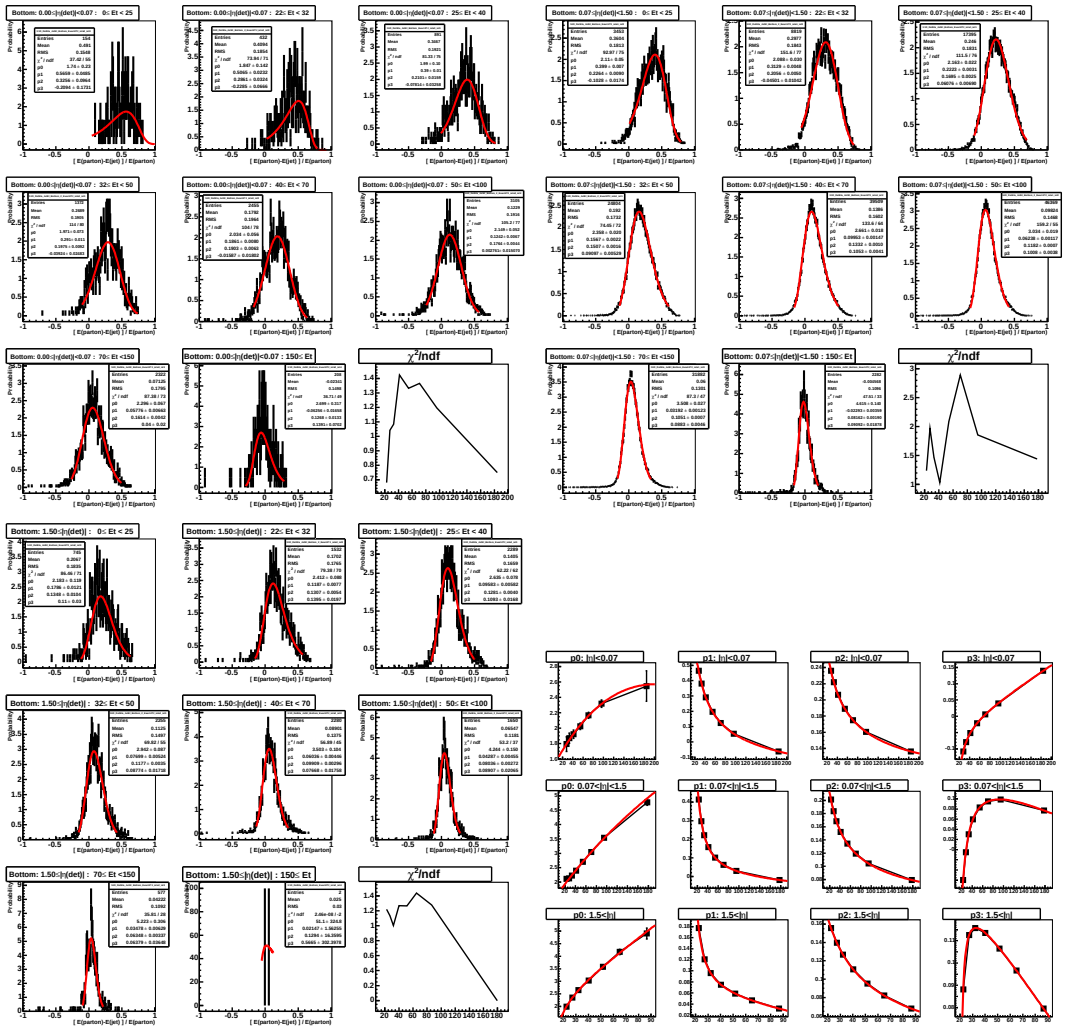

Figure 6.8: The bottom quark energy TF's for the different jet E_T ranges fitted by the modified form of Gaussian: The top left 9 plots are ξ distributions in $|\eta(\text{det.})| < 0.07$, the top right 9 plots are those in $0.07 \leq |\eta(\text{det.})| < 1.5$, and the bottom left 9 plots are those in $1.5 \leq |\eta(\text{det.})|$. The bottom right plots in each 9-plot show the χ^2/ndf as a function of jet E_T. The bottom right 9 plots show the fitting results of p_0, p_1, p_2, and p_3 (The horizontal axes are jet E_T).

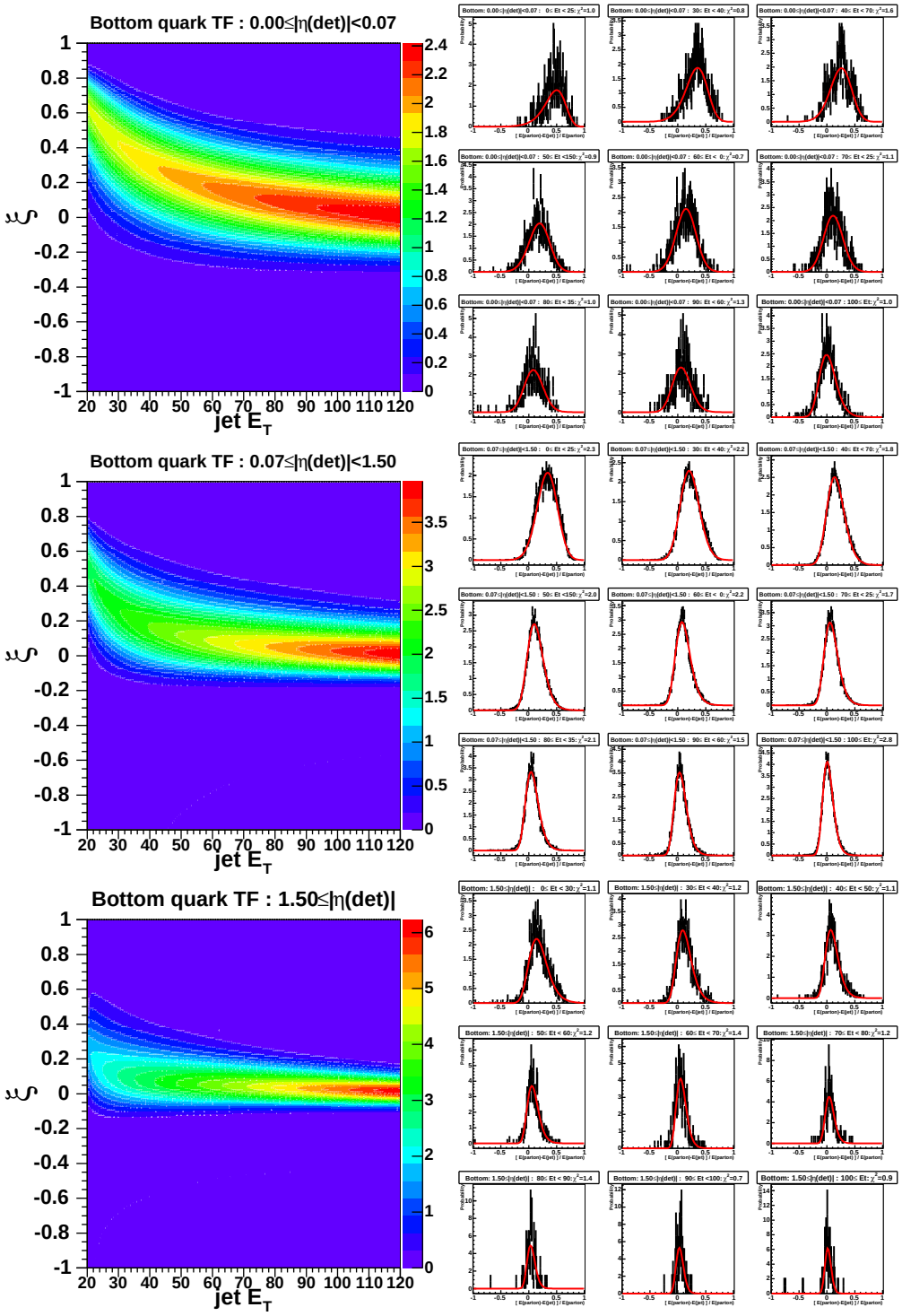

Figure 6.9: The jet energy TF's of bottom quark: The left 3 plots show the parameterized TF's, normalized at given jet E_T. The right 3 9-plot's show the checks of parameterized TF with the different jet E_T ranges from ranges to make the parameterized TF's.

6.2.7 Transfer Function of Missing E_T and Its ϕ

The transfer functions of missing E_T and its ϕ depend on all the object reconstructions. The observed missing E_T dependence is simply used. The missing E_T ($\not\!\!E_T$) and ϕ of missing E_T ($\phi(\not\!\!E_T)$) response variables are defined as $\xi_{\not\!\!E_T} \equiv (\not\!\!E_T - \nu_T)/\nu_T$ and $\xi_{\phi(\not\!\!E_T)} \equiv \phi(\not\!\!E_T) - \phi(\nu)$, where ν_T is p_T of neutrino.

The missing E_T response, $\xi_{\not\!\!E_T}$, distributions are fitted by the modified form of Gaussian (Eq. 6.10) with the replacement of σ by the cubic function of $\xi_{\not\!\!E_T}$. The ϕ of missing E_T response, $\xi_{\phi(\not\!\!E_T)}$, distributions are fitted by T-distribution (Eq. 6.11).

$$p(\xi_{\not\!\!E_T}; \not\!\!E_T) d\xi_{\not\!\!E_T} = p_0(\not\!\!E_T) \exp\left[-\frac{\{\xi_{\not\!\!E_T} - p_1(\not\!\!E_T)\}^2}{2\{p_2(\not\!\!E_T) + p_3(\not\!\!E_T)\xi_{\not\!\!E_T} + p_4(\not\!\!E_T)\xi^2_{\not\!\!E_T} + p_5(\not\!\!E_T)\xi^3_{\not\!\!E_T}\}^2} \right] d\xi_{\not\!\!E_T} \tag{6.10}$$

$$p(\xi_{\phi(\not\!\!E_T)}; \not\!\!E_T) d\xi_{\phi(\not\!\!E_T)} = p_0(\not\!\!E_T) \frac{\Gamma(\frac{p_1(\not\!\!E_T)+1}{2})}{\sqrt{\pi p_1(\not\!\!E_T)}\Gamma(\frac{p_1(\not\!\!E_T)}{2})} [1 + \frac{[p_2(\not\!\!E_T)\xi_{\phi(\not\!\!E_T)}]^2}{p_1(\not\!\!E_T)}]^{-\frac{p_1(\not\!\!E_T)+1}{2}} d\xi_{\phi(\not\!\!E_T)} \tag{6.11}$$

The parameterization procedures are the same as the jet energy transfer functions. Figure 6.10 shows the fittings of missing E_T response, $\xi_{\not\!\!E_T}$, distributions. The left plot of Fig. 6.12 shows the parameterized missing E_T transfer function. Figure 6.11 shows the fittings of ϕ of missing E_T response, $\xi_{\phi(\not\!\!E_T)}$, distributions. The right plot of Fig. 6.12 shows the parameterized ϕ of missing E_T transfer function.

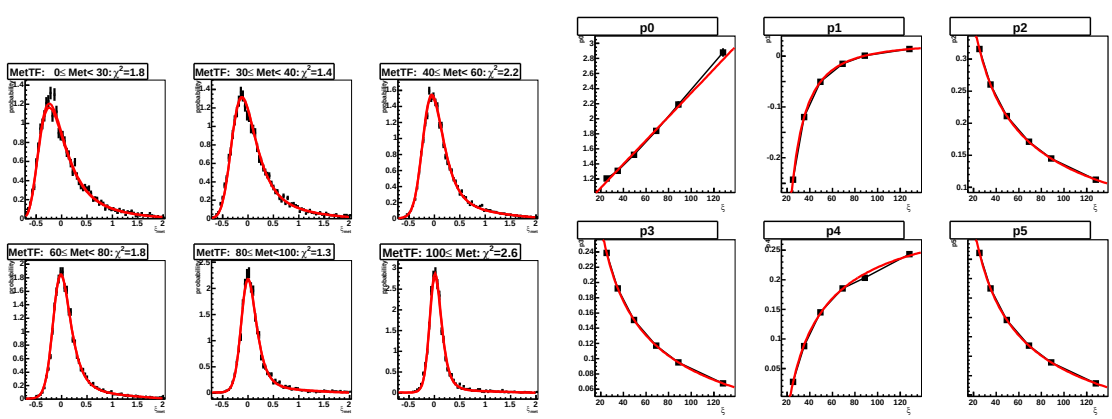

Figure 6.10: The missing E_T TF: The left 6 plots show the $\xi_{\not\!\!E_T}$ distributions with the different $\not\!\!E_T$ ranges. The right 6 plots show the $\not\!\!E_T$ dependences of fitting parameters.

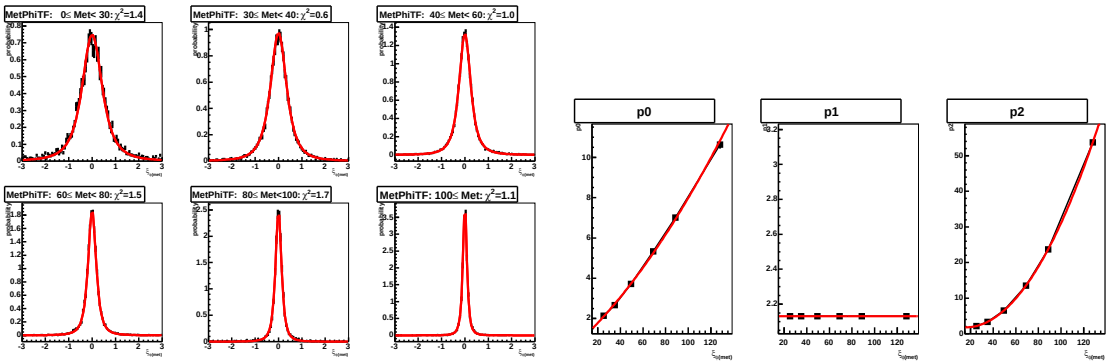

Figure 6.11: The ϕ of missing E_T TF: The left 6 plots show the $\xi_{\phi(\not{E}_T)}$ distributions with the different $\not{E}_T$ ranges. The right 3 plots show the $\not{E}_T$ dependences of fitting parameters.

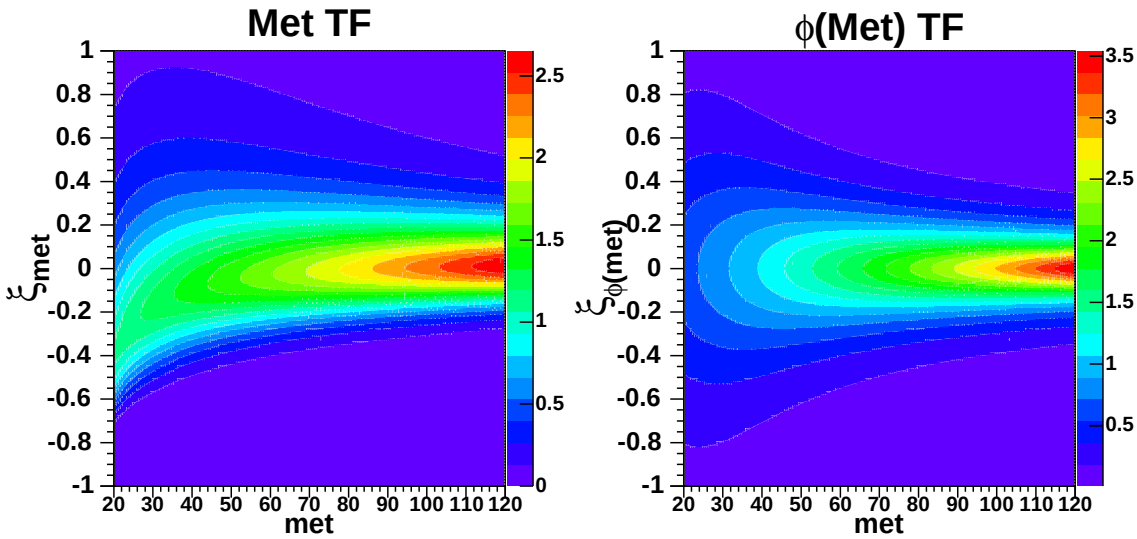

Figure 6.12: The parameterized $\not{E}_T$ and $\phi(\not{E}_T)$ TF's: The left plot shows the parameterized $\not{E}_T$ TF, and the right plot shows the parameterized $\phi(\not{E}_T)$. These are normalized at a given $\not{E}_T$.

6.3 Top Pair Invariant Mass Reconstruction

The DLM is used to reconstruct the $t\bar{t}$ invariant mass, $\sqrt{s_{t\bar{t}}}$, event by event. The algorithm is slightly different from that in top mass reconstruction, because the top mass is a dynamical parameter while $\sqrt{s_{t\bar{t}}}$ is not. The $t\bar{t}$ production matrix element is not used to reconstruct $\sqrt{s_{t\bar{t}}}$ since the production property of $q\bar{q} \to t\bar{t}$ is of the current interest and it is necessary to avoid the bias by assuming the standard model or the massive gluon production matrix element. Thus $[d\sigma/d\Phi(q\bar{q} \to t\bar{t})]'$ is defined where the production matrix is assumed to be a constant. Per path likelihood and per event likelihood are defined as Eqs.(6.12) and (6.13),

$$L_{\text{path}}(\mathbf{y}_j|\mathbf{x}_i) \equiv N \left[\frac{d\sigma}{d\Phi}(q\bar{q} \to t\bar{t})\right]' w(\mathbf{y}_j|\mathbf{x}_i), \tag{6.12}$$

$$L_{\text{ev}}(\sqrt{s_{t\bar{t}}}_j|\mathbf{y}_j) \equiv \frac{1}{N_{\text{path}}} \sum_i L_{\text{path}}(\mathbf{y}_j|\mathbf{x}_i)\delta[\sqrt{s_{t\bar{t}}}_j - (\sum x_i)^2]. \tag{6.13}$$

A mean value of $\sqrt{s_{t\bar{t}}}$ in per event likelihood is used as a reconstructed $\sqrt{s_{t\bar{t}}}$ in the event,

$$< \sqrt{s_{t\bar{t}}} >_{\text{ev}} = \int \sqrt{s_{t\bar{t}}} L_{\text{ev}}(\sqrt{s_{t\bar{t}}}_j|\mathbf{y}_j) d\sqrt{s_{t\bar{t}}}. \tag{6.14}$$

There are 3 differences in the likelihood formulation from the likelihood used in the top quark mass reconstruction. First, neither the $q\bar{q} \to t\bar{t}$ nor the $gg \to t\bar{t}$ production matrix element is used. Second, the delta function is inserted in per event likelihood to get event-by-event $\sqrt{s_{t\bar{t}}}$. Third, we assume M_{top} is 175 GeV/c^2 and that the SM is valid for the decay matrix elements of t and $\bar{t}$. In the following sections $\sqrt{s_{t\bar{t}}}$ reconstruction are tested using mostly SM $t\bar{t}$ samples.

6.3.1 Path Calculations

DLM requires significant CPU time because $d\sigma/d\Phi w(\mathbf{y}|\mathbf{x})$ are calculated many times (one million paths per event in this analysis). CPU time can be saved significantly by using importance sampling [56], instead of scanning the final parton momenta with the flat way. The images of calculation of the top quark propagator, the decay matrix element, and the transfer function weights are shown in Fig. 6.13, with $M_{\text{top}} = 175$ GeV/c^2 constraint. The Lorentzian (Breit-Wigner) weights of top quark and W boson give the large effects. Thus the importance samplings are used basically for these Lorentzians.

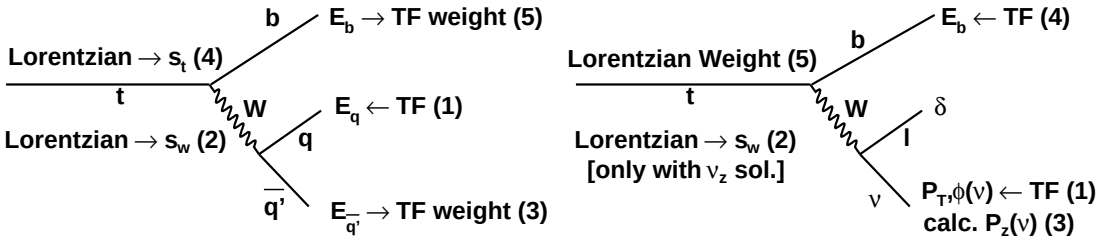

Figure 6.13: The images of the reconstruction procedures in W boson hadronic decay (left) and W boson leptonic decay (right). Numbers in the bracket are the orders of reconstruction.

The top propagator, the decay matrix element, and the transfer function weights are inferred by the following ways to calculate the weights of top hadronic decay side.

1. A W-daughter momentum and s_W are inferred from TF and the Lorentzian.
2. Another W-daughter momentum and TF weight are calculated.
3. s_t is inferred from the Lorentzian.
4. b-quark momentum is determined with $M_b \equiv 0$ assumption. Then, TF weight is calculated.

To calculate the weight of top leptonic decay side,

1. p_T and ϕ of neutrino are inferred from TF (Lepton momentum is assumed to be perfectly measured).
2. s_W with $p_z(\nu)$ solution is inferred from Lorentzian: s_W range with $p_z(\nu)$ solution is calculated from $p_x(l), p_y(l), p_x(\nu)$ and $p_y(\nu)$, as in Eq. (6.15).
3. 2 $p_z(\nu)$s are calculated. The fractional area of Lorentzian with $p_z(\nu)$ solution is calculated as the weight.
4. b-quark momentum is inferred from TF.
5. Top propagator weights are calculated for 2 $p_z(\nu)$s.

s_W range with p_z solutions is given by

$$s_W \geq 2p_T(l)p_T(\nu)\left[1 - \cos\Delta\phi(l,\nu)\right] \geq 0, \tag{6.15}$$

$$s_W \leq - 2p_T(l)p_T(\nu)\left[1 + \cos\Delta\phi(l,\nu)\right] \leq 0. \tag{6.16}$$

Because the physics s_W has the positive value, only the higher s_W range should be considered. Sometimes this range is at the high side tail of the Lorentzian. The Lorentzian random number generator is prepared with $p_z(\nu)$ solutions to avoid generating the s_W without $p_z(\nu)$ solution. The example is shown in Fig. 6.14. The initial state weight (Eq. 6.3) is calculated from the energy-momentum conservation.

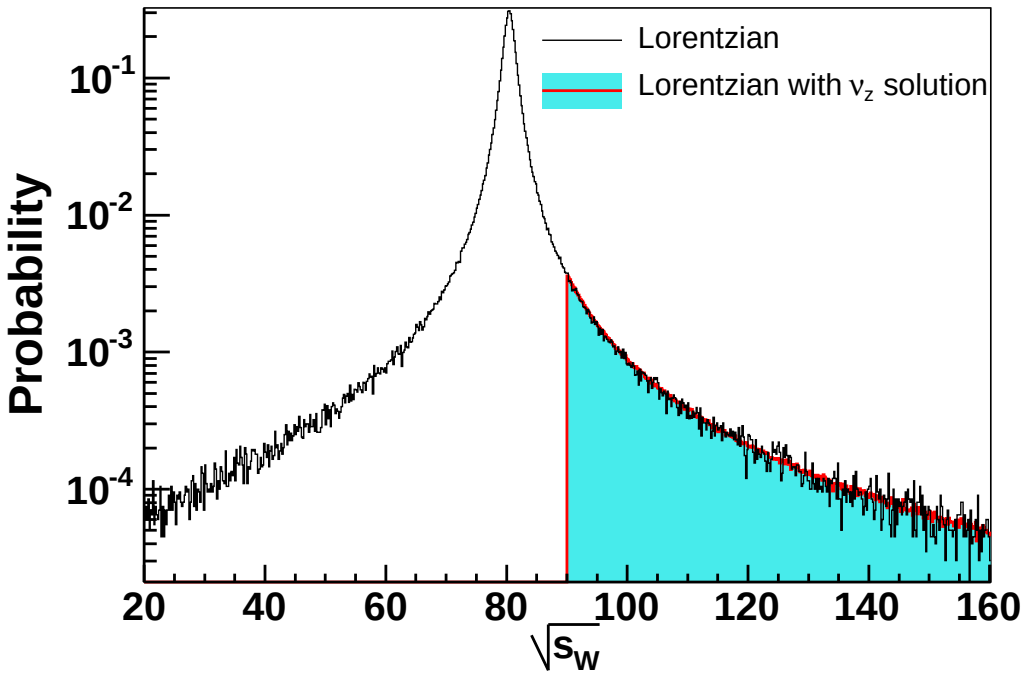

Figure 6.14: The example with $2p_T(l)p_T(\nu)\,[1-\cos\Delta\phi(l,\nu)] = 90^2$ GeV$^2/c^2$ case. Only ~3% of Lorentzian have the $p_z(\nu)$ solution in this case.

6.3.2 $\sqrt{s_{t\bar{t}}}$ Reconstruction with SM $t\bar{t}$ Correct Combination

Figure 6.15 shows the examples of the event likelihood distributions using the SM $t\bar{t}$ MC ($M_{\rm top} = 175$ GeV$/c^2$) with the correct combination. The most probable values (MPVs) of the likelihood distributions look close to generator level $\sqrt{s_{t\bar{t}}}$ from these plots. The resolutions between MPV's and mean values are compared. By taking the mean values of the event likelihood distributions, the resolution is better than MPVs because there are double-peak events by 2 $p_z(\nu)$ solutions as seen in Fig. 6.15 and taking of a wrong peak gives worse effects. Thus the event $\sqrt{s_{t\bar{t}}}$ is reconstructed from Eq. (6.14).

Figure 6.16 shows the reconstructed $\sqrt{s_{t\bar{t}}}$ and the event by event difference (reconstruction - generator $\sqrt{s_{t\bar{t}}}$) distributions. The reconstructed $\sqrt{s_{t\bar{t}}}$ agrees fairly well with generator level $\sqrt{s_{t\bar{t}}}$, but slightly biased ~ 1.3 GeV$/c^2$.

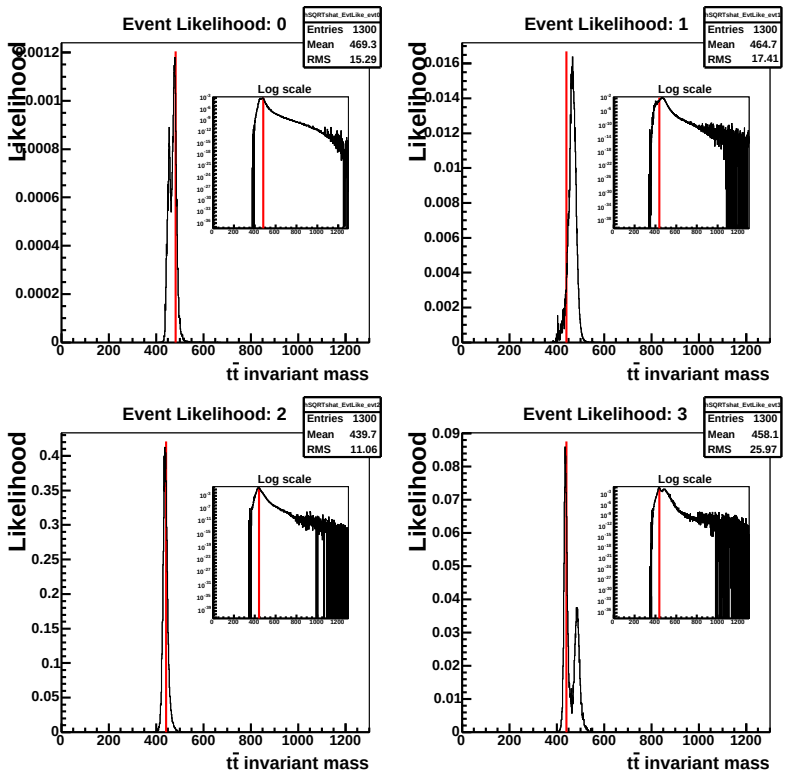

Figure 6.15: The examples of event likelihood using the SM $t\bar{t}$ MC with the correct combination. The red lines are the true values from generator information.

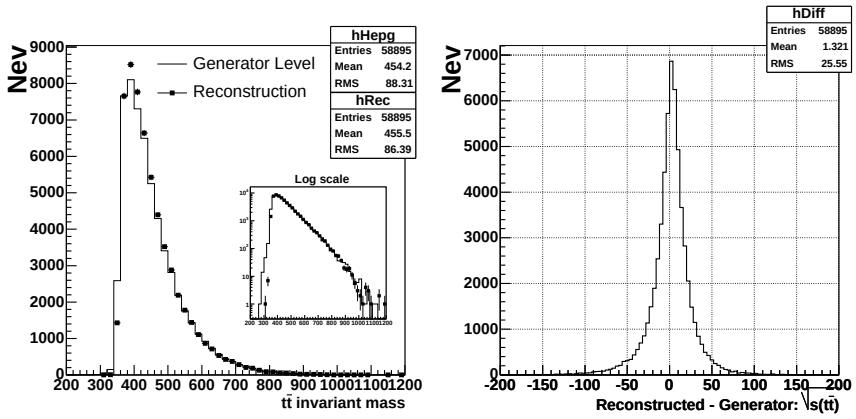

Figure 6.16: The left plot shows the $t\bar{t}$ invariant mass distributions of the generator level (histogram) and the reconstruction (dots). The right plot shows the difference between the true values and the reconstructed values of the $t\bar{t}$ invariant mass.

6.3.3 Combination Selection

In this section, the relation between the combination (parton to jet assignment) and the $\sqrt{s_{t\bar{t}}}$ resolution, and the combination selection are discussed. There are 12 combinations with 1 b-tagging and 3 b-taggings, 4 combinations with 2 b-taggings, and 24 combinations with 4 b-taggings. The 4 b-taggings case is neglected because its fraction is very small (There is no event with 4 b-taggings in the real data). The combination selection efficiencies using SM $t\bar{t}$ MC are tested with the parton-jet-matched events. Figure 6.17 shows the logarithmic ratio of the correct combination likelihood to the others, $\log(L_{\text{comb.}}/L_{\text{correct}})$, and the largest event likelihood combination. From these plots, the correct combination and the combination with exchanging of W daughter quarks tend to have the large likelihood, and the other combination effects are relatively small. Table 6.3 shows the combination selection efficiencies by selecting the largest event likelihood combination.

	Correct combination	Exchange of W quarks	Sum of left 2 columns
1 or 3 b-tags	37.4%	30.3%	67.7%
2 b-tags	50.5%	39.1%	89.6%

Table 6.3: The combination selection efficiencies by selecting largest likelihood combination.

Next, the $\sqrt{s_{t\bar{t}}}$ resolutions by the 3 reconstruction ways are compared.

1. All the combination likelihoods are added.
2. Only the best likelihood combination is used.
3. The best and the second best likelihood combinations are added.

Figure 6.18 shows the resolution comparison from the 3 ways. The first option gives the best resolution because it always contains the correct combination effect. However, these 3 options give almost the same resolutions. The only best combination is used because of the CPU time. The combination selection efficiency is stable from 0.1 to 1 million path calculations. The 1 million path calculations for each combination are performed to reconstruct $\sqrt{s_{t\bar{t}}}$. By selecting the best combination with 0.1 million path calculations, and then calculating 1 million paths, the results can be obtained by roughly 6 times faster than adding all combinations in 1 b-tagging case.

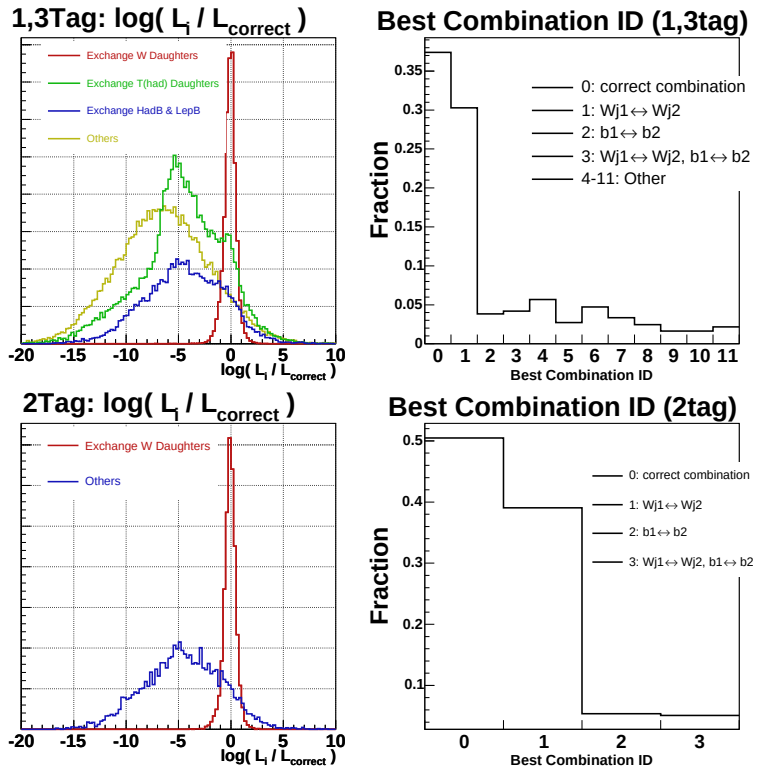

Figure 6.17: The logarithmic ratios of the correct combination likelihood to the others, $\log(L_{\text{comb.}}/L_{\text{correct}})$, (left: arbitrary scale), and the largest likelihood combination (right) for 1, 3 b-tagging and 2 b-tagging events.

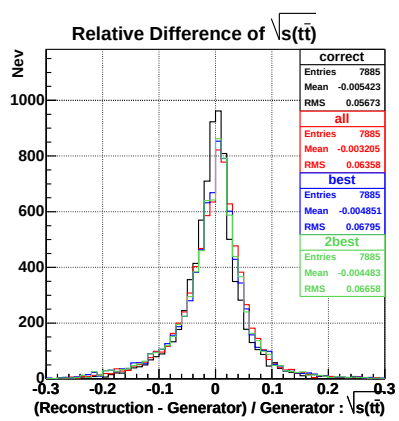

Figure 6.18: The comparison of the reconstructed $\sqrt{s_{t\bar{t}}}$ resolutions, using the all (red), the best (blue), and the best and second (green) combinations.

Chapter 7

Extraction of Coupling Strength

In this chapter, the likelihood fitting of the couping strength, λ, is discussed. To fit λ the reconstructed signal $\sqrt{s_{t\bar{t}}}$ p.d.f of $q\bar{q} \to t\bar{t}$ process is defined first, which has 3 massive gluon parameters. Then the reconstructed $\sqrt{s_{t\bar{t}}}$ p.d.f of the background process is defined. The $q\bar{q} \to t\bar{t}$ process is called signal even if $\lambda = 0$, because the massive gluon and the standard model $q\bar{q} \to t\bar{t}$ processes can not be treated separately. The other processes are defined as background.

7.1 Signal Reconstructed $\sqrt{s_{t\bar{t}}}$ P.D.F

The decay of top (anti-top) quarks from the massive gluon including interference with the SM process is the same as the standard model top quark decay and the difference is only in the production matrix element as mentioned before. If the resolution of reconstructed $\sqrt{s_{t\bar{t}}}$ depend mainly on parton level $\sqrt{s_{t\bar{t}}}$ and not much depend on the production property of $q\bar{q} \to t\bar{t}$ (which is validated later using Z' sample), the reconstructed signal $\sqrt{s_{t\bar{t}}}$ p.d.f is described by the convolution of parton level $\sqrt{s_{t\bar{t}}}$ p.d.f and the resolution function which depend on the parton level $\sqrt{s_{t\bar{t}}}$. The signal reconstructed $\sqrt{s_{t\bar{t}}}$ p.d.f is defined by

$$p_s[\sqrt{s_{t\bar{t}}}_r; \boldsymbol{\alpha}]d\sqrt{s_{t\bar{t}}}_p \equiv N(\boldsymbol{\alpha}) \int \left[\frac{d\sigma}{d\sqrt{s_{t\bar{t}}}_p}\right]_{\mathrm{SM}:q\bar{q}\to t\bar{t}} \epsilon(\sqrt{s_{t\bar{t}}}_p) R(\sqrt{s_{t\bar{t}}}_p; \boldsymbol{\alpha}) f(\sqrt{s_{t\bar{t}}}_r - \sqrt{s_{t\bar{t}}}_p; \sqrt{s_{t\bar{t}}}_p) d\sqrt{s_{t\bar{t}}}_p, \quad (7.1)$$

where $\sqrt{s_{t\bar{t}}}_r$ is the reconstructed $\sqrt{s_{t\bar{t}}}$, $\sqrt{s_{t\bar{t}}}_p$ is the parton level $\sqrt{s_{t\bar{t}}}$, $\boldsymbol{\alpha}$ is the massive gluon parameters (Γ, M, λ), N is the normalization factor, ϵ is the acceptance, R is the (Massive Gluon)/(SM) differential cross section ratio and f is the resolution function.

$$N(\boldsymbol{\alpha})^{-1} = \int \left[\frac{d\sigma}{d\sqrt{s_{t\bar{t}_p}}}\right]_{\mathrm{SM}:q\bar{q}\to t\bar{t}} R(\sqrt{s_{t\bar{t}_p}};\boldsymbol{\alpha})\epsilon(\sqrt{s_{t\bar{t}_p}})d\sqrt{s_{t\bar{t}_p}} \tag{7.2}$$

$$\begin{aligned} R(\sqrt{s_{t\bar{t}_p}};\boldsymbol{\alpha}) &\equiv \frac{[d\sigma/d\sqrt{s_{t\bar{t}_p}}]_{\mathrm{MG}}}{[d\sigma/d\sqrt{s_{t\bar{t}_p}}]_{\mathrm{SM}}} = \frac{|\mathcal{M}_{\mathrm{prod}}(s_{t\bar{t}_p};\boldsymbol{\alpha})|^2_{\mathrm{MG}}}{|\mathcal{M}_{\mathrm{prod}}(s_{t\bar{t}_p})|^2_{\mathrm{SM}}} \\ &= 1 + 2\lambda\frac{s_{t\bar{t}_p}(s_{t\bar{t}_p}-M^2)}{(s_{t\bar{t}_p}-M^2)^2+M^2\Gamma^2} + \lambda^2\frac{s_{t\bar{t}_p}^2}{(s_{t\bar{t}_p}-M^2)^2+M^2\Gamma^2} \end{aligned} \tag{7.3}$$

In Eq.(7.1) the differential cross section ratio is used to describe the massive gluon parton level $\sqrt{s_{t\bar{t}}}$ because by taking the ratio many factors are canceled, like PDFs, the top propagators, the decay matrix elements, and the Jacobian's. Thus the differential cross section ratio is written by the simple formula (Eq. 7.3). Each factor in Eq.(7.1) is explained hereafter.

To describe $\left[\frac{d\sigma}{d\sqrt{s_{t\bar{t}_p}}}\right]_{\mathrm{SM}:q\bar{q}\to t\bar{t}}\epsilon(\sqrt{s_{t\bar{t}_p}})$, the histogram of SM $q\bar{q} \to t\bar{t}$ process from the PYTHIA MC sample ($M_{\mathrm{top}} = 175$ GeV/c^2) after the event selection is used, as shown in Fig. 7.1, because it will be hard to convolute the resolution function by the analytical way. Even if this distribution is fitted by a function, the step by step separation is necessary to convolute the resolution function.

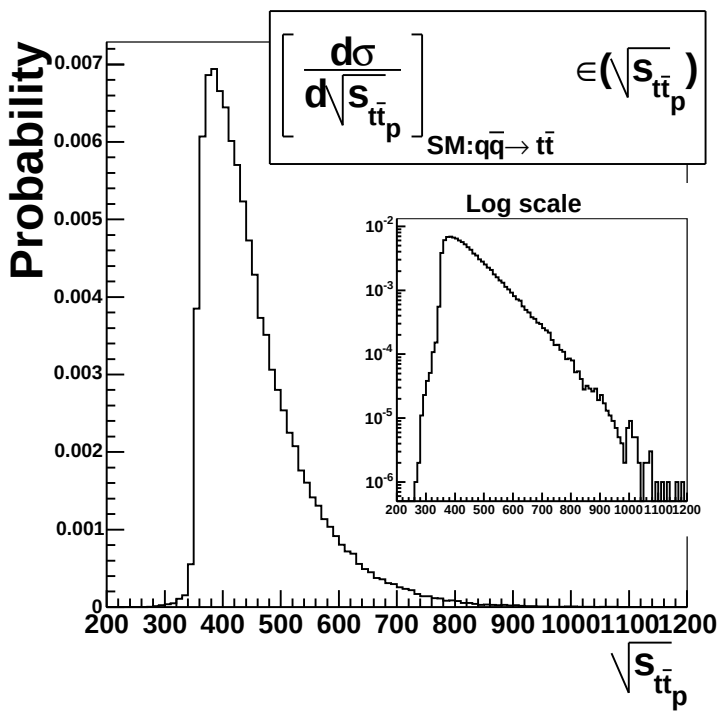

Figure 7.1: The SM parton level $q\bar{q} \to t\bar{t}$ $\sqrt{s_{t\bar{t}}}$ distribution after the event selection.

The selection efficiencies, $\epsilon(\sqrt{s_{t\bar{t}_p}})$, of the massive gluon samples could depend on the massive gluon parameters, but as shown in Fig. 7.2 these agree with the SM $q\bar{q} \to t\bar{t}$ process within the statistical uncertainties. If $\epsilon(\sqrt{s_{t\bar{t}_p}})$ depend on the massive gluon parameters, the effect should be larger at larger $|\lambda|$, but this is not the case.

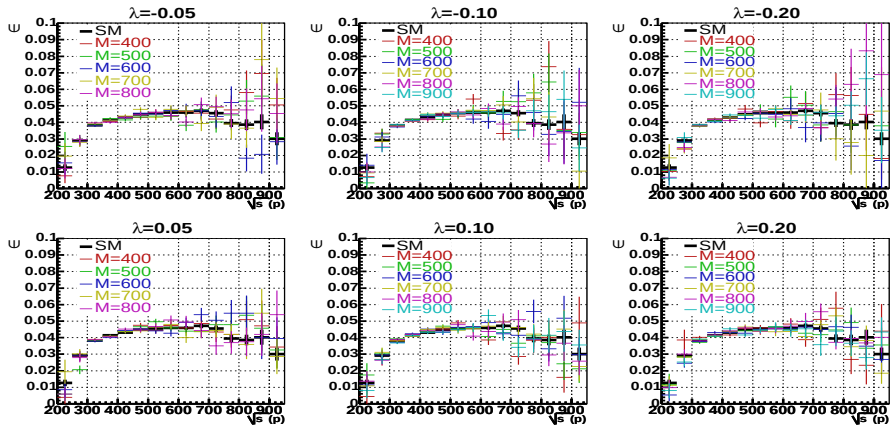

Figure 7.2: The event selection efficiencies as a function of $\sqrt{s_{t\bar{t}_p}}$ for the various massive gluon parameters.

The parton level (Massive Gluon)/(SM) differential cross section ratios are checked with a few parameter points by taking Monte Carlo ratios, as shown in Fig. 7.3. These ratios are described well by Eq.(7.3) times $\sigma_{\text{total}}(\text{SM})/\sigma_{\text{total}}(\text{MG})$.

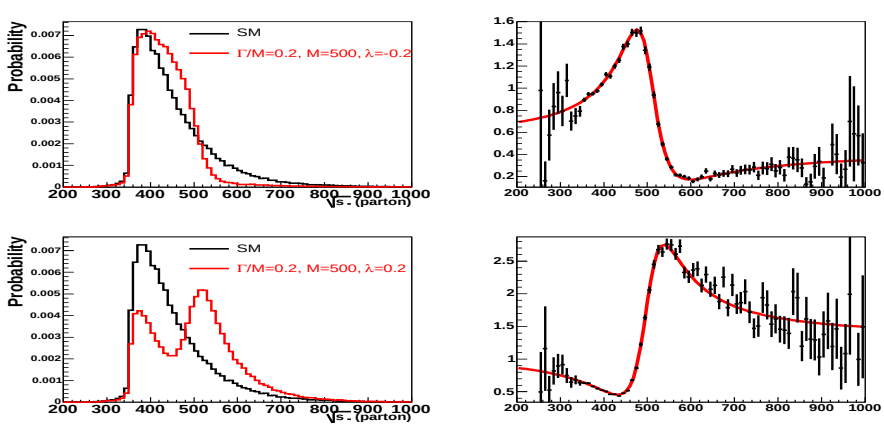

Figure 7.3: The left plots show the parton level $q\bar{q} \to t\bar{t}$ $\sqrt{s_{t\bar{t}}}$ distributions. The right plots are the ratios of MG/SM histograms with the ratio function times $\sigma_{\text{total}}(\text{SM})/\sigma_{\text{total}}(\text{MG})$ (red line).

The resolution function, $f(\sqrt{s_{t\bar{t}_r}} - \sqrt{s_{t\bar{t}_p}}; \sqrt{s_{t\bar{t}_p}})$, is estimated from the SM $q\bar{q} \to t\bar{t}$ MC, as shown in Fig. 7.4. The $\sqrt{s_{t\bar{t}_p}}$ range is separated according to Table 7.1. These distributions are fitted by the Johnson SU function + Gaussian:

$$\begin{aligned} f(x) &= p_0 \frac{p_4}{p_2\sqrt{2\pi}\sqrt{y^2+1}} \exp\left[-\frac{1}{2}\left\{p_3 + p_4 \log(y + \sqrt{y^2+1})\right\}\right] \\ &+ (1-p_0)\frac{1}{\sqrt{2\pi}p_6} \exp\left[-\frac{(x-p_5)^2}{2p_6^2}\right], \end{aligned} \tag{7.4}$$

where

$$x = \sqrt{s_{t\bar{t}_r}} - \sqrt{s_{t\bar{t}_p}}, \quad y = \frac{x - p_1}{p_2}, \tag{7.5}$$

and the fit parameters are $p_i = p_i(\sqrt{s_{t\bar{t}_p}})$. Although there exists $\sqrt{s_{t\bar{t}}}$ reconstruction bias as shown in Fig. 7.4, the resolution function contains the bias information.

The parameterization is performed in the same way as the light quark TF parameterization. Figure 7.5 shows the final loop of p_i fittings. The extrapolations of the $p_i(\sqrt{s_{t\bar{t}_p}})$ fitting to lower/upper $\sqrt{s_{t\bar{t}_p}}$ values is inappropriate. The edge points of the fit value are used for lower/upper $\sqrt{s_{t\bar{t}_p}}$ values ($\sqrt{s_{t\bar{t}_p}} = 700$ GeV/c^2 value is used for p_0 at $\sqrt{s_{t\bar{t}_p}} > 700$ GeV/c^2).

Figure 7.6 shows the parameterized resolution function, normalized at each $\sqrt{s_{t\bar{t}_p}}$. $\sqrt{s_{t\bar{t}_p}} = 350$ GeV/c^2 resolution function is used at $\sqrt{s_{t\bar{t}_p}} < 350$ GeV/c^2 and $\sqrt{s_{t\bar{t}_p}} = 800$ GeV/c^2 at $\sqrt{s_{t\bar{t}_p}} > 800$ GeV/c^2.

$\sqrt{s_{t\bar{t}_p}}$ (GeV/c^2) range	350 - 500	500 - 560	560 - 620	620-700	700 - 800
$\sqrt{s_{t\bar{t}_p}}$ (GeV/c^2) interval	10	20	30	40	50

Table 7.1: The $\sqrt{s_{t\bar{t}_p}}$ step to fit the resolution function.

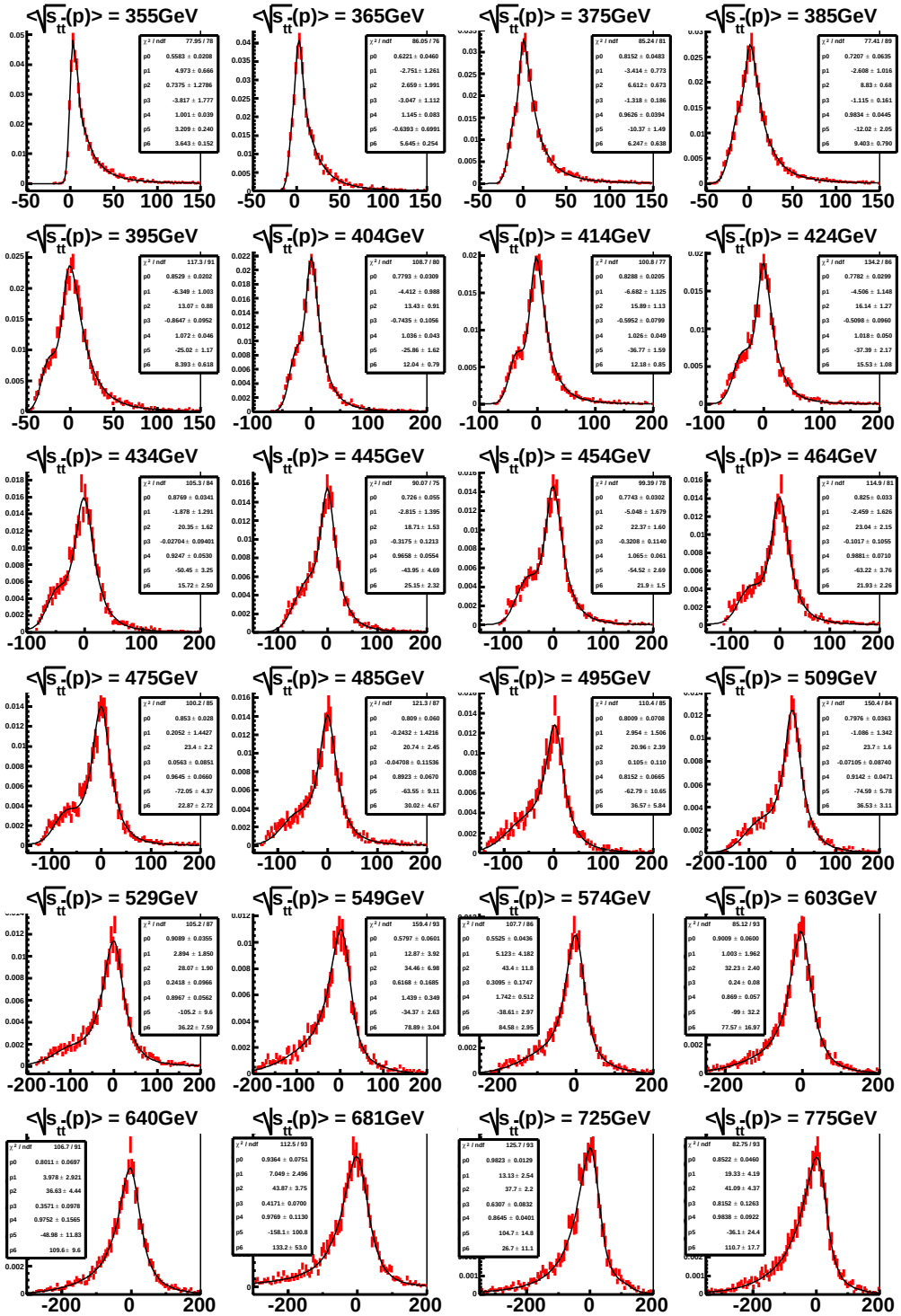

Figure 7.4: The resolution function fitted by Johnson SU function + Gaussian: The horizontal axis is $\sqrt{s_{t\bar{t}_r}} - \sqrt{s_{t\bar{t}_p}}$, and the vertical axis is probability.

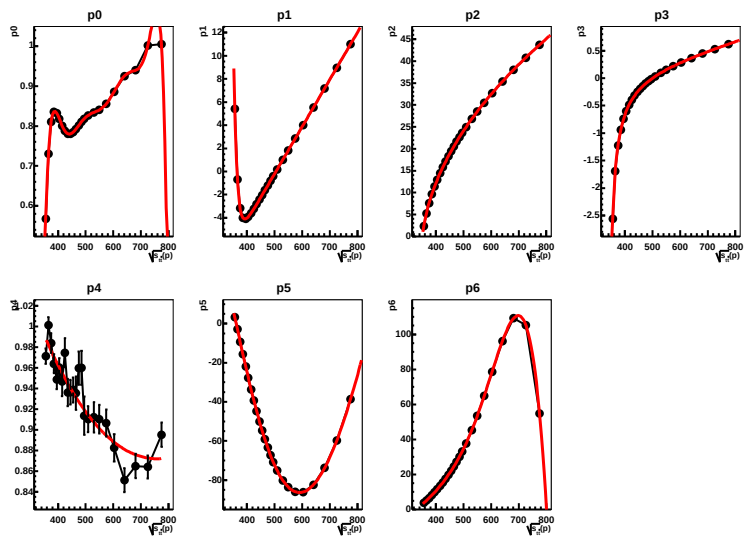

Figure 7.5: The final iteration of the fitting of the parameters $p_i(\sqrt{s_{t\bar{t}_p}})$.

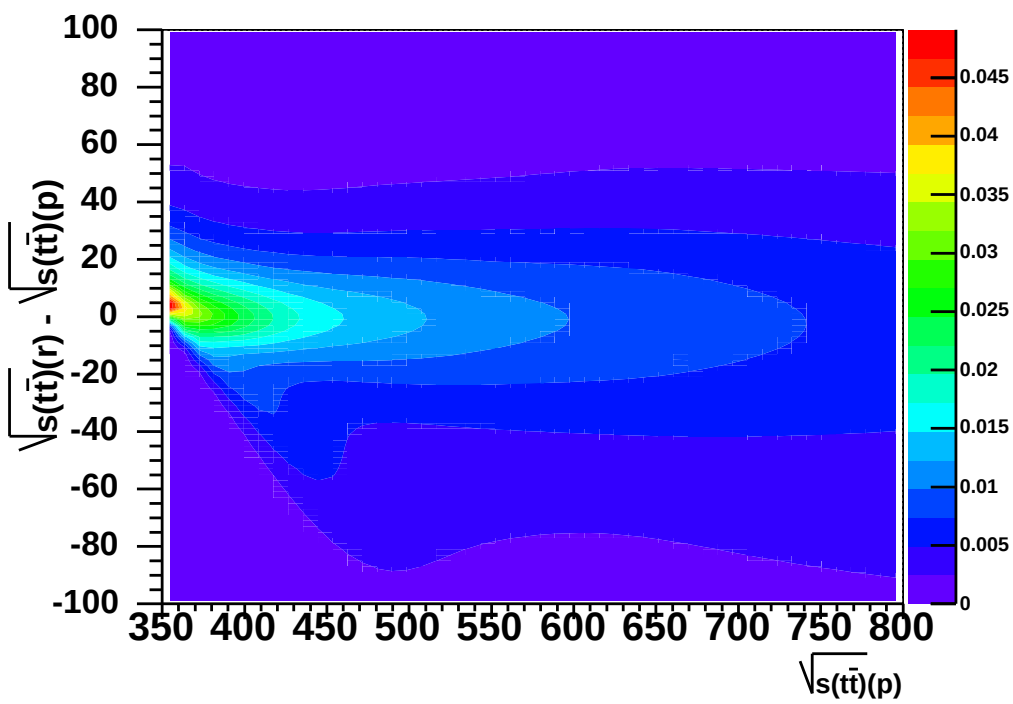

Figure 7.6: The parameterized resolution function, normalized at each $\sqrt{s_{t\bar{t}_p}}$ point.

7.1.1 Reconstructed $\sqrt{s_{t\bar{t}}}$ P.D.F with SM Process

Figure 7.7 shows the reconstructed SM $q\bar{q} \to t\bar{t}$ $\sqrt{s_{t\bar{t}}}$ distribution and the function of Eq.(7.1) at $\lambda = 0$ (whatever Γ or M is). The distribution (histogram) and the function (red line) agree well except for $\sqrt{s_{t\bar{t}_r}} < 350$ GeV/c^2. The disagreement at $\sqrt{s_{t\bar{t}_r}} < 350$ GeV/c^2 does not affect the final results because the background events mentioned later do not have the events at this point (the top mass is constrained to 175GeV/c^2).

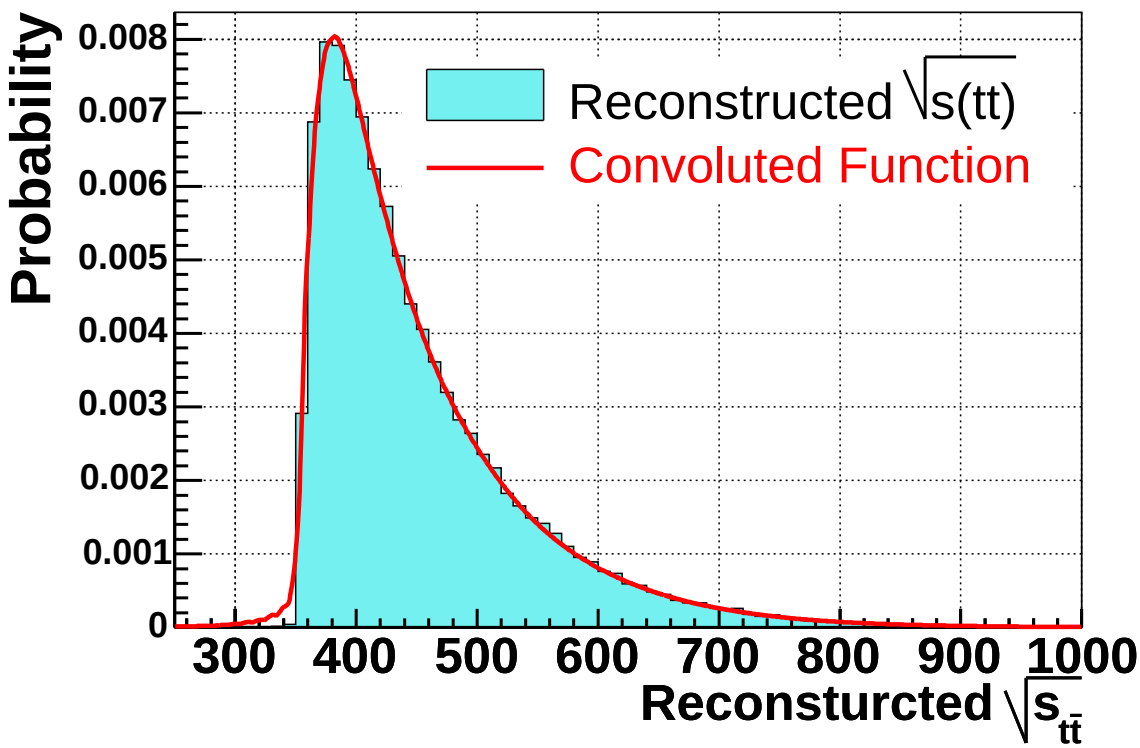

Figure 7.7: The SM $q\bar{q} \to t\bar{t}$ reconstructed $\sqrt{s_{t\bar{t}}}$ distribution (light-blue histogram) and the convoluted signal $\sqrt{s_{t\bar{t}}}$ p.d.f at $\lambda = 0$ (red line).

7.1.2 Check of Resolution Function with Z' Sample

The parameterized resolution function is given by the SM $q\bar{q} \to t\bar{t}$ process MC. This function is used also for the massive gluon processes. Whether or not the resolution function depend on the massive gluon parameters is tested. $q\bar{q} \to Z' \to t\bar{t}$ process is better for this kind of checks than the massive gluon process. Z' samples are generated using PYTHIA default settings without $\gamma/Z/Z'$ interference, with $M(Z') = 350 - 900$ GeV/c^2 in 50 GeV/c^2 interval ($\sim$5 thousand events survive after the event selections). The left plot of Fig. 7.8 shows the example of $\sqrt{s_{t\bar{t}_p}}$

distribution with $M(Z') = 700$ GeV/c^2, which has the long low invariant mass tail. To check the resolution function, the following function is used to account for the parton level low invariant mass tail,

$$p(\sqrt{s_{t\bar{t}_r}} - \sqrt{s_{t\bar{t}_p}}) \equiv \sum_{i=1}^{Nbin} \left[p_{\sqrt{s_{t\bar{t}_p}}}(i) f(\sqrt{s_{t\bar{t}_r}} - \sqrt{s_{t\bar{t}_p}}; \sqrt{s_{t\bar{t}_p}}(i)) \right], \tag{7.6}$$

where $p_{\sqrt{s_{t\bar{t}_p}}}(i)$ is i-th bin content of $\sqrt{s_{t\bar{t}_p}}$ distribution (like the left plot of Fig. 7.8) and $f(\sqrt{s_{t\bar{t}_r}} - \sqrt{s_{t\bar{t}_p}}; \sqrt{s_{t\bar{t}_p}}(i))$ is the resolution function given by the SM $q\bar{q} \to t\bar{t}$ process.

The right plot of Fig. 7.8 shows the reconstructed $\sqrt{s_{t\bar{t}}}$ distribution and the p.d.f (Eq. 7.6). This agreement is from the fact that the top quark decay is the same as SM and the production matrix element is not included to reconstruct $\sqrt{s_{t\bar{t}}}$ by DLM. Figure 7.9 shows the same kind of tests for the various $M(Z')$'s. The resolution function depends little on X of $q\bar{q} \to X \to t\bar{t}$ process from these checks. Thus the same resolution function is used also for the p.d.f of $\sqrt{s_{t\bar{t}_r}}$ in the massive gluon processes.

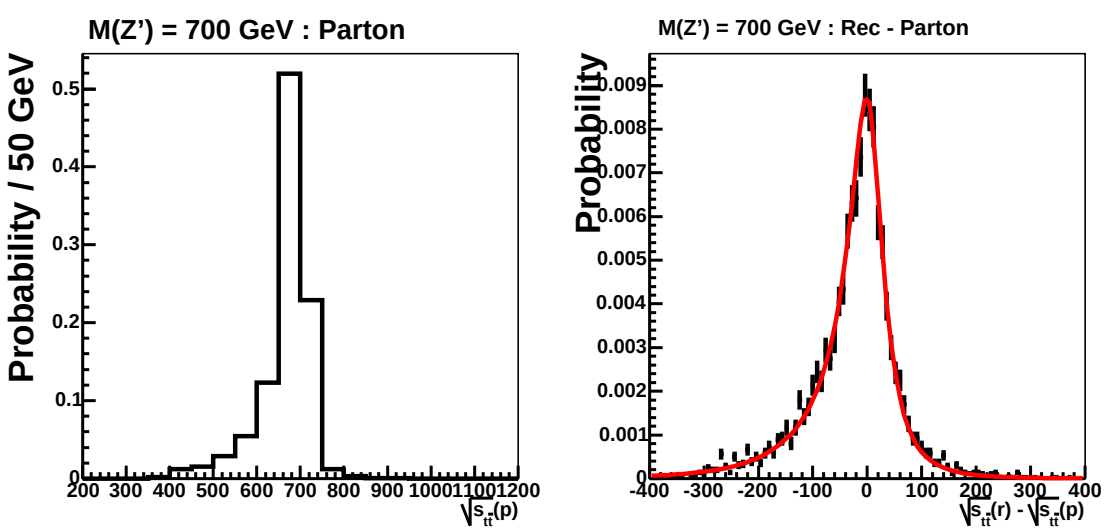

Figure 7.8: The example of Z' process: The parton level $\sqrt{s_{t\bar{t}}}$ distribution (left) and the difference between reconstructed and parton level $\sqrt{s_{t\bar{t}}}$ (right) with M(Z')=700 GeV/c^2.

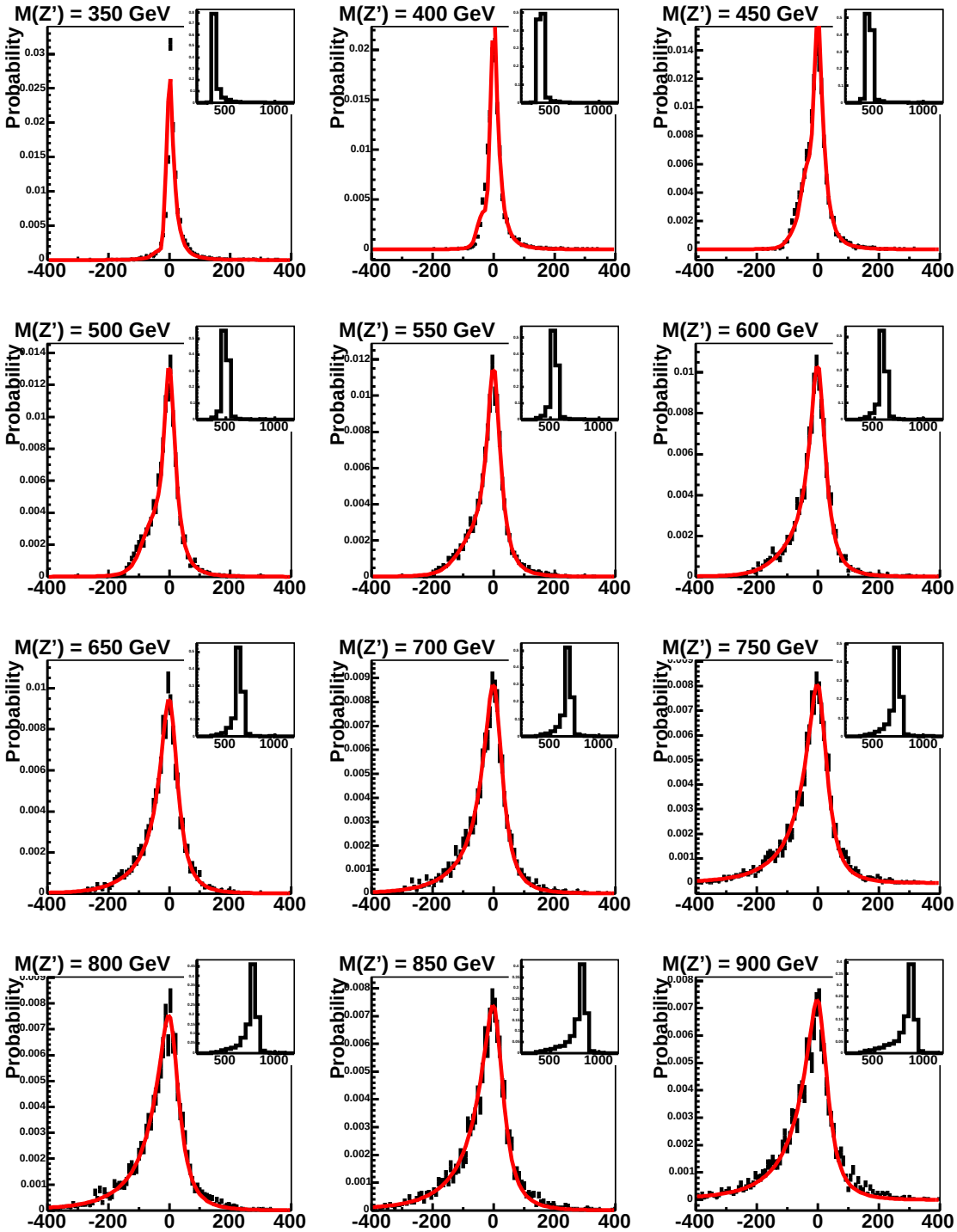

Figure 7.9: The differences between reconstructed and parton level $\sqrt{s_{t\bar{t}}}$, and the resolution functions (red lines) for the various $M(Z')$, each top right plot is the parton level $\sqrt{s_{t\bar{t}}}$ distribution.

7.1.3 Reconstructed $\sqrt{s_{t\bar{t}}}$ P.D.F for Massive Gluon

Figure 7.10 shows the reconstructed $\sqrt{s_{t\bar{t}}}$ distributions and the p.d.f from Eq.(7.1) at the various mass and λ points. The more examples of the massive gluon reconstructed $\sqrt{s_{t\bar{t}}}$ p.d.f's are shown in Appendix A.

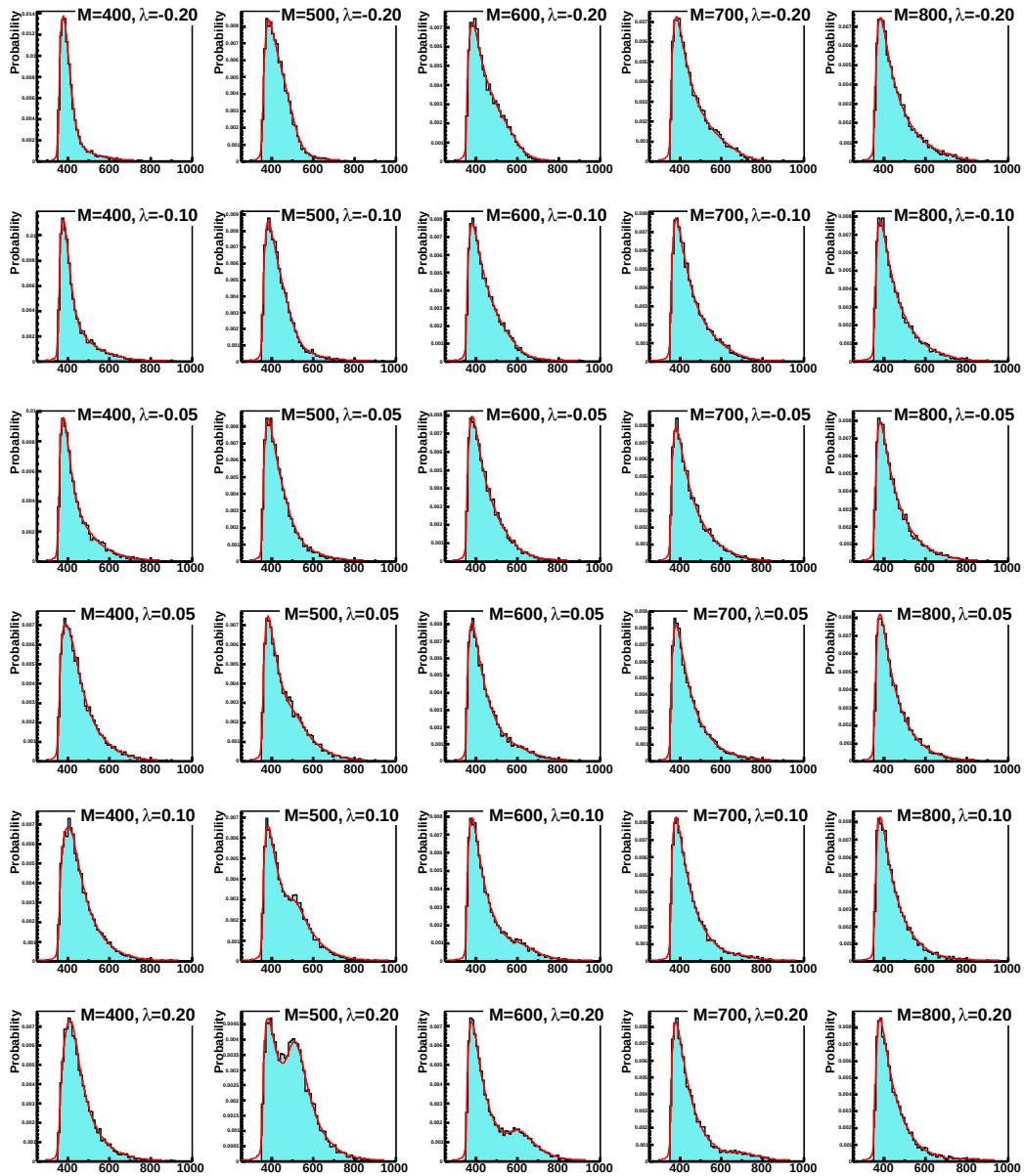

Figure 7.10: The reconstructed $\sqrt{s_{t\bar{t}}}$ distributions (light-blue histogram) and the convoluted signal $\sqrt{s_{t\bar{t}}}$ p.d.f's (red lines) for the various mass and λ points at $\Gamma/M = 0.2$.

7.2 Background Reconstructed $\sqrt{s_{t\bar{t}}}$ P.D.F

In the massive gluon search, $gg \to t\bar{t}$ process is the background ($q\bar{q} \to t\bar{t}$ process is categorized as signal). To estimate the number of $gg \to t\bar{t}$ events, the theoretical fraction in $t\bar{t}$ events from Ref. [13], $F_{gg} = 0.16 \pm 0.05$, is used. The number of $gg \to t\bar{t}$ process is estimated by $N(gg \to t\bar{t}) \equiv F_{gg}(N_{\text{data}} - N_{\text{non}-t\bar{t}})$. The background estimations in 1.9 fb^{-1} are summarized in Table 7.2.

To reconstruct "background $\sqrt{s_{t\bar{t}}}$", the same method used for the signal is applied. Figure 7.11 shows each reconstructed background $\sqrt{s_{t\bar{t}}}$ distribution. All the distributions are combined to define the reconstructed background $\sqrt{s_{t\bar{t}}}$ p.d.f. Figure 7.12 shows the total background $\sqrt{s_{t\bar{t}}}$ distribution fitted by Johnson SU + 2 Gaussian's.

$$
\begin{aligned}
p_b(\sqrt{s_{t\bar{t}}}_r) &= f_1 \frac{\delta}{\lambda\sqrt{2\pi}\sqrt{y^2+1}} \exp\left[-\frac{1}{2}\left\{\gamma + \delta \log(y + \sqrt{y^2+1})\right\}^2\right] \\
&+ \frac{f_2}{\sqrt{2\pi}\sigma_1} \exp\left[-\frac{(\sqrt{s_{t\bar{t}}}_r - \mu_1)}{2\sigma_1^2}\right] + \frac{(1-f_1-f_2)}{\sqrt{2\pi}\sigma_2} \exp\left[-\frac{(\sqrt{s_{t\bar{t}}}_r - \mu_2)}{2\sigma_2^2}\right], \quad (7.7) \\
y &= \frac{\sqrt{s_{t\bar{t}}}_r - \xi}{\lambda}, \quad (7.8)
\end{aligned}
$$

where $f_1, f_2, \xi, \lambda, \gamma, \delta, \sigma_1, \mu_1, \sigma_2$ and μ_2 are the fit parameters.

Process	Number	Modeling
WW	2.53 ± 0.27	PYTHIA
WZ	0.94 ± 0.08	PYTHIA
ZZ	0.09 ± 0.01	PYTHIA
s-channel single top	2.00 ± 0.20	MAD-EVENT
t-channel single top	1.94 ± 0.17	MAD-EVENT
$Z \to l^+l^-$	2.39 ± 0.28	ALPGEN
Wbb	16.53 ± 6.66	ALPGEN
Wcc/Wc	12.88 ± 5.23	ALPGEN
Mistags	16.65 ± 3.64	ALPGEN
QCD fake (Non-W)	13.62 ± 11.68	ALPGEN
$gg \to t\bar{t}$	48.23 ± 15.57	DATA
Total Background	117.80 ± 19.83	-
Data	371	-

Table 7.2: The background estimations in 1.9 fb^{-1}.

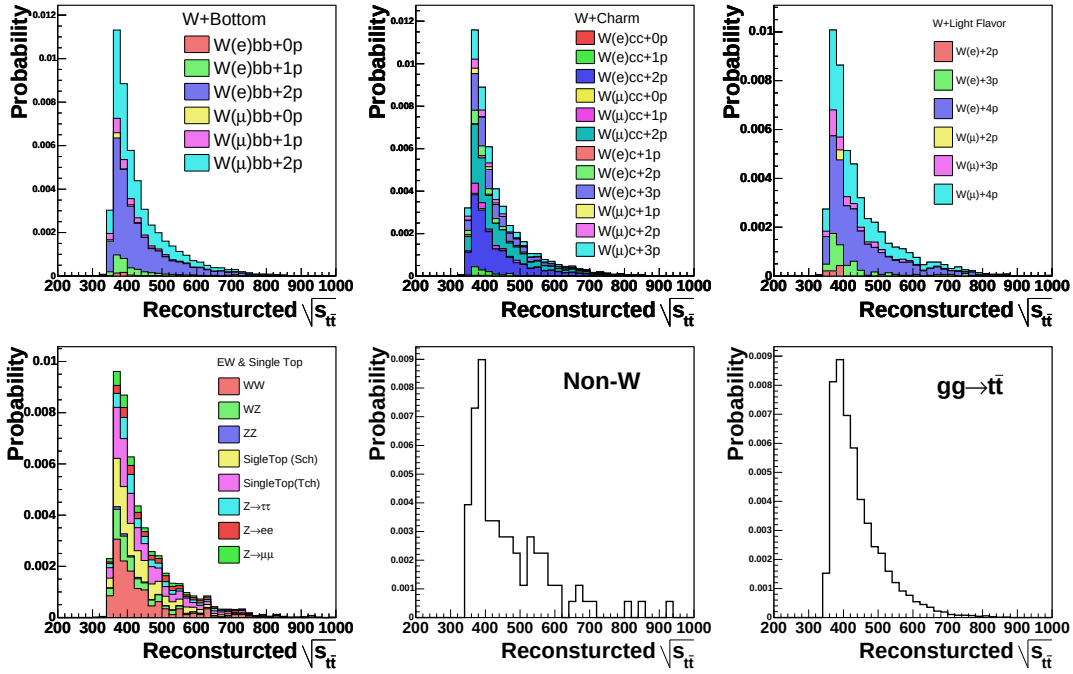

Figure 7.11: The reconstructed "background $\sqrt{s_{t\bar{t}}}$" distributions.

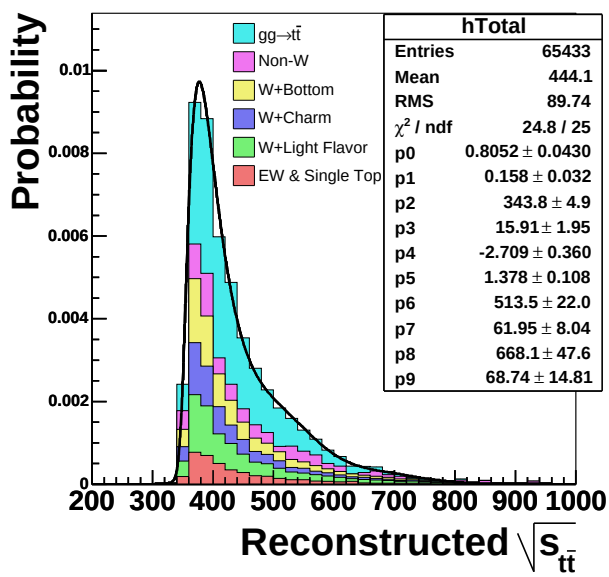

Figure 7.12: The total "background $\sqrt{s_{t\bar{t}}}$" p.d.f, fitted by Johnson SU + 2 Gaussian's.

7.3 Likelihood Fit of Coupling Strength

The likelihood of the massive gluon parameters (Γ, M, λ) is defined by the unbinned extended likelihood with the Gaussian constraint on the total background number,

$$L(\boldsymbol{\alpha}, \nu_s, \nu_b) \equiv G(\nu_b; \nu_b^{\rm exp}, \sigma_b^{\rm exp}) P(N; \nu) \prod_{i=1}^{N} \frac{\nu_s p_s(\sqrt{s_{t\bar{t}_r}}(i); \boldsymbol{\alpha}) + \nu_b p_b(\sqrt{s_{t\bar{t}_r}}(i))}{\nu}, \quad (7.9)$$

where $\boldsymbol{\alpha}$ is the massive gluon parameters (λ, M, Γ), G and P stand for Gaussian and Poisson terms, $\nu_b^{\rm exp}$ is the central value of expected background number, $\sigma_b^{\rm exp}$ is the uncertainty of the total background number, N is the observed number of events, $p_s(\sqrt{s_{t\bar{t}_r}}(i); \boldsymbol{\alpha})$ is i-th event signal $\sqrt{s_{t\bar{t}_r}}$ probability (Eq. 7.1), $p_b(\sqrt{s_{t\bar{t}_r}}(i))$ is i-th event background $\sqrt{s_{t\bar{t}_r}}$ probability (Eq. 7.8), ν_s and ν_b are the signal and background numbers $(\nu \equiv \nu_s + \nu_b)$.

The pseudo data is obtained by the following way to perform the pseudo experiments (PEs). The total number of events, $N = 371$, is fixed to the same number as real data. The background number in a PE is given by the Poisson fluctuation around $\nu_b^{\rm exp}$. The signal number is given by [N - (background number)]. The $\sqrt{s_{t\bar{t}}}$'s of pseudo data are obtained at random from the template histograms of the signal and background. The likelihood function (Eq. 7.9) is maximized for the parameters (λ, ν_s, ν_b) by MINUIT [66] at a given massive gluon mass and width point. The confidence interval is given by the calculation of the likelihood at the maximized point of ν_s and ν_b at a given massive gluon mass and width.

7.4 Linearity Tests of Coupling Strength

The likelihood function (Eq. 7.9) is tested by performing the pseudo experiments using the true mass and decay width.

An example of pseudo experiment using the MC sample ($\lambda = 0.2$, $M = 500$ GeV/c^2 and $\Gamma/M = 0.2$) is performed. To perform the likelihood fit, the true mass and decay width are assumed. The left plot of Fig. 7.13 shows the pseudo data and the signal+background function using the best fitting values. The likelihood is calculated as a function of λ by using the best values of ν_s and ν_b. The right plot of Fig. 7.13 shows $-2\log[L(\lambda)/L_{\rm max}]$, $\lambda = 0.20^{+0.04}_{-0.03}$ is obtained in this pseudo experiment.

The same kind of 10 thousand pseudo experiments are performed at various masses, decay widths and λ's (Table 7.3), and the best fit λ is obtained with the assumption of the true mass and decay width. Figure 7.14 shows the best fitted λ distributions with $M = 500$ GeV/c^2 and $\Gamma/M = 0.2$ case. As shown in these plots, the fitted λ's have the broad distributions and the mean values do not perfectly describe the true

values of λ's, but fairly agree within RMS.

The re-weighting technique described in Appendix B is used to obtain the templates of the massive gluon processes.

Γ/M	λ	Mass (GeV/c^2)
0.05	-0.2, -0.1, -0.05, 0.05, 0.1, 0.2	400, 500, 600, 700, 800
0.1		
0.2		
0.3	-0.4, -0.2, -0.1, 0.1, 0.2, 0.4	
0.4		
0.5	-0.6, -0.3, -0.15, 0.15, 0.3, 0.6	

Table 7.3: The parameter points to test the linearity of λ.

Figure 7.15 shows the mean values of the fitted λ distributions as a function of the true λ at each mass and decay width. The error bars are the RMS's of the fitted λ distributions. As shown in these plots, λ determinations become hard (large RMS) at the wide decay width, high mass, and $M = 400$ GeV/c^2 points (around the peak of $\sqrt{s_{t\bar{t}}}$ distribution).

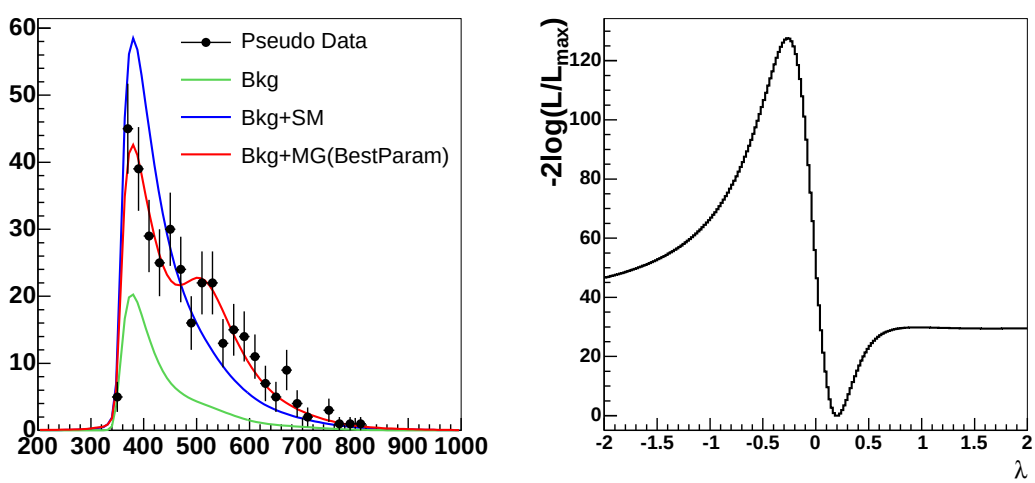

Figure 7.13: An example of pseudo experiment: The pseudo data distribution and the signal+background best fit functions (left), and $-2\log[L(\lambda)/L_{\max}]$ (right).

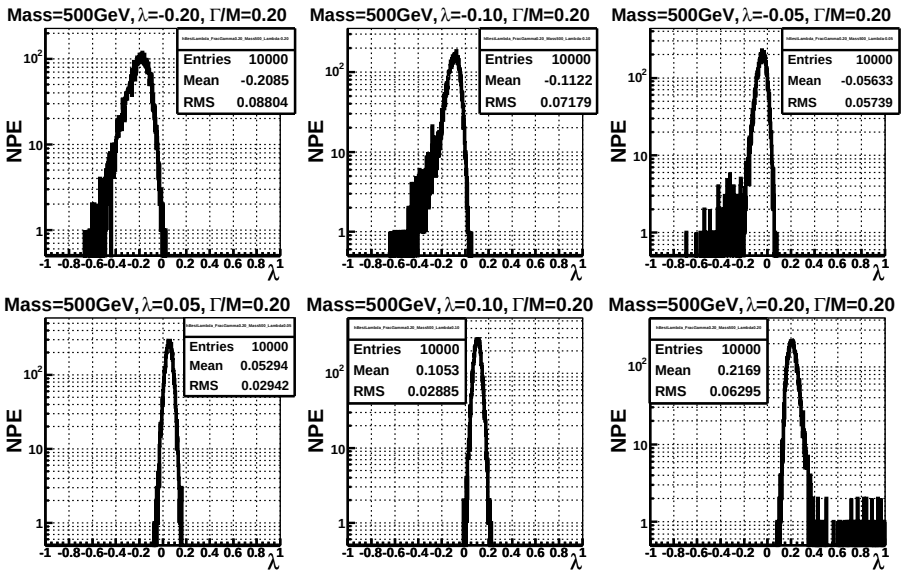

Figure 7.14: The best fit λ distributions from the 10 thousand PEs at $|\lambda| = 0.05$, 0.1, 0.2, $M = 500$ GeV/c^2 and $\Gamma/M = 0.2$.

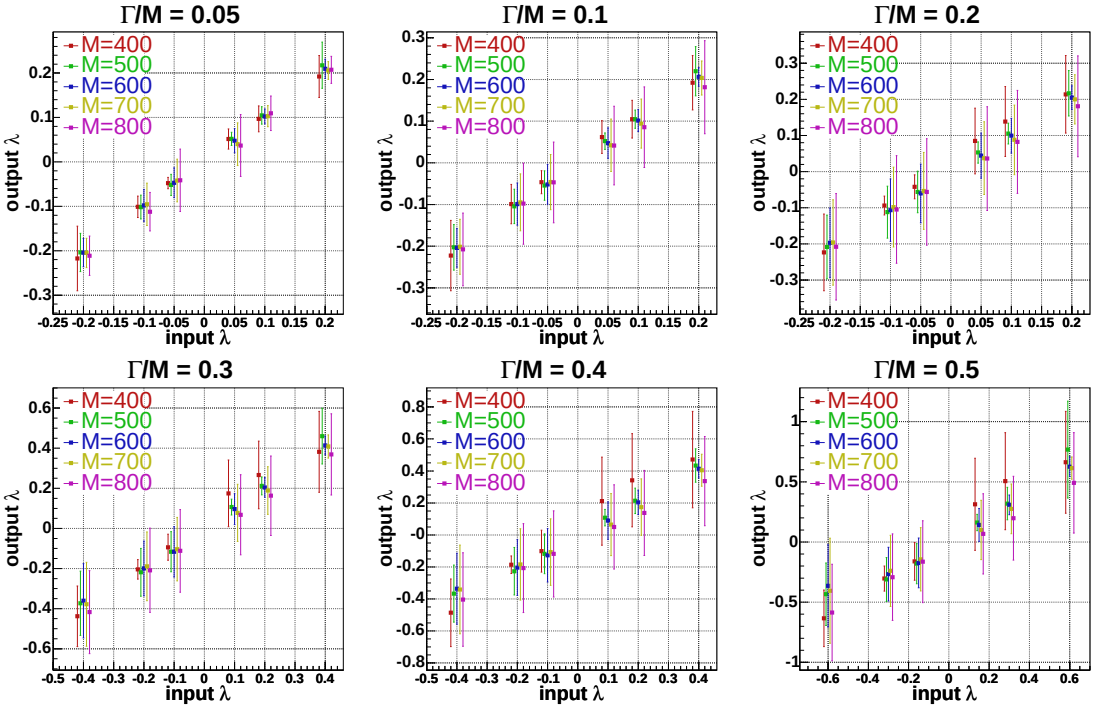

Figure 7.15: The mean values of the fitted λ distributions as a function of the true λ from 10k PEs. The lengths of the bar represent the RMS.

7.4.1 Consistency with SM Expectations

In this section the fitted λ fluctuations from the standard model pseudo data are studied, assuming only statistical fluctuation. The PYTHIA MC of $q\bar{q} \to t\bar{t}$ and the background template histograms are used to get the pseudo data, and the likelihood fit is performed to see how much the fitted λ fluctuates from the standard model $q\bar{q} \to t\bar{t}$ events. The left plot of Fig. 7.16 shows the image of 1σ, 2σ, and 3σ of the fluctuations from the standard model $q\bar{q} \to t\bar{t}$ events, with the perfect Gaussian case. 1σ, 2σ, and 3σ correspond to $1-\gamma = 0.6827$, 0.9544 and 0.9973. The right plot of Fig. 7.16 shows the example of the fitted λ fluctuations assuming $\Gamma/M = 0.2$ and $M = 500$ GeV/c^2 from the 10 thousand pseudo experiments. As shown in this plot, if the fitted λ distribution have the long tail, the evidence or observation become hard.

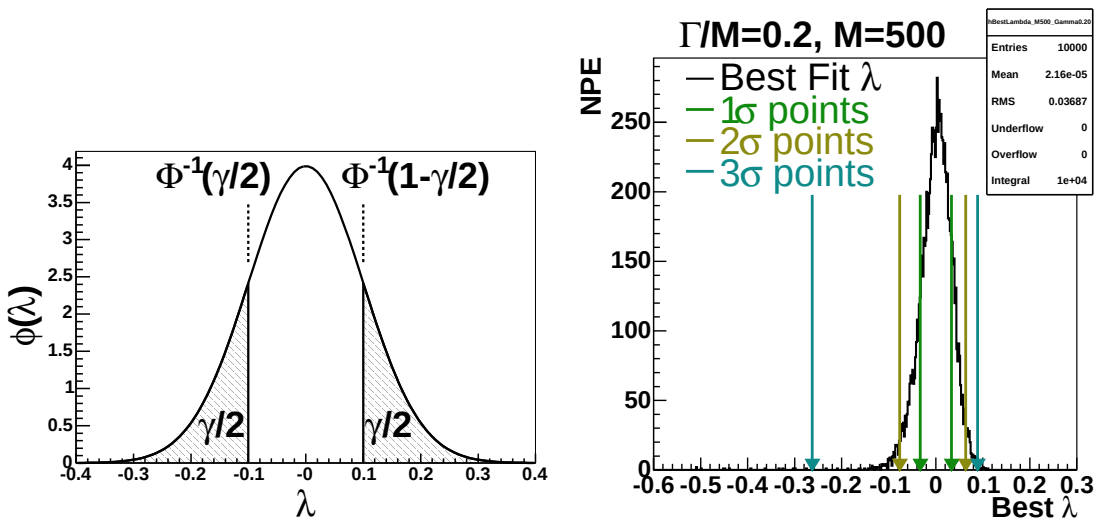

Figure 7.16: The left figure shows the usual confidence interval of $1-\gamma$ confidence level, Φ^{-1} is the quantile, imitating Ref. [57]. The right plot shows the example of the actual pseudo experiments assuming $\Gamma/M = 0.2$ and $M = 500$ GeV/c^2.

The same kind of tests are performed with the parameter points in Table 7.4. The results are shown in Fig. 7.17.

Γ/M	0.05, 0.1, 0.2, 0.3, 0.4, 0.5
M (GeV)	400, 450, 500, 550, 600, 650, 700, 750, 800

Table 7.4: The massive gluon parameter points to test the fitted λ fluctuations with the standard model pseudo data.

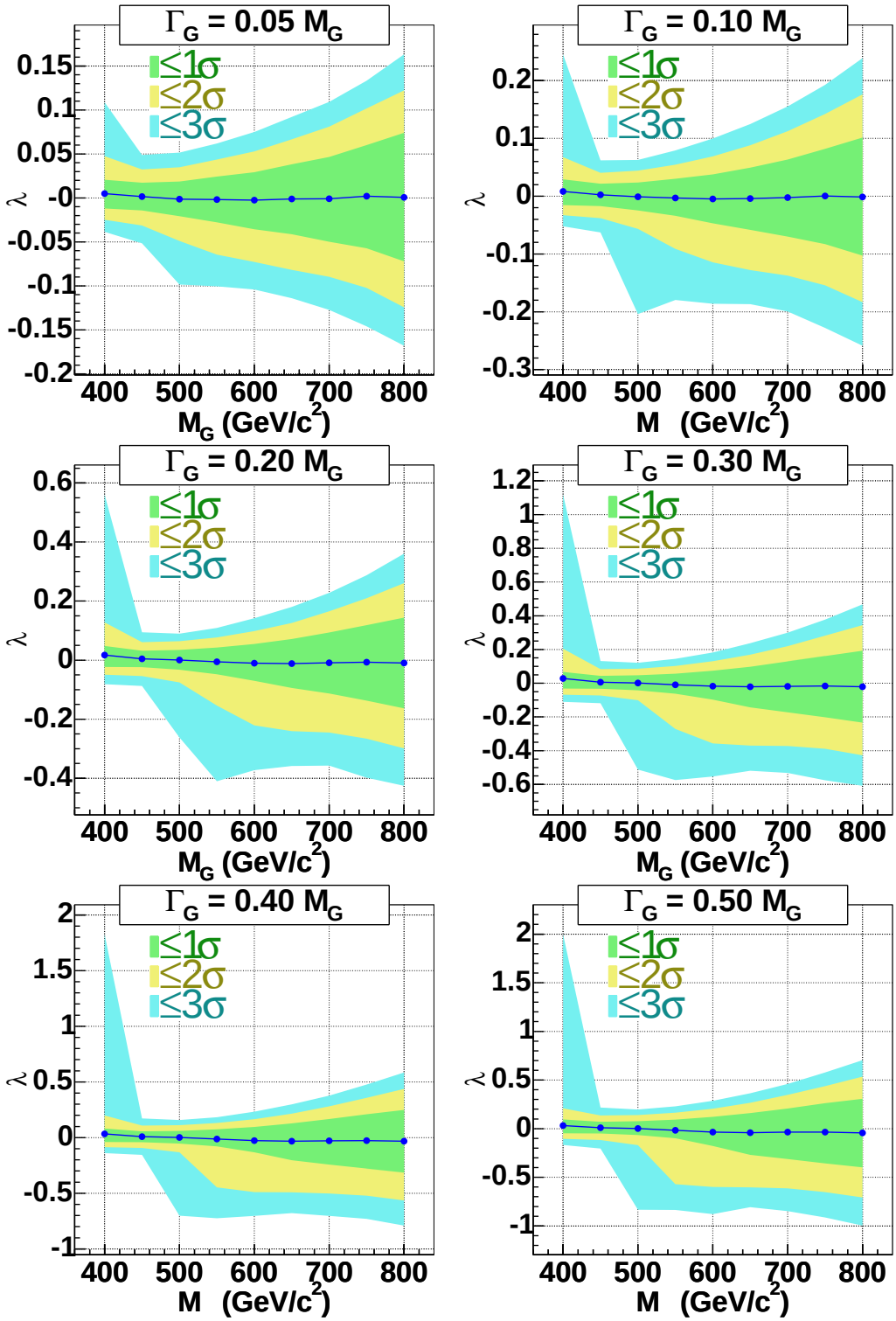

Figure 7.17: The expected fitted λ fluctuations assuming each mass and width (statistical fluctuation only). The vertical axes represent the fitted λ fluctuations and the horizontal axes are the assumed masses, with the fixed widths.

If the fitted λ values of the real data assuming the various masses and decay widths are consistent with the fluctuations from the standard model, the lower and upper limits on λ are set at the massive gluon parameters in Table 7.4. No massive gluon is assumed to get the expected lower and upper limits. Figure 7.18 shows the example of 95% C.L. lower/upper limits (95% C.L. corresponds to $-2\log(L/L_{\max}) = 3.84$).

Figure 7.19 shows the mean and RMS of the expected 95%C.L. lower and upper limits on λ at the various mass and decay width points.

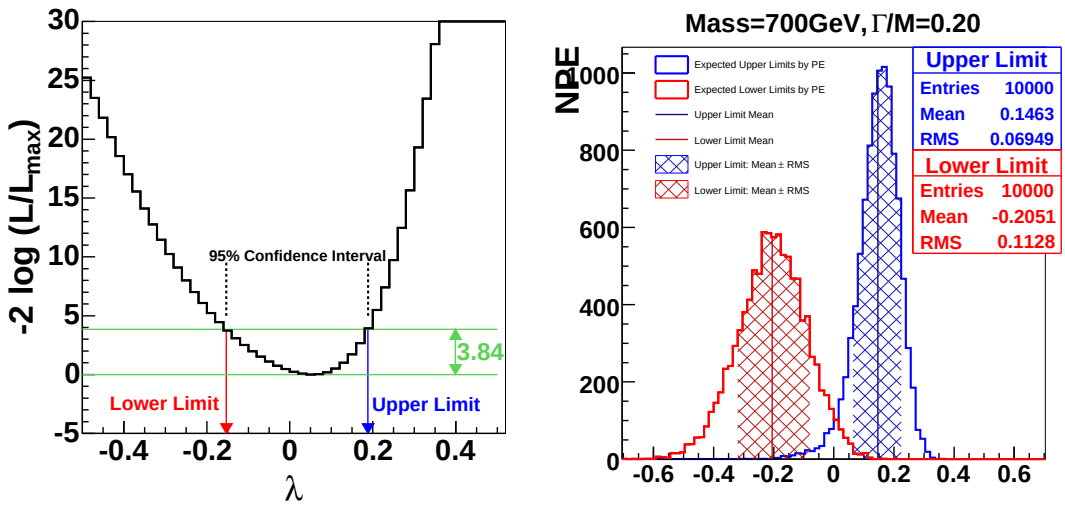

Figure 7.18: One pseudo experiment example: The 96% C.L. lower and upper limits (left), the lower and upper limits distributions from the 10 thousand psueudo experiments (right), assuming $\Gamma/M = 0.2$ and $M = 700$ GeV/c^2 (statistical fluctuation only).

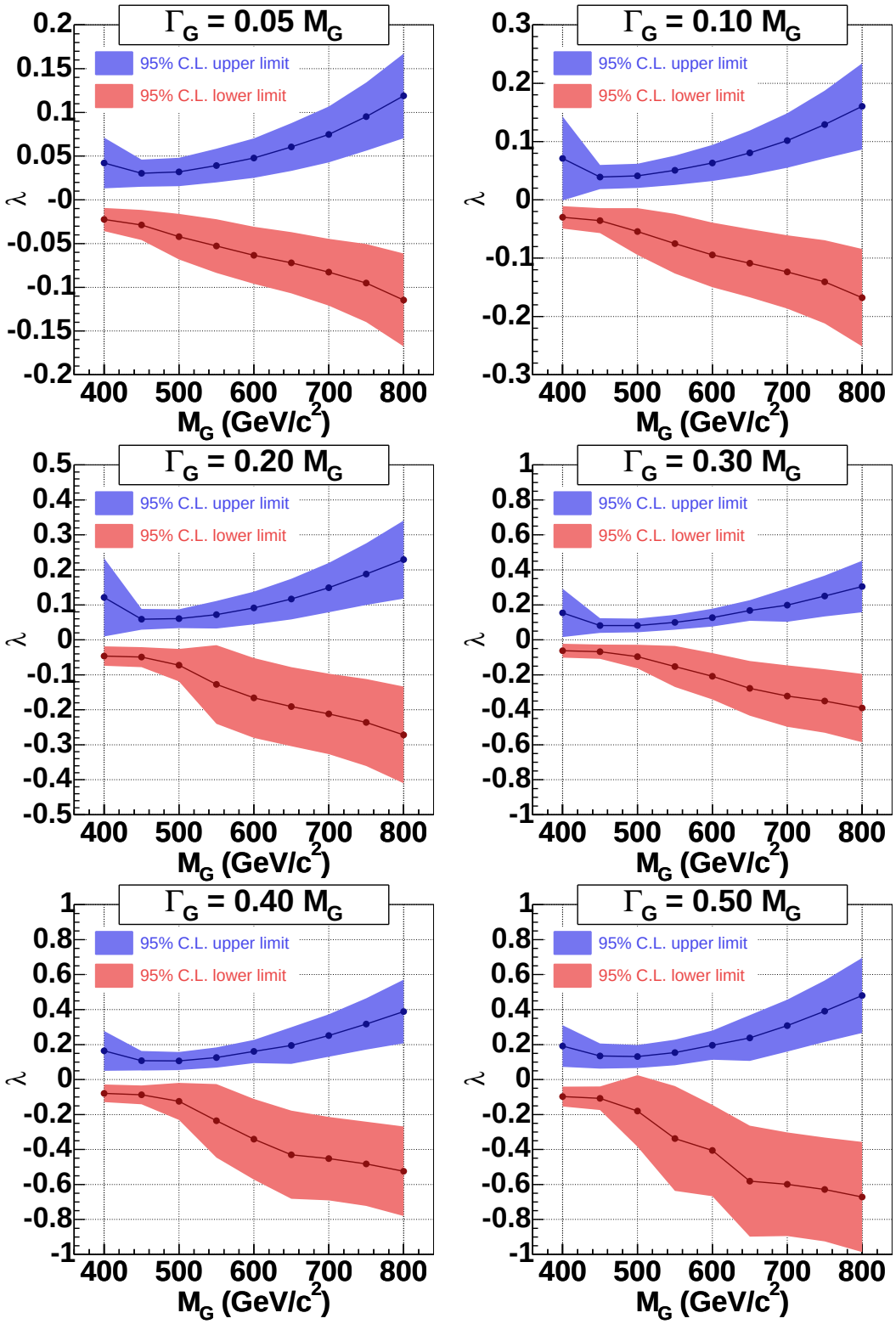

Figure 7.19: The expected 95%C.L. lower and upper limits assuming each Γ/M and mass point (statistical fluctuation only).

Chapter 8

Systematic Uncertainties

In this Chapter, the systematic uncertainties, mainly due to the uncertainties in our understanding of the detector responses, on λ are estimated. The systematic sources listed in Table 8.1 affect the shape of the reconstructed $\sqrt{s_{t\bar{t}}}$. Because the massive gluon total cross section information is not used in the analysis, the uncertainties on the absolute scale like the integrated luminosity, the lepton IDs, the trigger efficiencies, and so on do not affect the results. The fitted λ shifts from the nominal result, $\Delta\lambda$, depend on the massive gluon parameters, $\boldsymbol{\alpha} = (\lambda, M, \Gamma)$. The systematic uncertainties are estimated up to the very high values of $|\lambda|$ to check the overall effects. The massive gluon parameter points for the estimation of $\Delta\lambda$ are listed in Table 8.2. Because there are 657 parameter points and ~ 65 systematic sources, the more than 40 thousand $\times$ (number of pseudo experiments per massive gluon parameter and systematics source) are needed. The only one pseudo experiment per massive gluon parameter and systematic source is performed due to the wide parameter space. To get the average effects on the shifts of the fitted λ from the nominal results, the likelihood function and the pseudo experiment procedure are modified to avoid performing the large number of pseudo experiments. The likelihood function is modified to estimate the systematic uncertainties as following,

$$L_{\text{sys.}}(\boldsymbol{\alpha}) \equiv \prod_{\text{sig/bkg}} \prod_{\text{ibin}=1}^{\text{Nbin}} \left[\frac{\nu_s p_s(\sqrt{s_{t\bar{t}_r}}(\text{ibin}); \boldsymbol{\alpha}) + \nu_b p_b(\sqrt{s_{t\bar{t}_r}}(\text{ibin}))}{\nu} \right]^{\text{N(ibin)}} . \tag{8.1}$$

The template histograms are utilized to calculate $L_{\text{sys.}}(\boldsymbol{\alpha})$. The signal and background template histograms are scaled to $(N - \nu_b^{\text{exp}})$ and ν_b^{exp}. The ν_b, ν_s, and ν are fixed to $\nu_b = \nu_b^{\text{exp}}$, $\nu_s = (N - \nu_b^{\text{exp}})$ and $\nu = N$ in the likelihood function (Eq. 8.1).

The template histograms are obtained by the re-weighting of MC sample, described in Appendix B. Table 8.1 shows systematic uncertainty sources and the processes.

Systematic Source	Signal	Background
Jet Energy Scale	◯	All
Top Mass	◯	$gg \to t\bar{t}$
ISR/FSR	◯	$gg \to t\bar{t}$
Generator	◯	$gg \to t\bar{t}$
NLO	◯	$gg \to t\bar{t}$
PDF	◯	$gg \to t\bar{t}$, Wbb, Wcc/Wc, W+LF
b-tag Efficiency	◯	All
Multiple Interaction	◯	All
W+Jets Q^2 Scale	×	Wbb
Background Fraction	×	All
Lepton P_T	◯	All

Table 8.1: The sources and the processes of systematic uncertainties.

Γ/M	λ	Mass (GeV/c^2)
0.05	-0.5 $\sim$ 0.5: 0.05 interval (21 points)	400 $\sim$ 800: 50 interval (9 points)
0.1		
0.2	-1.0 $\sim$ 1.0: 0.1 interval (21 points)	
0.3		
0.4	-1.5 $\sim$ 1.5: 0.1 interval (31 points)	
0.5		

Table 8.2: The parameter points to study the systematic effects.

8.1 Nominal Response of Coupling Strength

The nominal response by the likelihood function (Eq. 8.1) are tested before the study of systematic uncertainties. The PYTHIA SM $t\bar{t}$ re-weighted histograms are used as the nominal signal sample. Figure 8.1 shows the likelihood fit results. As can be seen from the plots there are large errors at large $|\lambda|$ and large Γ/M, because the reconstructed $\sqrt{s_{t\bar{t}}}$ p.d.f changes little at these points as shown in Appendix A. The slopes and intercept at $\lambda = 0$ are shown in Table 8.3, which are consistent with 1 and 0 on the whole with the nominal sample.

	$\Gamma/M = 0.05$	$\Gamma/M = 0.10$	$\Gamma/M = 0.20$	$\Gamma/M = 0.30$	$\Gamma/M = 0.40$	$\Gamma/M = 0.50$
M=400	0.98 ± 0.08 0.002 ± 0.007	0.98 ± 0.07 0.003 ± 0.009	1.01 ± 0.09 0.007 ± 0.018	1.03 ± 0.09 0.010 ± 0.022	1.05 ± 0.08 0.016 ± 0.028	1.06 ± 0.09 0.022 ± 0.031
M=450	1.02 ± 0.07 0.004 ± 0.007	1.02 ± 0.07 0.005 ± 0.008	1.02 ± 0.08 0.008 ± 0.015	1.03 ± 0.09 0.009 ± 0.020	1.03 ± 0.08 0.011 ± 0.024	1.04 ± 0.08 0.013 ± 0.028
M=500	0.98 ± 0.05 0.005 ± 0.006	0.99 ± 0.05 0.006 ± 0.008	1.02 ± 0.06 0.009 ± 0.014	1.02 ± 0.07 0.009 ± 0.018	1.03 ± 0.06 0.010 ± 0.023	1.04 ± 0.07 0.011 ± 0.027
M=550	0.99 ± 0.04 0.006 ± 0.006	1.00 ± 0.04 0.006 ± 0.008	1.02 ± 0.05 0.009 ± 0.015	1.02 ± 0.06 0.008 ± 0.019	1.03 ± 0.05 0.010 ± 0.022	1.03 ± 0.06 0.012 ± 0.027
M=600	1.01 ± 0.04 0.006 ± 0.007	1.01 ± 0.04 0.006 ± 0.009	1.02 ± 0.04 0.009 ± 0.016	1.02 ± 0.05 0.009 ± 0.020	1.03 ± 0.05 0.011 ± 0.024	1.03 ± 0.05 0.011 ± 0.029
M=650	1.01 ± 0.03 0.008 ± 0.007	1.01 ± 0.03 0.009 ± 0.009	1.03 ± 0.04 0.011 ± 0.016	1.03 ± 0.04 0.011 ± 0.023	1.03 ± 0.04 0.011 ± 0.026	1.04 ± 0.04 0.011 ± 0.032
M=700	1.03 ± 0.03 0.006 ± 0.007	1.03 ± 0.03 0.007 ± 0.010	1.04 ± 0.04 0.009 ± 0.019	1.04 ± 0.04 0.010 ± 0.025	1.04 ± 0.04 0.010 ± 0.029	1.04 ± 0.04 0.010 ± 0.035
M=750	1.04 ± 0.03 0.006 ± 0.008	1.05 ± 0.04 0.007 ± 0.012	1.05 ± 0.04 0.009 ± 0.021	1.05 ± 0.04 0.008 ± 0.028	1.05 ± 0.04 0.008 ± 0.032	1.05 ± 0.04 0.006 ± 0.040
M=800	1.08 ± 0.03 0.004 ± 0.010	1.08 ± 0.04 0.006 ± 0.014	1.06 ± 0.04 0.006 ± 0.024	1.06 ± 0.05 0.004 ± 0.033	1.06 ± 0.04 0.003 ± 0.036	1.06 ± 0.04 0.0005 ± 0.046

Table 8.3: The slopes (top values in each block) and intercepts at $\lambda = 0$ (bottom value in each block) at the various mass and width points using nominal distributions.

8.2 Top Quark Mass and Jet Energy Scale (JES)

The systematic uncertainties due to the uncertainties of top quark mass [59] and jet energy scale [58] would be correlated, as described in Ref. [18]. To estimate the systematic uncertainties due to the top quark mass and JES uncertainties, both top mass and JES are shifted by $\pm 1\sigma$ at the same time. These uncertainties are estimated by re-weighting PYTHIA MC sample with top masses of 173 and 177 GeV/c^2. The top mass effect in the single top process is ignored. For JES, the effects on the reconstructed $\sqrt{s_{t\bar{t}}}$ from the acceptances are included, and the effects from all the processes are estimated.

The left plots of Fig. 8.2 show the changes of the reconstructed $\sqrt{s_{t\bar{t}}}$ shapes by shifting top quark mass by ± 2 GeV/c^2 and JES by $\pm 1\sigma$ with the SM $q\bar{q} \to t\bar{t}$ process. The right plot of Fig. 8.2 shows the fitted λ values by changing the top mass and JES. In this example the systematic uncertainty of λ is $\Delta\lambda = -0.012 + 0.013$ by taking (minimum output)-(nominal output) and (maximum output)-(nominal output).

Figure 8.3 shows the summary plots of systematic uncertainties due to the top mass and JES uncertainties at the various massive gluon parameter points. There are 2 issues in these estimations. First, there can be the double-peak of likelihood distributions because the template distribution can not be explained with the nominal fit functions. The jump of $\Delta\lambda$ between $\lambda = 0.2$ and $\lambda = 0.3$ at the massive gluon mass=800 GeV/c^2 and $\Gamma/M = 0.5$ is this case. Second, the likelihood function uses

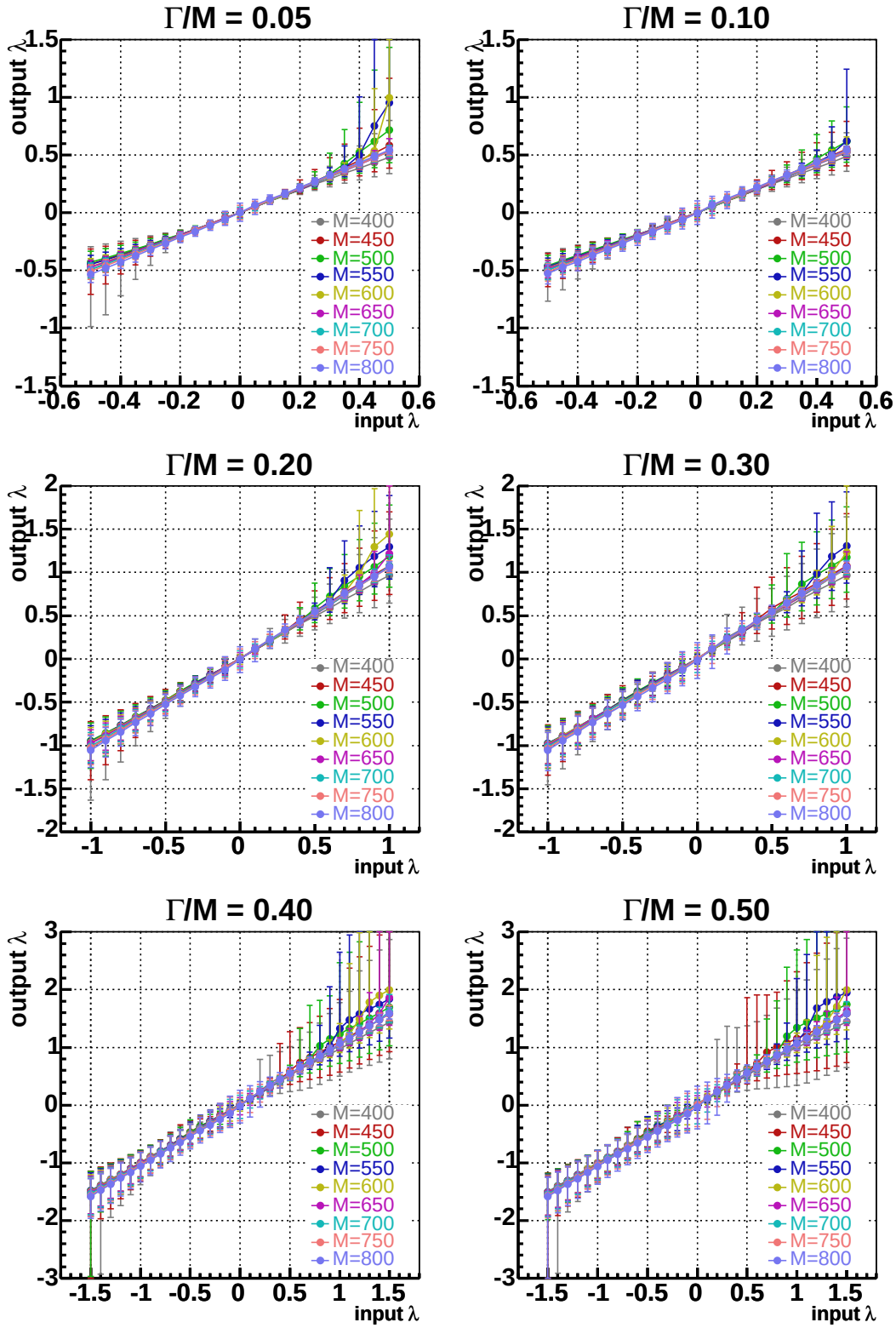

Figure 8.1: The likelihood fit results using the nominal distributions.

only the shape information and the signal reconstructed $\sqrt{s_{t\bar{t}}}$ distributions do not change so much at very large λ as can be seen at Appendix A. The jump of $\Delta\lambda$ between $\lambda = 0.3$ and $\lambda = 0.35$ at mass=500 GeV/c^2 and $\Gamma/M = 0.05$ is this case. These shifts are kept using as systematic uncertainties.

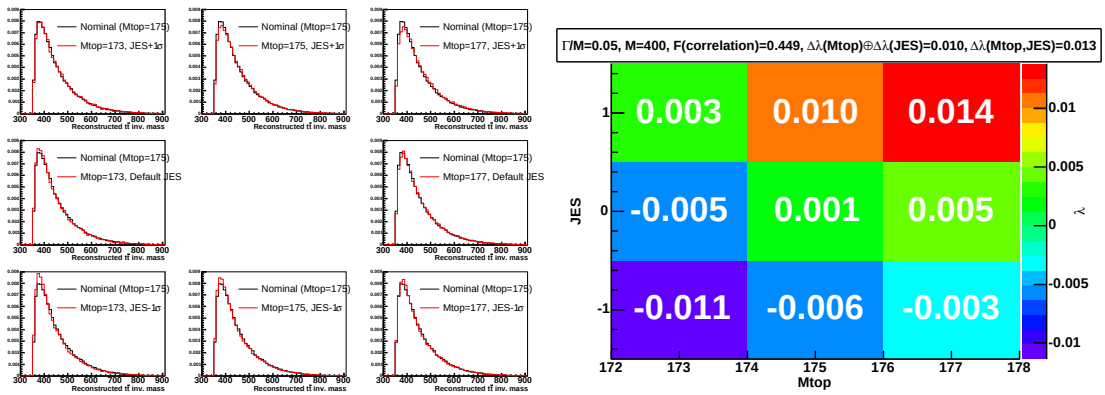

Figure 8.2: The example of systematic uncertainty due to the top quark mass and JES uncertainties: The left plots show the changes of shape by shifting top mass by ± 2 GeV/c^2 and JES by $\pm 1\sigma$. The right plot shows the best fitted λ by shifting top mass by ± 2 GeV/c^2 and JES by $\pm 1\sigma$ assuming the massive gluon $M = 400$ GeV/c^2 and $\Gamma/M = 0.05$.

8.3 Parton Distribution Function (PDF)

The 3 types of contributions from the PDF uncertainties are considered using the CTEQ [60] and MRS [60] PDF sets. The relative weights of MRST72, MRST75, and CTEQ6L to CTEQ5L (default) PDF set, and those of CTEQ6M's 20 eigen-vector $\pm 1\sigma$ values to the central value are used for the estimations.

- The PDFs from the different groups with the same α_s: The difference between MRST72 and CTEQ5L is considered.
- The difference in α_s: The difference between MRST72 and MRST75 is considered.
- The uncertainties of 20 eigen vectors in CTEQ parameterization: These are estimated using each CTEQ6M eigen vector uncertainty. The differences of each eigen vector $\pm 1\sigma$ value from the central value of CTEQ6M are added quadratically.

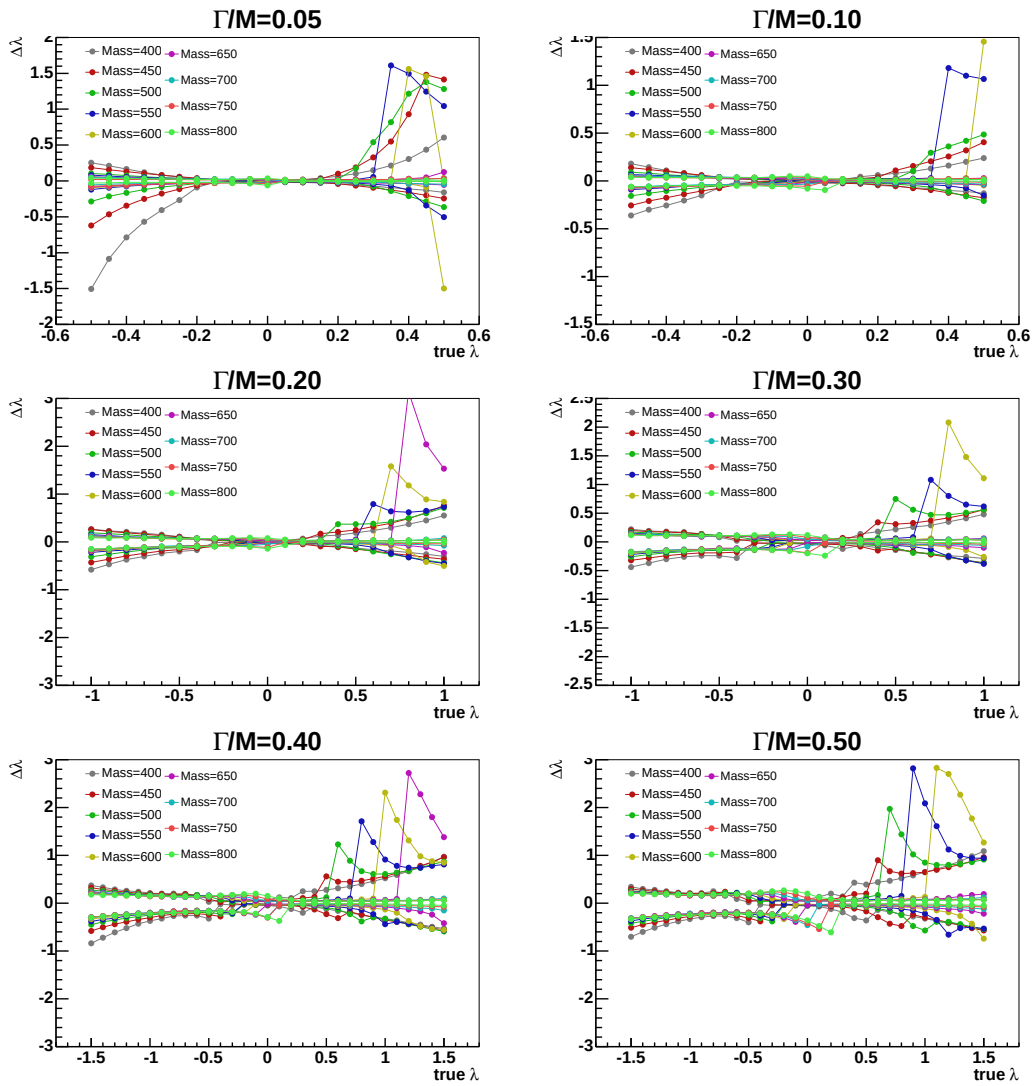

Figure 8.3: $\Delta\lambda$ as a function of true λ from the top mass and JES uncertainties at the various massive gluon masses and widths.

Figure 8.4 shows the relative event weights as a function of generator level $\sqrt{s_{t\bar{t}}}$. At the most of the massive gluon parameter points, the difference between MRST72 and MRST75 gives the largest systematic uncertainty, as shown in Figs. 8.5 and 8.6. PDF has the direct Q^2 dependence, it yields special effects compared to the other systematic uncertainties.

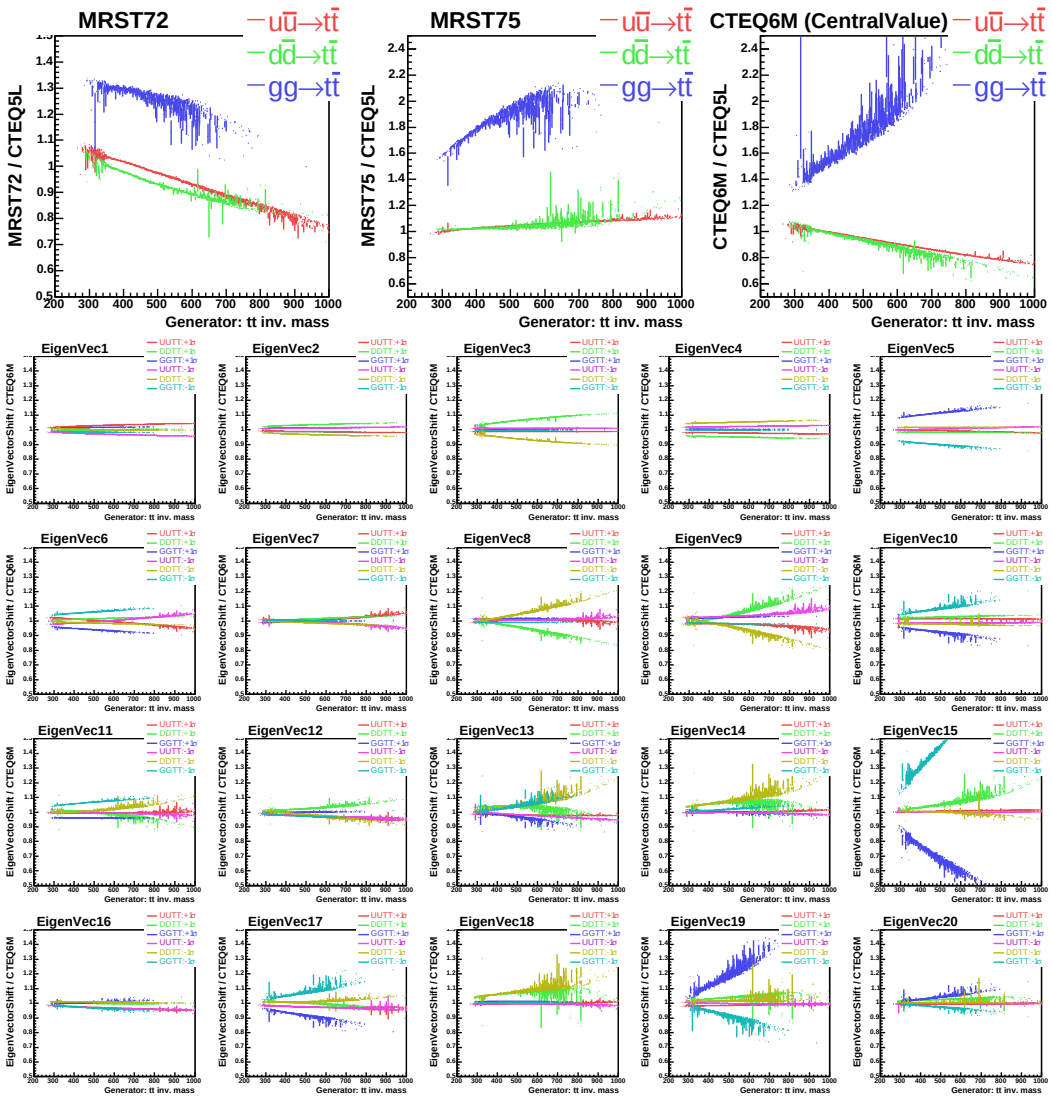

Figure 8.4: The top 3 plots show the relative weights of the different PDF sets to CTEQ5L, and the bottom 20 plots show the relative weights of 20 eigen vectors to CTEQ6M central value, as a function of generator level $\sqrt{s_{t\bar{t}}}$.

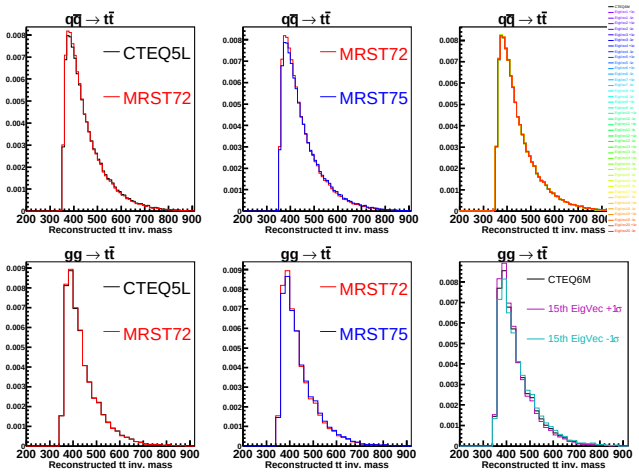

Figure 8.5: The reconstructed SM $\sqrt{s_{t\bar{t}}}$ distributions in $q\bar{q} \to t\bar{t}$ (tops) and $gg \to t\bar{t}$ (bottoms) processes. In $q\bar{q} \to t\bar{t}$ process, the effects from the eigen vector uncertainties are small (Top right plots show the 20 eigen vector $\pm 1\sigma$ variations, which are almost identical). In $gg \to t\bar{t}$ process, the difference between MRST72 and MRST75 and the uncertainty of 15th eigen vector gives the visible shape change.

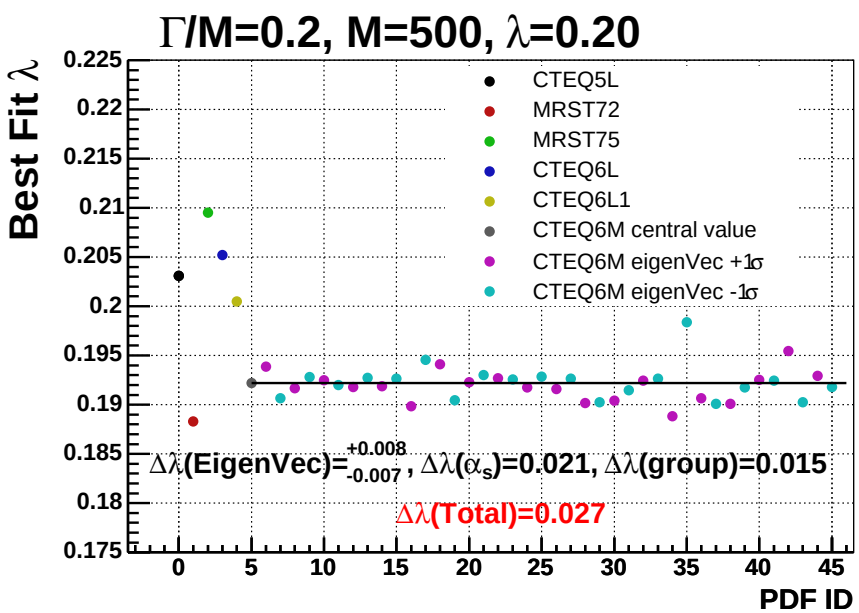

Figure 8.6: An example of the best fitted λs for the different PDFs at Γ/M=0.2, M=500GeV/c^2, and $\lambda = 0.2$.

8.4 Initial and Final State Gluon Radiation

There are uncertainties on the initial state radiation (ISR) and the final state radiation (FSR) due to the emissions of gluon in QCD, which are estimated with Drell-Yan data [62]. The MC samples are generated with the radiation modeling adjusted to have *less* or *more* radiation. Normally the fitted λs by *less* and *more* gluon radiation modelings have the opposite values compared to the nominal response. However, at a few parameter points ISR (FSR) *less* and *more* responses shift to the same side due to the MC statistics. In this case the larger shifts are considered as one side ($\Delta\lambda$ has only plus or minus value) systematic uncertainties.

8.5 Generator

The MC generator systematic uncertainties are estimated by HERWIG [63] and PYTHIA difference. HERWIG considers the $t\bar{t}$ spin correlations while PYTHIA does not. These generators are independent and have the different hadronization models and the tuning of underlying events. One side systematic uncertainties are assigned. The effects from non-$t\bar{t}$ processes are ignored.

8.6 NLO

The systematic uncertainties due to the LO and NLO difference are estimated by using MC@NLO with MRST02 and CTEQ5M PDF sets. We do not know the actual effect of NLO for the the massive gluon, we assumed that the re-weighting technique can be applied also in NLO with the same way as LO (NLO effect would be more complicated). The negative weight events exists in NLO MC, which are re-weighted with the negative value. The larger one side shifts between MRST02 and CTEQ5M are assigned as the systematic uncertainty if the shifts are the same side. If the shifts are opposite sides, the 2 sides ($\Delta\lambda$ has both plus and minus values) systematic uncertainties are assigned asymmetrically.

8.7 W+Jets Q^2 Scale

The systematic uncertainties due to W+jets Q^2 scale uncertainties are estimated by using the Q scale factors, 0.5 and 2.0 (default scale is 1.0) using ALPGEN [65] MC samples. The 2 side systematic uncertainties are assigned asymmetrically.

8.8 Background Fraction

The systematic uncertainties due to the uncertainties of the background fractions are estimated by shifting each background fraction by $\pm 1\sigma$ in Table 7.2. The 2 side

systematic uncertainties are assigned asymmetrically.

8.9 B-tagging Efficiency

The systematic uncertainties from the jet E_T dependence of *SecVtx* b-tagging scale factor are estimated. The event weights are estimated by taking the scale factor slopes as a function of jet E_T, as shown in Fig. 8.7. The 2 side systematic uncertainties are assigned asymmetrically.

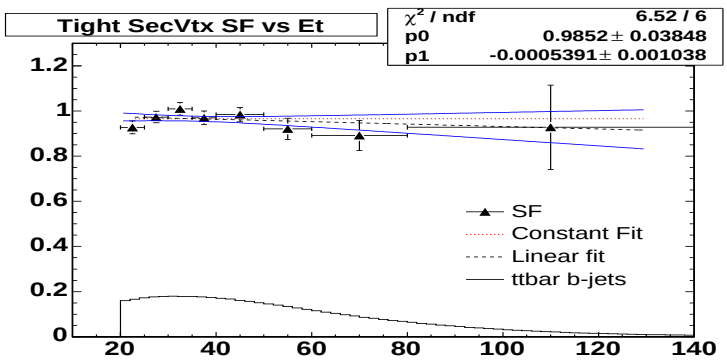

Figure 8.7: The data-MC ratio of tagging efficiency as a function of jet E_T. The blue lines show the uncertainties.

8.10 Multiple Interaction

The systematic uncertainties are estimated from the data and MC differences in number of vertices. One side systematic uncertainties are assigned. The scale factors described in Table 8.4 are applied.

Number of vertices	1	2	3	4	≥ 5
Scale Factor	0.792	0.995	1.65	4.21	7.90

Table 8.4: Scale factors from the ratio of data/MC according to the number of vertices.

8.11 Lepton P_T

The systematic uncertainties due to the lepton p_T uncertainty is estimated by shifting the lepton p_T by $\pm 1\%$. The 2 side systematic uncertainties are assined asymmetrically.

8.12 Total Systematic Uncertainties

All the systematic uncertainties are added quadratically by assuming each systematic uncertainty source is uncorrelated (except for top mass and jet energy scale uncertainties). Figure 8.8 shows the example of total systematic uncertainties at $M = 450$ GeV/c^2 and $\Gamma/M = 0.1$. The total systematic uncertainties at the other parameters are listed in Appendix C. The top mass and jet energy scale uncertainties give the largest uncertainties of the fitted λ.

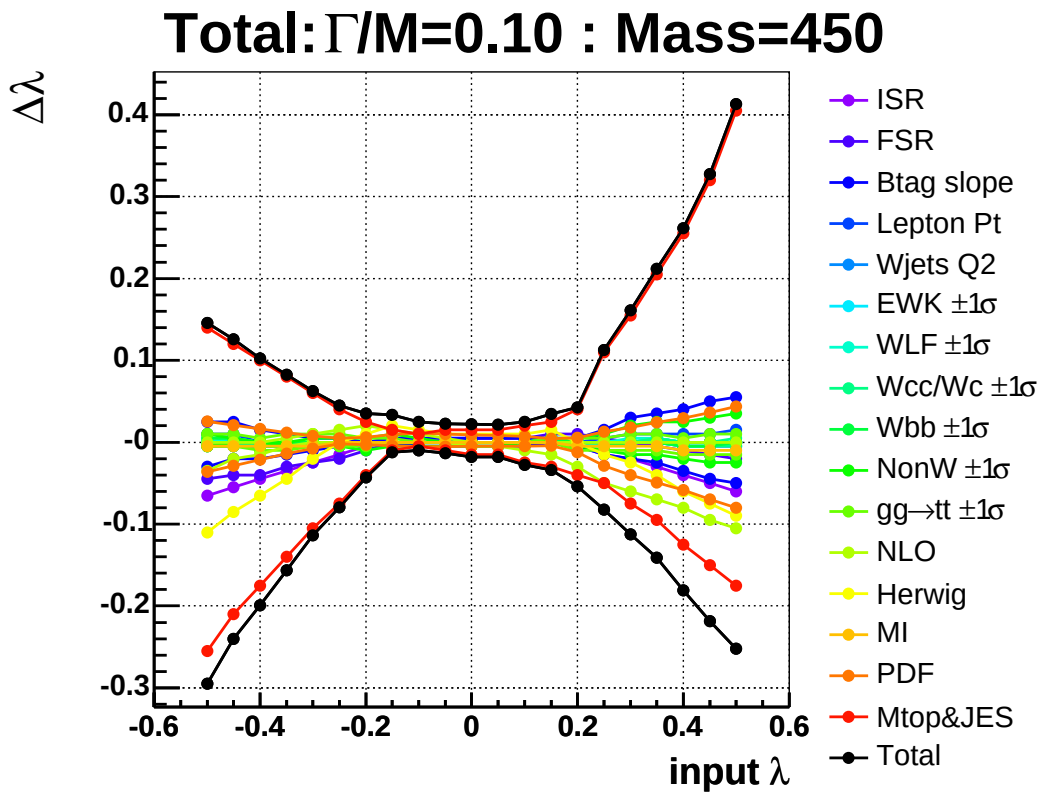

Figure 8.8: The total Systematic uncertainties as a function of true λ at the massive gluon mass is 450 GeV/c^2 and $\Gamma/M = 0.1$.

8.13 Incorporation of Systematic Uncertainties

The systematic uncertainties are incorporated into the likelihood function to calculate the 95% C.L. lower and upper limits on λ by the following way,

$$L'(\lambda) \equiv L(x) \times \int_{-\infty}^{\infty} \frac{1}{\sqrt{2\pi}\left(\frac{\Delta_-(x)+\Delta_+(x)}{2}\right)} \exp\left[-\frac{(\lambda - x)^2}{2\Delta(x)^2}\right] dx, \tag{8.2}$$

where L' is the likelihood function including the systematic uncertainties, L is the likelihood function without the systematic uncertainties (Eq. 7.9), Δ_- and Δ_+ are the negative and positive systematic errors, and Δ is Δ_- if $\lambda < x$ and Δ_+ if $\lambda > x$.

The linear functions are assumed between the estimated points of $\Delta(x)$. The likelihood function is smeared by the asymmetric Gaussian, is not integrated by the numerical way. The left plot of Fig. 8.9 shows an example of the likelihood including the systematic uncertainties for the same pseudo-data as Fig. 7.18. The right plot is an example of the "jump-up" systematic uncertainty effect due to $M_{\rm top}$ and JES: the jump-up effect gives no problem to set the limits, because the jump-up points are far away from the 95% C.L. limits (3.84 in the horizontal axis).

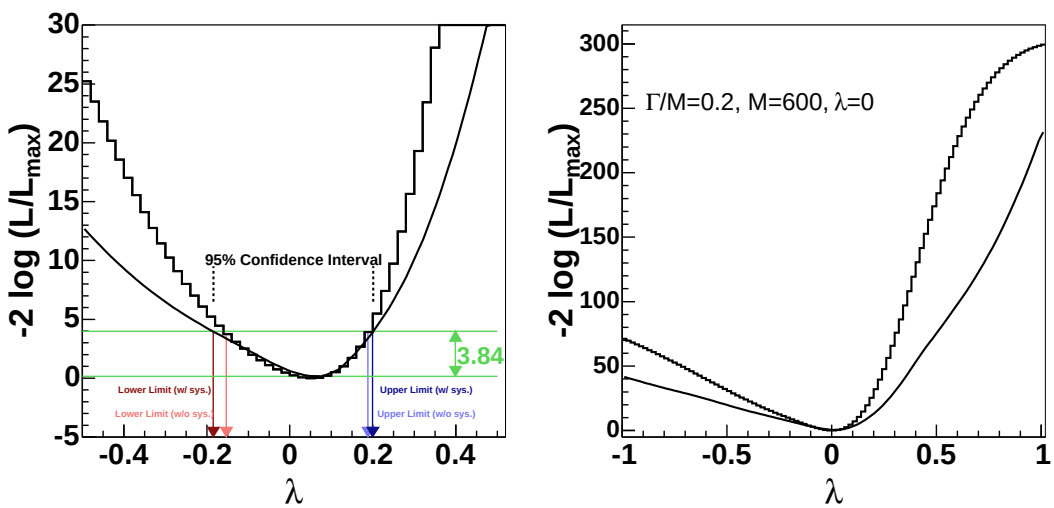

Figure 8.9: Example of the lower/upper limit shifts by the systematic uncertainties at $\Gamma/M = 0.20$, $M = 700$ GeV, $\lambda = 0$ (left) and $\Gamma/M = 0.20$, $M = 600$ GeV and $\lambda = 0$ (right). The histograms are the likelihood functions without the systematic effects, and the smooth lines are the likelihood functions with the systematic effects.

Chapter 9

Results and Conclusion

9.1 Results

The results of the massive gluon search are summarized in this section.

9.1.1 Top Pair Invariant Mass Distribution

Figure 9.1 shows the data and the standard model $t\bar{t}$ invariant mass distributions reconstructed by DLM. The Kolmogorov-Smirnov (KS) probability is 42.3%.

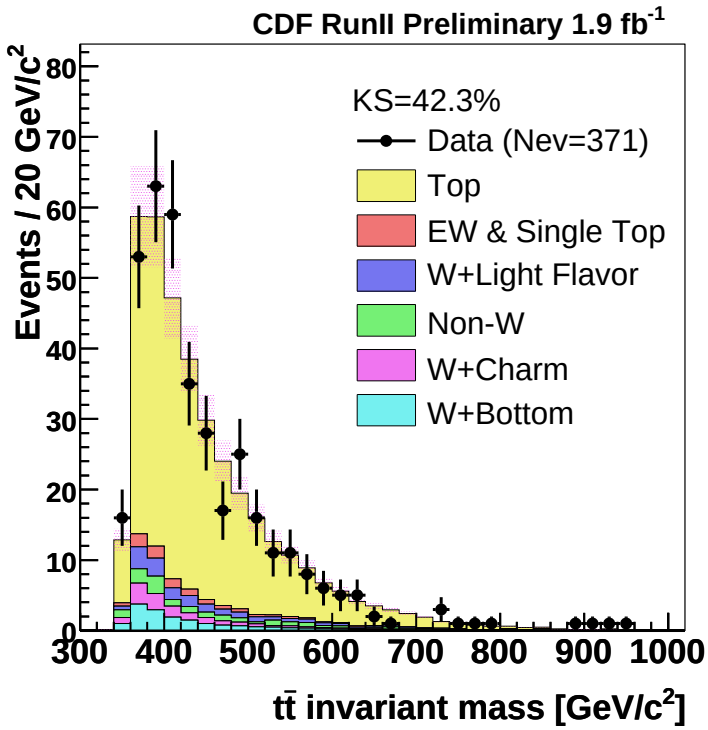

Figure 9.1: $t\bar{t}$ invariant mass distribution (black points) with SM predicted distribution (histogram). The pink hatch is the background normalization uncertainty.

9.1.2 Consistencies with the Standard Model Expectations

The left plot of Fig. 9.2 shows an example of the likelihood fit. The black points, green, blue, red lines are the data distribution with error bars, the background, the standard model, and the massive gluon $\sqrt{s_{t\bar{t}}}$ functions, respectively. The functions (lines) are normalized to the best fit numbers. The fit is performed with $M = 800$ GeV/c^2 and $\Gamma/M = 0.1$. The best fit value of λ (0.148) has the positive value because the there are more data at > 800 GeV/c^2 and less data around 650 GeV/c^2 than the standard model expectations (blue line).

The right plot of Fig. 9.2 shows the data consistency check with the standard model expectations assuming the same mass and decay width. The 10 thousands of pseudo experiments using the standard model MC are performed to know the statistical fluctuations with current amount of data. The obtained λ (0.148) is consistent with the standard model expectations at the level of $\sim 1.7\sigma$.

The same kind of consistency checks are performed by varying the mass (from 400 to 800 GeV/c^2) and the decay width (Γ/M from 0.05 to 0.50) of the massive gluon. The λs obtained from the likelihood fit are consistent with the standard model expectations, as shown in Fig. 9.3. Thus no massive gluon evidence is obtained at the explored parameter regions.

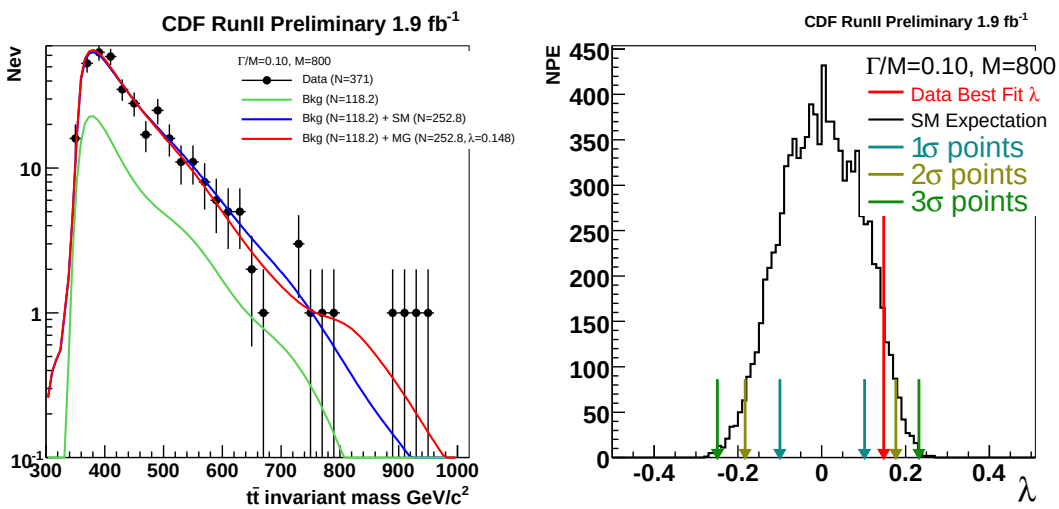

Figure 9.2: An example of the likelihood fit (left) and the consistency with the standard model from the statistical fluctuations (right).

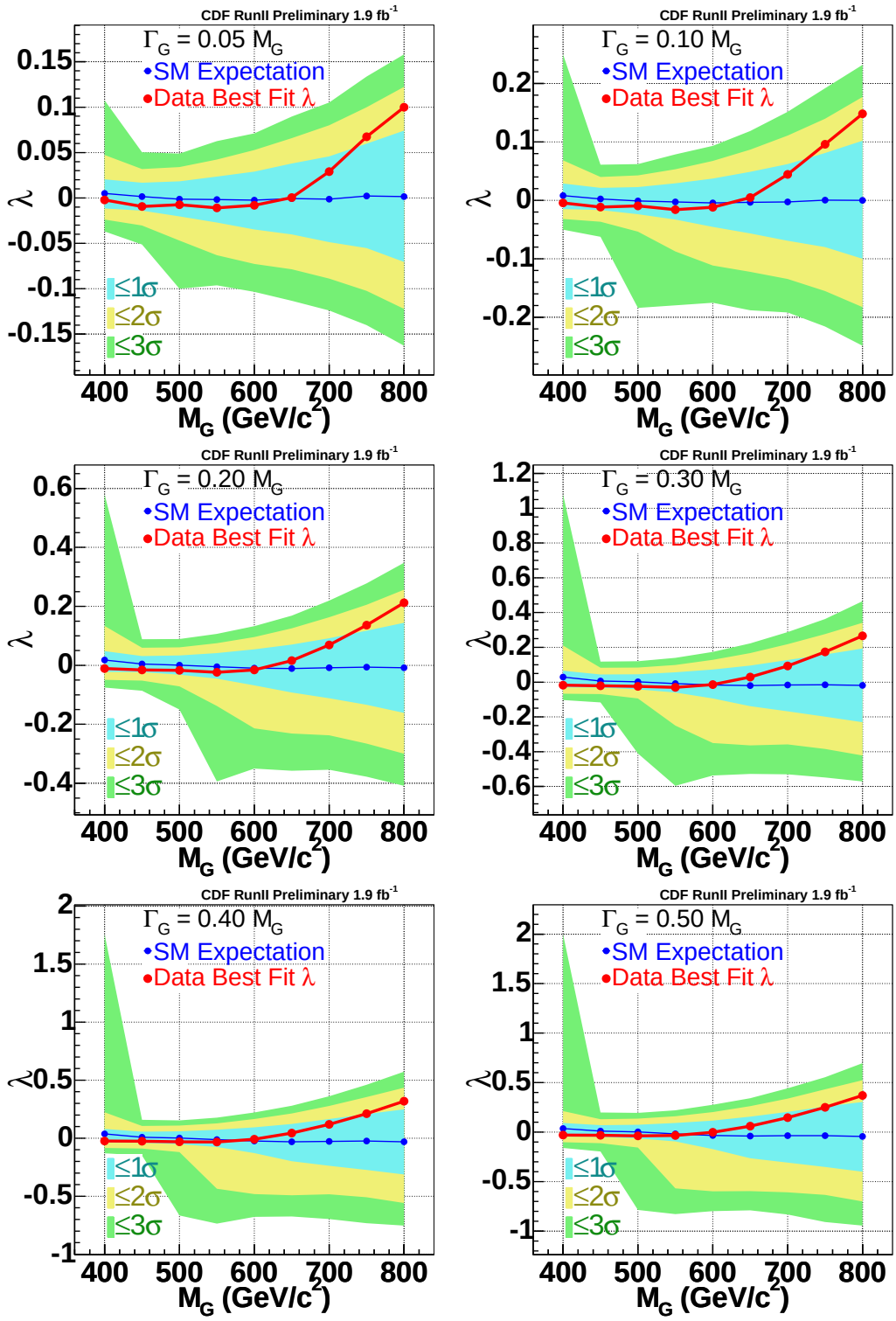

Figure 9.3: The best fitted λs of data (red) as a function of massive gluon mass for the 6 width points, $0.05 \leq \Gamma/M \leq 0.5$. The blue, light blue, yellow, green regions are the central value, 1, 2, and 3 σs from SM expectations.

9.1.3 Limits on Coupling Strength

The obtained data is consistent with the standard model predictions, thus the limits on the coupling strength are set.

Figure 9.4 is an example of the limits at $\Gamma/M = 0.1$ and $M = 800$ GeV/c^2. The left plot shows the 95% C.L. upper and lower limits on λ including the systematic uncertainties. The right plot shows the same limits obtained from data (arrows), and the expected limits from the pseudo experiments using the standard model MC (histograms). The dashed lines are the mean values of the expected limits, and the hatch regions show the mean $\pm$ RMS regions.

Figure 9.5 shows the summary plots of the 95% C.L. upper and lower limits obtained from data (blue and red points/lines) together with the expected limits by the pseudo experiments using the standard model MC (hatch regions). The yellow regions are excluded by the 1.9 fb^{-1} data obtained at CDF. The scales of limits on λ largely depend on the width. Only the white regions are allowed in 95% confidence level. The observed lower and upper limits are also summarized in Tables 9.1 and 9.2.

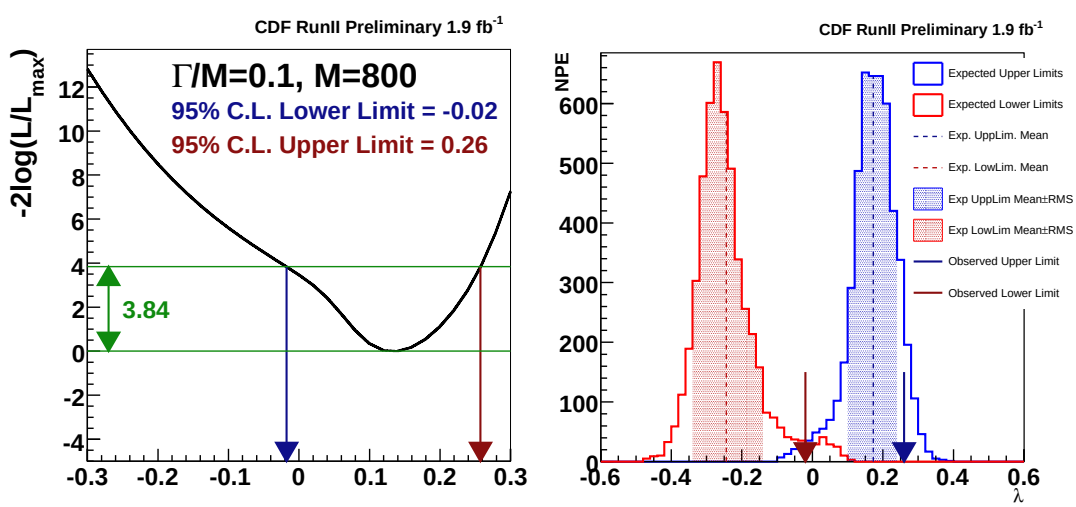

Figure 9.4: The left plot shows an example of the likelihood distribution to obtain the 95% C.L. limits at $\Gamma/M = 0.1$ and $M = 800$ GeV/c. The right plot shows the obtained limits (arrows) with the expected limits obtained by the standard model MC (histograms).

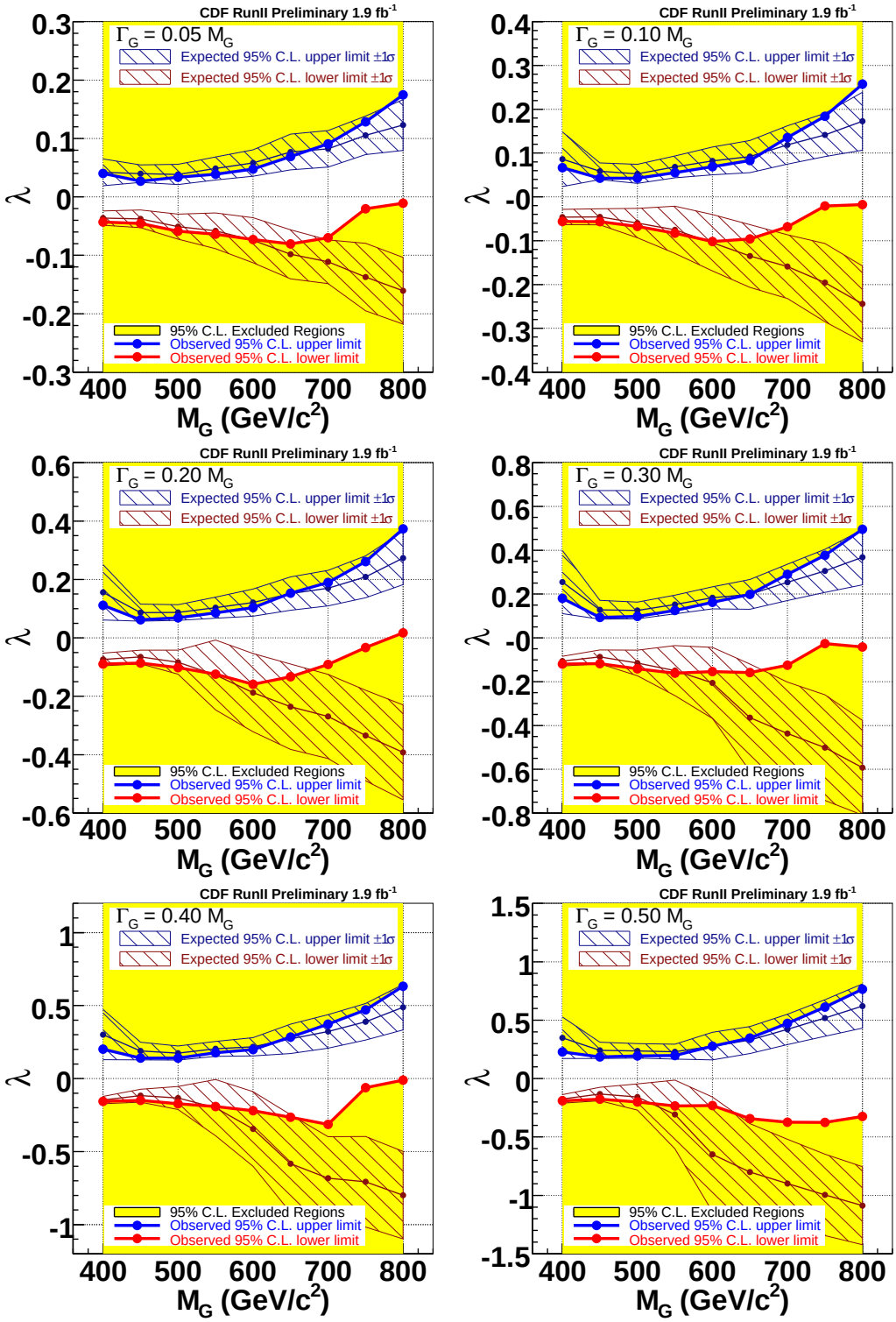

Figure 9.5: Limits on λ as a function of the massive gluon mass at each width including the systematic uncertainty effects. The yellow regions are excluded, and only the white regions are allowed in 95% confidence level.

M (GeV/c^2) \ M/Γ	0.05	0.10	0.20	0.30	0.40	0.50
400	-0.043	-0.056	-0.089	-0.12	-0.16	-0.19
450	-0.045	-0.057	-0.086	-0.12	-0.15	-0.18
500	-0.059	-0.067	-0.10	-0.14	-0.17	-0.20
550	-0.064	-0.083	-0.12	-0.16	-0.19	-0.23
600	-0.073	-0.10	-0.16	-0.15	-0.22	-0.23
650	-0.081	-0.096	-0.13	-0.16	-0.26	-0.34
700	-0.070	-0.068	-0.091	-0.13	-0.31	-0.37
750	-0.020	-0.021	-0.033	-0.026	-0.063	-0.37
800	-0.011	-0.017	0.017	-0.042	-0.011	-0.32

Table 9.1: Observed 95% C.L. lower limits

M (GeV/c^2) \ M/Γ	0.05	0.10	0.20	0.30	0.40	0.50
400	0.040	0.067	0.11	0.18	0.20	0.23
450	0.027	0.042	0.062	0.094	0.14	0.19
500	0.034	0.043	0.069	0.098	0.14	0.19
550	0.039	0.055	0.085	0.13	0.18	0.20
600	0.048	0.069	0.10	0.16	0.20	0.28
650	0.069	0.083	0.15	0.20	0.28	0.35
700	0.091	0.14	0.19	0.29	0.37	0.47
750	0.13	0.18	0.26	0.38	0.47	0.61
800	0.17	0.26	0.37	0.50	0.63	0.76

Table 9.2: Observed 95% C.L. upper limits

9.1.4 Cross Checks

The primary effect of the massive gluon appears in the top quark pair invariant mass distribution. If the massive gluon exists, the secondary effect will appear in the p_T distributions of the top quarks. The p_Ts of the top quarks are reconstructed in the same way as the top quark pair invariant mass by the DLM. There is no significant discrepancy from the standard model expectations, as shown in Fig. 9.6.

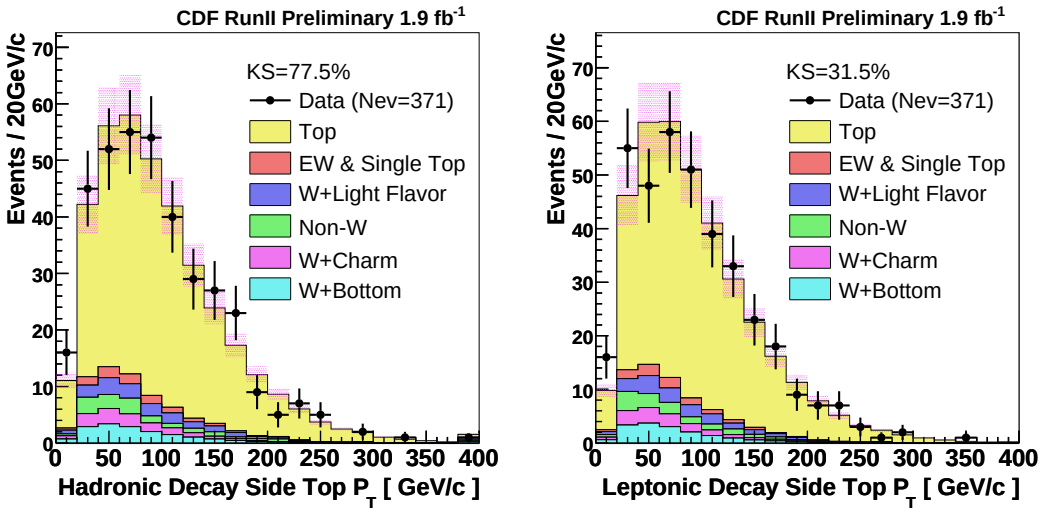

Figure 9.6: The top quark p_T distributions of data (black points) and the SM predictions (histograms) in the hadronic (left) and leptonic (right) decays.

Because the transfer functions are completely derived from the standard model MC, the transfer function response variables of data and MC are compared. Figure 9.7 shows the response variable distributions, which are obtained by taking the parton momenta with the maximum likelihood. The jet and missing E_T responses are defined as $[E_T(\text{jet}) - E_T(\text{quark})]/E_T(\text{quark})$ and $[\not{E}_T - p_T(\nu)]/p_T(\nu)$. Data and the standard model MC distributions are consistent with each other.

As a check of the likelihood of the DLM, the magnitudes of likelihood in data and the standard model MC are compared. The likelihood distributions are consistent with each other, as shown in Fig. 9.8.

The comparisons of the basic input variables used in the event selection and DLM between data and the standard model expectations are shown in Appendix D.

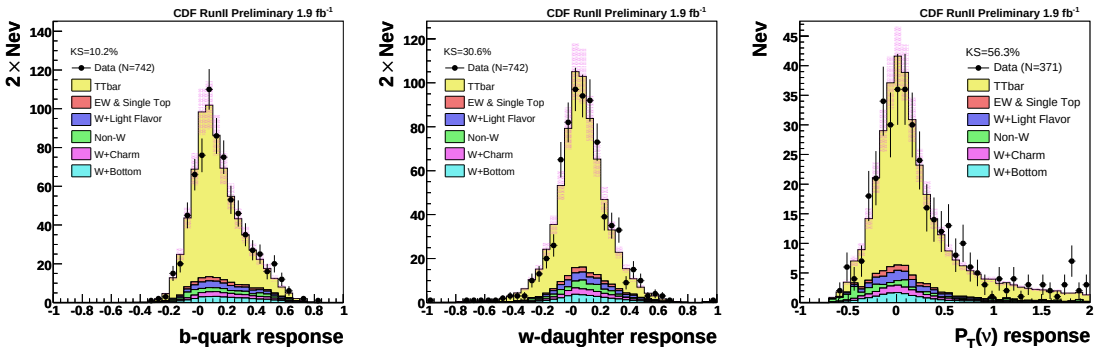

Figure 9.7: The data (black points) and the standard model MC (histograms) most probable response variables of E_T of b-quark (left), light-quark (middle), and the p_T of neutrino (right).

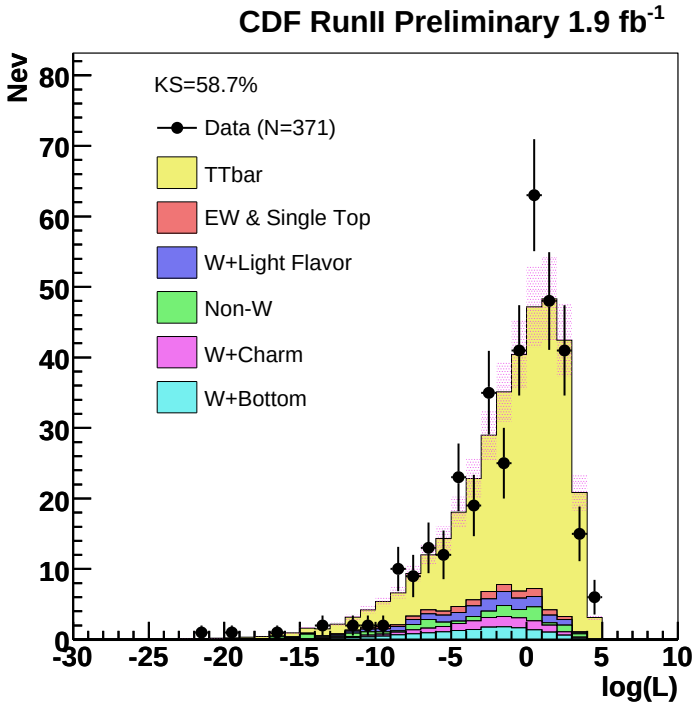

Figure 9.8: The likelihood distributions of data (black points) and the standard model MC (histogram).

9.2 Conclusion

The top quark pair production mechanism is studied through the $t\bar{t}$ production cross section and the top quark mass measurements, and the search for new particle decaying to $t\bar{t}$. The CDF RunII high p_T lepton dataset are used up to 1.9 fb^{-1} of data. The top quark pair production cross section is measured using two different b-tagging algorithms. The results are roughly 1σ higher than the standard model expectation of 6.7 pb at the top mass of 175 GeV/c^2. The top quark mass is measured using the W boson mass constraint to reduce the jet energy scale uncertainty, which was the largest systematic uncertainty at the previous measurement of the top quark mass by DLM [54]. The search for the massive gluon is performed using the DLM. The observed $t\bar{t}$ invariant mass distribution is consistent with the standard model predictions. The fitted massive gluon coupling strengths are consistent with the standard model predictions for the wide range of the mass and width within the statistical fluctuation. The upper and lower limits are set on the coupling strength of the massive gluon.

The large uncertainty of the top quark pair production cross section measurement is caused by the background estimation, especially in the W+jets process due to the poor knowledge of the higher order cross sections. There have been the recent results which can reduce the uncertainty of the W+jets estimation by measuring the cross section of W+heavy flavor ($b\bar{b}$, $c\bar{c}$ and $1c$) process independently. The Wc production cross section is measured using the soft-lepton-tagging technique using the fact that the charge of lepton from W boson decay and the charge from semi-leptonic decay of charm meson are opposite [67]. The W+$b\bar{b}$ production cross section is measured by looking at the mass distribution of b-tagged jets using the heaviness of the bottom hadron mass [68].

The systematic uncertainty of the top quark mass measurement is dominant uncertainty, which can not be improved by increasing the amount of data. Since the analysis technique itself is now mature enough, more efforts to reduce the systematic uncertainty are necessary for a more precise measurement of the top quark mass.

The search for the massive gluon decaying to $t\bar{t}$, which interfere with the standard model top quark pair production process, is the first attempt in the world. Although there is no evidence of the massive gluon using the current data, the massive gluon could still exist outside the range of explored parameter regions. Tevatron provides the unique opportunity of the search for the new particle decaying to $t\bar{t}$ in the $q\bar{q}$ annihilation process, because gg fusion process is dominant at the upcoming LHC experiment. Tevatron will provide more than three times of data analyzed in this dissertation, and our hope is to improve the search limit or to find the evidence of the massive gluon using data from the CDF RunII experiment. The heaviness of the top quark mass is still a mystery, and the existence of a new particle could explain it and open the window to physics beyond the standard model.

Appendix A

Massive Gluon Probability Density Functions

The reconstructed top quark pair invariant mass ($\sqrt{s_{t\bar{t}}}$) probability density function (p.d.f) is parameterized by Eq.(7.1). There are 3 parameters (decay width, mass, and coupling strength) of the massive gluon. The $\sqrt{s_{t\bar{t}}}$ p.d.fs in the quark pair annihilation of the standard model (SM) plus the massive gluon (MG) with the interference effects are shown in this appendix (Figs. A.1-A.6) for the various parameter points in Table A.1. The positive and negative λ cases are shown separately. In these p.d.fs, the enhancements at $\sqrt{s_{t\bar{t}}} > M$ ($\sqrt{s_{t\bar{t}}} < M$) and the suppressions at $\sqrt{s_{t\bar{t}}} < M$ ($\sqrt{s_{t\bar{t}}} > M$) are seen if λ is positive (negative). The reconstruction effect smears these characteristics. The black lines in the plots show the standard model p.d.f. The effects in the top quark pair invariant mass shape are larger with smaller mass and smaller decay width at the same coupling strength (λ), and vice versa.

Γ/M	Range of λ	M (GeV/c^2)
0.05 (Fig. A.1)	$[-0.5, 0.5]$	$[400, 800]$
0.10 (Fig. A.2)	$[-0.5, 0.5]$	$[400, 800]$
0.20 (Fig. A.3)	$[-1.0, 1.0]$	$[400, 800]$
0.30 (Fig. A.4)	$[-1.0, 1.0]$	$[400, 800]$
0.40 (Fig. A.5)	$[-1.5, 1.5]$	$[400, 800]$
0.50 (Fig. A.6)	$[-1.5, 1.5]$	$[400, 800]$

Table A.1: The parameter regions of the massive gluon p.d.fs in Figs. A.1-A.6.

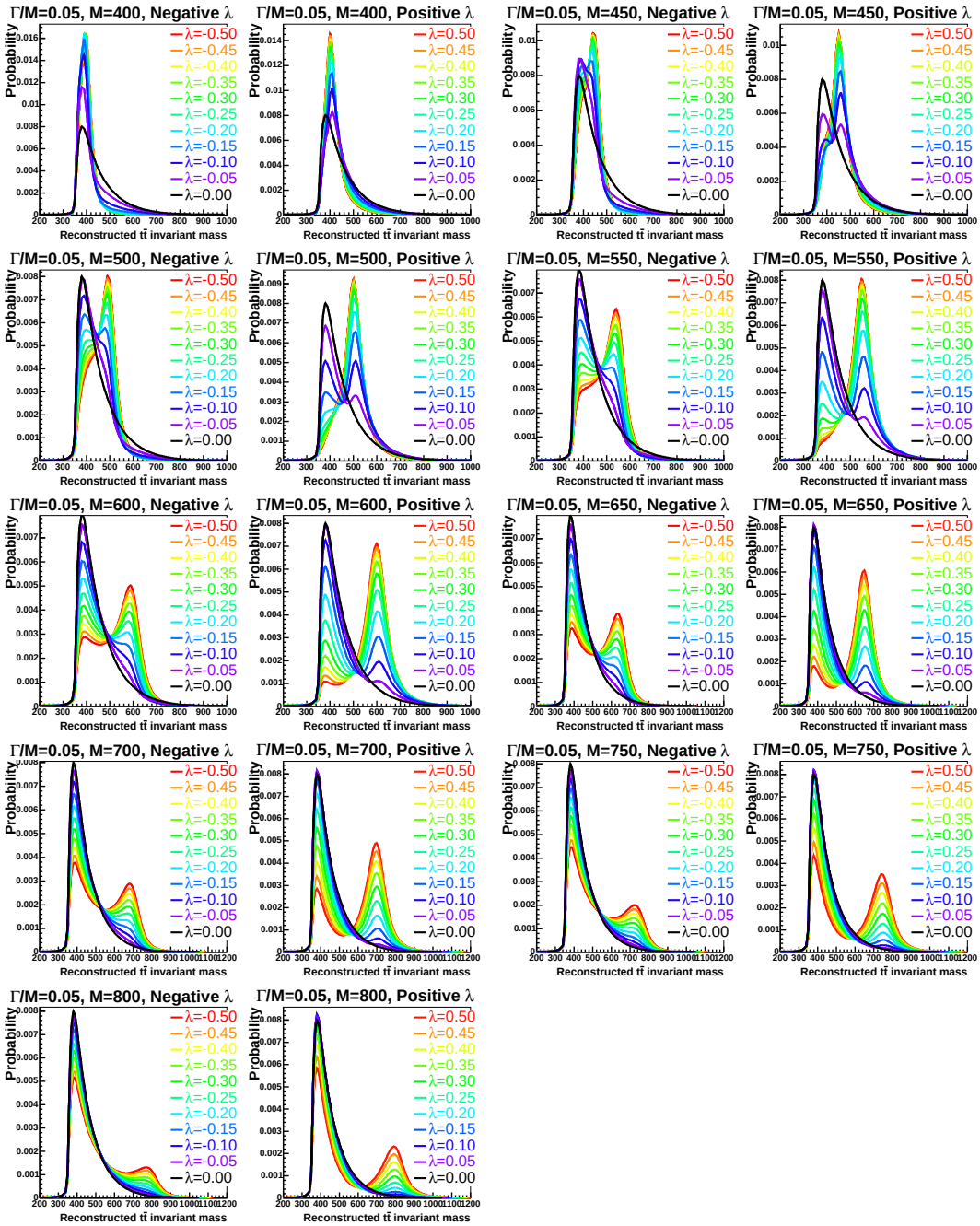

Figure A.1: The SM+MG reconstructed $\sqrt{s_{t\bar{t}}}$ p.d.fs with $\Gamma/M = 0.05$.

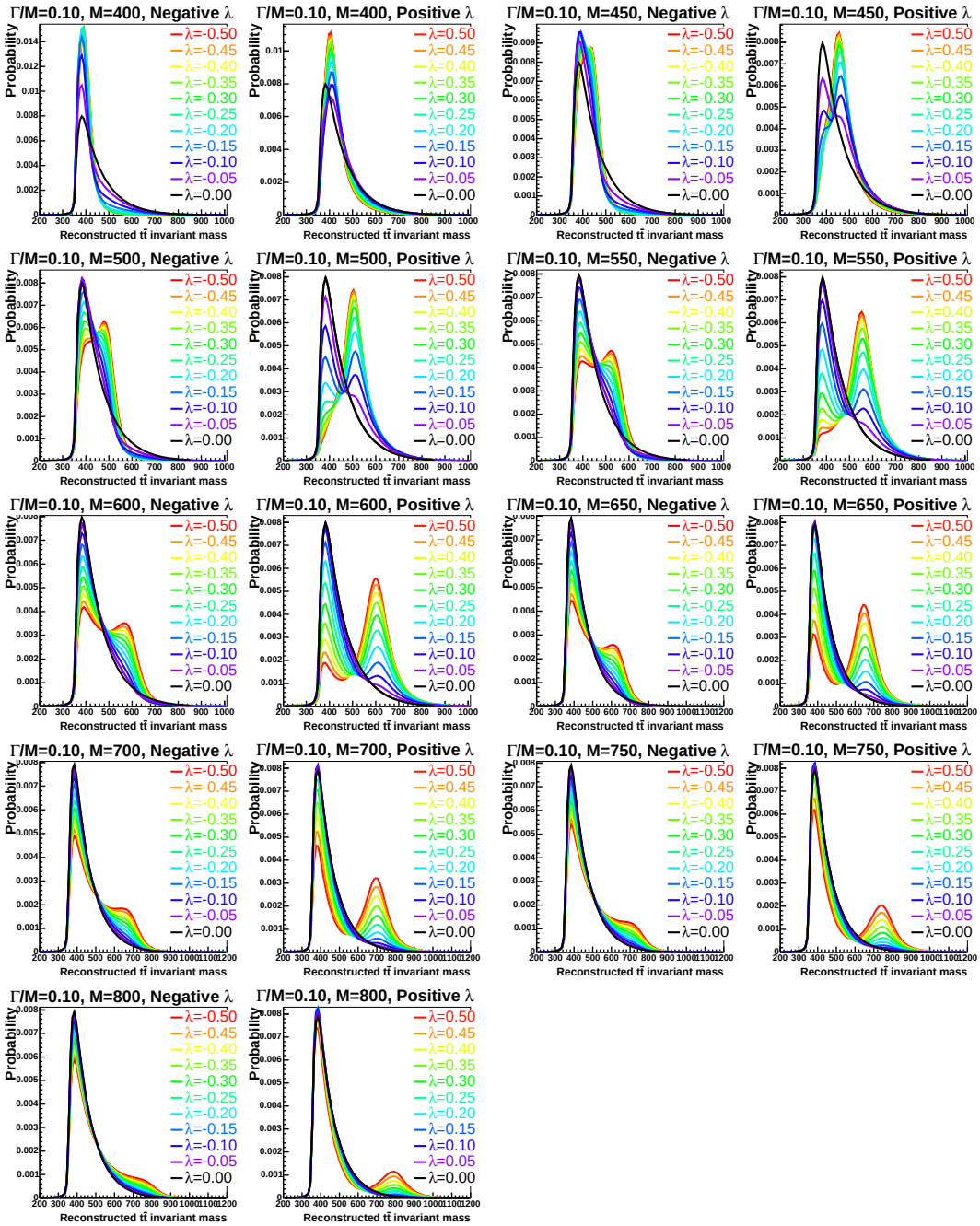

Figure A.2: The SM+MG reconstructed $\sqrt{s_{t\bar{t}}}$ p.d.fs with $\Gamma/M = 0.10$.

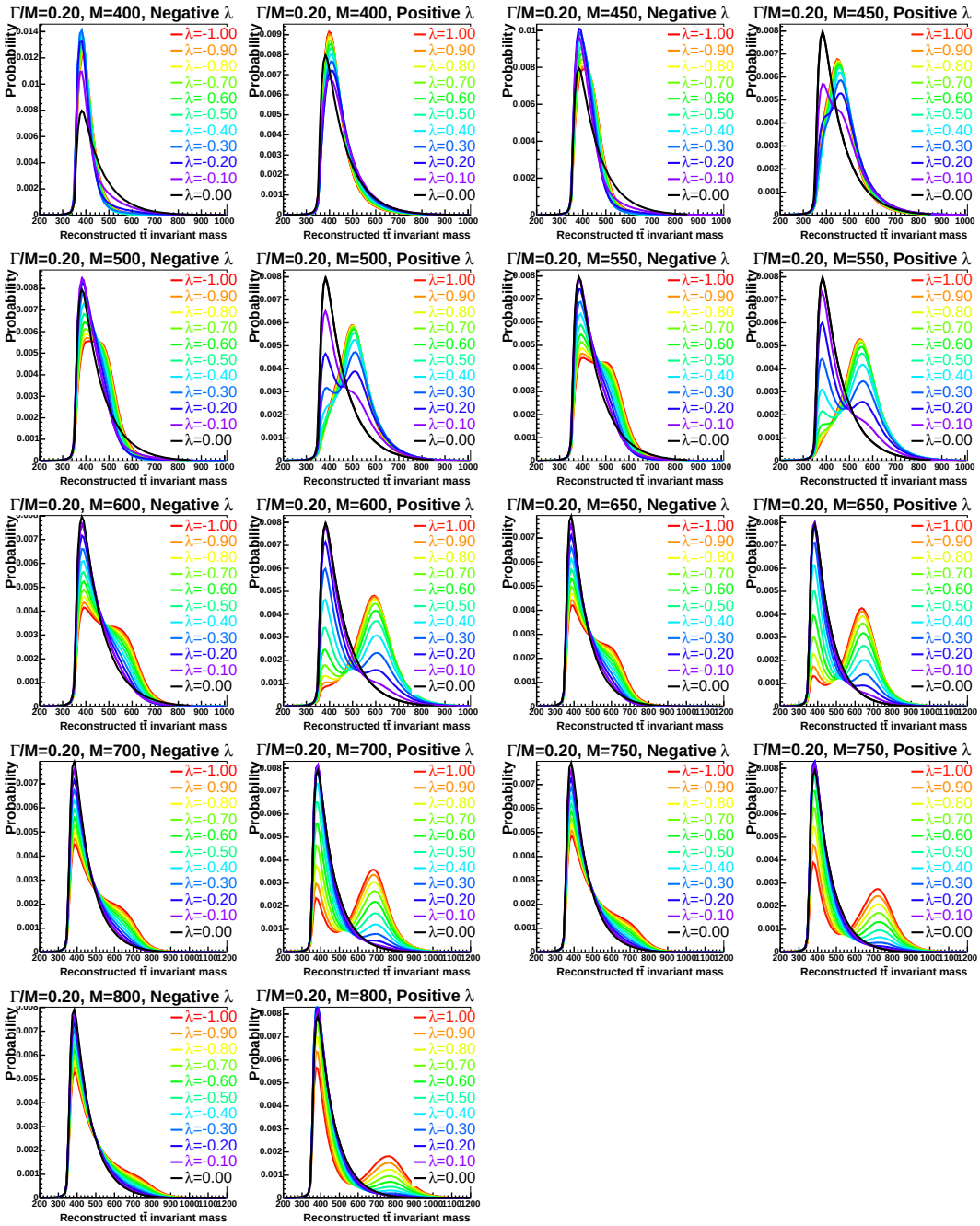

Figure A.3: The SM+MG reconstructed $\sqrt{s_{t\bar{t}}}$ p.d.fs with $\Gamma/M = 0.20$.

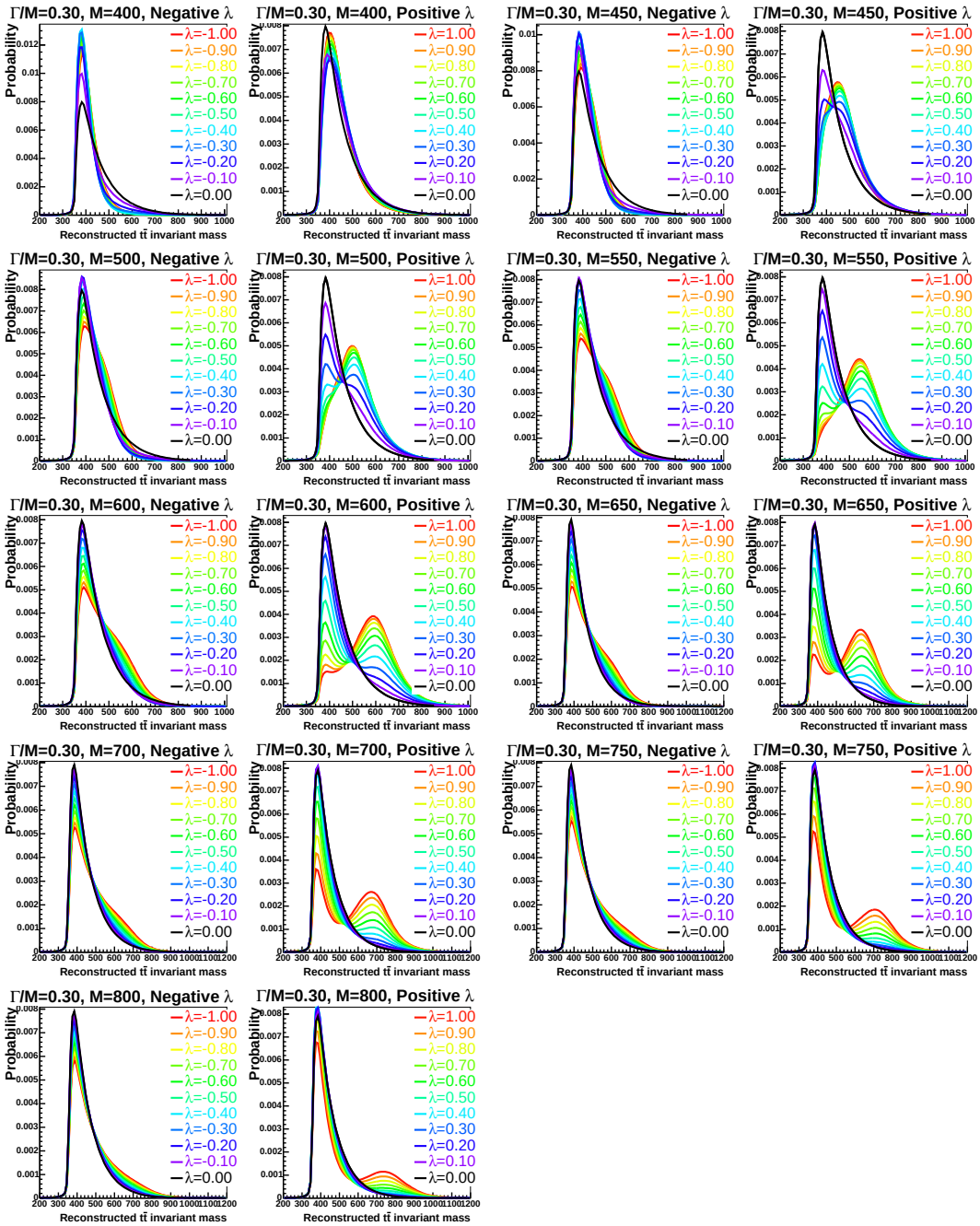

Figure A.4: The SM+MG reconstructed $\sqrt{s_{t\bar{t}}}$ p.d.fs with $\Gamma/M = 0.30$.

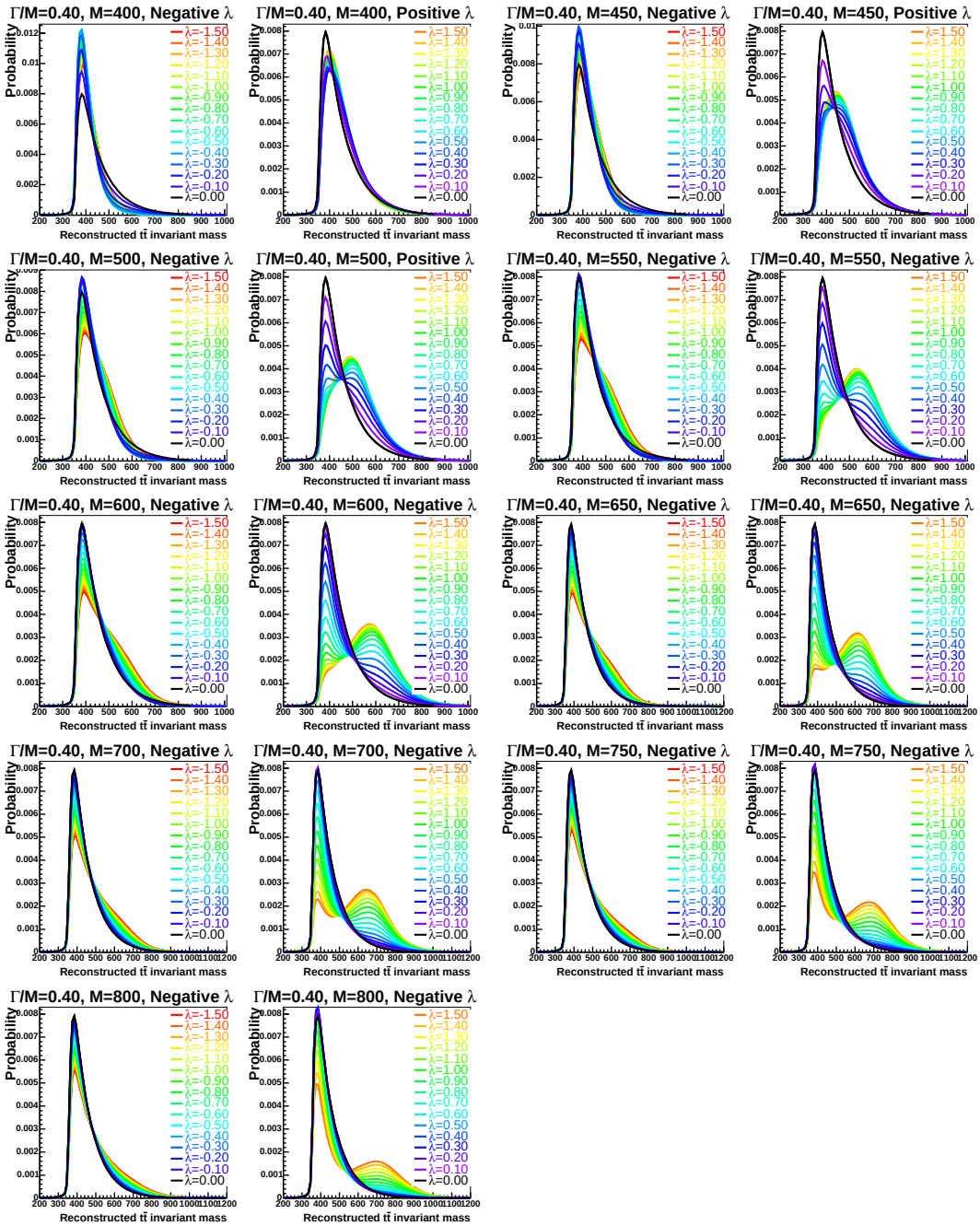

Figure A.5: The SM+MG reconstructed $\sqrt{s_{t\bar{t}}}$ p.d.fs with $\Gamma/M = 0.40$.

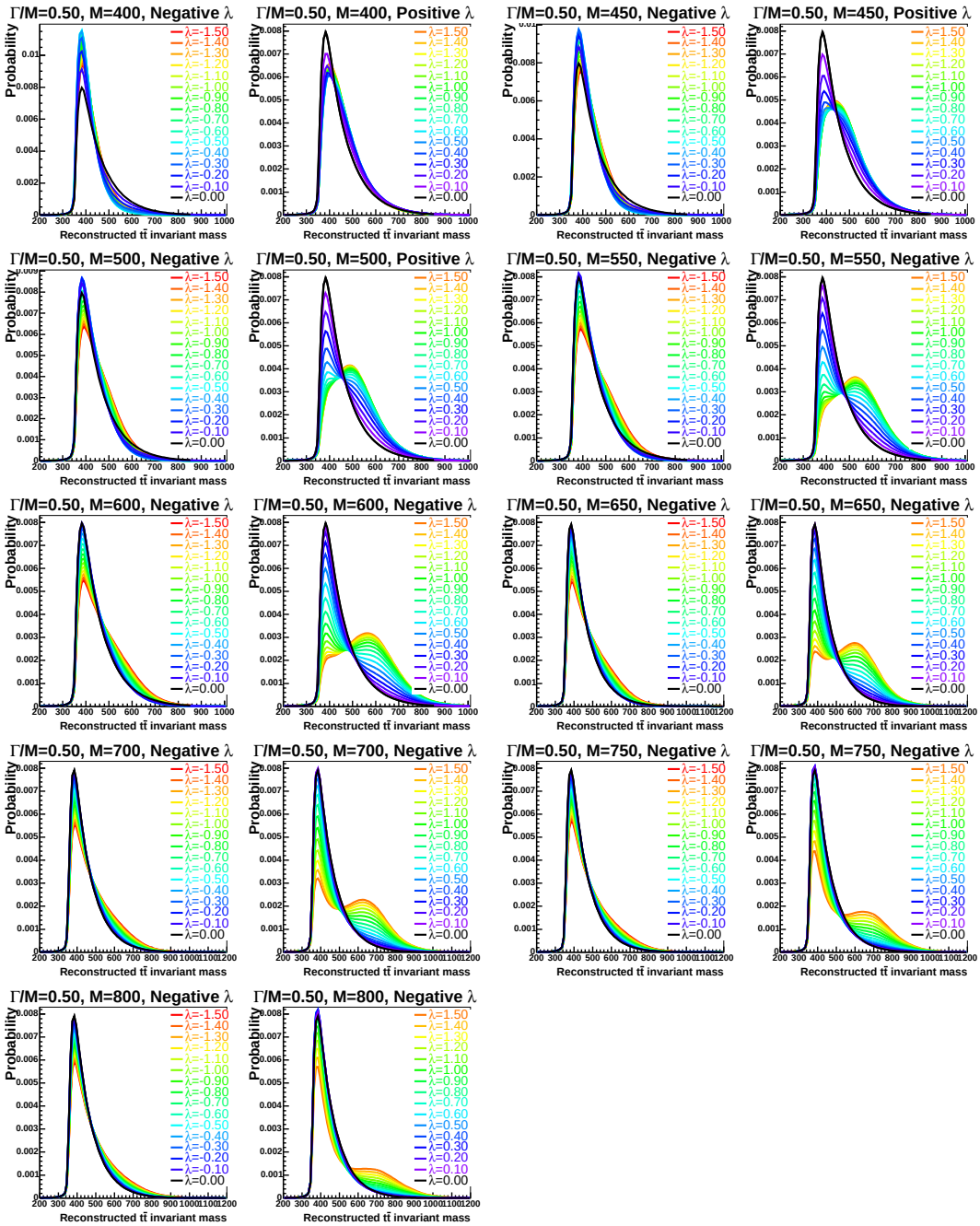

Figure A.6: The SM+MG reconstructed $\sqrt{s_{t\bar{t}}}$ p.d.fs with $\Gamma/M = 0.50$.

Appendix B

Monte Carlo Re-weighting

The difference between the standard model and the massive gluon process is only in the production matrix element. Thus, the standard model Monte Carlo sample is re-weighted, instead of generating Monte Carlo sample for the huge parameter space. The weight is simply production matrix ratio (MG/SM) in Eq.(7.3). Figures B.1 and B.2 are the comparisons of the generated massive gluon and the re-weighted standard model distributions of the reconstructed $\sqrt{s_{t\bar{t}}}$ and observed level p_T. The generated and re-weighted distributions agree well as shown in the plots (Various other low level quantities not shown here also agree). The re-weighting technique is used especially in the studies of systematic uncertainties, because there are many sources of systematic uncertainties and the many explored massive gluon parameters.

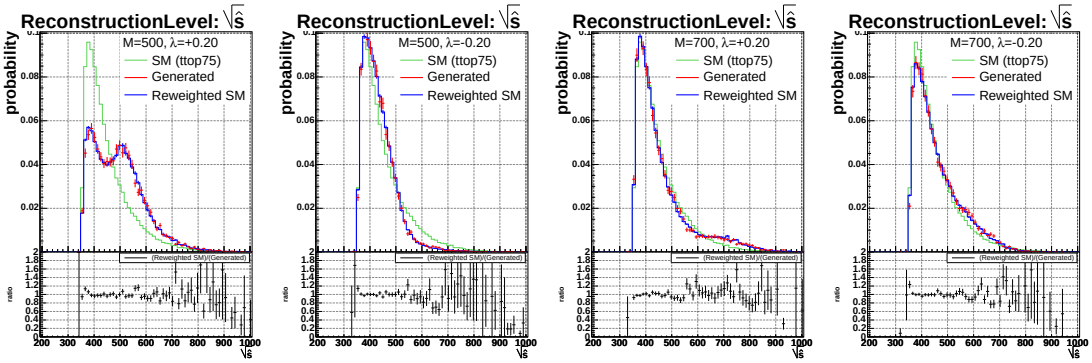

Figure B.1: The standard model (green), generated (red) and re-weighted (blue) reconstructed $\sqrt{s_{t\bar{t}}}$ distributions with $\lambda = \pm 0.2$, $M = 500, 700$ GeV$/c^2$, and $\Gamma/M = 0.2$. Each bottom plot shows the (re-weighted)/(generated) ratio.

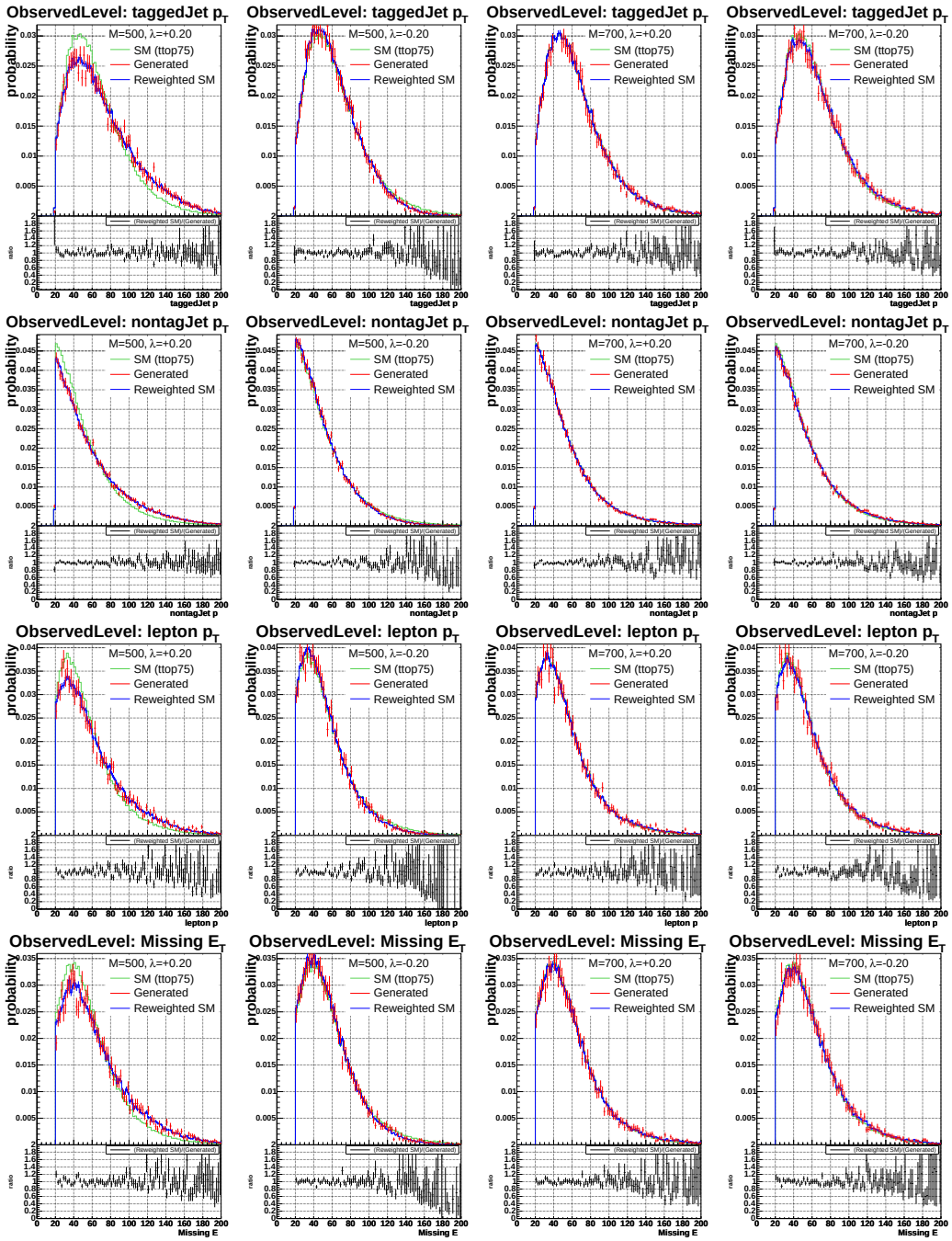

Figure B.2: The standard model (green), generated (red) and re-weighted (blue) observed level p_T distributions with $\lambda = \pm 0.2$, $M = 500, 700$ GeV/c^2, and $\Gamma/M = 0.2$. Each bottom plot shows the (re-weighted)/(generated) ratio.

Appendix C

All Systematic Uncertainties

All the systematic uncertainties are shown in Figs. C.1-C.6 at the parameter points in Table 8.2. The black points/lines show the total uncertainties ($\Delta\lambda$) as a function of true λ. There are some "jump-up" points at the large λs in these plots. These jump-ups do not affect the final results of the lower and upper limits on the coupling strength, because the obtained λs are close to 0 and the obtained limits are away from the jump-ups. The meanings of the words at the right of each plot are summarized in Table C.1. The contributions from the uncertainty of top quark mass and the jet energy scale are large as a whole. The contributions from the difference between LO and NLO are large at the large mass. The contributions from the PDF uncertainty are large at the large decay width.

Abbreviation	Meaning
ISR	Initial state radiation uncertainty
FSR	Final state radiation uncertainty
Btag slope	Uncertainty on E_T dependence of b-tagging efficiency
Lepton PT	Uncertainty on lepton p_T measurement
Wjets Q2	Uncertainty on Q^2 definition in $W + b\bar{b}$ process
EWK $\pm 1\sigma$	Uncertainties on the electroweak background processes
WLF $\pm 1\sigma$	Uncertainty on the W+light flavors background process
Wcc/Wc $\pm 1\sigma$	Uncertainty on the W+charm quarks background process
Wbb $\pm 1\sigma$	Uncertainty on the W+bottom quarks background process
NonW $\pm 1\sigma$	Uncertainty on the QCD fake background process
$gg \to t\bar{t}$ $\pm 1\sigma$	Uncertainty on the $gg \to t\bar{t}$ background process
NLO	Difference between LO and NLO
Herwig	Difference between PYTHIA and HERWIG
MI	Uncertainty on the multiple interaction
PDF	Uncertainty on the parton distribution function
Mtop&JES	Correlated uncertainty on top quark mass and jet energy scale
Total	Addition of all the contributions quadratically

Table C.1: The meanings of the abbreviations in Figs. C.1-C.6.

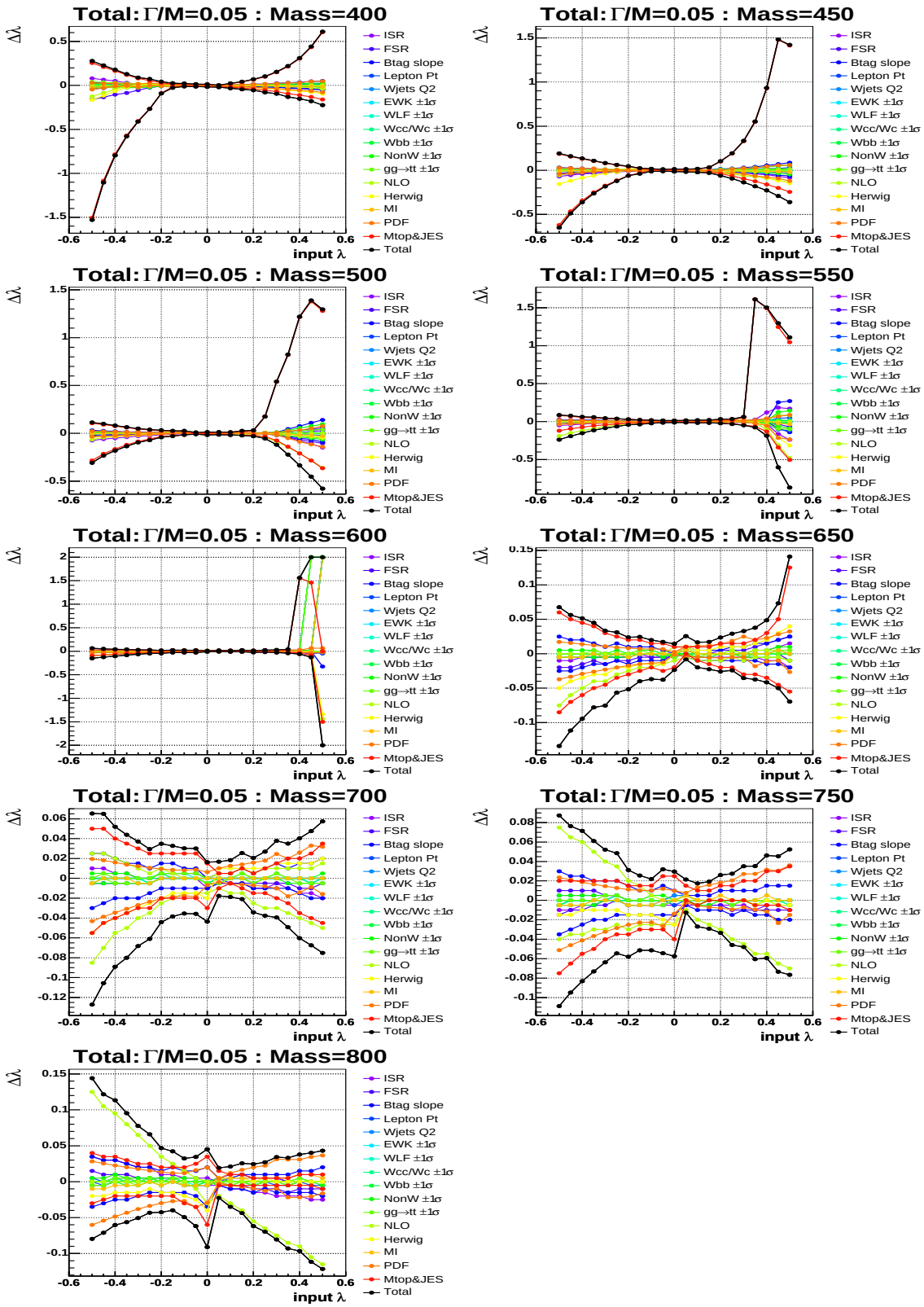

Figure C.1: Total systematic uncertainties as a function of true λ at $\Gamma/M = 0.05$.

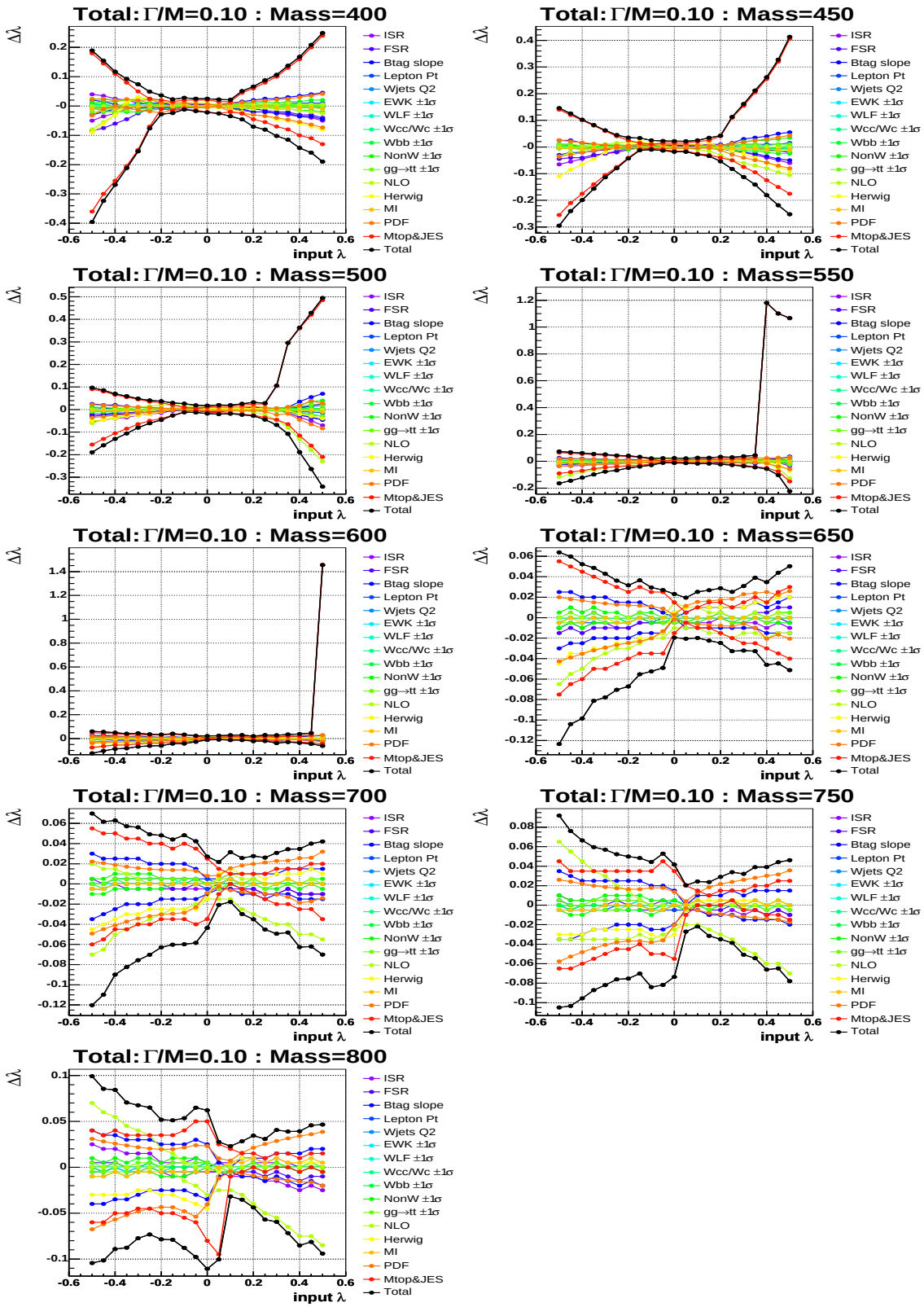

Figure C.2: Total systematic uncertainties as a function of true λ at $\Gamma/M = 0.10$.

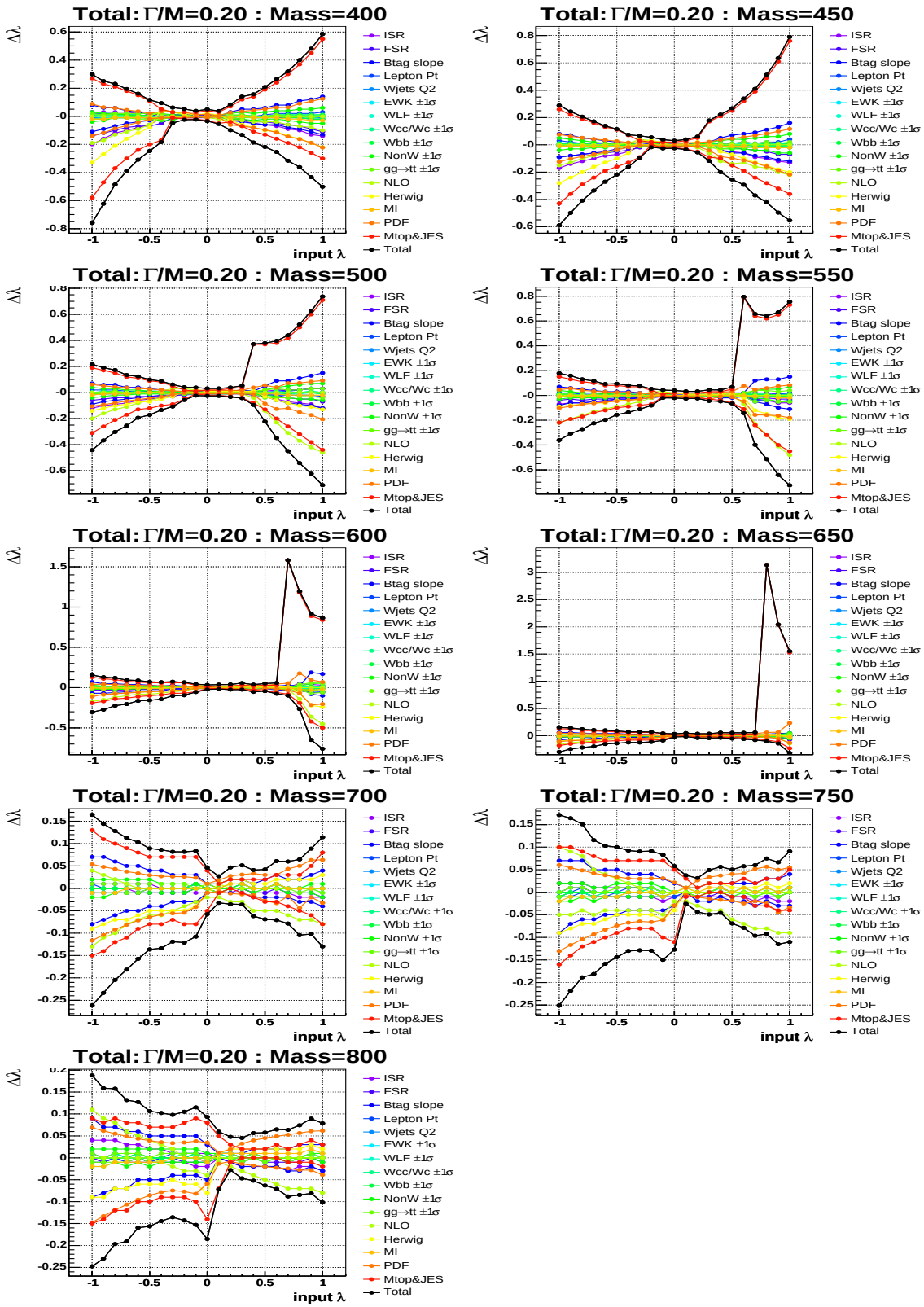

Figure C.3: Total systematic uncertainties as a function of true λ at $\Gamma/M = 0.20$.

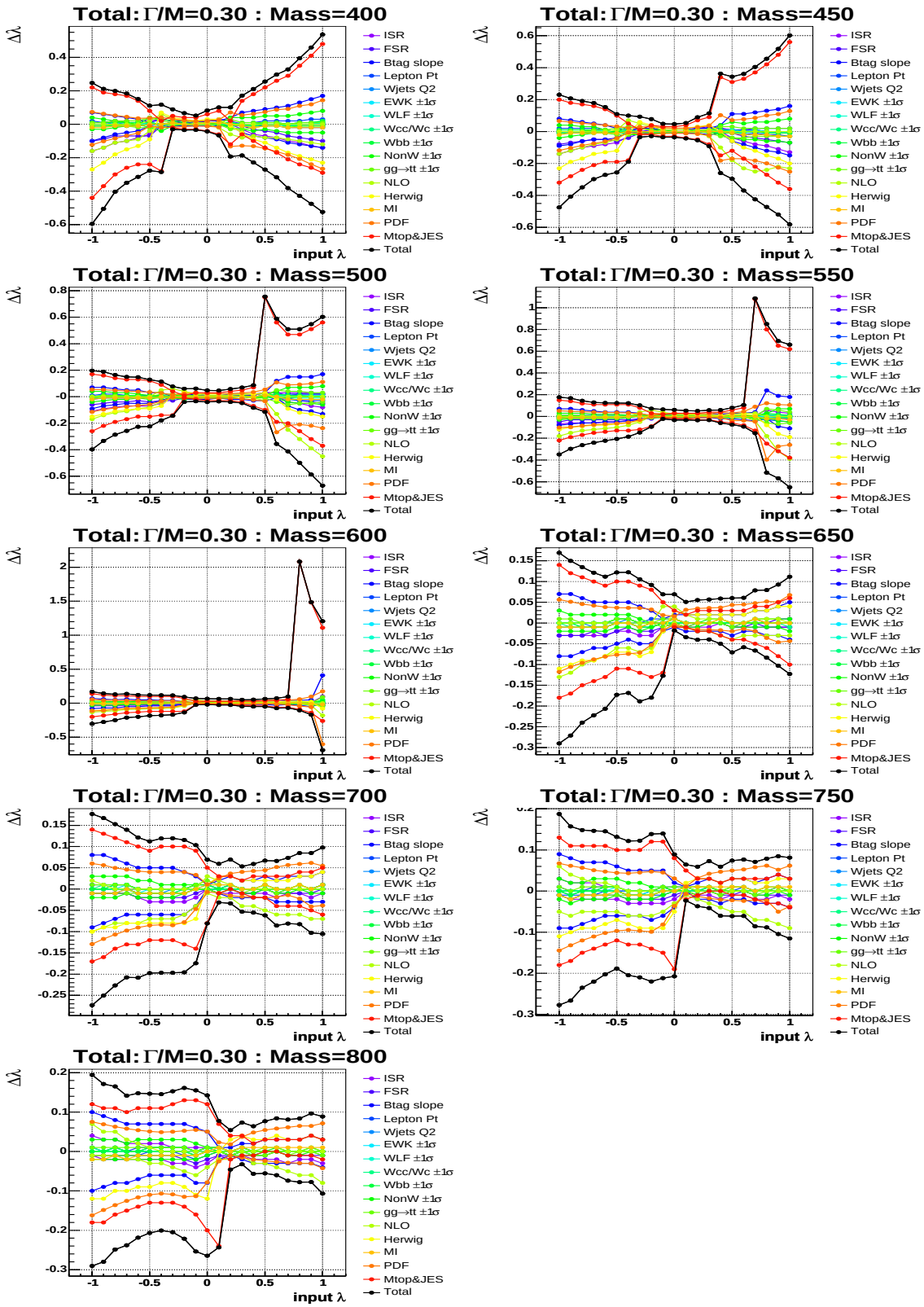

Figure C.4: Total systematic uncertainties as a function of true λ at $\Gamma/M = 0.30$.

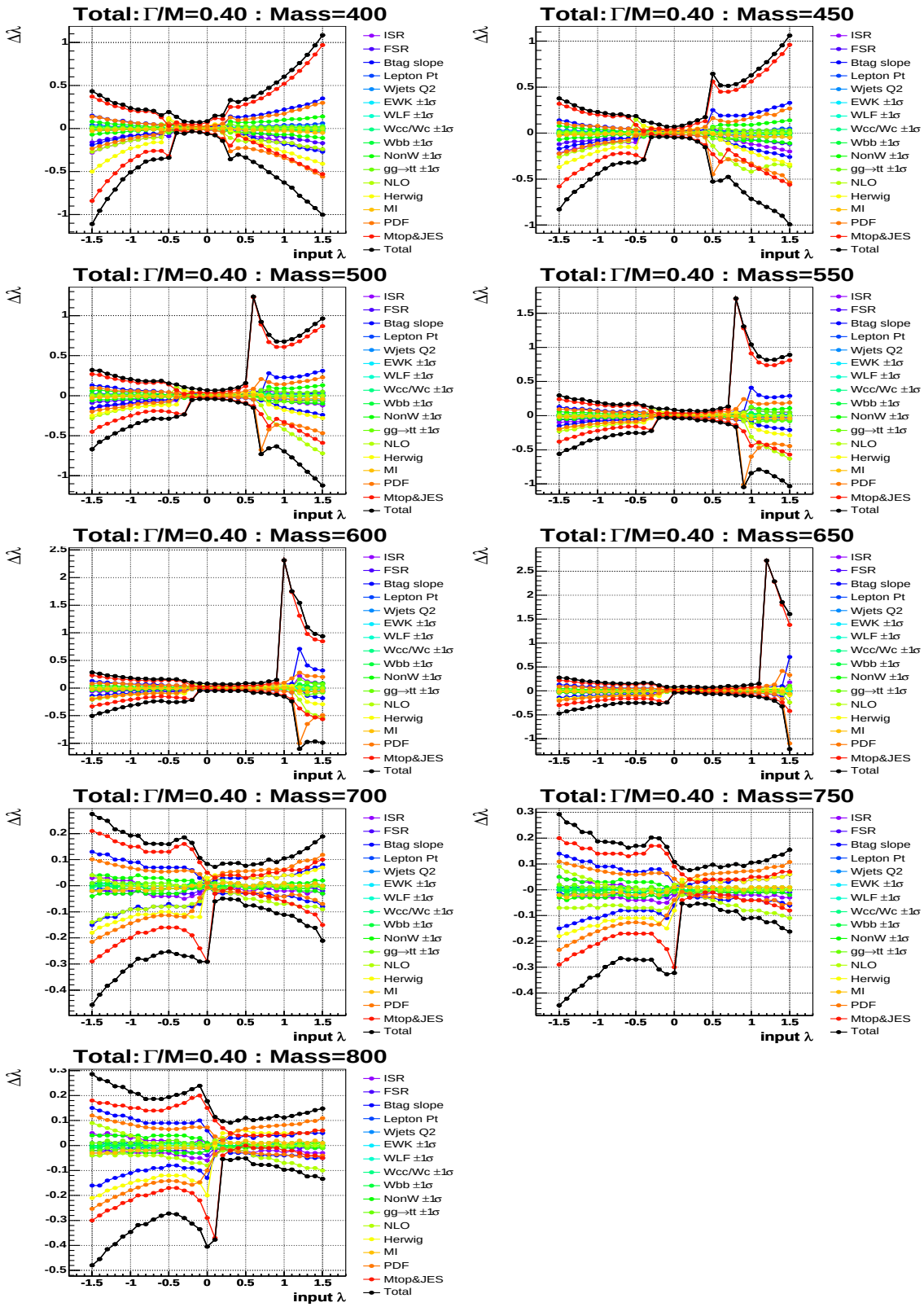

Figure C.5: Total systematic uncertainties as a function of true λ at $\Gamma/M = 0.40$.

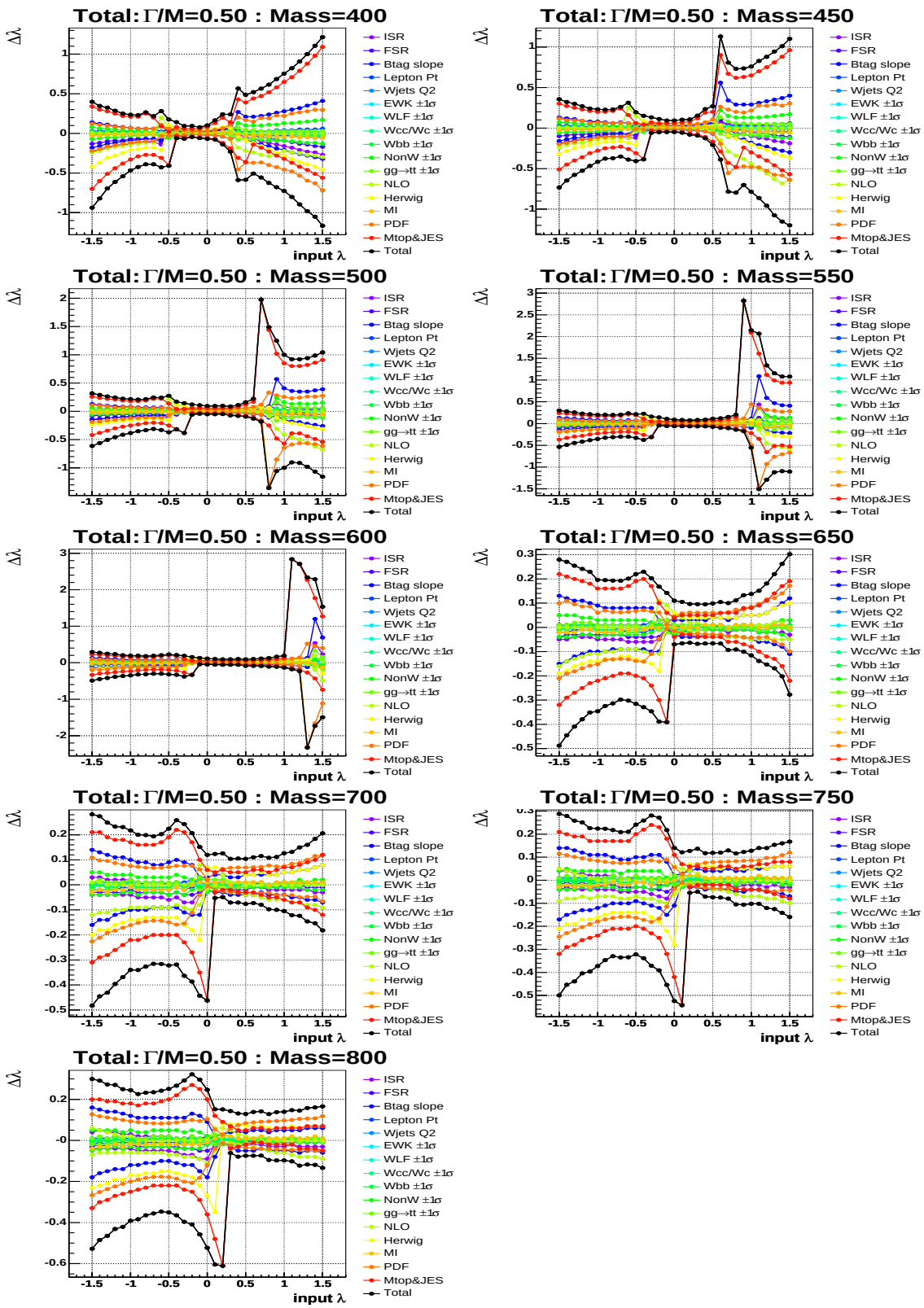

Figure C.6: Total systematic uncertainties as a function of true λ at $\Gamma/M = 0.50$.

Appendix D

Comparison between Data and Simulations

In this appendix, the basic observed quantities are compared between data and the standard model MC after the lepton+jet event selections. Any significant discrepancy indicate the mis-modeling of CDF detector simulations or the existence of new physics. The distributions of data and the SM modeling agree well as a whole, which reflects the quality of CDF simulations.

Figure D.1 shows the E_T, η(physics), η(detector), ϕ, and EM fraction distributions of the tight jets ($E_T \geq 20$ GeV, $|\eta(\text{det.})| \leq 2.0$) with the order of jet E_T.

Figure D.2 shows the E_T, η(detector), ϕ, and EM fraction distributions of b-tagged jets.

Figure D.3 shows the vertex $c\tau$, mass, χ^2, p_T, L_{xy}, and number of good tracks distributions related to the $SecVtx$ tagging obtained from the b-tagged jets.

Figure D.4 shows the p_T, η, ϕ, and charge distributions of leptons (electrons and muons). The bumpy distributions of η and ϕ come from the fiducial volume of the detector coverages.

Figure D.5 shows the missing E_T, ϕ of $\not\!\!E_T$, W transverse mass, and H_T (the scalar sum of E_T of jets, p_T of lepton, and missing E_T) distributions.

Figure D.6 shows the distributions of number of vertices, z of primary vertex, and the difference between z_0 of lepton and z of primary vertex. The number of vertices distribution shows the significant discrepancy between data and the simulations. This is because the increasing performance of the Tevatron makes the more multiple interactions and MC simulation could not catch up with its performance. This discrepancy is covered as the systematic uncertainty in the multiple interaction modeling.

Figure D.7 shows the ΔR distributions. All the possible combinations from the lepton and 4 jets are listed.

Figure D.8 shows the $\Delta\phi$ distributions. All the possible combinations from the lepton, missing E_T, and 4 jets are listed.

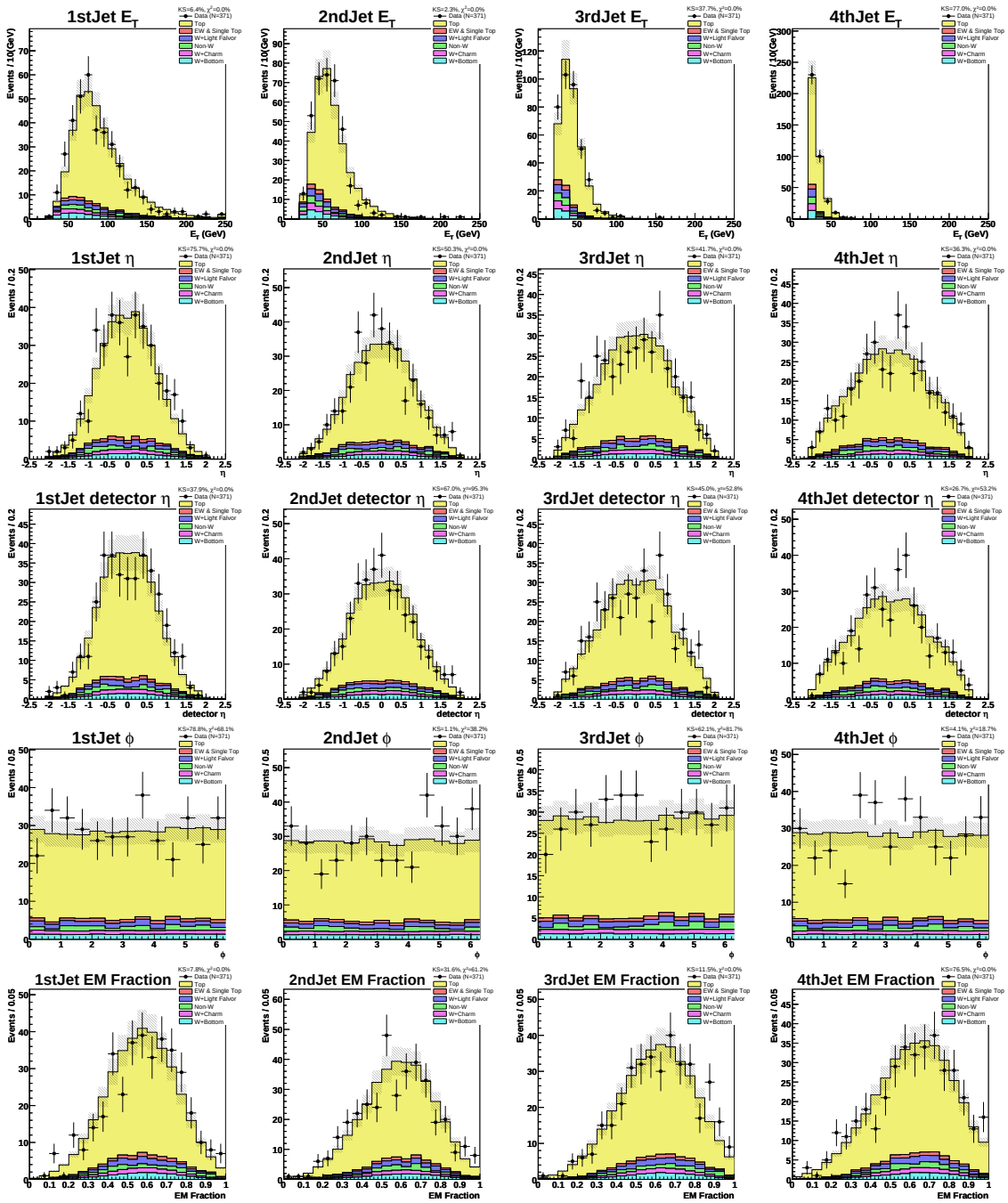

Figure D.1: Kinematic distributions of tight jets.

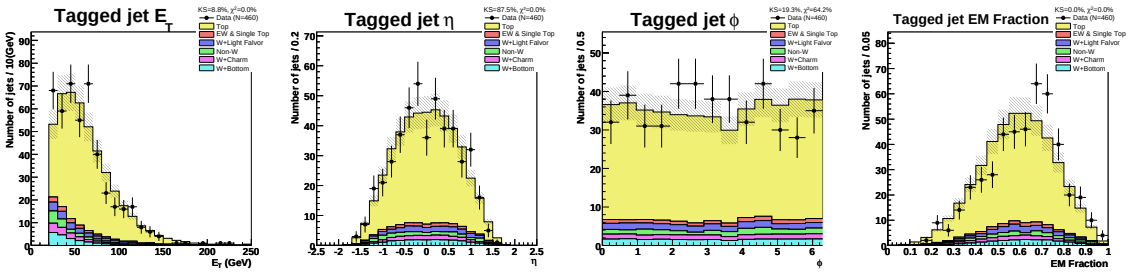

Figure D.2: *SecVtx* b-tagged jet distributions.

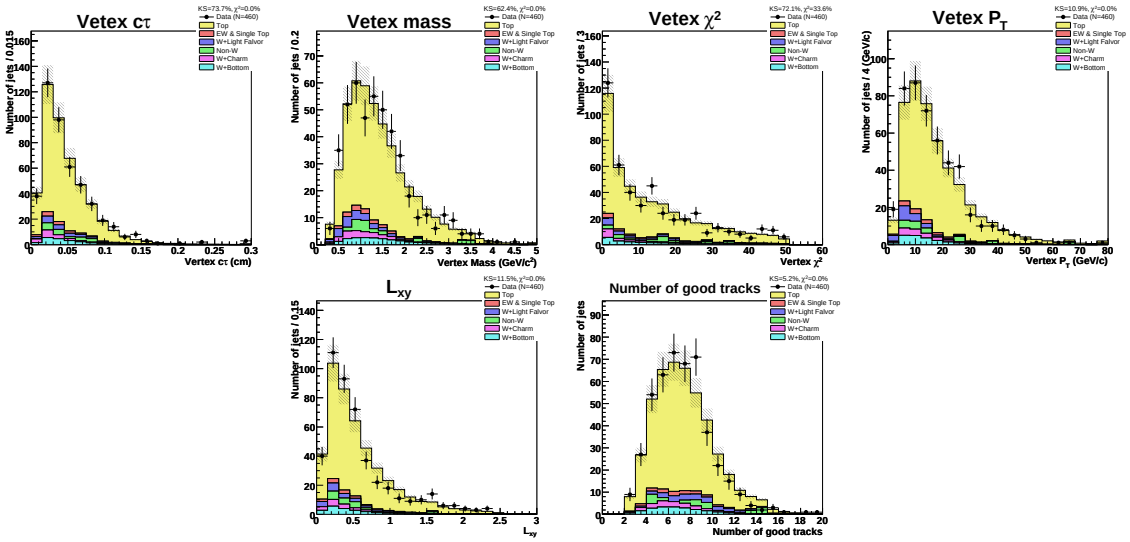

Figure D.3: *SecVtx* b-tagging related distributions.

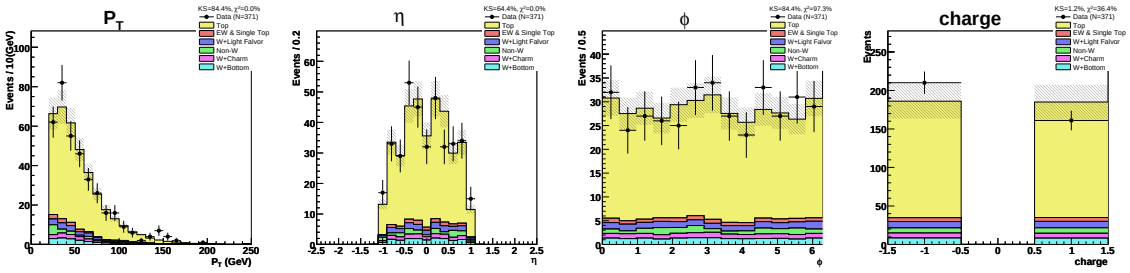

Figure D.4: Kinematic distributions of leptons.

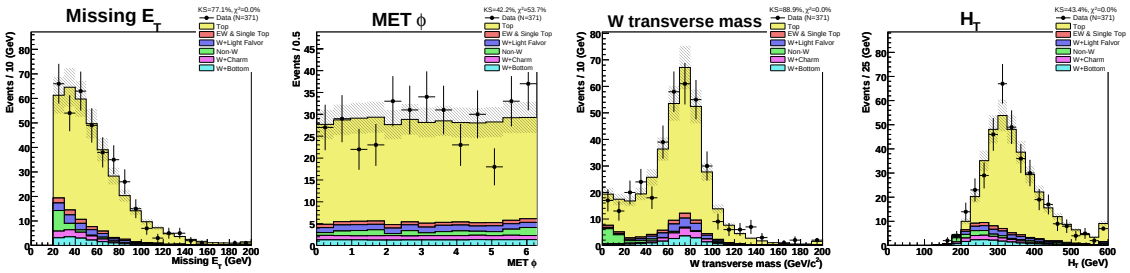

Figure D.5: The missing E_T, *phi* of $\not\!\!E_T$, W transverse mass, and H_T distributions.

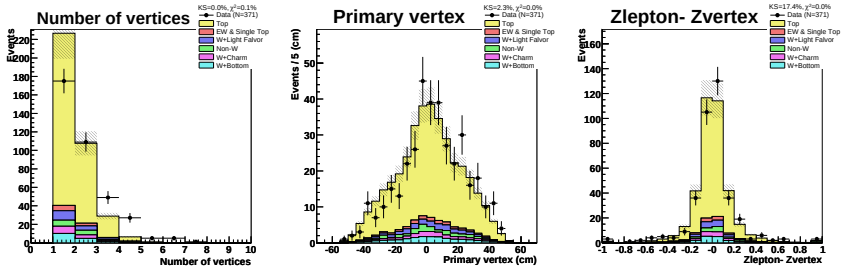

Figure D.6: Vertex related distributions.

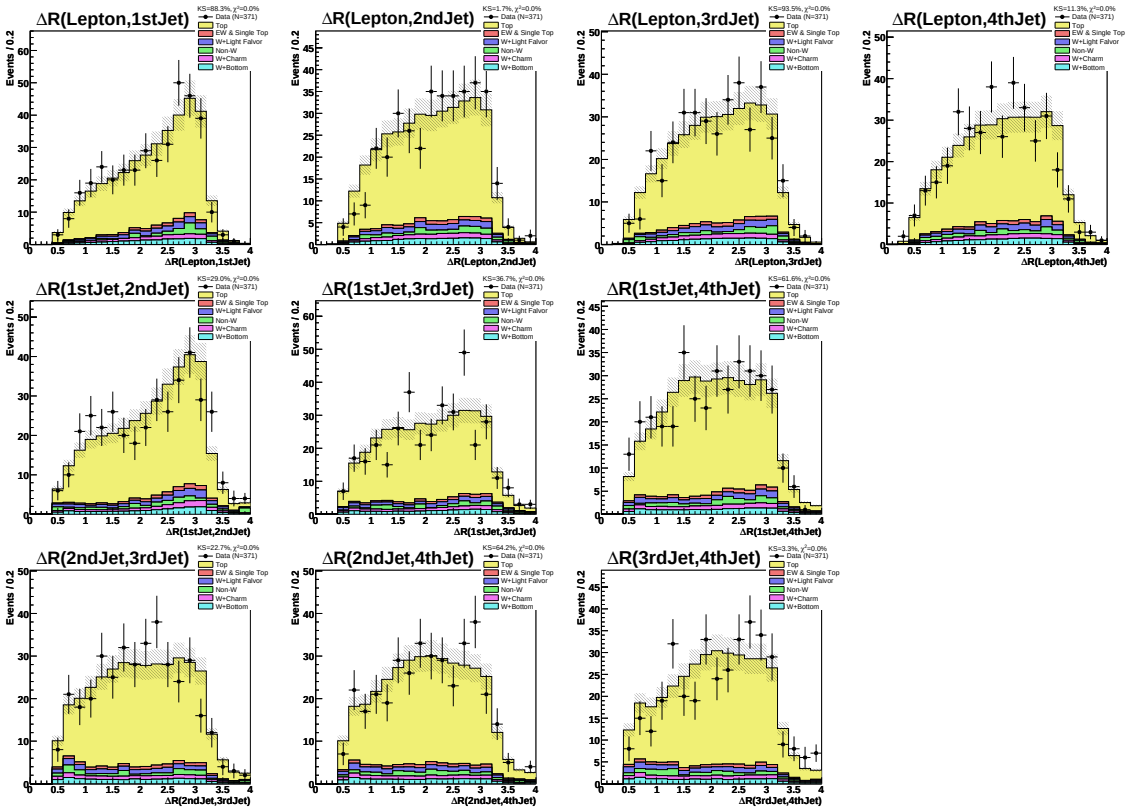

Figure D.7: ΔR distributions.

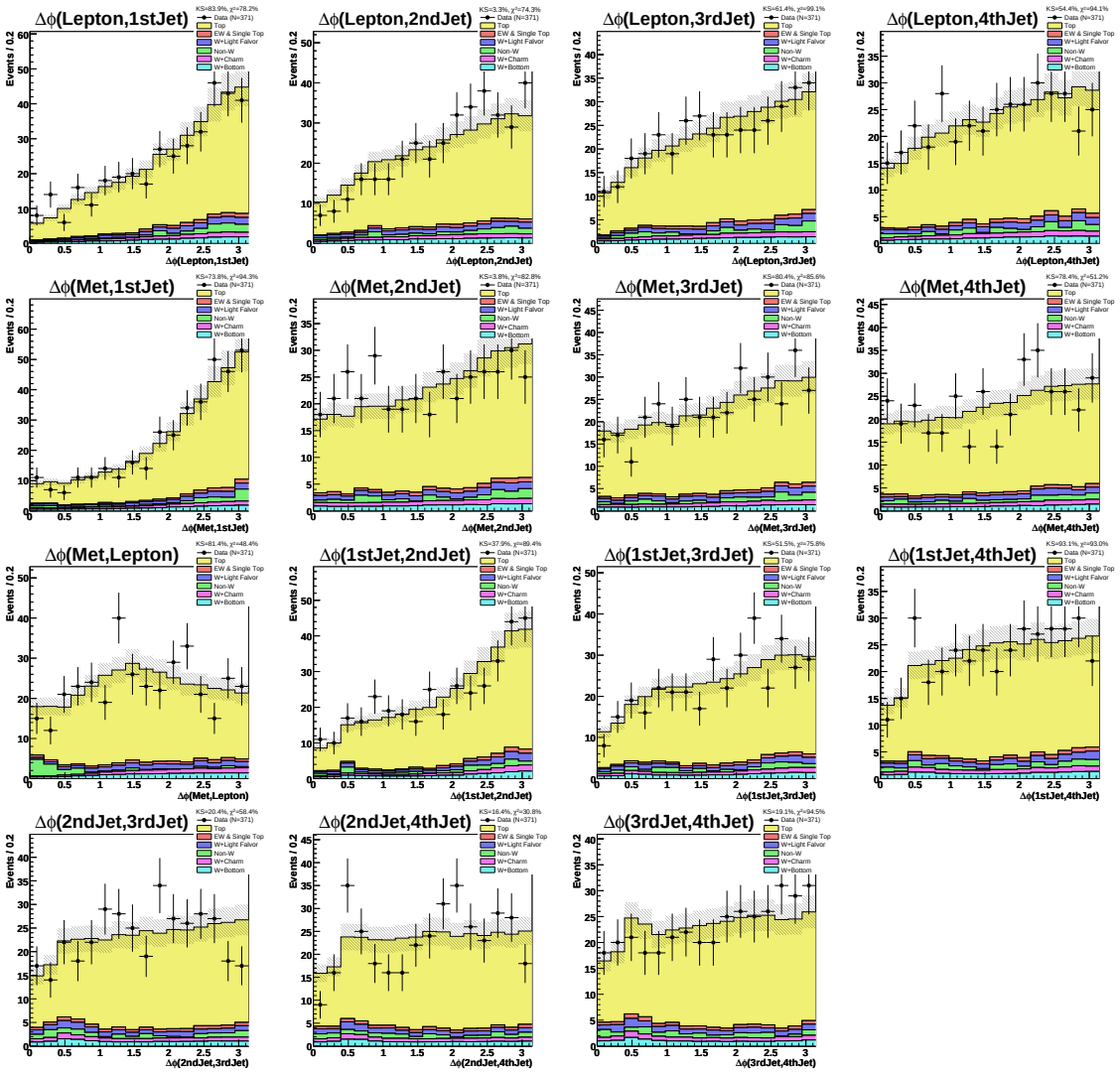

Figure D.8: $\Delta\phi$ distributions.

Bibliography

[1] D. J. Gross and F. Wilczek, "Asymptotically free gauge theories", Phys. Rev. D**8**, 3633 (1973)

[2] H. D. Politzer, "Asymptotic freedom: An approach to strong interactions", Phys. Rept., **14**, 129 (1974)

[3] S. L. Glashow, "Partial symmetries of weak interactions", Nucl. Phys., **22**, 579 (1961)

[4] A. Salam and J. C. Ward, "Electromagnetic and weak interactions", Phys. Lett., **13**, 168 (1964)

[5] S. Weinberg, "A model of leptons", Phys. Rev. Lett., **19**, 1264 (1967)

[6] P. W. Higgs, "Broken symmetries and the masses of gauge bosons", Phys. Rev. Lett. **13**, 508 (1964)

[7] R. Barate *et al.*, "Search for the standard model Higgs boson at LEP", Phys. Lett. B**565**, 61 (2003)

[8] The LEP Collaboration, The LEP Electroweak Working Group, "Precision Electroweak Measurements and Constraints on the Standard Model", Tech. Report CERN-PH-EP/2007-039, CERN, 2007

[9] E. Rice *et al.*, "Search for structure in $\sigma(e^+e^- \rightarrow \ hadrons)$ between $\sqrt{s} = 10.34$ and 11.6 GeV", Phys. Rev. Lett. **48**, 906 (1982)

[10] F. Abe *et al.*, "Observation of top quark production in $p\bar{p}$ collisions with the Collider Detector at Fermilab", Phys. Rev. Lett. **74**, 2626 (1995)

[11] S. Abachi *et al.*, "Observation of the top quark", Phys. Rev. Lett. **74**, 2632 (1995)

[12] The CDF Collaboration, the D0 Collaboration, the Tevatron Electroweak Working Group, "Combination of CDF and D0 Results on the Top-Quark Mass", hep-ex/0404010

[13] M. Cacciari *et al.*, "The $t\bar{t}$ cross-section at 1.8 and 1.96 TeV: A study of the systematics due to parton densities and scale dependence", J. High Energy Phys. **0404**, 068 (2004)

[14] The CDF Collaboration, "Combination of CDF top quark pair production cross section measurements up to 750 pb^{-1}", CDF public note, 8148 (2006)

[15] M. Kobayashi and T. Masukawa, "CP violation in the renormalizable theory of weak interaction", Prog. Theor. Phys. **49**, 652 (1973)

[16] C. Hill and S. Parke, "Top quark production: Sensitivity to new physics", Phys. Rev. D**49**, 4454 (1994)

[17] E. Eichten and K. Lane, "Multiscale technicolor and top production", Phys. Lett. B**327**, 129 (1994)

[18] T. Affolder *et al.*, The CDF Collaboration, "Search for New Particles Decaying to $t\bar{t}$ in $p\bar{p}$ Collisions at $\sqrt{s} = 1.8$ TeV", Phys. Rev. Lett. **85**, 2062 (2000)

[19] T. Aaltonen *et al.*, The CDF Collaboration, "Search for Resonant $t\bar{t}$ Production in $p\bar{p}$ Collisions at $\sqrt{s} = 1.96$ TeV", FERMILAB-PUB-0= 7-455-E. Submitted to Phys. Rev. Lett. September 6, 2007.

[20] V.M. Abazov *et al.*, The D0 Collaboration, " Search for Narrow $t\bar{t}$ Resonances in $p\bar{p}$ Collisions at $\sqrt{s} = 1.8$ TeV", Phys. Rev. Lett. **92**, 221801 (2004)

[21] T. Sjostrand *et al.*, "High-Energy-Physics Event Generation with PYTHIA 6.1", Comput. Phys. Commun. **135**, 238 (2001)

[22] Joey Thompson, "Introduction to Colliding Beams at Fermilab", FERMILAB-TM-1909
The detailed information is available at the web pages.
`http://www-bdnew.fnal.gov/operations/rookie_books/rbooks.html`
`http://www-bd.fnal.gov/lug/runII_handbook/RunII_index.html`

[23] D. Patterson, "The FNAL 200-MeV Linac", FERMILAB-MISC-1986-01

[24] C.W. Schmidt, "Review of Negative Hydrogen Ion Sources", FERMILAB-LU-166

[25] Cockcroft, J.D. and Walton, E.T.S., "Experiments with High Velocity Positive Ions. II. The Disintegration of Elements by High Velocity Protons", Proc. R. Soc. London A**137**, 229 (1932)

[26] L. W. Alvarez *et al.*, "Berkeley Proton Linear Accelerator", Rev. Sci. Instr. **26**, 111 (1955)

[27] E.L. Hubbard, "Booster Synchrotron", FERMILAB-TM-0405

[28] C. Hojvat *et al.*, "The Multiturn Charge Exchange Injection System for the Fermilab Booster Accelerator", *IEEE Transactions on Nuclear Science*, NS-**26**, 3149 (1979)

[29] S. D. Holmes, " Status of the Fermilab Main Injector and Recycler", FERMILAB-CONF-97-298

[30] M. D. Church and J. P. Marriner, "The Antiproton Sources: Design and Operation", *Annu. Rev. Nucl. Part. Sci.*, **43**, 253 (1993)

[31] D. M. Mohl, G. Petrucci, L. Thorndahl and S. van der Meer, "Physics and technique of stochastic cooling", Phys. Rep. **58**, 73 (1980)

[32] G. Jackson, "The Fermilab recycler ring technical design report. Rev. 1.2", FERMILAB-TM-1991

[33] S. Nagaitsev *et al.*, " Experimental Demonstration of Relativistic Electron Cooling", Phys. Rev. Lett. **96**, 044801 (2006)

[34] "Design report Tevatron 1 Project", FERMILAB-DESIGN-1982-01

[35] F. Abe *et al.*, "The CDF II detector: Technical design report", Tech. Report FERMILAB-Pub-96/390-E (1996)

[36] A. Sill *et al.*, "SVX-II: CDF Run II silicon tracking projects", Nucl. Instrum. Method, A**447**, 1 (2000)

[37] C. S. Hill *et al.*, "L00: Operational experience and performance of the CDF II silicon detector", Nucl. Instrum. Methods, A**530**, 1 (2004)

[38] A. Affolder *et al.*, "ISL: Intermediate silicon layers detector for the CDF experiment", Nucl. Instrum. Method A**543**, 84 (2000)

[39] T. Affolder *et al.*, "COT central outer tracker", Nucl. Instrum. Methods, A**526**, 249 (2004)

[40] L. Balka *et al.*, "The CDF central electromagnetic calorimeter", Nucl. Instrum. Methods, A**267**, 272 (1988)

[41] S. Bertolucci *et al.*, "The CDF central and endwall hadronic calorimeters", Nucl. Instrum. Methods, A**267**, 301 (1988)

[42] M. Albrow *et al.*, "The CDF plug upgrade electromagnetic calorimeter: Test beam result", Nucl. Instrum. Methods, A**480**, 524 (2002)

[43] "Shower Maximum Detector for the CDF Plug Upgrade Calorimeter", Nucl. Instrum. Meth. A**412**, 515 (1998)

[44] G. Ascoli *et al.*, "The CDF central muon detector", Nucl. Instrum. Methods, A**268**, 33 (1988)

[45] T. Affolder *et al.*, "Measurement of the Top Quark Mass with the Collider Detector at Fermilab", Phys. Rev. D**63**, 032003 (2001)

[46] A. Abulencia *et al.*, "Measurement of the tt-bar Production Cross Section in p anti-p Collisions at $\sqrt{s} = 1.96$ TeV ", Phys. Rev. Lett. **97**, 082004 (2006)

[47] D. Buskulic *et al.*, "Measurements of R_b with impact parameters and displaced vertices", Phys. Lett. B**313**, 535 (1993)

[48] A. Abulencia *et al.*, "Measurement of the tt-bar Production Cross Section in $p\bar{p}$ Collisions at $\sqrt{s} = 1.96$ TeV using Lepton + Jets Events with Jet Probability b-tagging", Phys. Rev. D**74**, 072006 (2006)

[49] D. Acosta *et al.*, "The CDF Luminosity Monitor", Nucl. Instrum. Meth. A**461**, 540 (2001)

[50] K.Kondo, "Dynamical Likelihood Method for Reconstruction of Events with missing Momentum", J. Phys. Soc. Jpn, **57**, 4126 (1988)

[51] K.Kondo, "Dynamical Likelihood Method for Reconstruction of Events with missing Momentum2", J. Phys. Soc. Jpn, **60**, 836 (1991)

[52] K.Kondo, T. Chikamatsu and S.Kim, "Dynamical Likelihood Method for Reconstruction of Events with missing Momentum3", J. Phys. Soc. Jpn, **62**, 1177 (1993)

[53] K.Kondo, "Dynamical Likelihood Method for Reconstruction of Quantum Process", arXiv:hep-ex/0508035

[54] A. Abulencia *et al.*, "Measurement of the Top Quark Mass with the Dynamical Likelihood Method using Lepton plus Jets Events with b-tags in $p\bar{p}$ Collisions at $\sqrt{s} = 1.96$ TeV ", Phys. Rev. D**73**, 092002 (2006)

[55] A. Abulencia *et al.*, "Precise Measurement of the Top Quark Mass in the Lepton+Jets Topology at CDF II", Phys. Rev. Lett. **99**, 182002 (2007)

[56] P. J. Smith, M.Shafi, and H. Gao, "Quick simulation: A review of importance sampling techniques in communication systems", IEEE J.Select.Areas Commun., **15**, 597 (1997)

[57] G. Cowan, Oxford University Press, "Statistical Data Analysis"

[58] A. Bhatti *et al.*, "Determination of the jet energy scale at the Collider Detector at Fermilab", NIM A**556**, 375 (2006)

[59] The Tevatron Electroweak Working Group, "Combination of CDF and D0 Results on the Mass of the Top Quark", arXiv:hep-ex/0703034

[60] H.L. Lai *et al.*, CTEQ Collaboration, "Global QCD Analysis of Parton Structure of the Nucleon: CTEQ5 Parton Distributions", Eur. Phys. J. C**12**, 375 (2000)
J. Pumplin *et al.*, "New Generation of Parton Distributions with Uncertainties from Global QCD Analysis", JHEP 0207, 012 (2002)
`http://www.phys.psu.edu/~cteq/`

[61] A.D. Martin *et al.*, "Parton Distributions and the LHC: W and Z Production", Eur. Phys. J. C**14**, 133 (2000)
`http://durpdg.dur.ac.uk/hepdata/mrs.html`

[62] A. Abulencia *et al.*, The CDF Collaboration, "Top Quark Mass Measurement Using the Template Method in the Lepton + Jets Channel at CDF II", Phys. Rev. D**73**, 032003 (2006)

[63] G. Corcella *et al.*, "HERWIG 6.5: an event generator for Hadron Emission Reactions With Interfering Gluons (including supersymmetric processes)", JHEP 0101, 010 (2001)

[64] S. Frixione and B.R. Webber, "Matching NLO QCD computations and parton shower simulations", JHEP 0206, 029 (2002)
S. Frixione, P. Nason and B.R. Webber, "Matching NLO QCD and parton showers in heavy flavour production", JHEP 0308, 007 (2003)

[65] M.L. Mangano, M. Moretti, F. Piccinini, R. Pittau, A. Polosa, "ALPGEN, a generator for hard multiparton processes in hadronic collisions", JHEP **0307**, 001 (2003), hep-ph/0206293

[66] CERN Program Library entry, D506

[67] T. Aaltonen *et al.*, The CDF Collaboration, "First Measurement of the Production of a W Boson in Association with a Single Charm Quark in $p\bar{p}$ Collisions at $\sqrt{s} = 1.96$ TeV", arXiv:hep-ex/07112901

[68] The CDF Collaboration, "Measurement of the b-jet Cross-Section for $W^{\pm} + b\bar{b}$", CDF public note, 8410 (2006)

Appendix E

Publication List

.

Published Papers

1. A. Abulencia *et al.*, The CDF Collaboration, "Precise Measurement of the Top Quark Mass in the Lepton+Jets Topology at CDF II", Phys. Rev. Lett. **99**, 182002 (2007)

2. A. Abulencia *et al.*, The CDF Collaboration, "Measurement of the $t\bar{t}$ Production Cross Section in $p\bar{p}$ Collisions at $\sqrt{s} = 1.96$ TeV using Lepton+Jets Events with Jet Probability b-tagging", Phys. Rev. D **74**, 072006 (2006)

3. A. Abulencia *et al.*, The CDF Collaboration, "Measurement of the $t\bar{t}$ Production Cross Section in $p\bar{p}$ Collisions at $\sqrt{s} = 1.96$ TeV", Phys. Rev. Lett. **97**, 082004 (2006)

Oral Reports

1. J. Naganoma, "Search for Resonant $t\bar{t}$ Pair Production in the Lepton+Jets Channel at CDF", American Physical Society Meeting, Jacksonville, Florida, April 2007

2. J.Naganoma, "Top Quark Properties at CDF", DOE Annual Fermilab Program Review Poster Session, Fermilab, Batavia, Illinois, May 2006